

ELECTROCHEMICAL CHARACTERIZATION AND MODELING OF FUEL CELLS  
VIA AC IMPEDANCE AND RESIDENCE TIME DISTRIBUTION

Except where reference is made to the work of others, the work described in this dissertation is my own or was done in collaboration with my advisory committee.  
This dissertation does not include proprietary or classified information.

---

Robert Rex Underwood Payne

Certificate of Approval:

---

W. Robert Ashurst  
Assistant Professor  
Chemical Engineering

---

Bruce J. Tatarchuk, Chair  
Professor  
Chemical Engineering

---

Jin Wang  
Assistant Professor  
Redd Eminent Scholar Chair  
Chemical Engineering

---

R. Mark Nelms  
Professor  
Electrical Engineering

---

George T. Flowers  
Dean  
Graduate School

ELECTROCHEMICAL CHARACTERIZATION AND MODELING OF FUEL CELLS  
VIA AC IMPEDANCE AND RESIDENCE TIME DISTRIBUTION

Robert R. U. Payne

A Dissertation  
Submitted to  
the Graduate Faculty of  
Auburn University  
in Partial Fulfillment of the  
Requirements for the  
Degree of  
Doctor of Philosophy

Auburn, Alabama  
December 19, 2008

ELECTROCHEMICAL CHARACTERIZATION AND MODELING OF FUEL CELLS  
VIA AC IMPEDANCE AND RESIDENCE TIME DISTRIBUTION

Robert Rex Underwood Payne

Permission is granted to Auburn University to make copies of this dissertation at its discretion, upon request of individuals or institutions and at their expense. The author reserves all publication rights.

---

Signature of Author

---

Date of Graduation

## VITA

Robert Rex Underwood Payne, son of Dr. Robert Rex and Lila Ward Payne, was born in Birmingham, Alabama on Super Bowl Sunday January 20, 1980. He graduated in 1998 from Christ Church Episcopal School in Greenville, South Carolina, where he starred in football wearing number 88 in honor of Auburn University wide receiver Terry Beasley and Pittsburgh Steelers legend Lynn Swann (who won his fourth and final Super Bowl on the author's birthday). He attended the University of the South in Sewanee, Tennessee, where he expanded his mind to understand the forces of the universe while majoring in Physics and minoring in Theatre. During a thermodynamics class in 2001, he learned about fuel cells, which ignited a desire to pursue a career in researching and developing them. He earned his Bachelors of Science degree in 2002, at which time he had determined he would seek a chemical engineering degree, although he knew not where. After three weeks in Europe, he resolved that he would decline Washington University in Saint Louis and instead enroll in Auburn University, where both of his parents and several other relatives had previously studied. Two weeks later while visiting his father in Birmingham, he met his soul mate Katherine Beck Coxhead, daughter of George Leavell and Susan Cross Coxhead. In August of 2003, he entered graduate school after completing the requisite undergraduate courses over the previous year. On May 27, 2006, he and Katherine were married in Gadsden, Alabama, and the couple is expecting their first child near his graduation date in December of 2008.



DISSERTATION ABSTRACT  
ELECTROCHEMICAL CHARACTERIZATION AND MODELING OF FUEL CELLS  
VIA AC IMPEDANCE AND RESIDENCE TIME DISTRIBUTION

Robert Rex Underwood Payne

Doctor of Philosophy, December 19, 2008  
(B.S., The University of the South, 2002)

277 Typed Pages

Directed by Bruce J. Tatarchuk

The performance of commercially available fuel cells was tested under a variety of test conditions and models were formulated to explain the experimental results. Several techniques were applied to single cells and groups of cells, each probing a different phenomenon responsible for limiting the power output of the cells.

Nonuniformity of fuel cells in a stack can drastically affect the total power output, because a stack of cells in series can only provide as much electrical current as the weakest cell. Uniformity of polymer electrolyte membrane (PEM) fuel cell voltage was measured for each cell of the 47 cells in a Nexa™ stack operating with 0 W and 800W supplied to an external load. Manufacturing consistency was assessed by comparing the mean cell potential of 10 different stacks.

To minimize the cost of operating a stack, PEM fuel cells must be capable of withstanding higher impurity concentrations, which was accomplished by adding a manual purge line into the fuel exhaust line of a Nexa™ stack. The critical flow rate of the anode exhaust was determined by feeding gas diluted with up to 7% N<sub>2</sub> to a stack supplying up to 200 W to an external load. The residence time distribution (RTD) of impurities in the stack was evaluated by injecting a pulse of inert gas and simultaneously measuring the time dependent voltage of each cell in the stack. A number of different compartmental flow models were developed to replicate the experimental data, but with minimal success; however, the added exhaust line successfully improved the impurity tolerance of the stack.

Determining which and to what extent physical processes limit the electrical output of fuel cells is critical for evaluating system designs and performing diagnostics. Impedance spectroscopy was applied to cells to test the dynamic response of fuel cells and stacks thereof. Equivalent circuit models were fitted to the data, with each circuit element representing a different physical phenomenon. Data were measured at load currents for individual and groups of cells in the Nexa™ stack and to solid oxide button cells and larger cells in a 5-cell planar stack. A pulsed load was applied to individual NEXA™ stacks and stack pairs in series and parallel, and the dynamic potential response was measured. A similar pulsed load was applied to the stack model to simulate the resulting potential wave, which compared favorably with the experimental data. By testing uniformity, impurity tolerance, and dynamic load response, valuable information about fuel cells has been obtained and may be predicted from the formulated models.

## ACKNOWLEDGEMENTS

The work presented herein was supported by the US Army through contracts DASG 60-00-C-0070 and W56HZV-05-C0686. The author would like to thank his advisor, Dr. Bruce Tatarchuk, for the opportunity to study the subject that motivated him to become a chemical engineer and for his ideas, which he freely shared. The author would also like to thank Dr. Wenhua Zhu for his motivation and general expertise. Additionally, he would like to express his gratitude to his committee for their suggestions and discussion.

The author would especially like to thank his wife for her enduring patience, support, and understanding throughout this process.

Style manual or journal used:           *The Journal of Power Sources*          

Computer software used:                           Microsoft Word

## TABLE OF CONTENTS

|  |   |    |
|--|---|----|
| List of Tables                                     | xii   |    |
| List of Figures                                    | xiv   |    |
| Section A: Introduction and Literature Review      |   |    |
| I  | General Introduction  | 1  |
| II   | Literature Review   | 4  |
|  | II.1 Electrochemistry of Fuel Cells   | 4  |
|  | II.1.1 General Concepts   | 4  |
|  | II.1.2 Thermodynamics of Reactions  | 6  |
|  | II.1.3 Reaction Kinetics  | 8  |
|  | II.2 Fuel Cell Components   | 12 |
|  | II.2.1 History of the PEMFC   | 12 |
|  | II.2.2 Polymer Electrolyte  | 13 |
|  | II.2.3 Electrode Catalyst Layer   | 15 |
|  | II.2.4 Membrane Electrode Assembly  | 18 |
|  | II.2.5 Flow Field Plate   | 19 |
|  | II.2.6 Current Collector  | 19 |
|  | II.3 Measurement Techniques Applicable to Fuel Cells                        | 20 |
|  | II.3.1 Residence Time Distribution Theory                                   | 20 |
|  | II.3.2 Polarization Curves  | 24 |
|  | II.3.3 Electrochemical Impedance Spectroscopy                               | 27 |
|  | II.4 Nomenclature   | 33 |
|  | II.5 References   | 36 |
| Section B: Articles Submitted to Refereed Journals |   |    |
| III  | Uniformity Analysis at MEA and Stack Levels for a Nexa PEM Fuel Cell System | 51 |
|  | III.1 Introduction  | 51 |
|  | III.2 Experimental  | 52 |
|  | III.3 Results and Discussion  | 53 |
|  | III.3.1 Nexa™ Stack Warm-Up and Cool-Down                                   | 53 |
|  | III.3.2 Stack Polarization Curves   | 54 |
|  | III.3.3 MEA and Stack Uniformity  | 55 |
|  | III.3.4 MEA and Stack Statistic Data Analysis                               | 56 |

|       |  |     |
|-------|--|-----|
| III.4 | Conclusion   | 58  |
| III.5 | Acknowledgements   | 58  |
| III.6 | References   | 59  |
| IV    | Critical Flow Rate of Anode Fuel Exhaust in a PEM Fuel Cell System                 | 72  |
| IV.1  | Introduction   | 72  |
| IV.2  | Experimental   | 73  |
| IV.3  | Results and Discussion   | 75  |
|       | IV.3.1 Fuel Gas and Its Exhaust Management in the Anode Stream                     | 75  |
|       | IV.3.2 Purge Cell and MEA Voltage in the Stack                                     | 78  |
|       | IV.3.3 Critical Flow Rate of the Anode Fuel Exhaust                                | 80  |
|       | IV.3.4 Fuel Cell Stack Efficiency and Overall System Efficiency                    | 83  |
| IV.4  | Conclusions  | 85  |
| IV.5  | Acknowledgements   | 86  |
| IV.6  | Nomenclature   | 86  |
| IV.7  | References   | 88  |
| V     | PEM Stack Test and Analysis in a Power System at Operational Load via AC Impedance | 97  |
| V.1   | Introduction   | 97  |
| V.2   | Experimental Details   | 99  |
| V.3   | Results and Discussion   | 101 |
|       | V.3.1 Small Signal Applied to the EIS Test   | 101 |
|       | V.3.2 Ohmic Resistance in the Nyquist Plots  | 102 |
|       | V.3.3 Single Cell Tests and Impedance Data Interpretation                          | 103 |
|       | V.3.4 Group Cell Tests and Impedance Data Interpretation                           | 104 |
|       | V.3.5 Stack Test and Impedance Data Interpretation                                 | 105 |
| V.4   | Conclusion   | 110 |
| V.5   | Acknowledgements   | 111 |
| V.6   | References   | 111 |
| VI    | Equivalent Circuit Elements for PSpice Simulation of PEM Stacks at Pulse Load      | 120 |
| VI.1  | Introduction   | 120 |
| VI.2  | Experimental   | 123 |
| VI.3  | Results and Discussion   | 127 |
|       | VI.3.1 Stack Current-Voltage Curves Through Periodic Current Interruption          | 127 |
|       | VI.3.2 Stack Impedance Data and Simulation   | 127 |
|       | VI.3.3 Stack Operation in Parallel   | 131 |
|       | VI.3.4 Stack Operation in Series   | 132 |
|       | VI.3.5 PSpice Simulation versus Experimental Data                                  | 133 |
| VI.4  | Conclusions  | 135 |
| VI.5  | Acknowledgements   | 136 |

|                             |   |     |
|-----------------------------|---|-----|
| VI.6                        | References  | 136 |
| VII                         | Equivalent Circuit Modeling of SOFC cells and Stacks at Load  | 152 |
| VII.1                       | Introduction  | 152 |
| VII.2                       | Experimental  | 153 |
| VII.3                       | Results and Discussion  | 155 |
|                             | VII.3.1 Button Cells  | 155 |
|                             | VII.3.2 Full Cell Stack   | 167 |
| VII.4                       | Conclusions   | 174 |
| VII.5                       | Acknowledgements  | 175 |
| VII.6                       | Nomenclature  | 175 |
| VII.7                       | References  | 176 |
| Section C: Unpublished Work |   |     |
| VIII                        | Equivalent Circuit Models and Kinetic Parameters for Commercial PEM Fuel Cells Obtained from Impedance Spectroscopy | 200 |
| VIII.1                      | Introduction  | 200 |
| VIII.2                      | Experimental  | 201 |
| VIII.3                      | Equivalent Circuit Models   | 202 |
|                             | VIII.3.1 Cathode Equivalent Circuit   | 204 |
|                             | VIII.3.2 Anode Equivalent Circuit and Kinetic Parameters  | 205 |
| VIII.4                      | Summary   | 209 |
| VIII.5                      | Nomenclature  | 209 |
| VIII.6                      | References  | 211 |
| IX                          | Residence Time Distribution of Anode Impurity Pulses in a PEM Stack   | 222 |
| IX.1                        | Introduction  | 222 |
| IX.2                        | Experimental  | 223 |
| IX.3                        | Experimental Results  | 224 |
|                             | IX.3.1 Determining Anode Volume   | 226 |
|                             | IX.3.2 Determining Crossover  | 227 |
|                             | IX.3.3 Model Description  | 228 |
|                             | IX.3.4 Manifold Model   | 229 |
|                             | IX.3.5 Fuel Cell Models   | 231 |
| IX.4                        | Summary   | 239 |
| IX.5                        | Nomenclature  | 239 |
| IX.6                        | References  | 242 |
| X                           | Conclusions and Future Recommendations  | 255 |
| X.1                         | Conclusions   | 255 |
|                             | X.1.1 Chemical Techniques   | 255 |
|                             | X.1.2 Electric Techniques   | 256 |
| X.2                         | Future Recommendations  | 257 |
|                             | X.2.1 Further SOFC Applications   | 257 |

|       |   |     |
|-------|---|-----|
| X.2.2 | Improving Evaluation of Kinetic Constants | 258 |
| X.2.3 | Improving RTD Measurements                | 258 |



## LIST OF TABLES

|     |   |     |
|-----|---|-----|
| 2.1 | Enthalpies and Entropy Values at Different Temperatures   | 39  |
| 2.2 | Names and Attributes of Different Fuel Cells  | 40  |
| 2.3 | Exchange Current Density of HOR and ORR on Different Metals                                     | 41  |
| 2.4 | Impedance Equations for Different Circuit Elements  | 42  |
| 3.1 | Statistical Analysis of MEA Voltage   | 60  |
| 4.1 | Fuel and Exhaust Gas Composition from 50 to 200 W at Different Flow Rates                       | 89  |
| 5.1 | Membrane Thickness Estimation   | 113 |
| 6.1 | Fitted Circuit Elements for Individual Stacks   | 139 |
| 6.2 | Fitted Circuit Elements for Stack Pairs in Series and Parallel                                  | 140 |
| 6.3 | Comparison of Pulse Voltage between Simulation and Measurement                                  | 141 |
| 7.1 | Fitted Circuit Elements for Button Cell Anodes with Different Catalysts                         | 180 |
| 7.2 | Fitted Circuit Elements for Button Cell Anodes at Varying Temperature and Load Current          | 181 |
| 7.3 | Fitted Circuit Elements for Button Cell Cathodes at Varying Temperature and Load Current        | 182 |
| 7.4 | Comparison of Fitted Values Between a Parallel RC and Finite Diffusion Element for Button Cells | 183 |
| 7.5 | Fitted Circuit Elements for Planar Cells with Varying Anode Feeds                               | 184 |
| 7.6 | Fitted Circuit Elements for Planar Cells at Varying Load Currents                               | 185 |
| 7.7 | Comparison of Fitted Values Between Button Cells and Planar Cells                               | 186 |

|     |   |     |
|-----|---|-----|
| 7.8 | Comparison of Fitted Values Between a Parallel RC and Finite Diffusion Element for Planar Cells | 187 |
| 8.1 | Fit Parameters for Different Three RC Models  | 213 |
| 8.2 | Fit Parameters of RL Model and Nested RC Model  | 214 |
| 8.3 | Reaction Parameters Obtained from Equivalent Circuit Fits                                       | 215 |
| 9.1 | Number of Tanks-in-Series Required to Model the Manifold  | 244 |

## LIST OF FIGURES

|      |  |    |
|------|--|----|
| 2.1  | Diagram of Grove's Cell                                    | 43 |
| 2.2  | Diagram of Nafion Structure                                | 44 |
| 2.3  | Diagram of Flow Field Patterns                             | 45 |
| 2.4  | Diagram of Tanks-In-Series Model                           | 46 |
| 2.5  | Typical Polarization Curve for a Fuel Cell                 | 47 |
| 2.6  | Nyquist Plot for a Single Electrode                        | 48 |
| 2.7  | Bode Plot for a Single Electrode                           | 49 |
| 2.8  | Nyquist Plot for the Finite Diffusion Element              | 50 |
| 3.1  | Diagram of Single PEM Fuel Cell                            | 61 |
| 3.2  | Picture of Nexa™ Power Module                              | 62 |
| 3.3  | Startup Parameters Plotted as Functions of Time            | 63 |
| 3.4  | Stack Temperature at Different Loads                       | 64 |
| 3.5  | Stack Cool-Down Curves                                     | 65 |
| 3.6  | Polarization Curves at Different Temperatures              | 66 |
| 3.7  | Stack Resistance and Power Plotted as Functions of Current | 67 |
| 3.8  | Individual Cell Voltages for Ten Different Stacks          | 68 |
| 3.9  | Comparison of Cell Voltages with 0 and 800 W at Load       | 69 |
| 3.10 | Distribution Curves of Cells at 800 W                      | 70 |
| 3.11 | Statistical MEA Voltage in Ten Different Stacks            | 71 |

|     |  |     |
|-----|--|-----|
| 4.1 | Diagram of Experimental Setup  | 90  |
| 4.2 | Simple Flow Diagram for Fuel Cell Stack  | 91  |
| 4.3 | Purge Cell Voltage with Different Compositions and Exhaust Flow Rates          | 92  |
| 4.4 | Purge Cell Voltage with Different Exhaust Flow Rates                           | 93  |
| 4.5 | Purge Cell Voltage at 200 W, 700 W, and 1200 W                                 | 94  |
| 4.6 | Purge Cell Voltage at 100 W and 200 W  | 95  |
| 4.7 | Purge Cell Voltage with Hydrocarbon Reformate Feed                             | 96  |
| 5.1 | Theoretical Nyquist Plot of a PEM Fuel Cell                                    | 114 |
| 5.2 | Nyquist Plots of Individual Cells at Different Currents                        | 115 |
| 5.3 | Nyquist Plots of Cell Groups at .20 A  | 116 |
| 5.4 | Nyquist Plots of Cell Groups at 5.0 A  | 117 |
| 5.5 | Nyquist Plots of Stack #308 at Different Currents with System Controller       | 118 |
| 5.6 | Nyquist Plots of Stack #308 at Different Currents without System<br>Controller | 119 |
| 6.1 | Diagram of AC Impedance Measurements   | 142 |
| 6.2 | Polarization Curves at Different Temperatures                                  | 143 |
| 6.3 | Bode Plots of Stack #515   | 144 |
| 6.4 | Nyquist Plots of Stack #515  | 145 |
| 6.5 | Nyquist Plots of Stack # 818   | 146 |
| 6.6 | Nyquist Plots of Stacks in Parallel  | 147 |
| 6.7 | Nyquist Plots of Stacks in Series  | 148 |
| 6.8 | Comparison of Simulation to Experimental Data for Stack #515                   | 149 |

|      |  |     |
|------|--|-----|
| 6.9  | Comparison of Simulation to Experimental Data for Stacks in Parallel | 150 |
| 6.10 | Comparison of Simulation to Experimental Data for Stacks in Series   | 151 |
| 7.1  | Picture of Button Cell   | 188 |
| 7.2  | Picture of Planar Cell   | 189 |
| 7.3  | Nyquist Plot of Button Cell Anode with Varying Concentration         | 190 |
| 7.4  | Equivalent Circuit for Button Cell Anode                             | 191 |
| 7.5  | Equivalent Circuit for Button Cell Cathode                           | 192 |
| 7.6  | Nyquist Plot of Button Cell Cathode with Varying Concentration       | 193 |
| 7.7  | Comparison of Sum of Electrodes to Total Cell Nyquist plot           | 194 |
| 7.8  | Nyquist Plots of Planar Cell Fitted to Differing Time Constants      | 195 |
| 7.9  | Potential of Reference Electrodes as a Function of Load Current      | 196 |
| 7.10 | Nyquist Plot of Button Cell Cathode from Total-Cell Fits             | 197 |
| 7.11 | Planar Cell Equivalent Circuit Model                                 | 198 |
| 7.12 | Nyquist Plot of Stack Fitted to Differing Time Constants             | 199 |
| 8.1  | Three RC Equivalent Circuit with a Nested RC                         | 216 |
| 8.2  | Cathode Equivalent Circuit at High Current                           | 217 |
| 8.3  | Nyquist Plots Fitted with Two Cathode Models                         | 218 |
| 8.4  | Exchange Current from Equivalent Circuit with Capacitor              | 219 |
| 8.5  | Exchange Current from Equivalent Circuit with Phase Element          | 220 |
| 8.6  | Anode Equivalent Circuit with Adsorption                             | 221 |
| 9.1  | Evenly Spaced Cell Voltages with Offset                              | 245 |
| 9.2  | Cell Voltages near the Anode Outlet with Offset                      | 246 |

|      |   |     |
|------|---|-----|
| 9.3  | All Cell Voltages with No Offset                                    | 247 |
| 9.4  | Diagram of Flow Scheme from Ballard <sup>®</sup> Patent             | 248 |
| 9.5  | Cell Voltages near the Anode Outlet at Higher Flow Rate with Offset | 249 |
| 9.6  | Picture of Septum and Pipe Feeding the Anode                        | 250 |
| 9.7  | Comparison of Experimental Data to Stirred Model Predictions        | 251 |
| 9.8  | Comparison of Experimental Data to Plug Model Predictions           | 252 |
| 9.9  | Diagram of the Mixed Model  | 253 |
| 9.10 | Comparison of Experimental Data to Mixed Model Predictions          | 254 |

## **Section A**

### **Introduction and Literature Review**

#### **Chapter I**

##### **General Introduction**

Energy production is a critical issue of the present day, being discussed as frequently in the global main stream media as in the scientific community. Most of the attention is due to concerns about fossil fuels, which are the world's leading source for energy production. The price of oil is currently one of the most prevalent issues in the US and has been rising since the 1970's due in part to the inflationary practices of central banks. Environmental concerns are also associated with fossil fuels, not just in the area where they are extracted, but also everywhere else due to exhausted greenhouse gas. Political issues precipitate from the environmental issues, as oil production is limited in the US; hence, the US is at the mercy of oil producing nations, with whom relations are strained. Politicians further exploit the environmental concerns to aggrandize the government by means such as proposing new taxes on carbon emission. The problem is compounded by the exponential growth in energy demand, so the need for alternate energy sources is paramount. Fuel cells are a form of alternate energy that may constitute

a sizable chunk of the world's energy, after they have been further researched and developed.

The work presented in this dissertation involves electrochemical measurement techniques applied to fuel cell stacks in order to formulate models that predict said behavior. These techniques and models can be more electrical in origin or more chemical; however, they help to bridge gap between the disciplines of electrical and chemical engineering. Primarily, the research contained herein is related to stack uniformity, impurity tolerance, and dynamic response of fuel cells.

The work is divided into three sections, each with a number of chapters. The first section is an introduction to fuel cells, basic electrochemistry, and some of the measurement techniques used in the experiments. The second section consists of four articles published in the *Journal of Power Sources* and a fifth that is in submission. The first article is a study of uniformity of cells in a stack and of different stacks showing that manufacturing inconsistency and stack design resulting in decreased performance of certain cells and stacks. The next chapter examines the benefits of continuously purging the anode gas manifold, which is proven to improve stack impurity tolerance. The last three articles in the second section focus on impedance spectroscopy measurements, which are fitted to equivalent circuit models to understand the dynamic behavior of fuel cells and to determine which and to what extent physical processes are limiting cell performance. The third section contains two chapters that were not deemed suitable or worthwhile for publication. The first exhibits how equivalent circuit models fitted to impedance spectra may be used to obtain kinetic parameters. The final chapter gives



extensive results on residence time distribution experiments, to which compartmental flow models were fitted.

Fuel cell models, such as those mentioned in this work, are an integral part to enabling real-world fuel cells to become more prevalent power sources. Models are helpful for designing new fuel cell systems and performing diagnostics on underperforming stacks. Tests have been performed on commercially available fuel cell stacks in order to formulate predictive models explaining concepts of electrochemistry, reaction engineering, and fluid dynamics.

## Chapter II

### Literature Review

The following chapter is a review of the fundamental concepts and techniques utilized in this research including: (i) electrochemistry of fuel cells, (ii) fuel cell components, and (iii) measurement techniques applicable to fuel cells.

#### II.1. Electrochemistry of Fuel Cells

##### *II.1.1. General Concepts*

A fuel cell is an electrochemical device that converts the chemical energy stored in its reactants into electrical energy by means of a chemical reaction. Fuel cells operate on the same premise as batteries; however, fuel cells are continuously fed, whereas batteries have an exhaustible fuel supply. The reactants are supplied to separate electrodes where they are oxidized or reduced. The reduced species in most fuel cell applications is oxygen, while the oxidized species (fuel) is a hydrogen carrier such as methanol, methane, ammonia, or simply hydrogen gas.

The simplest type of fuel cell uses hydrogen gas as its fuel with an overall reaction of



This concept was first demonstrated in 1839 by William Grove [1] using an experimental setup similar to the one depicted in Fig. 2.1. First, water was electrolyzed into hydrogen and oxygen by supplying an electrical current. Replacing the power source with a load, the electrolyzed gases reacted to produce water and electrical energy. The different methods of operation are characteristic of two distinct types of electrochemical cells: a galvanic cell produces electricity, and an electrolytic cell consumes electrical energy [2]. Therefore, Grove's cell was first operated electrolytically in order to generate the gasses, and then energy was produced galvanically. Since fuel cells produce electrical energy, they are galvanic cells.

As shown in Fig. 2.1, the overall reaction is composed of two independent half-reactions, which occur at two electrodes in a single cell. The anode is the electrode at which oxidation occurs; thus, it is the electron source for the circuit. In Grove's fuel cell, the anode reaction is the hydrogen oxidation reaction (HOR), wherein hydrogen is dissociated at the electrode surface into protons and electrons:



On the other hand, the cathode is the electrode where reduction occurs, effectively providing a sink for the electrons produced at the anode. The electrons pass through the external circuit, while the protons diffuse through the electrolyte to the cathode. These species combine with oxygen at the cathode through the oxygen reduction reaction (ORR):



Because negatively charged electrons travel to the cathode, it is often called the positive (+) terminal, while the anode is referred to as the negative (-) terminal. A voltage exists

between the two terminals and is related to the thermodynamics associated with the reactions taking place at the electrodes.

### *II.1.2. Thermodynamics of Reactions*

The amount of energy available for electric power in an electrochemical cell is based on the thermodynamics of the reactants and products of the overall cell reaction. Every substance in the universe has internal energy due to translational, vibrational, and electronic effects [3]. In order to create a given system, a certain amount of internal energy is required. All substances have a heat of formation or enthalpy of formation, which is the amount of energy required to create the substance including the work that must be done on the atmosphere to make room for it. For a given reaction, the enthalpy of the reaction can be calculated from the difference between the enthalpies of formation of the products and reactants. So for the overall reaction in Grove's cell, the reaction enthalpy [4] can be computed as

$$\Delta H_{rxn} = \Delta H_f(H_2O) - \Delta H_f(H_2) - \frac{1}{2}\Delta H_f(O_2) \quad (2.1.4)$$

where the  $\frac{1}{2}$  is multiplied to the oxygen term due to the stoichiometry of the reaction (i.e. two moles of oxygen react per one mol of hydrogen and water).

During chemical reactions, heat is also transferred to or away from the system; thus, enthalpy values alone do not account for the total energy available for electrical work. The Gibbs free energy accounts for heat transfer due to a reaction according to the expression

$$\Delta G_{rxn} = \Delta H_{rxn} - T\Delta S_{rxn} \quad (2.1.5)$$

where the entropy of reaction is computed in an analogous manner to the enthalpy of reaction. Table 2.1 lists some enthalpy and entropy values at different temperatures.

Using these values and the thermodynamic relationships given earlier, the  $\Delta G_{rxn}$  can be calculated at 25°C as -237.16 kJ/mol and at 100°C as -227.24 kJ/mol [5]. These energies can be converted into voltages using the following relationship

$$E = -\frac{\Delta G_{rxn}}{zF} \quad (2.1.6)$$

so the maximum voltages for Grove's cell operating at 25°C and 100°C are 1.229 V and 1.178 V, respectively. Often, electrode potentials are available for individual electrode reactions at standard conditions. In order to calculate the electrode potential at a given temperature from a standard electrode potential, the following expression is used:

$$E = E^0 + \frac{1}{zF} \int_{T^0}^T \int_{T^0}^T \frac{C_p}{T} dT^2 \quad (2.1.7)$$

If the entropy is assumed to be constant, the integral is replaced with  $\Delta S_{rxn} \cdot \Delta T$ . The standard potential is that of a given electrode reaction at standard conditions. The standard state is necessary, because potential varies with temperature (as just shown) and with pressure.

Another useful thermodynamic relationship exists between the Gibbs free energy and the chemical potential, which is written as

$$dG = \sum_i (\mu_i^0 + R_{ig} T \ln a_i) dn_i \quad (2.1.8)$$

The significance of the above equation is that it is the basis for deriving an expression [6] that shows how potential varies with reactant and product concentration. This is called the Nernst equation and is written for the overall reaction as

$$E = E^0 + \frac{R_{ig} T}{2F} \ln \frac{a_{H_2} a_{O_2}^{1/2}}{a_{H_2O}} \quad (2.1.9)$$

Because fuel cells operate at conditions at which gases are approximately ideal and because the activity of water is commonly considered to be unity, the Nernst equation simplifies to

$$E = E^0 + \frac{R_{ig}T}{2F} \ln p_{H_2} p_{O_2}^{1/2} \quad (2.1.10)$$

The Nernst equation quantitatively explains that the more reactant is present, the more potential energy is available. This notion is intuitive due to the fact that reactions occur at the surface of an electrode/catalyst surface, so that a higher surface concentration of reactant would tend to react more readily. The Nernst potential, however, is only applicable to a cell that is not reacting appreciably, i.e. it is an open circuit potential. In order to understand how potential varies with concentration in a cell which is producing current, electrochemical kinetics must be investigated.

### *II.1.3. Reaction Kinetics*

Electrochemical reaction kinetics involves the study of the mechanisms responsible for charge-transfer dynamics at the solution-electrode interface. The rate of an electrochemical reaction is strongly dependent on electrode potential; therefore, a relationship between reaction rate, potential, and reactant concentration is the ultimate goal in determining kinetics. Because electrochemical charge-transfer reactions obey Faraday's law (shown below),

$$I = \frac{dq}{dt} = zF \frac{dn}{dt} \quad (2.1.11)$$

they are often referred to as Faradaic processes. Dynamic changes in rate and potential can occur due to processes in which no charge is transferred across the interface, but are

not considered in kinetics. Examples of non-Faradaic processes are catalytic adsorption and desorption, as well as electric double-layer charging and discharging. Non-Faradaic processes do not often have as pronounced an effect on the reaction rate; hence, the Faradaic processes are the most significant in obtaining an approximate expression relating current, potential, and reactant concentration.

Considering a unimolecular elementary redox reaction occurring between substances *ox* and *red*,



both the forward and reverse reactions are taking place simultaneously with a net reaction rate of

$$r_{net} = r_f - r_b = k_f C_{ox} - k_b C_{red} \quad (2.1.13)$$

When the above reaction is taking place at an electrode, the oxidation reaction rate can be considered as an anodic current density expressed by

$$i_a = zFr_b = zFk_b C_{red} \quad (2.1.14)$$

Similarly, the cathodic contribution to the overall current density is written

$$i_c = zFr_f = zFk_f C_{ox} \quad (2.1.15)$$

yielding an overall current density of

$$i = zF(k_f C_{ox} - k_b C_{red}) \quad (2.1.16)$$

The vast majority of rate-constants exhibit an exponential dependence on the inverse of temperature, which Arrhenius expressed [7] as

$$k = A_f e^{-E_A/R_g T} \quad (2.1.17)$$

The activation energy is related to an energy barrier that must be overcome in order for the reaction to proceed. Bard et al. give a slightly oversimplified explanation of the terms, with the exponential term representing the probability of the reaction taking place and the frequency factor, to the number of attempts before the reaction takes place [2]. The activation energy can also be labeled with a more thermodynamic term, the standard internal energy of activation. This is representative of the change in internal energy at standard conditions necessary in order to go from the minimum potential energy level for a species to the top of the energy barrier. Using the thermodynamic relationships given earlier and assuming that the standard enthalpy and standard internal energy are equivalent in the condensed-phase reaction, the Arrhenius equation can be rewritten as

$$k = A'_f e^{-\Delta G^\ddagger / R_g T} \quad (2.1.18)$$

To make the above equation particularly useful, suppose that when an electrode is at standard potential, the value of the standard free energy of activation is  $\Delta G_0^\ddagger$ . Then, defining the transfer coefficient such that for the anode,

$$\Delta G_a^\ddagger = \Delta G_{0a}^\ddagger - (1 - \alpha) z F (E - E^0) \quad (2.1.19)$$

and for the cathode

$$\Delta G_c^\ddagger = \Delta G_{0c}^\ddagger + \alpha z F (E - E^0) \quad (2.1.20)$$

These relationships can be combined with the Arrhenius equation (Eq. 2.1.18) to give

$$k_f = A_{ff} \exp\left(-\Delta G_{0c}^\ddagger / RT\right) \exp\left[-\alpha z f (E - E^0)\right] \quad (2.1.21)$$

$$k_b = A_{fb} \exp\left(-\Delta G_{0a}^\ddagger / RT\right) \exp\left[(1 - \alpha) z f (E - E^0)\right] \quad (2.1.22)$$



The above equations can now be applied to Eq. 2.1.16 yielding a relationship between current, potential, and reactant concentration of the form

$$i = zFk^0 \left[ C_{ox}^* e^{-\alpha z f (E - E^0)} - C_{red}^* e^{(1-\alpha) z f (E - E^0)} \right] \quad (2.1.23)$$

The above equation is a form of the Butler-Volmer equation, which is the corner-stone of electrode kinetics. The expression can also be derived from electrochemical potentials in a kinetic model [8]. In order to more conveniently represent Eq. 2.1.23 in a form that will easily reduce to the Nernst equation at appropriate conditions,  $k^0$  must be replaced.

At equilibrium, the Nernst equation governs the electrode potential, and the net current is zero. Since there is no net reaction rate, reactants are not being depleted near the electrode surface and will be concentrated the same as in the bulk solution; thus, the Nernst equation can then be written for Eq. 2.1.12 in exponential form as

$$\frac{C_{ox}^b}{C_{red}^b} = e^{z f (E_{eq} - E^0)} \quad (2.1.24)$$

Despite the absence of a net current at equilibrium, cathodic and anodic currents do exist taking on an equivalent value called the exchange current:

$$i_0 = zFk^0 C_{ox}^b e^{-\alpha z f (E_{eq} - E^0)} \quad (2.1.25)$$

Raising both sides of Eq. 2.1.24 to  $-\alpha$ , then combining with Eq. 2.1.25 gives

$$\left( \frac{C_{ox}^b}{C_{red}^b} \right)^{-\alpha} = e^{-\alpha z f (E_{eq} - E^0)} = \frac{i_0}{zFk^0 C_{ox}^b} \quad (2.1.26)$$

which can be rearranged as

$$i_0 = zFk^0 C_{ox}^b (1-\alpha) C_{red}^b{}^{-\alpha} \quad (2.1.27)$$

Dividing Eq. 2.1.23 by Eq. 2.1.27 and using Eq. 2.1.24 to eliminate the concentration ratios of reactants to products:

$$\frac{i}{i_0} = \frac{C_{ox}^*}{C_{ox}^b} e^{-\alpha z f \eta} - \frac{C_{red}^*}{C_{red}^b} e^{(1-\alpha) z f \eta} \quad (2.1.28)$$

where  $\eta = E - E_{eq}$ .

It should be noted that  $z$  is only included in the current-overpotential equation (Eq. 2.1.28) to maintain consistency; however, it can be considered unity, because the relationship only effectively describes simple single electrode reactions with no side reactions. Reactions involving more than one electron transfer (like the HOR and ORR), are often broken into a step by step sequence of reactions and/or side reactions wherein one electron is transferred. For these reaction mechanisms, each step is characterized by a Butler-Volmer equation quantifying the portion of the total current is supplied by said step. Further detail of the derivation of a current-overpotential equation can be found in Chapter VIII.

## II.2. Fuel Cell Components

### II.2.1. History of the PEMFC

Fuel cells are essentially constantly recharged batteries, so like batteries they require reactants, electrodes, and an electrolyte solution. As previously mentioned, a voltaic cell must have two electrodes, which are responsible for transferring electrons from the anode, through the load, and then to the cathode. The electrolyte provides a medium wherein the ions associated with each electrode reaction can easily exist in a

dissolved phase. The solution also enables reactants to diffuse to and products to diffuse away from the electrode surface.

Several different types of fuel cells exist, each operating in a slightly different manner. The primary attribute that distinguishes one kind from another is the electrolyte; hence, most fuel cell types are named for their electrolyte. Table 2.2 shows the names and attributes for a few of the working fuel cells. Most of the research contained herein is on polymer electrolyte membrane (or proton exchange membrane) fuel cells often referred to by the acronym PEM or PEMFC.

General Electric was the pioneer in creating a PEMFC for NASA to use in the early spacecrafts of the 1960's. The cells did not perform as well as the alkali fuel cells of their day due to water management issues; thus, they were ultimately not employed on the Apollo missions for which they had been developed. GE also chose to scrap their PEMFC research, because catalyst costs were much higher than the competing fuel cells at the time. Not until the late '80's was the interest in PEMFCs rekindled. They were further developed to utilize smaller amounts of catalyst far more efficiently, effectively combating the cost and power density limitation that led to their demise in the '60's. Today, PEMFCs are amongst the forms of alternate energy receiving the most funding for research and development [1]. In discussing the composition of PEM cells, the following topics will be discussed: the electrolyte, electrodes, reactant delivery system, bipolar plates, and current collectors.

### *II.2.2. Polymer Electrolyte*

As indicated by the nomenclature of the different classifications of fuel cells, the most significant aspect of a PEMFCs composition is the polymer electrolyte. The

electrolyte is an ion exchange membrane that also acts as a gas separator. Several different forms of polymer electrolytes are employed in PEMFCs, but they are similar to a large degree.

Nafion<sup>®</sup> has been developed by Dupont since the '60's and is the most famous membrane as well as the standard against which others are compared. The structure of Nafion is similar to that of Teflon, or polytetrafluoroethylene (PTFE). The advantages of a PTFE-like structure are in the strong carbon-fluoride bonds, rendering the material durable and non-reactive. Additionally, it is highly hydrophobic; hence, PTFE is often incorporated in the electrode pores to ensure that the reaction sites are not blocked, or flooded, by water. The reason that the PTFE formula must be modified to act as an ion exchange membrane is that the material needs fixed charge sites to allow ion transport. A sulphonic group is added to the chain to provide a charge site as in Fig. 2.2. Note that the exact formula of the sulphonic group varies between different types of Nafion and different membrane manufacturers.

Ionic conduction occurs in Nafion by two different mechanisms: one that is common to polymer membranes and the other, to liquid electrolytes [5]. In most polymer electrolytes, ions are conducted between charged sites due to microscopic vibrations occurring in the material. Vibration is common for any kind of molecule, and is one of the bases for the derivation of internal energy (as mentioned in Section II.1). The vibrational effects are aided by the amount of free volume in the polymer due to small pores. The physical transfer of ions takes place when vibrations between polymer chains cause an empty charge site to come into close proximity with a charged site occupied with an ion.

Of more significance in Nafion, is the transport of ions in an electrolytic manner, called the vehicle mechanism. Liquid-like behavior is observed in fuel cell membranes, because the free volume of the polymer (pores) absorbs water. Absorption of water is caused by the hydrophilic nature of the sulphonic groups, which theoretically agglomerate into clusters. Between the sulphonic agglomerates exist the nano-scale, free volume pores that absorb water. In essence, the pores and PTFE backbone exist in two phases: polymer and liquid. In the liquid phase, ions are dragged through the electrolyte by a mobile species, the vehicle. Because water is highly polar, it attracts protons to form hydronium complexes ( $\text{H}_3\text{O}^+$ ). The polar bonds are stronger than the electric attraction to the sulphonic groups; thus, water is able to act as the vehicle for conduction. The driving force for conduction is the electric field between the anode and cathode sides of the electrolyte. The anode in a voltaic cell has a negative charge, yet; since it is the location where protons are produced, it exhibits a positive charge relative to the electrolyte. The opposite is true at the cathode, where proton reaction leads to a negative charge relative to the electrolyte. The transport of protons is exacerbated by concentration gradients between anode and cathode, leading to diffusion. The only opposing force is the back-diffusion of water, due to the concentration gradient caused by electro-osmotic drag and production at the cathode. The evidence for the dominance of the vehicle mechanism over the vibration mechanism is in the strong dependence between conductivity and water content in Nafion [9–11].

### *II.2.3. Electrode Catalyst Layer*

The electrode reactions occurring within a PEMFC are the same as those in Grove's cell: the HOR at the anode and the ORR at the cathode. Because the membrane

must be hydrated for the cells to effectively produce current, the cell temperature must be well below the saturation temperature of water. These temperature limitations impose rigid restrictions on what materials may be used for electrodes. The reactions (especially the ORR) occur readily at low temperatures only on noble metals, which are far too expensive and heavy to be used as electrodes. They can, however, be used as catalysts which are bonded to the electrode surface at the solution interface. Table 2.3 shows the exchange current density for the HOR and ORR on various metal surfaces. Clearly the data reveal that platinum and platinum based alloys [14] (not shown the table) are the only feasible options for low temperature catalysts. In order to make efficient use of the expensive catalyst, it is supported by another material. Typically, the catalyst support is carbon because of its light weight, low price, corrosive resistance, and availability.

To demonstrate the kinetic restrictions in the catalyst layer, consider a Pt and a Pd surface at conditions similar to those described in Table 2.3. At large negative overpotentials, the contribution of the backward reaction to the Butler-Volmer equation (Eq. 2.1.28) is insignificant, such that the equation can be rewritten

$$i = i_0 e^{-\alpha z f \eta} \quad (2.2.1)$$

if mass transfer is neglected. This is called the Tafel form of the Butler-Volmer equation, although it is more often written in logarithmic form:

$$\eta = \frac{\ln i_0 - \ln i}{\alpha z f} \quad (2.2.2)$$

Using Eq. 2.2.1 at overpotentials of  $-1$  V, the maximum current densities for the HOR and ORR are  $25$  and  $3.45 \cdot 10^{-5}$  mA/cm<sup>2</sup> on Pt, and  $204$  and  $2.68 \cdot 10^{-7}$  mA/cm<sup>2</sup> on Pd (respectively) where  $\alpha_a = .5$  [15] and  $\alpha_c = .225$  [13]. Clearly the ORR limits the

performance of a fuel cell with either electrode, but much less so (two orders of magnitude at the specified potential) on Pt than on Pd.

The catalyst layer must be optimally constructed to ensure adequate functionality. Because each half reaction (Eq. 2.1.2 and Eq. 2.1.3) requires protons in order to take place and because protons exist in the form of hydronium ions (as discussed in the Section II.2.2), reactions can only occur where liquid water or sulphonic groups are present. The reaction also requires access to the reactant gasses, so the catalyst layer is constructed to be porous in nature. Since solid catalyst, gaseous reactant, and liquid or polymer electrolyte must be present near the reaction sites, they are often referred to as triple phase boundaries (TPB). The term TPB is misleading in that it insinuates that the reaction is only occurring where three phases co-exist. Geometrically, three shapes can only intersect at infinitesimally small points in space providing too small of a region for reactions to proceed at any significant rate. The actual zone in which reactions occur is at the catalyst-solution interface. Reactant gases dissolve in the electrolyte and diffuse to the reaction sites. The catalyst sites at which the reaction takes place are those near the gas-electrolyte interface [16], because hydrogen and oxygen are sparingly soluble and exhibit low diffusivity in Nafion and water. For this reason and for better gas diffusion, thin catalyst layers (often less than 50  $\mu\text{m}$ ) are preferred; however, too thin of a catalyst layer may result in too few reaction sites and too low of a catalyst loading. The thickness tradeoff must be balanced in designing the electrode, in order to facilitate optimum operation.

#### *II.2.4. Membrane Electrode Assembly*

The membrane electrode assembly (MEA) is composed of the electrolyte, catalyst, and electrode layers. MEAs are often referenced instead of each individual component, because of the construction methods used to bond the membrane to the electrode. Many of the details of the construction methods are clouded in proprietary processes; however, two different techniques are distinguishable [17]. The separate electrode method involves fixing the catalyst layers to each electrode before hot pressing the two electrodes to either side of the membrane. Alternatively, the catalyst layer can be applied to the membrane before the kinetically inert part of the electrode is fixed to the catalyst layer. Often the catalyst layer will be mixed with PTFE to help wick water away from the catalyst surface improving the kinetic performance of the electrode.

In addition to the catalyst layer, a PEMFC electrode is generally also made up of the gas diffusion layer (GDL). GDLs are porous solids that allow reactant gasses access to the reaction sites while providing a conductive path for the electricity produced in the cell. Additionally, the GDL provides mechanical support for the catalyst layer and assists in water transport. Typically carbon cloth or paper is used because of its light weight, high conductivity, noncorrosive nature, and inexpensive cost. The choice between carbon paper and cloth is based on the application. Carbon cloth absorbs more water and is thicker expanding into the gas delivery channels of the bipolar plates. Because of the thickness and expansion of cloth, carbon paper is generally preferred in thinner cells. Regardless of the electrode material, the MEA is typically sandwiched between two graphite plates.



### *II.2.5. Flow Field Plate*

Graphite plates (also called flow field plates) are responsible for delivering reactant gases to the GDL and conducting electricity to the current collectors. The plates are bigger than the MEA such that the edges around the MEA can be sealed from gas leaks by compressing the plates together. Open faced flow channels are machined into the plates to distribute the reactant gas across the entire surface area of the GDL. Many different patterns are used for the flow channels including parallel, serpentine, or interdigitated. Fig. 2.3 shows the distinction between different flow field patterns, although it should be noted that combinations of two or more may also be used.

When constructing FC stacks, bipolar plates, which act as flow field plates for the anode and cathode of the adjoining cells, are often preferred to using two separate graphite plates. The advantage in using one plate instead of two is that there is better electric conductivity (less contact resistance) than pressing two plates against one another. Bipolar plates also offer less size and weight than using two plates. The method in which bipolar plates are manufactured is the same as for single graphite plates, only both sides of the plate are machined with gas flow channels.

### *II.2.6. Current Collector*

At the ends of the stack, current collectors (also called bus plates) are pressed against the last anode and cathode flow field plates. Current collectors are typically made of a thick slab of copper in order to maximize electrical conductivity and minimize power loss. The chief objective of the bus plates is to form a conductive path to an external load. Because external wires must be connected to the current collectors, mechanical stability is required; thus, copper is used instead of carbon (or graphite), which is used

elsewhere throughout the stack. The key design flaw associated with thick copper current collectors is their high thermal conductivity [18]. Consequentially, more heat will be removed from the cells nearest the current collectors potentially causing them to experience operational abnormalities, such as flooding. Manufacturers must balance the tradeoff between minimizing power loss and heat loss when designing current collectors.

### **II.3. Measurement Techniques Applicable to Fuel Cells**

Fuel cells may be characterized using a wide range of measurement techniques, which are chemical and/or electrical in nature. The study of electrochemical systems is multidisciplinary involving electrical and chemical theories; hence, incorporating both sides in models is ideal. Since a fuel cell is in essence a chemical reactor, a reaction engineering technique, residence time distribution theory, will be applied to model gas distribution within the stack. Fuel cells must also be characterized electrically, which can be accomplished by polarization curves and electrochemical impedance spectroscopy. The following section will present an overview of residence time distribution theory, polarization curves, and electrochemical impedance spectroscopy.

#### *II.3.1. Residence Time Distribution Theory*

Nonidealities in reactors are assessed by examining the distribution of molecules' residence times, which are nonuniform due to quality of mixing. Reactors are often modeled using one of two extreme cases: a constantly stirred tank reactor (CSTR) in which perfect mixing occurs, and a plug flow reactor (PFR) in which there exists no mixing. In the physical world, reactor behavior deviates from these two extremes because of reactor design and imperfect manufacturing capabilities. For example, a

CSTR can exhibit some plug flow with bypass flow, which is not fully mixed with the rest of the tank exiting the tank much sooner than the other molecules that entered at the same time. In a PFR, a similar effect can take place due to some fluid flowing through the path of least resistance, thus channeling past most of the catalyst particles. Dead zones, on the other hand, are small, stagnant pockets where reactants continuously mix without being able to exit. In order to determine what kind of model to use for a given reactor, experiments must be performed and matched to theory.

The primary type of experiment for probing residence time distribution (RTD) involves inputting an inert tracer chemical into the reactor and measuring its time-dependent concentration in the exit flow. Tracers are chosen to have properties similar to the reactant that it is supposed to be modeling, except that it should not adsorb to any of the surfaces inside the reactor. Experiments are most often performed either by injecting a pulse of tracer and measuring until the reactor contains no more, or by adding a constant concentration (step input) of tracer and measuring until the system obtains a steady-state. Each type of tracer experiment has unique disadvantages. The drawbacks to the pulse injection are that sloppy injections can lead to error, the duration of the pulse must be much smaller than the residence time in the reactor, and that long tails in concentration data can lead to large analysis error. Step input methods also have shortcomings in that the differentiation of data can lead to large inaccuracies, a large quantity of tracer is needed and could be expensive, and that maintaining a constant inlet concentration can prove to be a challenge [7]. Whenever possible, the best method to minimize error would be to perform both tracer experiments in order to obtain an accurate model.

In order to discuss the modeling aspect of the RTD, a few terms must first be introduced. The RTD function quantifies the fraction of the fluid that has a certain residence time. For a pulse injection the RTD function is represented as

$$E(t) = \frac{\dot{V}C(t)}{n_{inj}} \quad (2.3.1)$$

and for a step input:

$$E(t) = \frac{d}{dt} \left[ \frac{C(t)}{C_{in}} \right] \quad (2.3.2)$$

The average residence time for molecules in a reactor is

$$\bar{t} = \int_0^{\infty} tE(t) dt \quad (2.3.3)$$

The other parameter that is most commonly used to describe the RTD is the variance, which gives an indication to how much more spread out the molecules are exiting the reactor from those entering. The variance is taken from the mean time being defined as

$$\sigma^2 = \int_0^{\infty} (t - \tau)^2 E(t) dt \quad (2.3.4)$$

Levenspiel gives a simple method for determining the mean time and variance from experimental time-dependent concentration data when said data is numerous as follows [19]:

$$\bar{t} = \frac{\sum tC(t)\Delta t}{\sum C(t)\Delta t} \quad (2.3.5)$$

and

$$\sigma^2 = \frac{\sum t^2 C(t)\Delta t}{\sum C(t)\Delta t} - \bar{t}^2 \quad (2.3.6)$$

Two models that are commonly used to model nonidealities in flow reactors are the tanks-in-series model and the dispersion model. The tanks-in-series model consists of a number of equally sized CSTRs that flow into one another in series (see Fig. 2.4). The model functions such that a single tank yields ideal CSTR behavior, while infinite tanks yield ideal PFR behavior. In order to determine how many tanks should be used to represent data, the mean time and variance can be used accordingly:

$$N = \frac{\bar{t}^2}{\sigma^2} \quad (2.3.7)$$

In the dispersion model, axial dispersion is considered due to mass transport by diffusion and convection. The mass transport term is added to the bulk flow term such that the molar flow rate of a tracer can be written as

$$\dot{n}_T = uAC_T - DA \frac{\partial C_T}{\partial x} \quad (2.3.8)$$

where flow is in the  $x$ -direction. The dispersion coefficient can be found from data correlations given by Levenspiel [19]. In comparing the dispersion model to the tanks-in-series model, it can be determined that there is an equivalency between the two. The condition of equivalence is written below as

$$N = 1 + \frac{uL}{2D} \quad (2.3.9)$$

although other correlations [20] exist as well. Due to the equivalence condition, the number of tanks can be solved for a portion of a reactor where experimental concentration data may not be readily available. Models may also be arranged in compartments, so that more complex schemes may be represented. A multitude of different compartmental models exist [7, 19, 21], wherein the arrangement of tanks in

each is dependent on the modeled reactor. Compartmental, tanks-in-series, and dispersion models will be applied to experimental RTD data in the work presented in Chapter IX.

### *II.3.2. Polarization Curves*

The simplest method for measuring the performance of an electrode (or cell) is by charting the current dependent polarization. When the net current passed through the electrode-solution interface is nonzero, then the electrode is said to be polarized. The degree of polarization is measured by the overpotential, which is the departure of electrode potential from its equilibrium value. As evident in the Butler-Volmer equation (Eq. 2.1.28), the overpotential increases in response to an increase in current, conversely the electrode potential is decreased. The inverse proportionality between working potential and current is much the same as the relationship between velocity and potential energy of a falling object: as the object accelerates, it loses potential energy as it is converted into kinetic energy. In comparing mechanical and electrical systems, the electrical analog to velocity is current [21]; however the electrical situation is far more complex due to several processes that limit the amount of useful energy obtained from an electrochemical cell.

The potential loss in a cell due to current is generally caused by kinetics, conduction, and mass transfer. The kinetic loss is due to overcoming an energy barrier (activation) in order for the chemical reaction to proceed. Even at very small currents, a relatively large amount of energy must be expended to surmount the activation barrier as evident in the Butler-Volmer relationship (Eq. 2.1.28). Potential loss from conduction occurs primarily because of the electrolyte's resistance to the flow of ions and, to a lesser

degree, because of the electrical resistance of cell interconnects. Both conductance and resistance (they are inversely proportional) are unchanged with current, so that the potential drop associated with them obeys Ohm's law

$$E = IR \quad (2.3.10)$$

hence, they are often referred to collectively as Ohmic losses. Mass transfer losses (or concentration losses) are associated with reactant starvation at the electrode surface.

Because of the distinctly different nature of the losses, it is possible to distinguish three different regions of the polarization curve where different losses are dominant. Fig. 2.5 shows a typical polarization curve for a fuel cell, and the three different regions. At extremely low currents, Ohmic and mass transfer losses are at a minimum, indicating that the drastic drop in potential from the equilibrium value is due to activation. In the moderate current region, the rate of reaction is still well below the maximum rate of mass transfer and the kinetic loss is relatively constant. Ohmic losses are responsible for the moderate current potential variation, which is distinctly linear (as predicted in Ohm's Law (Eq. 2.3.10)). The high current region is where mass transfer losses are dominant because of difficulty in the system of supplying reactant to one or both of the electrodes.

Often the drop in a cell's working potential is considered as a sum of overpotentials, each associated with a different type of loss. In doing so, the contribution of each process to the decrease in potential from the open-circuit value can be examined. The activation overpotential at high currents (Eq. 2.2.2) is rewritten:

$$\eta_{act} = \frac{(\ln i_0 - \ln i)}{\alpha z f} \quad (2.3.11)$$

(where the concentration term from the Butler-Volmer equation has been suppressed, because it will be accounted for in the concentration overpotential). The Ohmic losses (Eq. 2.3.10) may also be rewritten with new variables as

$$\eta_{\Omega} = IR_{\Omega} \quad (2.3.12)$$

For concentration polarization, losses become significant as the reaction rate (current) approaches a mass transport limited value, called the limiting current. The magnitude of current is given in general as

$$\frac{I}{zFA_s} = m(C^b - C^*) \quad (2.3.13)$$

The limiting current exists when reactant is consumed as fast as it can be supplied implying that  $C^* = 0$ ; thus, the limiting current can be written as

$$I_l = zFA_s m C^b \quad (2.3.14)$$

Combining the above two equations gives

$$\frac{C^*}{C^b} = 1 - \frac{I}{I_l} \quad (2.3.15)$$

The concentration overpotential can then be derived by substituting Eq. 2.3.15 into the Nernst relationship (Eq. 2.1.24) for each electrode:

$$\eta_{conc} = \frac{RT}{zF} \ln \left( 1 - \frac{I}{I_l} \right) \quad (2.3.16)$$

Summing the overpotentials, the current potential behavior a cell is

$$\begin{aligned} \eta &= \eta_{act}^a + \eta_{act}^c + \eta_{\Omega} + \eta_{conc}^a + \eta_{conc}^c \\ &= \frac{1}{f} \left[ \frac{\ln i_0^a - \ln i}{\alpha^a z^a} + \frac{\ln i_0^c - \ln i}{\alpha^c z^c} + fIR_{\Omega} + \frac{1}{z^a} \ln \left( 1 - \frac{I}{I_l^a} \right) + \frac{1}{z^c} \ln \left( 1 - \frac{I}{I_l^c} \right) \right] \end{aligned} \quad (2.3.17)$$



The parameters in Eq. 2.3.17 can be determined by fitting experimental  $I$ - $V$  data in the three regions where the different processes are dominant.

Although obtaining and analyzing polarization curves is simple, problems exist that are inherent in the method, especially in their application to fuel cells. Energy is obtained in fuel cells from exothermic reactions, meaning that heat is a product of the reactions. The amount of heat generated is dependent on the reaction rate (current); therefore, maintaining isothermal conditions at the catalyst layer over a range of currents is difficult. The temperature dependence of overpotential exists not only in the  $f$  term, but also in other parameters that are functions of temperature: the exchange current, mass transfer coefficient, reactant concentration, and membrane ion resistance. Each of these parameters is also a function of water content in a particular phase, which is also a function of temperature. Another limitation of polarization curves is in distinguishing between anodic and cathodic processes. One technique that overcomes the limitations of polarization curves is electrochemical impedance spectroscopy.

### *II.3.3. Electrochemical Impedance Spectroscopy*

Electrochemical Impedance Spectroscopy (EIS) is a method for characterizing electrochemical cells that is capable of decoupling the different limiting processes by probing their associated relaxation-times. Polarization curves are measured at steady-state so that the time dimension is negligible, whereas EIS employs AC signals of varying frequency to test time-dependent polarization. An EIS (or AC impedance) experiment is conducted by superimposing a sinusoidal wave onto the DC output of the cell and measuring the frequency response of the system over a given spectrum. System

perturbations must be small ( $< 10$  mV) to ensure that the I-V behavior is pseudo-linear over the test range [22].

EIS experiments may be performed potentiostatically by applying an AC potential and measuring the induced current or galvanostatically by applying an AC current measuring the resulting potential. Regardless of the method, determining potential and current enables the calculation of impedance by the AC form of Ohm's Law (Eq. 2.3.10)

$$E = IZ \quad (2.3.18)$$

In addition to the magnitude of the impedance, the phase angle between the potential and current is also measured. The phase angle is associated with the time lag between the peaks of the current and potential waves, such that the impedance can be written in polar coordinates as

$$Z = Z_{mag} \angle \phi \quad (2.3.19)$$

or in rectangular coordinates:

$$Z = Z_{mag} \cos \phi + jZ_{mag} \sin \phi \quad (2.3.20)$$

where the cosine term is the real component of impedance and the term multiplied by  $j$  is the imaginary component of impedance. In DC systems, the phase angle is  $0^\circ$ , which means that the sine term goes to zero implying that DC impedance (resistance) is the same as  $Z_{re}$ . When transient changes occur,  $Z_{im}$  (reactance or admittance) is responsible for any phase shift occurring between the current and voltage. EIS data are graphically presented primarily in one of two ways: a Bode plot or a Nyquist plot. In a Bode plot,  $Z_{mag}$  and  $\phi$  are charted as functions of frequency, while resistance is charted as a function of reactance in a Nyquist plot. Experimental data are fitted to models that theoretically describe the processes governing the performance of the cell under investigation.

### *II.3.3.1. Simple Equivalent Circuit*

The models used to extract information from EIS data are based on a physical circuit with a frequency response that matches that of the data. Equivalent circuit models may consist of real physical elements (such as resistors and capacitors), theoretical elements, or combinations of both. From the discussion in Section II.3.2, Ohmic losses are implicitly modeled simply with a resistor.  $R_{\Omega}$  encompasses the combined resistance of the electrolyte, bipolar plates, current collectors, and all other cell interconnects. In general, each electrode exhibits at least one relaxation time associated with charge transfer [2]. Relaxation times are frequently modeled with a resistor and capacitor in parallel yielding an  $RC$  time constant ( $R*C$ ). A resistor and capacitor in series will also be governed by a time constant, but is not the preferred configuration for physical and theoretical reasons. Physically, a capacitor will act as an open circuit under DC conditions as evident by applying zero frequency to the impedance equation for a capacitor (Table 2.4); therefore, no DC current can flow through a resistor and capacitor in series. Obviously, modeling a DC power source, such as a fuel cell, that cannot physically produce DC current would be erroneous. Theoretically, the parallel  $RC$  is based on two distinct paths for current flow. Faradaic current flows via charge-transfer across the electrode-solution interface, while non-Faradaic current flows transiently due to changes in composition at the interface without charge-transfer. One such source for non-Faradaic current is the limited distance that solvated ions of a given charge are capable of approaching the metal surface of opposite charge. The charge separation at the electrode surface (the double-layer) is similar to a physical capacitor, which consists of two plates of opposite charge separated by an insulating material. In a parallel  $RC$

equivalent circuit model for an electrode, the capacitor is related to the electric double-layer, and the resistor is related to charge-transfer.

From the previous discussion, it is evident that a simple model for a single electrode in solution is a parallel  $RC$  in series with an Ohmic resistance. The expected frequency response characteristics of the simple circuit are depicted in Figs. 2.6–7. Data in the Nyquist (Fig. 2.6) are plotted such that a low impedance value corresponds to a high frequency. At high frequency, the impedance of a capacitor approaches zero (see Table 2.4) meaning that the Ohmic resistance is the only source of impedance for the current; hence, the high frequency intercept of the  $Z_{re}$ -axis corresponds to the value of  $R_{\Omega}$ . As explained earlier, the impedance of a capacitor tends to zero at low frequency; thus, the low frequency intercept of the  $Z_{re}$ -axis corresponds to the value of  $R_{\Omega} + R_{ct}$ . Bode plots (Fig. 2.7) are not as simple to qualitatively analyze as Nyquist, but are useful for quantitatively fitting a model to experimental data.

### *II.3.3.2. Complex Equivalent Circuits/Elements*

While the simplest electrode reactions can be accurately represented with a simple  $RC$  circuit, more complex reactions require more elements to describe the electrode kinetics. The added elements can be physical elements, or they can be theoretical (distributed) elements that describe mass transfer or varied capacitance. There are several modifications that can be made to the general  $RC$  circuit, so only a few that are applicable to fuel cell reactions will be described in the following section.

Multi-step charge-transfer mechanisms can often exhibit more than one relaxation time depending on which step is rate-limiting. In general, a new group of elements (such as a parallel  $RC$ ) may be added corresponding to each adsorbed species.

Pseudocapacitance is one type of adsorption effect about which there has been a lot of discussion in the literature [23–26]. The origin of pseudocapacitance is due to the potential dependence of the surface coverage of an intermediate. Since the surface coverage corresponds to a charge by an equilibrium constant ( $k'$ ), the pseudocapacitance is defined as

$$C = \frac{dq}{dE} = \frac{k'd\theta}{dE} \quad (2.3.21)$$

It should be noted that the above capacitance behaves differently from the double-layer capacitance, because the surface coverage can only be changed when charge crosses the interface (Faradaically). The potential dependence of the capacitance requires that a distributed element be used in lieu of a physical capacitor in a model (more on this below). Some researchers have noted that in multi-step schemes that a negative capacitance (which is the same as inductance) can be observed. The layouts of the equivalent circuits including which and how many elements are required changes depending on the mechanism, although they are mathematically from derived theory [27].

Solid electrodes behave differently than liquid electrodes due to the complicated structure of the electrode-electrolyte interface. In order to represent the porous nature of a gas diffusion electrode, infinite numbers of resistors and capacitors are often used [28]. These transmission line models are constructed like a ladder, where each rung of the ladder is composed of a double-layer capacitance. Each rail consists of a resistor between each capacitive rung with one rail representing resistance in the solid phase and the other, resistance in the electrolyte. Transmission line models are generally very complicated to solve because their inverse Laplace transform contain infinite series of

exponential and/or error functions [29]. Typically equivalent circuits are preferred that consist of elements with values that are distributed with frequency.

The constant phase element (CPE) is a distributed element that models the dispersion of the dielectric constant. In ideally polarizable electrodes, there is no charge-transfer resistance; thus, they are modeled as a capacitor and resistor ( $R_\Omega$ ) in series, which would produce a vertical line on a Nyquist plot. On solid ideally polarizable electrodes, a straight line non-perpendicular line is observed due to the distribution of time constants. The CPE is often used to model such distribution with impedance expressed as

$$Z = Y_0^{-1} (j\omega)^{-\varphi} \quad (2.3.22)$$

where  $Y_0$  is a constant in  $F s^{\varphi-1}$  and  $\varphi$  is the rotation angle from a pure capacitor. The exact origin of the CPE is in debate, but the most prominent theories are that it is either due to surface roughness, or due to adsorption and a chemically inhomogeneous surface [30]. Whatever the cause, the experimental presence of CPE behavior is prevalent.

Diffusion is another phenomenon that must be modeled with distributed elements, three of which have been derived. The difference between the three is in the thickness of the diffuse layer: infinite, finite, and very thin. Diffusion of reactants in a fuel cell takes place in the porous electrode and in the electrolyte, which are of a set thickness; thus, the finite diffusion case is the only one that will be considered. The finite diffusion element has been derived [26] as

$$Z = \frac{W_i(1-j)}{\sqrt{\omega}} \tanh\left(\delta \sqrt{\frac{j\omega}{D_i}}\right) \quad (2.3.23)$$

where  $W_i$  is called the Warburg coefficient and is expressed as

$$W_i = \frac{R_{ig} T}{(z_i F)^2 A_s \sqrt{2}} \left( \frac{1}{C_i^b \sqrt{D_i}} \right) \quad (2.3.24)$$

The Warburg coefficient characterizes the mass transport of the reactant. The impedance due to diffusion will be large when the species concentration is low, and when diffusion is slow. Fig. 2.8 shows a Nyquist plot for the finite diffusion element. At high frequencies, diffusion reduces to the infinite case (which appears as a 45° line on a Nyquist); yet, at low frequencies, the plot turns over to the real axis yielding values for the constants in Eq. 2.3.23. By using the theories and circuit elements contained in Section II.3.3.1–2, a fuel cell equivalent circuit may be constructed.

#### II.4. Nomenclature

|          |   |
|----------|---|
| $A$      | cross-sectional area                                  |
| $A_f$    | frequency factor                                      |
| $A'_f$   | $\exp(\Delta S_0^\ddagger / R) / A_f$                 |
| $A_s$    | geometric area of electrode surface                   |
| $a_i$    | activity of species $i$                               |
| $C_i$    | concentration of species $i$                          |
| $C_{in}$ | concentration of step input                           |
| $C_p$    | heat capacity at constant pressure                    |
| $C_i^b$  | concentration of species $i$ in the bulk              |
| $C_i^*$  | concentration of species $i$ at the electrode surface |
| $D$      | dispersion coefficient [20]                           |

|                     |   |
|---------------------|---|
| $D_i$               | diffusion coefficient of species $i$      |
| $E$                 | potential                                 |
| $E_A$               | activation energy                         |
| $E_{eq}$            | equilibrium potential                     |
| $E^0$               | standard state potential                  |
| $F$                 | Faraday's constant                        |
| $f$                 | F/RT                                      |
| $G$                 | Gibbs free energy                         |
| $\Delta G_{rxn}$    | Gibbs free energy of reaction             |
| $\Delta G^\ddagger$ | standard free energy of activation        |
| $\Delta H_f$        | enthalpy of formation                     |
| $\Delta H_{rxn}$    | enthalpy of reaction                      |
| $I$                 | current                                   |
| $I_l$               | limiting current                          |
| $i$                 | current density                           |
| $i_0$               | exchange current density                  |
| $j$                 | imaginary constant ( $\sqrt{-1}$ )        |
| $k$                 | rate constant                             |
| $k_b$               | heterogeneous rate constant for oxidation |
| $k_f$               | heterogeneous rate constant for reduction |
| $k^0$               | standard heterogeneous rate constant      |
| $L$                 | length                                    |



|                      |   |
|----------------------|---|
| $N$                  | number of tanks-in-series                                   |
| $n_i$                | moles of species $i$  |
| $n_{inj}$            | moles in pulse injection                                    |
| $\dot{n}_i$          | molar flow rate of species $i$                              |
| $P$                  | stack pressure  |
| $p_i$                | partial pressure of species $i$                             |
| $q$                  | charge  |
| $R$                  | resistance  |
| $R_{ct}$             | charge-transfer resistance                                  |
| $R_{ig}$             | ideal gas constant (Avogadro's number * Boltzmann constant) |
| $R_{\Omega}$         | Ohmic resistance  |
| $r_b$                | reaction rate of backward reaction                          |
| $r_f$                | reaction rate of forward reaction                           |
| $r_{net}$            | net reaction rate   |
| $\Delta S_{rxn}$     | entropy of reaction   |
| $\Delta S^{\dagger}$ | standard entropy of activation                              |
| $T$                  | stack temperature   |
| $T^0$                | standard state temperature                                  |
| $t$                  | time  |
| $\bar{t}$            | mean residence time   |
| $u$                  | linear velocity   |
| $V$                  | total volume of modeled part                                |

|           |  |
|-----------|--|
| $\dot{V}$ | total volumetric flow rate   |
| $Z$       | impedance  |
| $Z_{im}$  | imaginary component of impedance (reactance)                         |
| $Z_{mag}$ | magnitude of impedance ( $\sqrt{Z_{re}^2 + Z_{im}^2}$ )              |
| $Z_{re}$  | real component of impedance (resistance)                             |
| $z$       | stoichiometric number of electrons involved in an electrode reaction |

### **Greek Letters**

|            |   |
|------------|---|
| $\alpha$   | transfer coefficient                          |
| $\delta$   | diffusion layer thickness                     |
| $\eta$     | overpotential ( $E - E_{eq}$ )                |
| $\theta$   | surface coverage of reactant                  |
| $\mu_i^0$  | standard state chemical potential             |
| $\sigma^2$ | variance                                      |
| $\phi$     | phase angle between two sinusoidal signals    |
| $\omega$   | angular frequency of a sinusoidal oscillation |

### **Superscripts**

|     |                                  |
|-----|----------------------------------|
| $a$ | process occurring at the anode   |
| $c$ | process occurring at the cathode |

## **II.5. References**

- [1] J. Larminie, A. Dicks, *Fuel Cell Systems Explained*, John Wiley & Sons Inc., New York, 1998, pp. 1, 61.

- [2] A. J. Bard, L. R. Faulker, *Electrochemical Methods: Fundamentals and Applications*, second ed., John Wiley & Sons Inc., New York, 1998, pp. 18, 88, 376.
- [3] P. A. Tipler, R. A. Llewellyn, *Modern Physics*, third ed., W. H. Freeman and Company, New York, 1999, p. 343.
- [4] J. W. Hill, R. H. Petrucci, *General Chemistry: An Integrated Approach*, second ed., Prentice-Hall, Upper Saddle River, NJ, 1999, pp. 766–816 (Chapter 18).
- [5] R. P. O’Hayre, S. W. Cha, W. Colella, F. B. Prinz, *Fuel Cell Fundamentals*, John Wiley and Sons Inc., New York, 2006, pp. 360, 111.
- [6] J. S. Newman, *Electrochemical Systems*, second ed., Prentice-Hall, Inc., Englewood Cliffs, NJ, 1991, p. 55.
- [7] H. S. Fogler, *Elements of Chemical Reaction Engineering*, third ed., Prentice Hall PTR, Upper Saddle River, NJ, 1999, p. 69 and 809–918 (Chapters 13–14).
- [8] T. Erdey-Grúz, *Kinetics of Electrode Processes*, Wiley-Interscience, New York, 1972, pp. (Chapter 1).
- [9] T. E. Springer, T. A. Zawodzinski, S. Gottesfeld, *J. Electrochem. Soc.* 138 (1991) 2334.
- [10] F. Damay, L. C. Klein, *Solid State Ionics*, 162–163, (2003) 261.
- [11] G. Pourcelly, A. Oikonomou, C. Gavach, *J. Electroanal. Chem.* 287 (1990) 43.
- [12] H. Kita, in: H. Bloom, F. Gutman (Eds.), *Electrochemistry*, Plenum Press, New York, 1967, p. 121.
- [13] D. S. Gnanamuthu, J. V. Petrocelli, *J. Electrochem. Soc.* 114 (1967) 1036.
- [14] A. Damjanovic, in: J. O’M. Bockris, B. E. Conway (Eds.), *Mod. Asp. Electrochem.*, 5, Plenum Press, New York, 1969, p. 369.
- [15] D. M. Bernardi, M. W. Verbrugge, *J. Electrochem. Soc.* 139 (1992) 2477.
- [16] R. O’Hayre, D. M. Barnett, F. B. Prinz, *J. Electrochem. Soc.* 152 (2005) A439.
- [17] S. Gottesfeld, T. A. Zawodzinski, in: R. C. Alkire, H. Gerischer, D. M. Kolb, C. W. Tobias (Eds.), *Adv. Electrochem. Sci. Eng.*, 5, John Wiley & Sons Inc., New York, 1997, p. 195.

- [18] R. H. Artibise, F. D. McKenney, J. Zimmermann, S. D. Gabrys, A. Mossman, PCT Int. Appl., WO 2006/071994 A1 (2006).
- [19] O. Levenspiel, *The Chemical Reactor Omnibook*, OSU Bookstores Inc., Corvallis, OR (2002).
- [20] O. Levenspiel, *Chem. Eng. Sci.* 17 (1962) 576.
- [21] J. B. Marion, S. T. Thornton, *Classical Dynamics of Particles and Systems*, fourth ed., Harcourt, Inc., Orlando, 1995, p. 132.
- [22] Gamry Instruments, *Basics of Electrochemical Impedance Spectroscopy*, Application Note, Warminster, PA, 2007, p. 6.
- [23] M. Sluyters-Rehbach, J. H. Sluyters, in: A. J. Bard (Ed.), *Electroanal. Chem.*, 4, Marcel Dekker, Inc., New York, 1970, p. 72.
- [24] J. O'M. Bockris, S. Srinivasan, *Fuel Cells: Their Electrochemistry*, McGraw-Hill Book Company, New York, 1969, p. 103.
- [25] E. Gileadi, B. E. Conway, in: J. O'M. Bockris, B. E. Conway (Eds.), *Mod. Asp. Electrochem.*, 3, Butterworths & CO., London, 1964, p. 397.
- [26] A. Lasia, in: B. E. Conway, J. O'M. Bockris, R. E. White (Eds.), *Mod. Asp. Electrochem.*, 32, Kluwer Academic / Plenum Publishers, New York, 1999, p. 143.
- [27] C. Cao, *Electrochimica. Acta.* 35 (1990) 837.
- [28] Y. Oren, A. Soffer, *J. Electrochem. Soc.* 125 (1978) 869.
- [29] C. Y. Yuh, J. R. Selman, *AIChE Journal* 34 (1988) 1949.
- [30] I. D. Raistrick, in: J. R. Macdonald (Ed.), *Impedance Spectroscopy: Emphasizing Solid Materials and Systems*, John Wiley & Sons, New York, 1987, p. 27.

**Table 2.1.** Enthalpies and entropies of formation for fuel cell reactants and products at temperatures of 298.15 and 360 K [5].

| Temperature (K) | Species          | $\Delta H_f$ (kJ/mol) | $\Delta S_f$ (J/mol · K) |
|-----------------|------------------|-----------------------|--------------------------|
| 298.15          | H <sub>2</sub>   | 0.00                  | 130.68                   |
|                 | O <sub>2</sub>   | 0.00                  | 205.00                   |
|                 | H <sub>2</sub> O | -285.83               | 69.95                    |
| 360             | H <sub>2</sub>   | 1.79                  | 136.14                   |
|                 | O <sub>2</sub>   | 1.81                  | 210.63                   |
|                 | H <sub>2</sub> O | -281.17               | 84.16                    |

**Table 2.2.** Characteristics of different types of fuel cells.

|                              | <b>PEMFC</b>  | <b>DMFC</b>                  | <b>SOFC</b>                                    | <b>MCFC</b>                               | <b>AFC</b>          | <b>PAFC</b>  |
|------------------------------|---|------------------------------|--|---|---------------------|--|
| <b>Electrolyte</b>           | Polymer   | Polymer                      | Ceramic<br>YSZ                                 | Molten<br>carbonate                       | Alkaline<br>liquid  | Phosphoric<br>acid                                 |
| <b>Conducting Ion</b>        | H <sup>+</sup>  | H <sup>+</sup>               | O <sup>2-</sup>                                | CO <sub>3</sub> <sup>2-</sup>             | OH <sup>-</sup>     | H <sup>+</sup>                                     |
| <b>Operating Temperature</b> | > 0-100°C   | 60-100 °C                    | 500 - 1000°C                                   | ~650 °C                                   | 50 – 200 °C         | ~220 °C  |
| <b>Fuel</b>                  | Pure H <sub>2</sub>   | CH <sub>3</sub> OH,<br>steam | CH <sub>4</sub> , CO,<br>H <sub>2</sub> , etc. | CH <sub>4</sub> , CO                      | Pure H <sub>2</sub> | Pure H <sub>2</sub>                                |
| <b>Power Range</b>           | < 150 kW  | < 5 kW                       | .2 – 1 MW                                      | .2 - > 1 MW                               | .5 – 10 kW          | 5 – 250 kW   |
| <b>Applications</b>          | Transportation, mobile<br>devices,<br>telecommunications, UPS | Low power<br>batteries       | Distributed<br>generation,<br>marine           | Biomass,<br>marine,<br>water<br>utilities | Space<br>vehicles   | Distributed<br>generation,<br>backup<br>generation |

**Table 2.3.** Exchange current density for fuel cell electrode reactions on different metal surfaces in acid solution at 1 atm and 298.15 K [12,13].

| Metal | $i_0$ (A/cm <sup>2</sup> ) |            |
|-------|----------------------------|------------|
|       | HOR                        | ORR        |
| Pt    | $5 \times 10^{-4}$         | $10^{-9}$  |
| Pd    | $4 \times 10^{-3}$         | $10^{-11}$ |
| Au    | $2 \times 10^{-6}$         | $10^{-13}$ |
| Rh    | $3 \times 10^{-3}$         | $10^{-11}$ |
| Ir    | $5 \times 10^{-4}$         | $10^{-11}$ |
| Ru    | $5 \times 10^{-4}$         | $10^{-12}$ |
| Os    | $1 \times 10^{-4}$         | $10^{-10}$ |

**Table 2.4.** Characteristic equations of physical circuit elements used in equivalent circuits.

| Circuit Element | Current-Potential Equation | Impedance Equation |
|-----------------|----------------------------|--------------------|
| Resistor        | $E = I R$                  | $Z = R$            |
| Capacitor       | $I = C (dE/dt)$            | $1/Z = j\omega C$  |
| Inductor        | $E = L (dI/dt)$            | $Z = j\omega L$    |



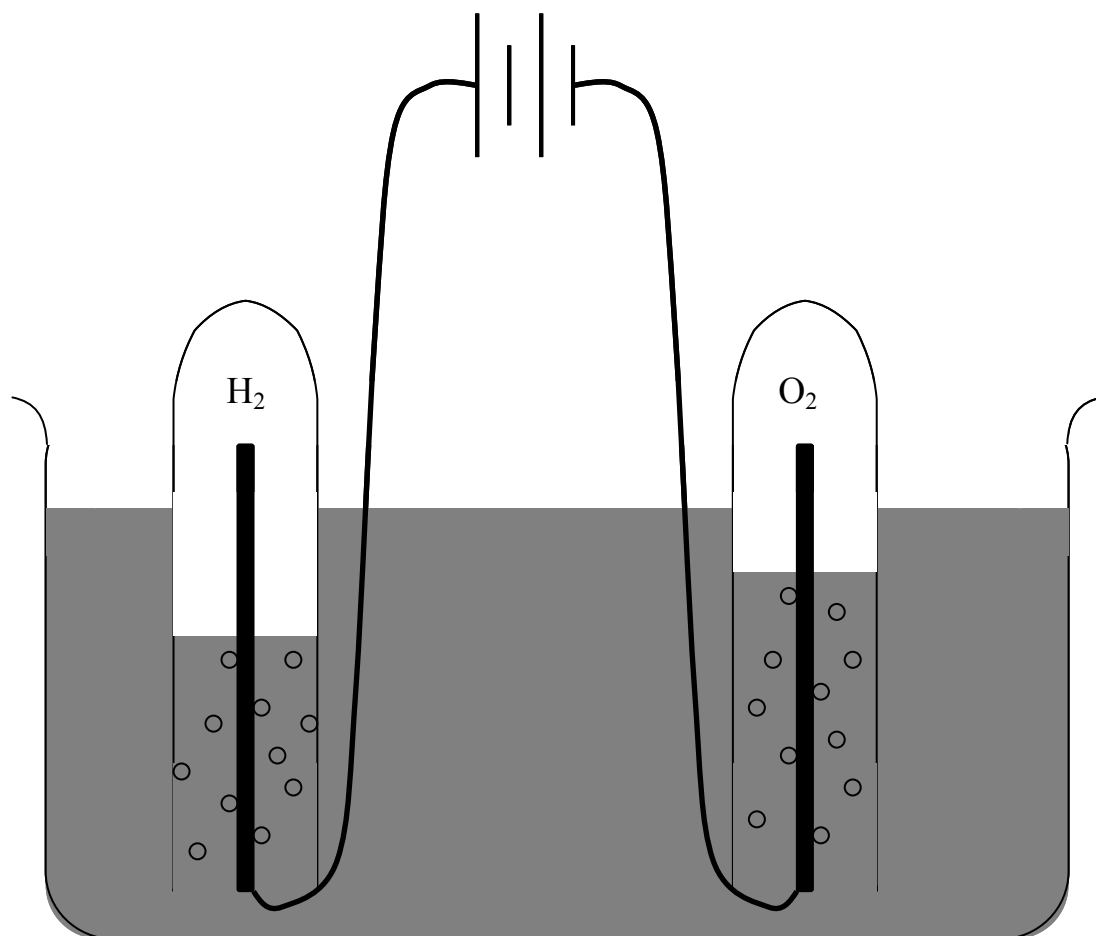
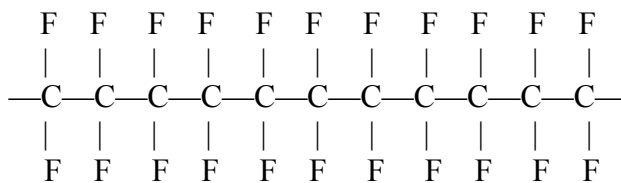


**Figure 2.1.** Diagram of the first fuel cell experiment performed by William Grove in 1839. First, electrolysis was performed on water (shown in the figure) to create hydrogen and oxygen gas. Afterward, the battery was replaced with a load, which was then powered by the fuel cell reactions.

### Polytetrafluoroethylene



### Nafion

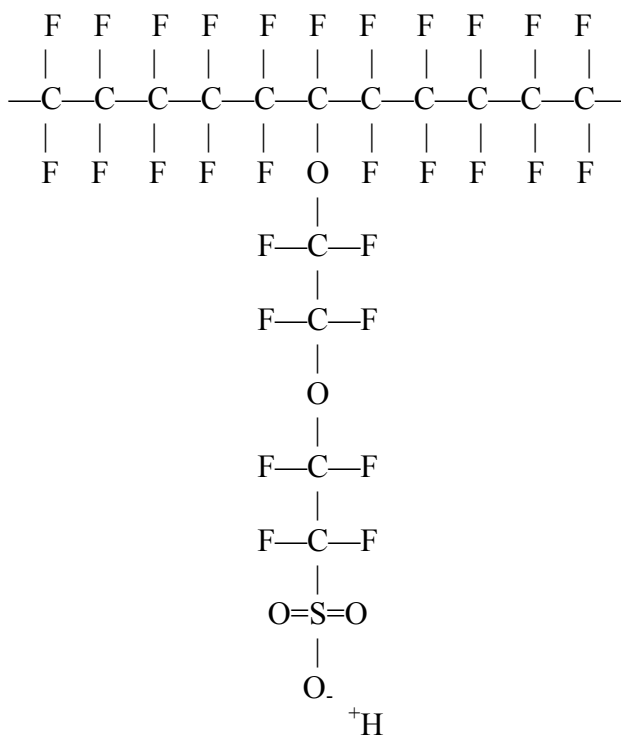
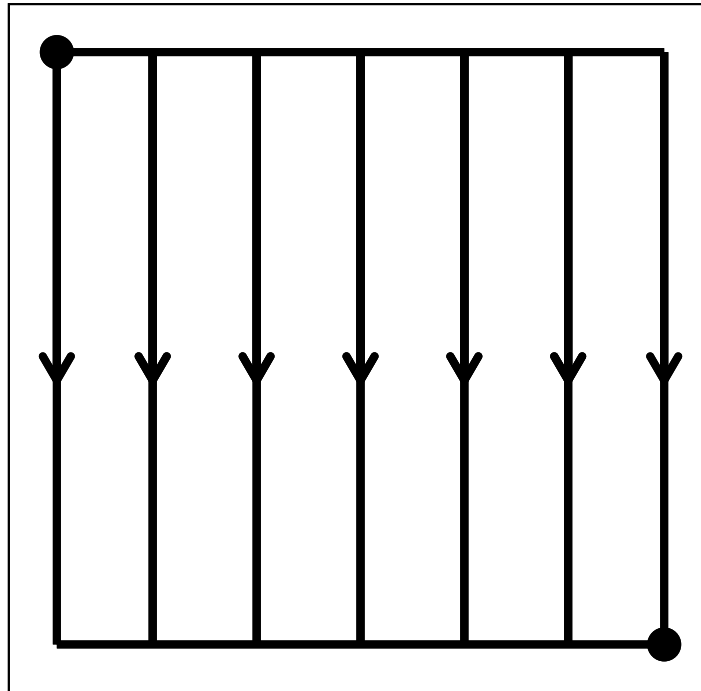


**Figure 2.2.** Diagram of the structure of PTFE and Nafion. The sulphonic group provides charge sites allowing proton conduction.

## Parallel



## Serpentine

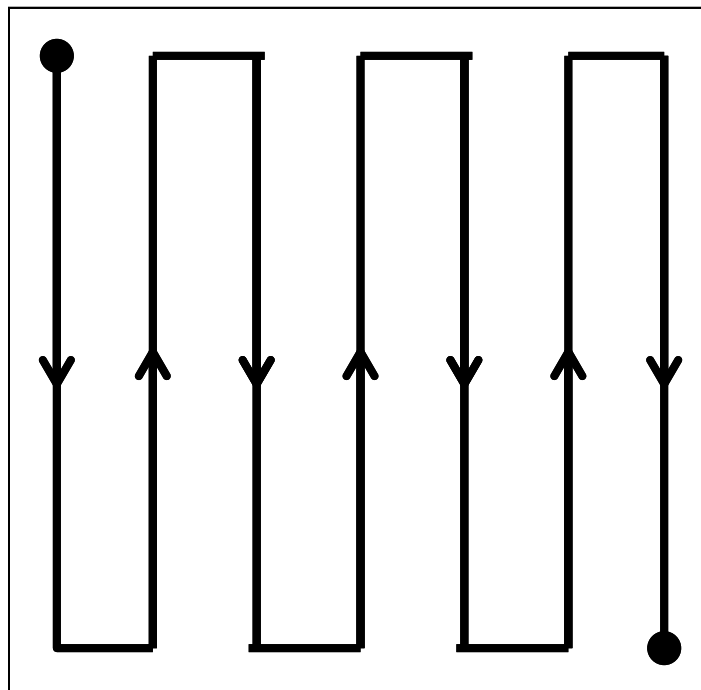


**Figure 2.3.** Diagram of parallel and serpentine flow field patterns.

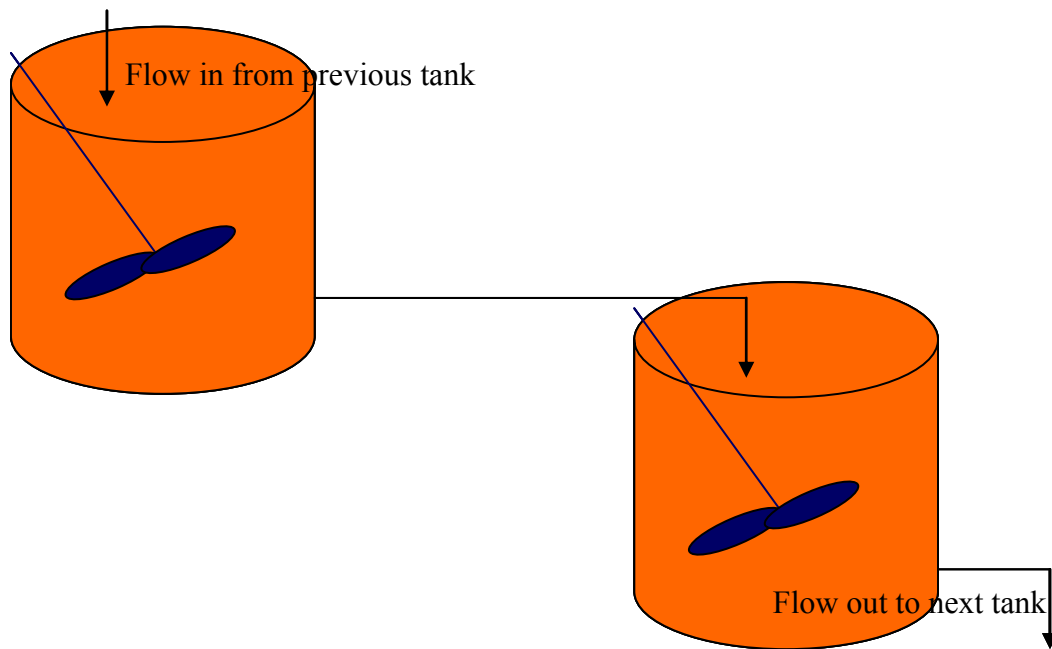


**Figure 2.4.** Diagram of two tanks-in-series. Any number of tanks may be added in series to model nonidealities in a flow reactor.

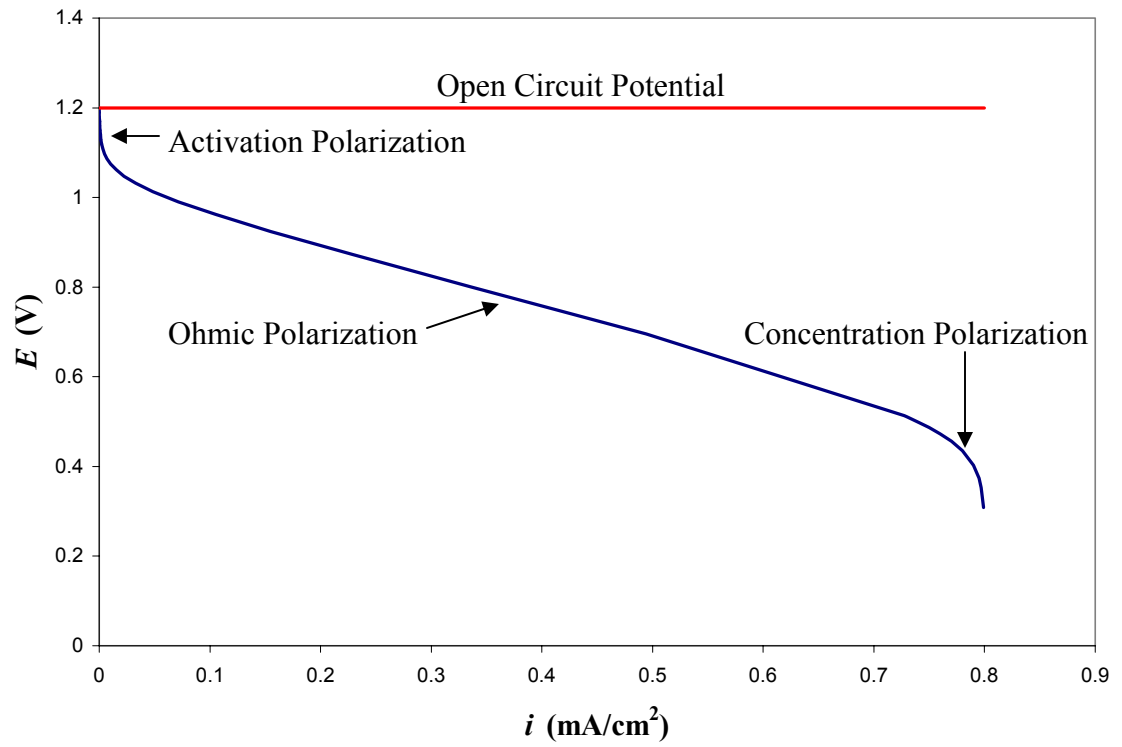


**Figure 2.5.** Typical  $I$ - $V$  curve for a fuel cell showing the open circuit potential and three regions dominated by different losses from the theoretical value. The loss governing each region is associated with a different process: electrode activation, charge transport, and mass transport.

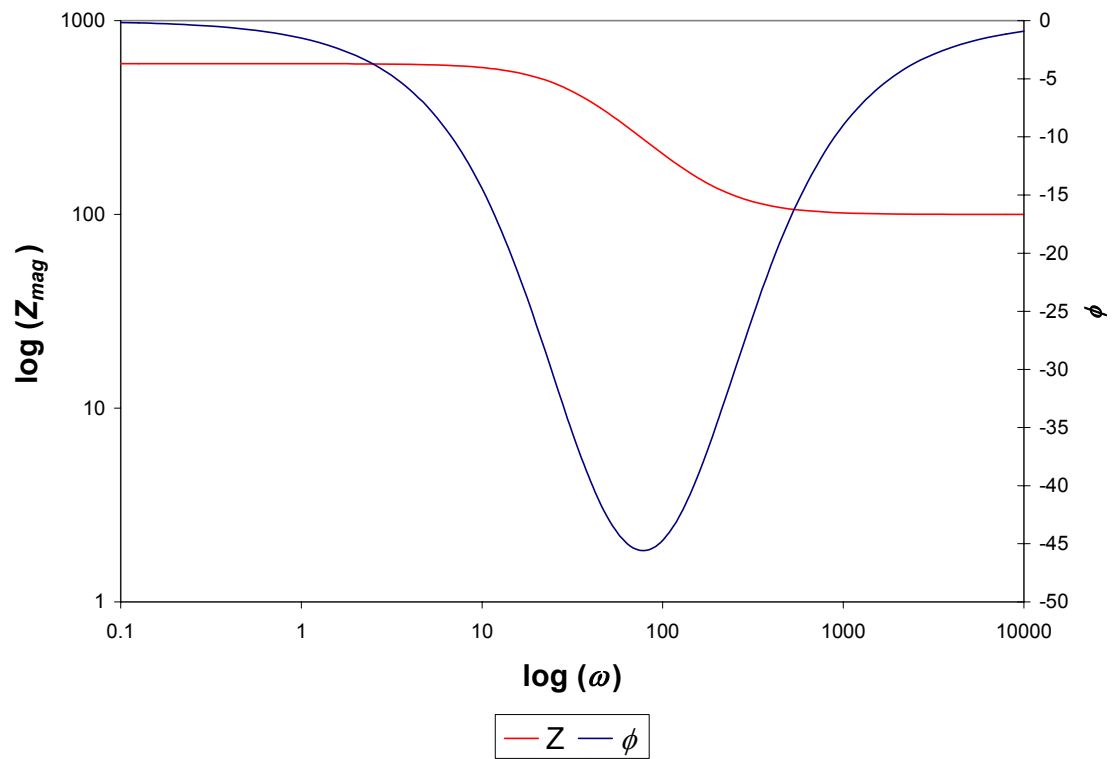


**Figure 2.6.** Bode plot for a parallel  $RC$  of  $500\ \Omega$  and  $1\ \mu\text{F}$  in series with a  $100\ \Omega$  resistor.

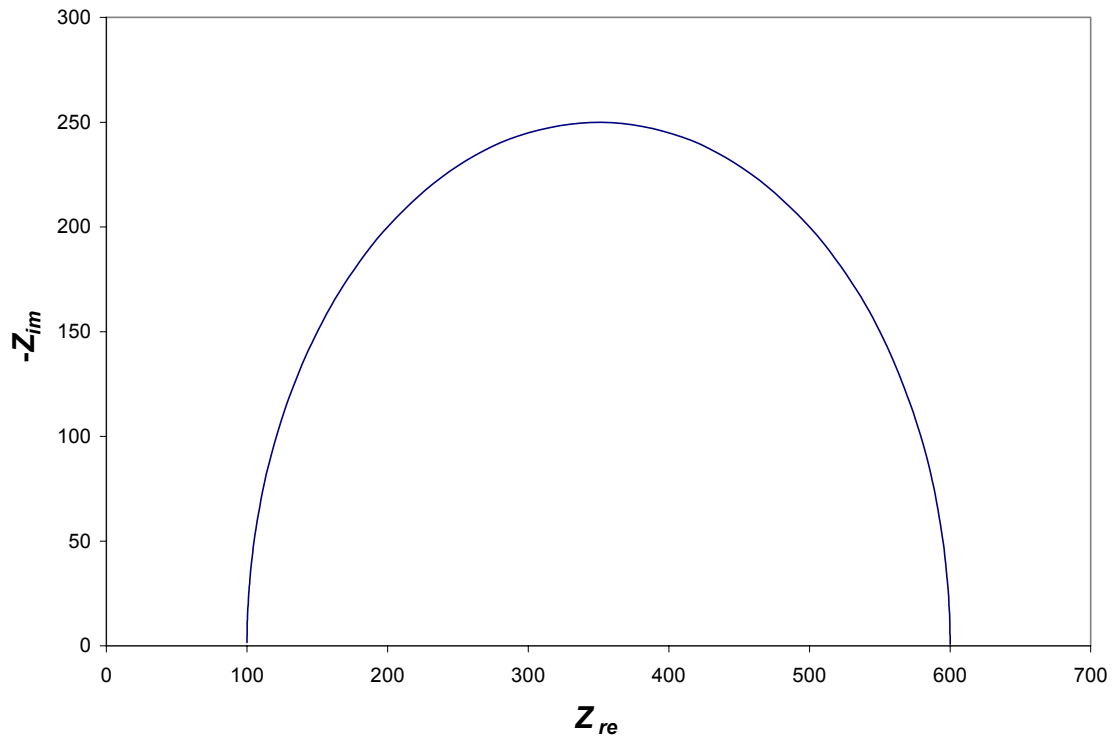


**Figure 2.7.** Nyquist plot for a parallel  $RC$  of  $500\ \Omega$  and  $1\ \mu\text{F}$  in series with a  $100\ \Omega$  resistor. The series resistance is at the high frequency (left-side)  $Z_{re}$  intercept, and the charge-transfer resistance is represented in the diameter of the semi-circle.

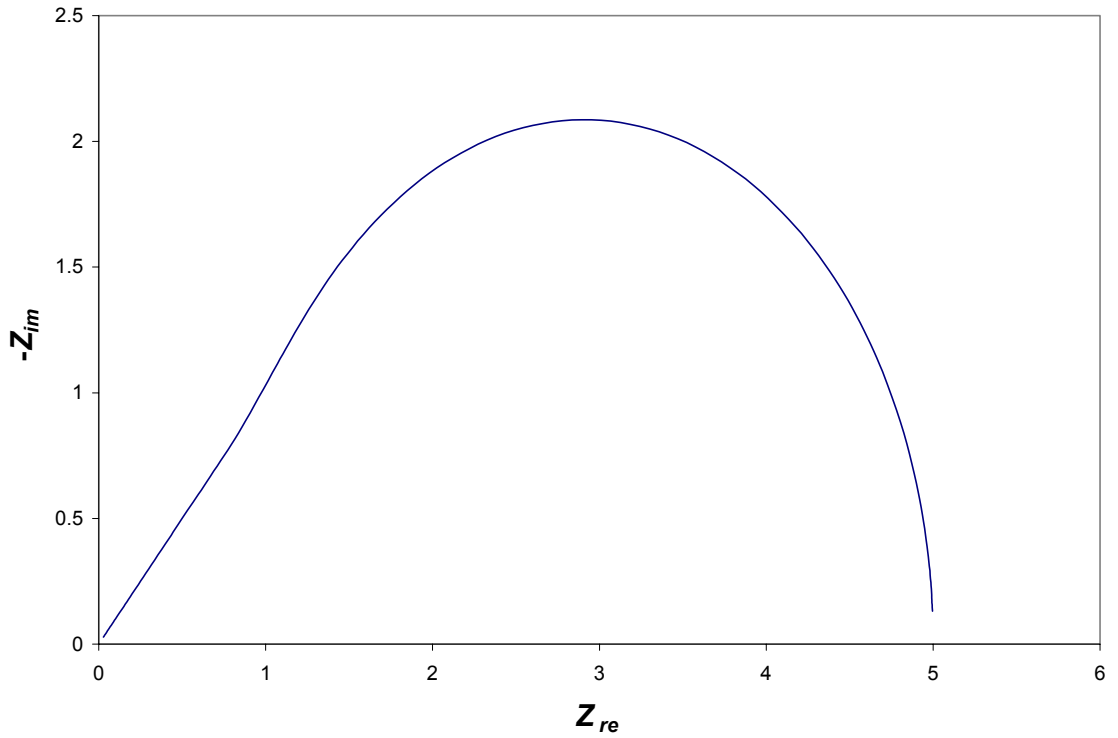


**Figure 2.8.** Nyquist plot of a finite diffusion element with  $W_i = 10 \Omega \cdot s^{-1/2}$  and  $\delta/D_i^{1/2} = .5 s^{1/2}$ . The high frequency side of the curve is the  $45^\circ$  line, which is characteristic of infinite diffusion. At lower frequencies, the curve reduces to a semicircle, which is characteristic of a parallel  $RC$ .



## **Section B**

### **Articles Submitted to Refereed Journals**

The following section contains five articles that have been submitted to refereed journals. All of the articles were written in collaboration with Dr. Wenhua H. Zhu. Note that the articles may repeat ideas that are discussed in previous chapters.

## **Chapter III**

### **Uniformity Analysis at MEA and Stack Levels for Nexa™ PEM Fuel Cell System**

#### **III.1. Introduction**

The mobile, portable power systems consist of two major power categories, continuous power and pulse power. Fuel cells are being widely investigated and applied for various electronics and communication equipment [1]. During continuous operation, the PEM fuel cell stack has demonstrated good power capability but poor response for instantaneous power demands. It usually takes 2~5 minutes to reach an acceptable operational condition because the polymer electrolyte membrane needs to be humidified for optimum performance. However, high power density, relatively quick start-up, rapid response to varying loads, and low operating temperature characteristics make the PEM fuel cells preferable for automobiles and other applications requiring high power

density [2]. Franseco et al. [3] discussed PEM fuel cell systems for a wide range of automotives and investigated the transient response to optimize the start-up using a PEM fuel cell stack model. Privette et al. [4] evaluated a ship service fuel cell (SSFC) system for power generation due to its high system level efficiency, few moving parts, little or no maintenance, and low acoustic and thermal signatures. There are many parameters that have effects on the PEM stack power output. The operational condition, MEA and stack features are related to the power output level. This paper describes efforts on uniformity analysis of Ballard Nexa™ stack at MEA and stack levels.

### **III.2. Experimental**

The Nexa™ power module (Ballard Power Systems - BPS) is a small, low maintenance and fully automated fuel cell system designed to be integrated into products for portable and back-up power markets. The stack has a specified net output power of 1200 W at full load with about 26 V. Hydrogen (>99.99%) and air are supplied to the sides of two gas channels formed in the flow field plates. The membrane-electrode-assembly (MEA) of the Nexa™ stack consists of the anode and cathode separated by a polymer membrane electrolyte. Each of the electrodes is coated on one side with a thin platinum catalyst layer. A single fuel cell consists of an MEA and two flow field plates as shown in Fig. 3.1. The Nexa™ stack has a total of 47 MEAs or cells connected in series through 48 flow-field plates. The preferred operating temperature is 65 °C at 1200 W power output. Ten of the Nexa™ stacks from Ballard were examined and tested in this work. The Nexa™ stack and experimental hard wares are shown in Fig. 3.2. The supply pressures to the stack were 5.0 psig for the fuel and 2.2 psig for air oxidant. The

operating pressure at fuel supply inlet was chosen at 40 psig. The stack was air cooled and had no outside fuel and oxidant humidification. The only by-products of the reaction were water and heat.

Electric loads (RBL488 TDI Transistor Devices-Dynaload® Division and 6060B HP DC Electronic load), Micronta digital multimeters, and Ohmite heat sink power resistors were taken to do the evaluations on the Nexa™ MEAs and stacks. The RBL488 single channel load is ideal for testing and analysis of fuel cells and batteries at high range current and constant power capabilities. The ultra-fast slew rate provides unmatched power supply transient testing capabilities. These features make the electric load a good solution for the fuel cell tests.

### **III.3. Results and Discussion**

#### *III.3.1. Nexa™ Stack Warm-Up and Cool-Down*

The PEM fuel cell stack has an essential checking sequence on MEA voltage, stack performance and operating conditions before the stack enters into its running state. The BPS Nexa™ power module is usually started in less than 2 minutes. If any of the start-up criteria are not met during the starting period, the system fails and stops. The stack number is viewed the same as the Nexa™ fuel cell serial number for convenient description. The NexaMon OEM software was employed for most Nexa™ data monitoring. If all starting criteria were met, the Nexa™ power module was able to run for start. The start-up parameters for the Nexa™ system #881 were partially shown on Fig. 3.3. The stack voltage was maintained at about 40 V without an external load after successful start-up at room temperature.

Then the Nexa™ power module was warmed up to a certain constant temperature at a specific load. The stack temperature only reached 32 °C in 10 minutes at a load of 5 A output current. The operation temperature was important for stack peak power capability. In order to evaluate the time requirement for rapid stack warm-up, the stack #768 was operated at a load of 1.39 Ω for one minute and then changed to a load of 0.68 Ω for the rest of operation period. Two different load levels were chosen for the stack here in order to reach 65 °C operating temperature for rapid stack warm-up. If this type of stack was well humidified, a higher power load (0.68 Ω) was applied to the stack #881. As shown in Fig. 3.4, two stacks (#768 and #881) at room temperature (25°C) reach 60 °C in about three minutes and operate at 65 °C after five minutes. Once the stack finished its operation, it was cooled down close to room temperature in about 20 minutes with no external load (Fig. 3.5). This is an acceptable condition for the Nexa™ power module to be shut off. As a whole, the Nexa™ stack is able to be warmed up to 65°C in 5 minutes for a 1200 W power output at 25°C room temperature.

### *III.3.2. Stack Polarization Curves*

The Nexa™ power module has a maximum voltage of 50 V and provides 1200 W of unregulated DC power output. The ambient temperature at rated power is allowed from 3 °C to 30 °C. The Nexa™ power module is a fully automated fuel cell system with low maintenance. It produces zero harmful emissions and permits indoor operations. The stack polarization curve provides significant parameters for power management and transient applications. The experimental polarization curve is slightly different between the positive and negative load increments because the produced water content is a function of load and the water content in membrane at equilibrium is time dependent.

The small difference is neglected in the polarization curve experiments. However, the automated system is not permitted to operate at a fixed temperature if the load is changed. The I-V curves for BPS PEM fuel cell system were measured with periodic current interruption (PCI) to maintain isothermal stack temperature. In details, the stack voltage was recorded at a certain current and temperature. Then the current was quickly interrupted and the system load was adjusted back to maintain isothermal stack temperature. By using the PCI technique, the polarization curves for the power module, i.e. stack #751, are plotted at 24 °C, 45 °C, and 65 °C as shown in Fig. 3.6. The stack was not operated at a high current level and room temperature (24 °C) because the mass transfer problem and concentration polarization may reduce the lifetime of the power module. The stack power output was measured at 1131 W at 43.5 A and 45 °C, and 1283 W at 45.5 A and 65 °C (Fig. 3.7). Both of these are very close to the Ballard specific point. The calculated stack resistance drops from 1.2  $\Omega$  to 0.1  $\Omega$  when the stack output current increases from 0.1 A to 5 A. The stack resistance has no obvious difference at 45-65 °C, especially at more than 10 A output current as shown in Fig. 3.7. The Nexa™ fuel cell system and stacks are able to work at high current levels. The uniformity and weakness analysis are important to the stack performance and its operation lifetime.

### *III.3.3. MEA and Stack Uniformity*

Ten Nexa™ power modules were individually operated at an approximate 800 W power output level. The MEA voltage in the stack was then measured until the power module reached a steady state, i.e. constant fuel pressure and stack temperature (57 °C). The voltage of all 47 MEAs in 10 stacks was shown in Fig. 3.8. The MEA series order is started from the hydrogen side to the compressed air side. Quite a few MEAs in different

stacks have the same lower voltage at the 46th and the 47th cells. Average voltage of all the MEAs was 0.638 V at 800 W. And this voltage is 224 mV lower than that of stacks at no external load, which has an average voltage of 0.862 V. The voltage at no external load is somewhat lower than the normal open circuit voltage from 0.900 V to 1.100 V. This is mainly decided by the different system design. Fig. 3.9 shows the voltage difference with an outside load and with no external load for the stack #308. Similarly, the MEAs in the stack #308 without an external load have a voltage of 0.870 V. But these MEAs have different voltage drops at 800 W loads. The difference between the MEA voltage is caused by electrode limited uniformity (catalyst distribution, electrode thickness, inner gas distribution etc.), MEA uniformity, and stack gas/liquid distribution management. Especially noticeable is that the 46th and 47th cells have much larger voltage drops than the other cells. The lower voltages of these cells highly reduce the high power capability for the stack systems. This may be caused by gas distribution problem, water flooding, or low reaction temperature at the compressor side. It will be extensively examined and diagnosed with electrochemical impedance spectroscopy.

#### *III.3.4. MEA and Stack Statistic Data Analysis*

For the individual Nexa™ stack, the statistical MEA data and the measured stack voltage were listed in Table 3.1. The second minimum and the second maximum voltage were also shown in the above table. The MEAs in the stack #792 has a lowest average voltage of 0.620 V and the MEAs in the stack #515 has a highest average voltage of 0.655 V. The difference of the MEA voltage sum between the two above stacks is 1.62 V and the difference of the measured stack voltage between two stacks is 1.44 V. The experimental statistical voltage is  $30.20 \pm 0.38$  V for each Nexa™ stack at 800 W power

output. The voltage normal distribution is shown in Fig. 3.10. The exact shape of the normal distribution depends on the MEA voltage mean and the standard deviation of the distribution. The standard deviation is a measure of spread and indicates the amount of departure of the values from the voltage mean. Differences in standard deviation values model the shape of the voltage distribution. Although most of the distribution remains symmetric, the distribution becomes flatter if all MEA voltages of ten stacks at load are put together. This increases the standard deviation, which corresponds to more diversity between the voltage observations. However, the Nexa™ MEA voltage has a sharp shape without an external load, which means it has small standard deviation and no voltage difference at no external load.

According to statistical data in Table 3.1, the average difference is 8.8% and the highest difference is 13.1% between the minimum MEA voltage in the stack and the mean value. This difference reveals that it is possible to increase the product power level and cut the cost per kilowatts by improving the weak electrodes or MEAs in the stack. The voltage difference is mostly caused by electrode, MEA, and stack uniformity. This reminds that operation of stacks in series or parallel should take the voltage difference into consideration. High power capability stacks with similar voltage at load are preferred for series or parallel operation.

The mean, maximum, and minimum data of the MEA voltage in ten Nexa™ stacks are shown in Fig. 3.11. The stack numbers from left to right in Table 3.1 are shown as 1 to 10 in Fig. 3.11, respectively. The MEAs have an average voltage of 0.638 V in the stack #751(1). But the stack also has the minimum voltage of 0.566 V and the second minimum voltage of 0.571 V. If the above MEA performance is improved

from the minimum voltage to the average level, the power capability is potentially increased by 11.3%. If a little more catalyst loading is applied to these electrodes with weak performance, or the gas distribution and purge system design are improved, the power module could potentially obtain a higher power output capability. This improvement prospectively reduces unit cost per kilowatts.

#### **III.4. Conclusion**

Uniformity analysis at MEA and stack levels has been conducted for the Nexa™ fuel cell system. The results of the MEAs and stack voltage at the load of 800 W reveal that difference exist among those MEAs at load in the same stack, especially the two cells at the air compressor side for the Nexa™ stack. The MEAs have an average voltage of 0.638 V in the stack #751. It also has the minimum voltage of 0.566 V. The improvement of the MEA performance from the minimum voltage to the average level potentially increases the stack power capability by 11.3%. This voltage difference reveals that it is possible to increase the product power capability and cut the cost per kilowatts by improving the weak performance electrodes or MEAs. This is likely realized by adding more catalysts to the electrodes, adjusting the gas distribution/purge system design, or changing with high-power-density MEAs in the stack.

#### **III.5. Acknowledgements**

This work was performed under a U. S. Army contract at Auburn University (DASG 60-00-C-0070) administered through the U.S. Army Space & Missile Defense Command. I would like to recognize Wenhua H. Zhu and Donald R. Cahela who were



the co-authors for the original article. I also wish to acknowledge contributions from Dr. Ryan Nickell, Mr. Dwight Cahela, and Ms. Georgian Allison during the work phases of this project. This article may be found in full in the *Journal of Power Sources* [5].

### **III.6. References**

- [1] L. P. Jarvis, T. B. Atwater, P. J. Cygan, *J. Power Sources* 79 (1999) 60–63.
- [2] V. Mehta, J. S. Cooper, *J. Power Sources* 114 (2003) 32–53.
- [3] M. D. Francesco, E. Arato, *J. Power Sources* 108 (2002) 41–52.
- [4] R. M. Privette, T. J. Flynn, M. A. Perna, R. Holland, R. Rahmani, C. Woodburn, S. W. Scoles, R. C. Watson, in: *Proceedings of the 34th Intersociety Energy Conversion Engineering Conference*, Vancouver, B.C., Canada, August 1-5 1999.
- [5] W. H. Zhu, R. U. Payne, D. R. Cahela, B. J. Tatarchuk, *J. Power Sources* 128 (2004) 231.

**Table 3.1.** Data statistics and sample analysis of MEA voltage in ten Nexa™ PEMFC power modules, individually measured at 800 W and 57°C (Confidence level, 98%).

| Serial number                  | 751       | 515       | 635       | 454       | 879       | 792       | 881       | 527       | 308       | 768       |
|--------------------------------|-----------|-----------|-----------|-----------|-----------|-----------|-----------|-----------|-----------|-----------|
| Mean                           | 0.6377    | 0.6547    | 0.6363    | 0.6334    | 0.6257    | 0.6203    | 0.6445    | 0.6511    | 0.6437    | 0.6358    |
| Standard error                 | 0.0030    | 0.0028    | 0.0015    | 0.0012    | 0.0020    | 0.0024    | 0.0019    | 0.0014    | 0.0021    | 0.0017    |
| Median                         | 0.6400    | 0.6570    | 0.6390    | 0.6340    | 0.6260    | 0.6240    | 0.6470    | 0.6520    | 0.6460    | 0.6380    |
| Mode                           | 0.6400    | 0.6640    | 0.6430    | 0.6350    | 0.6300    | 0.6280    | 0.6490    | 0.6520    | 0.6440    | 0.6360    |
| Standard deviation             | 0.0206    | 0.0190    | 0.0102    | 0.0079    | 0.0137    | 0.0162    | 0.0127    | 0.0094    | 0.0142    | 0.0114    |
| Sample variance                | 0.0004    | 0.0004    | 0.0001    | 0.0001    | 0.0002    | 0.0003    | 0.0002    | 0.0001    | 0.0002    | 0.0001    |
| Kurtosis                       | 3.7925    | 9.9260    | 1.3641    | 2.9148    | 12.0925   | 13.4662   | 7.3851    | 1.3543    | 16.3477   | 6.9503    |
| Skewness                       | -1.4933   | -2.7319   | -0.9486   | -0.5390   | -2.9227   | -3.0417   | -2.1169   | -0.5627   | -3.2389   | -2.1206   |
| Range                          | 0.105     | 0.106     | 0.05      | 0.048     | 0.085     | 0.103     | 0.077     | 0.05      | 0.098     | 0.065     |
| Minimum                        | 0.566     | 0.576     | 0.606     | 0.605     | 0.561     | 0.539     | 0.590     | 0.620     | 0.569     | 0.588     |
| Min2nd                         | 0.571     | 0.582     | 0.611     | 0.622     | 0.582     | 0.584     | 0.610     | 0.636     | 0.619     | 0.601     |
| Maximum                        | 0.671     | 0.682     | 0.656     | 0.653     | 0.646     | 0.642     | 0.667     | 0.670     | 0.667     | 0.653     |
| Max2nd                         | 0.662     | 0.679     | 0.653     | 0.649     | 0.642     | 0.639     | 0.665     | 0.666     | 0.662     | 0.650     |
| Mean-Minimum                   | 0.072     | 0.079     | 0.030     | 0.028     | 0.065     | 0.081     | 0.056     | 0.031     | 0.075     | 0.048     |
| Count                          | 47        | 47        | 47        | 47        | 47        | 47        | 47        | 47        | 47        | 47        |
| MEA voltage, $E_i$ (V)         | .638±.007 | .655±.006 | .636±.003 | .633±.003 | .626±.005 | .620±.005 | .645±.004 | .651±.003 | .644±.005 | .636±.004 |
| Sum, Statistic $E_{stack}$ (V) | 29.97     | 30.77     | 29.91     | 29.77     | 29.41     | 29.15     | 30.29     | 30.60     | 30.25     | 29.88     |
| Stack voltage, $E_{exp}$ (V)   | 30.32     | 30.76     | 29.86     | 29.96     | 29.66     | 29.32     | 30.57     | 30.95     | 30.47     | 30.09     |

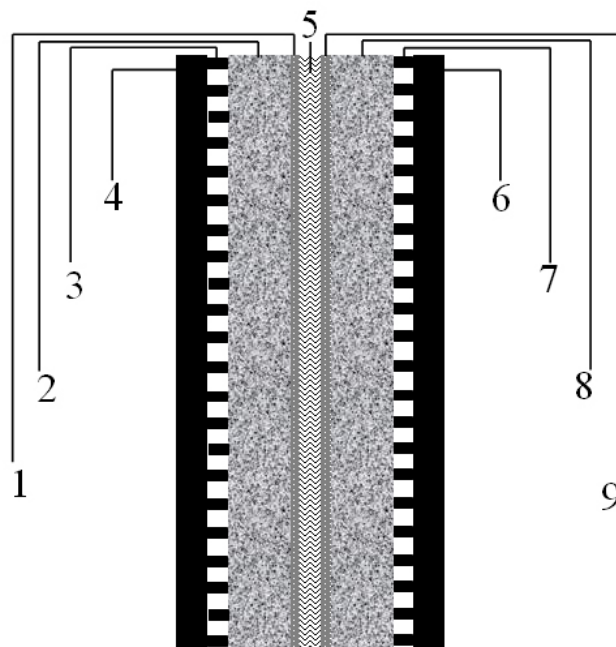


**Figure 3.1.** Single fuel cell and membrane electrode assembly in the PEM fuel cell stack. 1—Oxidant catalyst layer (cathode), 2—Oxidant diffusion layer, 3,4—Oxidant flow field plate, 5—Proton exchange membrane, 6,7—Fuel flow field plate, 8—Fuel diffusion layer, 9—Hydrogen catalyst layer (anode), 1,2,5,8,9—Membrane-electrode-assembly (MEA), and 1~9—single fuel cell unit.

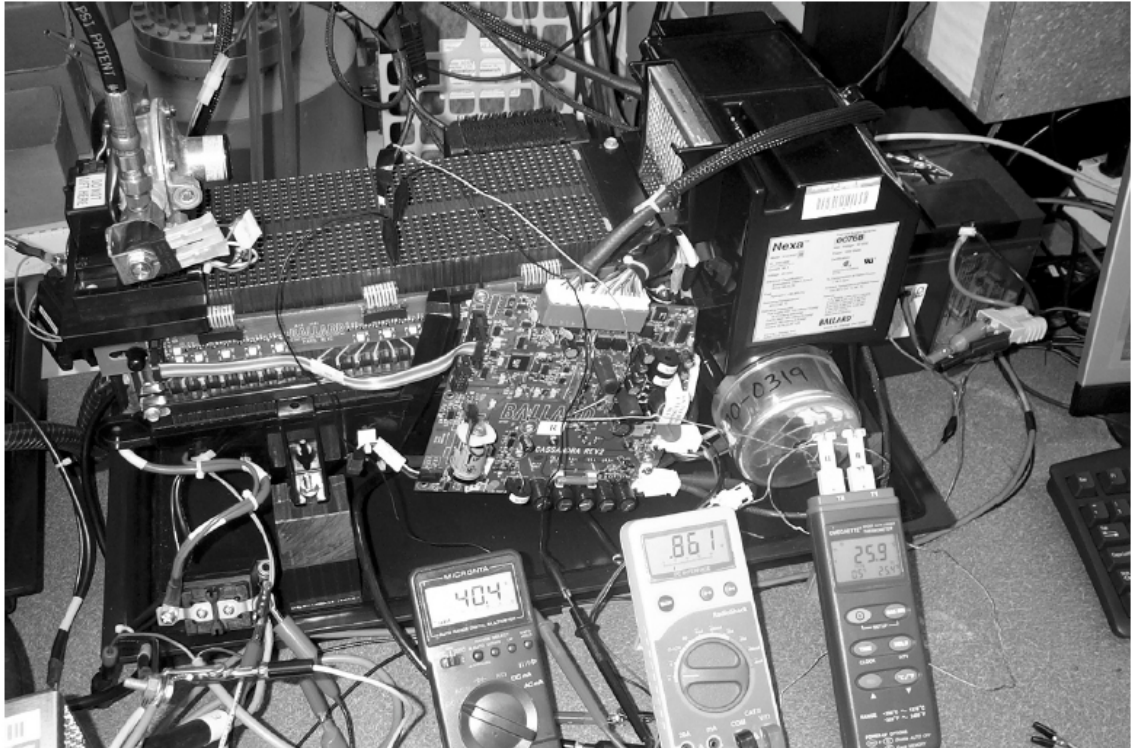


**Figure 3.2.** Nexa™ power module and experimental hardwares. Stack #768 voltage at 40.4 V and the 27<sup>th</sup> MEA's voltage at 0.861 V with no external load at room temperature.

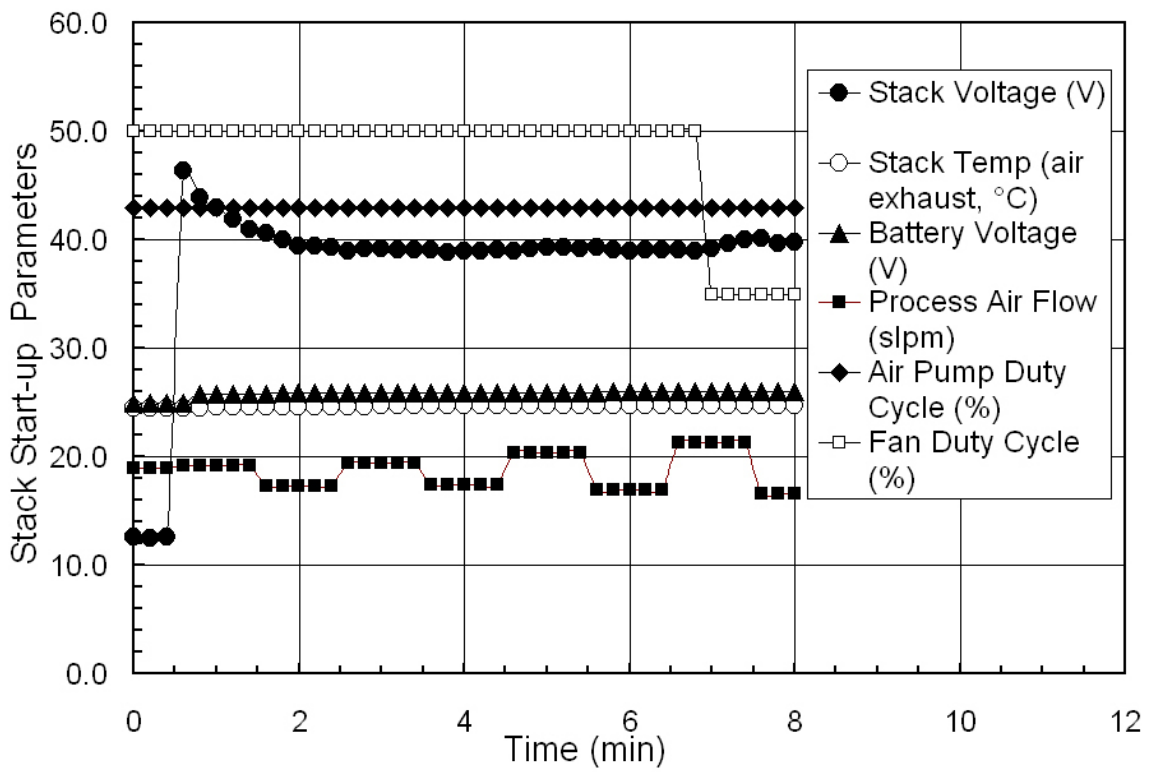


**Figure 3.3.** Nexa™ #881 start-up curves versus operation time. Indoor air and compressed Grade-5 hydrogen supply.

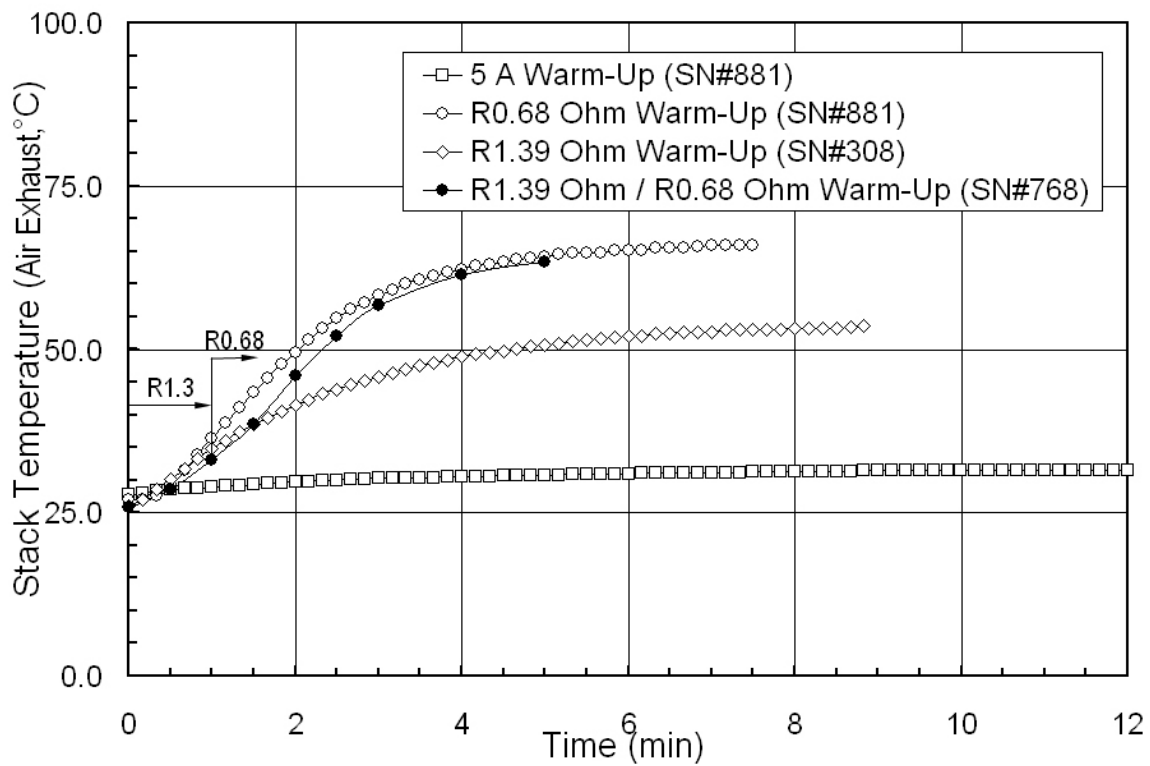


**Figure 3.4.** Stack temperature versus stack warm-up time. Indoor air and compressed Grade-5 hydrogen supply.

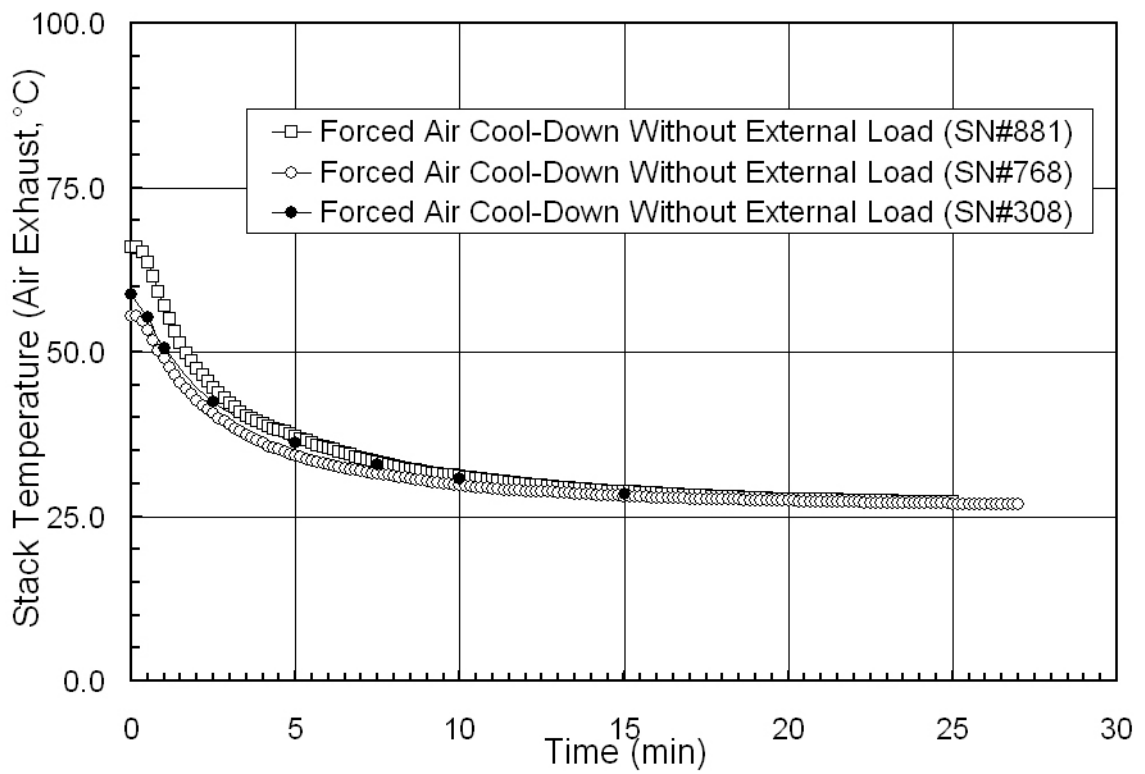
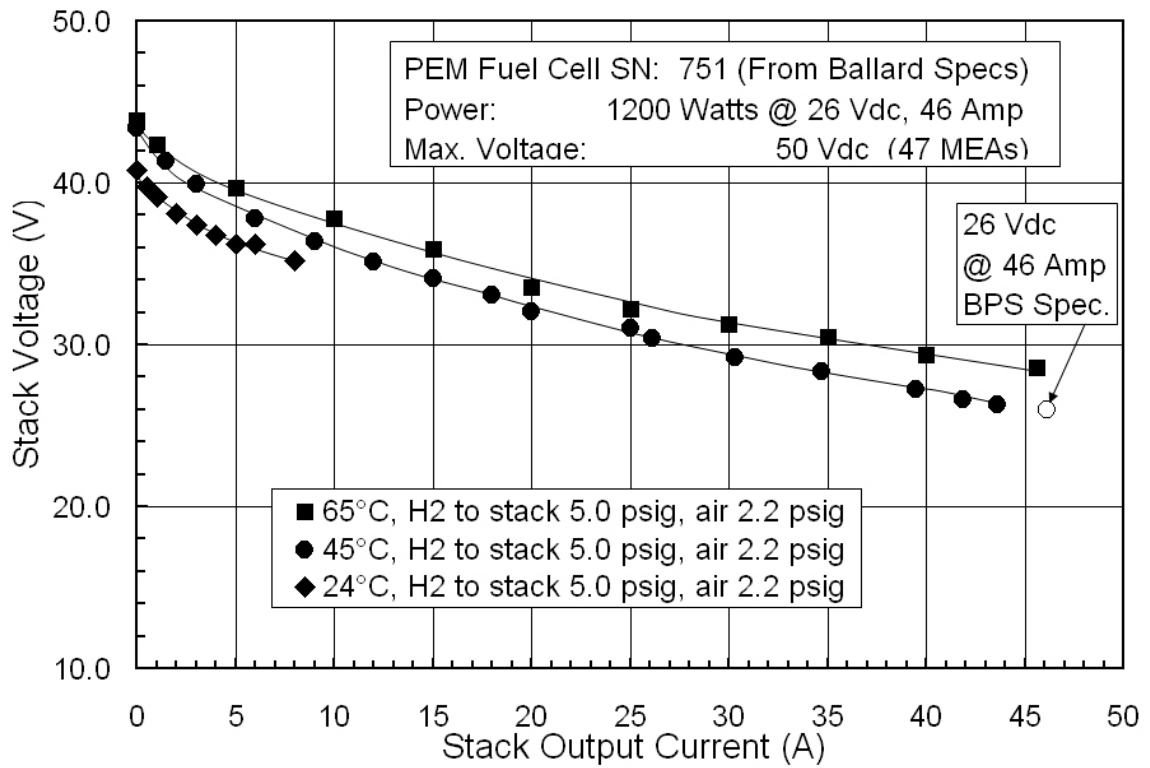


Figure 3.5. Stack cool-down curves with no external load measured from BPS Nexa™ stacks.



**Figure 3.6.** Polarization curves measured from the BPS Nexa™ stack with periodic current interruption to maintain isothermal stack temperature.



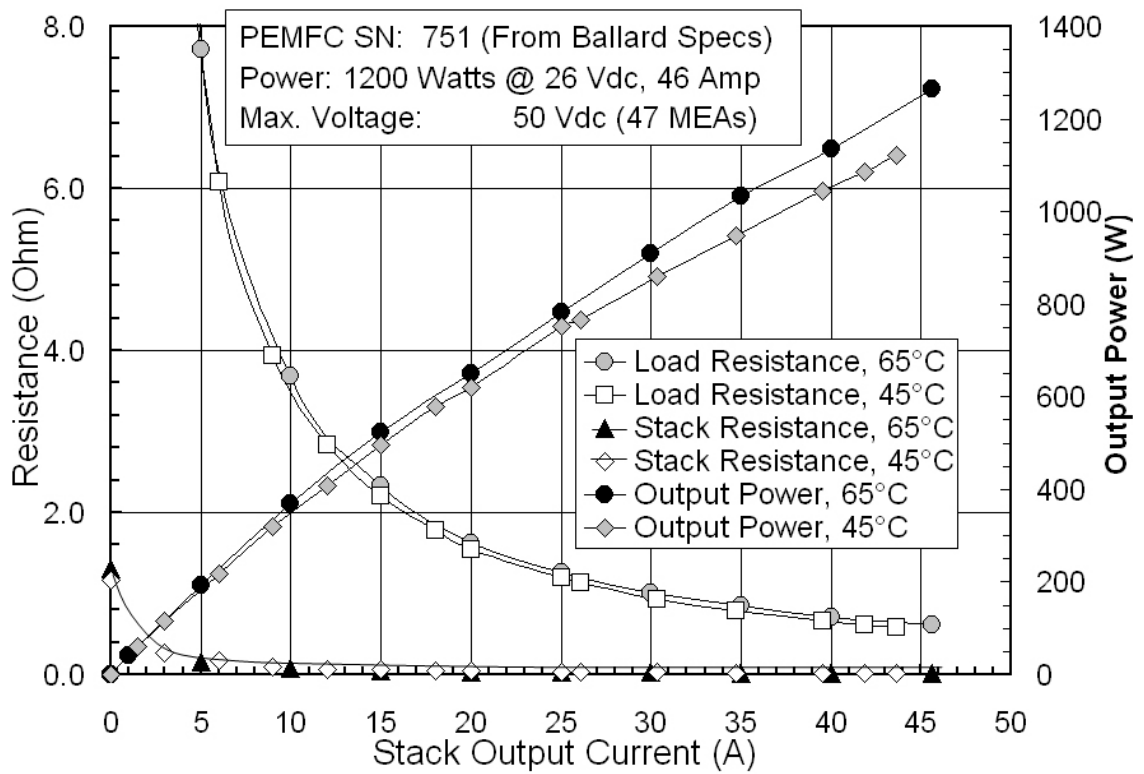
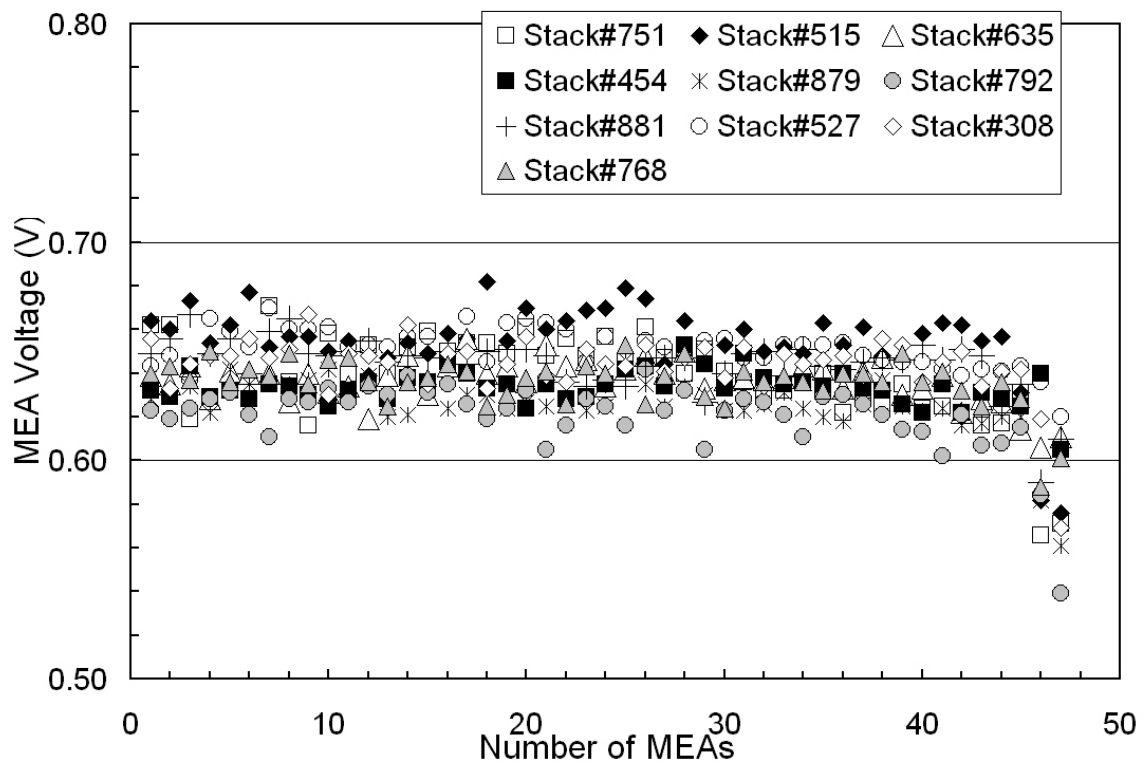
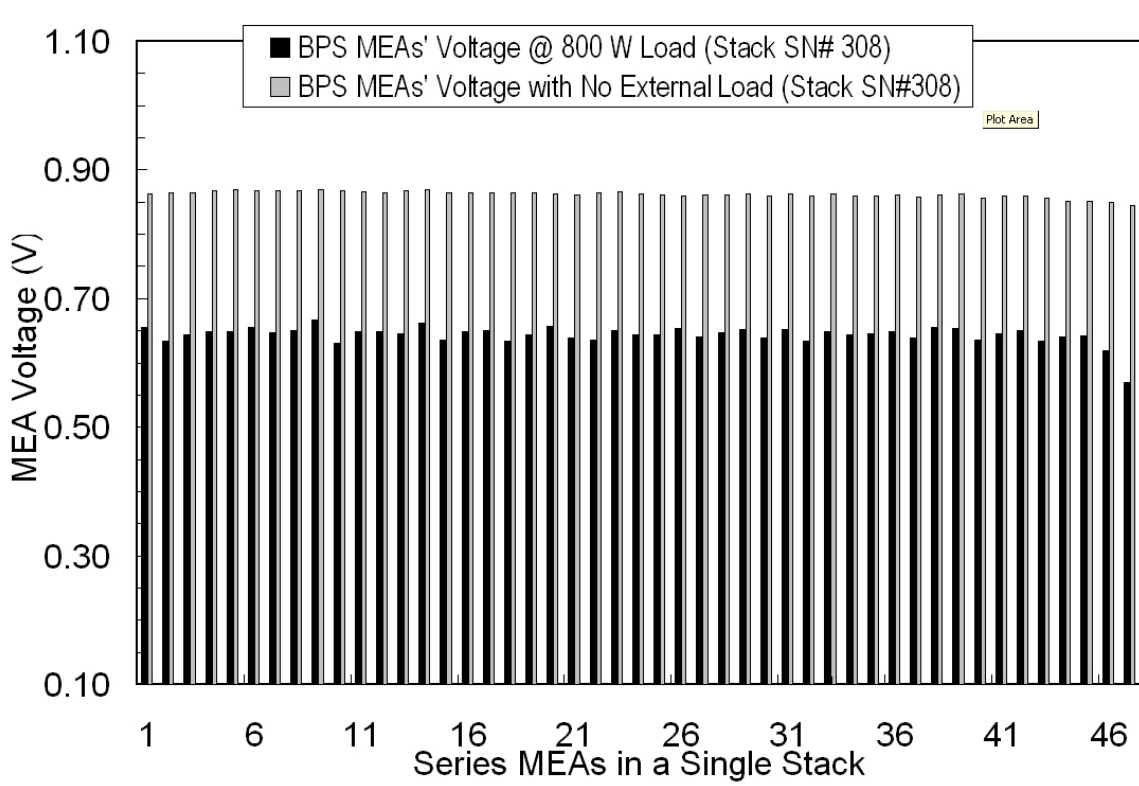


Figure 3.7. Stack resistance and output power as a function of stack output current.



**Figure 3.8.** Voltage of MEAs in series from hydrogen to oxygen side in ten BPS Nexa™ stacks. Stack power output 800 W at 57°C with indoor air and compressed Grade-5 hydrogen supply.



**Figure 3.9.** Voltage of MEAs in series with/without a load in the Nexa™ stack. Indoor air and compressed Grade-5 hydrogen supply.

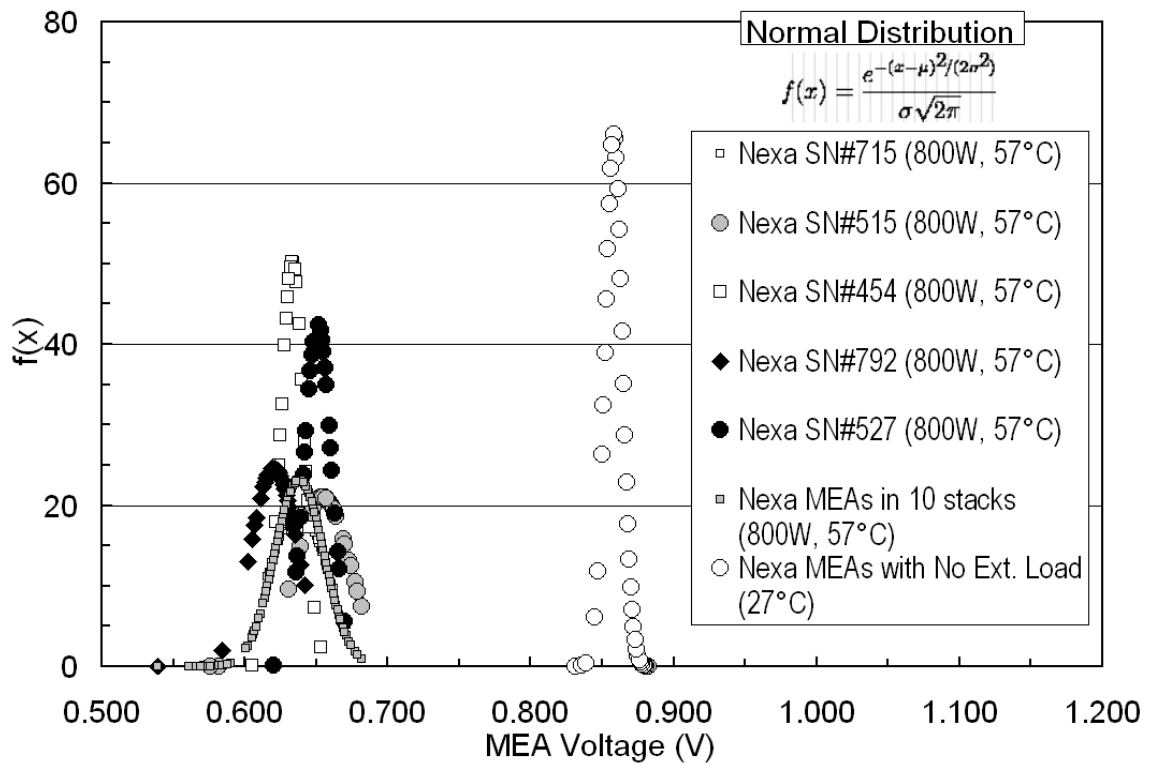


**Figure 3.10.** Normal distribution curves at a stack power output 800 W and 57°C with indoor air and compressed Grade-5 hydrogen supply.

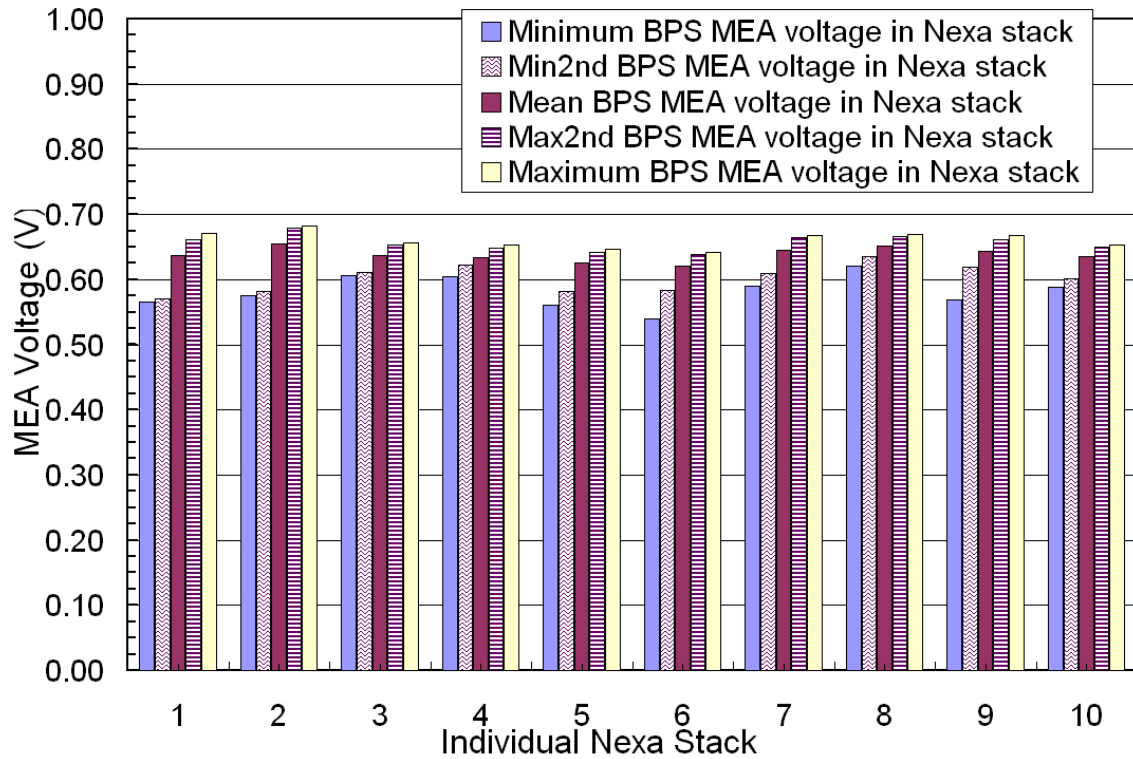


**Figure 3.11.** Statistical MEA voltage data in ten Nexa™ stacks. Stack power output 800 W at 57°C with indoor air and compressed Grade-5 hydrogen supply.

## **Chapter IV**

### **Critical Flow Rate of Anode Fuel Exhaust in a PEM Fuel Cell System**

#### **IV.1. Introduction**

The PEM fuel cell system is an emerging power source providing high power density, high energy conversion efficiency, and cleaner emissions than many other available technologies [1]. The system has many applications such as generating electricity, supplying hot water for baths, and heating cold room air by recovering heat from the electrochemical reactions. Its fuel gas at the anode side undergoes an electrochemical oxidation of hydrogen by losing electrons, while the exhausted inert gas and water vapor (or liquid) accumulate at the exit portion of flow channel. Oxygen is electrochemically reduced with hydrated protons at the cathode side, producing water and heat. Further co-generation or fuel recycle on the system operation of the polymer electrolyte fuel cell (PEFC) can be helpful for obtaining higher fuel and overall energy efficiency [2].

For a complete fuel cell system, the management of small amounts of exhaust gas in the anode side is significantly related to the system's energy efficiency and its operation lifetime. Most work on mathematical models and structure optimizations have been based on a unit PEM fuel cell [3]. No model and related work was found in the literature that addresses the anode gas flow and its exhaust in a stack and integrated

system. A fuel cell stack, including its control system, needs various optimal methods to operate and convert chemical energy to electricity as efficiently as possible for different fuel sources [4, 5]. Wells et al. [6] gave a resuscitation method and apparatus for which there was a decrease in stack performance. The system and its stack kept running rather than performing an emergency shutdown, if the fuel cell system successfully carried out this resuscitation process. Barton et al. [7] developed an apparatus for stack exhaust purge using purge conditions determined by comparing the performance of one or more fuel cells in a purge cell portion of the stack with one or more cells in the stack. As a whole, gas (fuel, oxidant, and exhaust) management, water (liquid and vapor) management, thermal (heat transfer) management, and power (energy) management are the four main areas for PEFC system design and safe operation. Water and thermal management exhibit a close relationship that has been widely investigated in order to develop MEAs and operate the PEFC system safely [8, 9]. Gas management is the primary design issue of the fuel cell system for both MEA membranes and system safety concerns. This is essential for the system to maintain operation after start-up and to prolong its operational lifetime. In this paper, the fuel gas in the anode side and its exhaust management are discussed in detail and the critical flow rate of anode exhaust is determined by suitable manual adjustment of the exhaust flow rate.

## **IV.2. Experimental**

A PEM fuel cell stack in a Nexa™ power module (Ballard Power Systems, SN00751) was tested in the laboratory. The Nexa™ power module is an automated PEFC system, providing unregulated DC power through the use of an external hydrogen

fuel supply. Its operation is limited only by the fuel purity requiring no more than 0.01% of total inert gases at a rated power of 1200 W. Hydrogen and air are supplied to two separate gas channels flowing through the flow field plates separately. The above PEM stack has a total of 47 MEAs (or cells) connected in series through 48 flow-field plates. The PEM stack and experimental schematic drawing are shown in Fig. 4.1. The operating pressure at the fuel supply inlet was chosen to be 20-40 psig. The fuel supply pressure to the stack was 5.0 psig, and the pressure of air oxidant was defined as 2.2 psig. The power system was air cooled and used no outside fuel or oxidant humidification. The lab test was conducted in a stack life time of no more than 78 hrs (The product operating life time is no less than 1500 hrs).

This system has its advantages: requiring low maintenance and being fully automated, portable, and highly integrated. The disadvantage of the system is that utilization of hydrogen feeds with high levels of inert gases or reformed gases is not convenient, because frequent purging for system restoration wastes fuel energy resulting in efficiency loss. It may cause system failure when the exhaust is released too frequently. Therefore, a manual purge line was added into the end of the Nexa™ fuel exhaust line in order to use the system for the anode fuel and exhaust experiment. Making use of the auto purge line, the fuel cell system was able to be normally started and shut down safely. By using a back pressure valve, the manual purge stream was separated from the Nexa™ exhaust line. A gas bubble meter was connected to the manual exhaust stream for accurate measurement of the gas flow rate (Fig. 4.2). The PEM fuel cell system was first fed with pure hydrogen fuel (>99.99%) according to the product operation manual. After the fuel cell system was started at *ca.* 200 W stack load



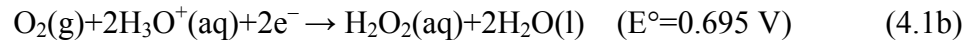
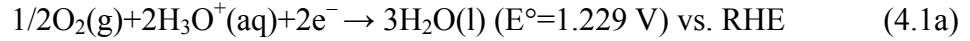
and allowed to reach a steady state at a constant current after approximately 20 min, the hydrogen fuel with inert gas was fed into the fuel cell system replacing the pure hydrogen fuel. The purge cell voltage was recorded by the NexaMon software (OEM 2.0 version) from Ballard. The Agilent 6890 gas chromatography system with enhanced integrator was utilized to measure the compositions of the fresh and exhaust gas streams. The flow rate was determined for feeds of either pure hydrogen or high levels of inert gases.

Higher polarization resistance exists at the cathode side rather than the anode side. In addition, water is formed at the cathode side, because catalyst-activated oxygen atoms react with protons to generate heat and water by taking electrons originally generated at the anode. This means that heat and water are mainly produced at the cathode side; thus, the effect of water vapor in the gas stream at the anode side is neglected when the fuel cell system is operated at 200 W stack power and *ca.* 30 °C stack temperature. Electronic loads (RBL488 Dynaload® Division and 6060B HP Electronic load) were applied to maintain a steady stack current.

### **IV.3. Results and Discussion**

#### *IV.3.1. Fuel Gas and Its Exhaust Management in the Anode Stream*

Gas (hydrogen fuel, air/O<sub>2</sub> oxidant, and their exhausts) management is an important issue for the design and operation of a complete PEM fuel cell system. Management of the fuel gas distribution and its exhaust stream(s) plays an important role in the operation of the PEM stack. This process is also related to the fuel efficiency and the overall system efficiency. The reaction in the aqueous acid at the cathode is the reduction of oxygen in air by receiving electrons as follows:



Some water produced at the cathode undergoes mass transfer by back-diffusion to the anode side for hydrogen electro-oxidation. The reaction at the anode is the oxidation of hydrogen by releasing electrons to the conductive electrode and on through the external load:



The protons produced exist as hydronium ions, which move toward the highly proton conductive polymer membrane. Most protons diffuse through the hydrated membrane, while the rest of hydrated protons are transported to the cathode by electroosmotic drag [1]. Water vapor in the gas exhaust streams, especially at the anode side, is neglected due to the low stack operating temperature (*ca.* 30 °C). The inlet flow rate can be directly measured by a mass flow meter/controller, or calculated using the measured exhaust flow rate and compositions of the inlet and the exhaust gases.

For a simple exhaust analysis, the PEM fuel cell system was operated at a constant current ranging from 50 W to 200 W of stack power. After the fuel gas stream flows into the common fuel cell inlet, it is assumed to be uniformly distributed to every flow field plate and anode unit, i.e.,  $X_{01} = X_{j1}$  ( $j = 1-47$ ) for hydrogen fuel and  $X_{02} = X_{j2}$  ( $j = 1-47$ ) for inert gas. The hydrogen fuel is approximately consumed at an equal rate in each cell. At each cell outlet, the gas composition is assumed equal. The exhaust line in the main flow channels is shown in Fig. 4.2. The pressure drop is quite small in both main flow channels. The small amount of gas crossover from each

electrode is neglected in this work. It is further assumed that the gas composition is the same at the auto purge and the manual purge outlets. Also, the auto purge frequency ( $f_p$ ) is assigned a value of  $\infty$ , which means the exhaust gas is purged equally at a small average flow rate. Thus, the total continuous volume is considered the same as that of exhaust gas purged during normal operation ( $0 < f_p < \infty$ ). From a mass balance and the above mentioned assumptions, the following equations can be constructed:

$$x_{a1} = x_{h1} \quad (4.3)$$

$$x_{a2} = x_{h2} \quad (4.4)$$

$$x_{e1} = x_{h1} \quad (4.5)$$

$$x_{e2} = x_{h2} \quad (4.6)$$

$$X_{01} + X_{02} = 1 \quad (4.7)$$

$$x_{h1} + x_{h2} = 1 \quad (4.8)$$

$$v_a + v_h = v_e \quad (4.9)$$

$$u_0 X_{01} - v_e x_{e1} = \frac{mI}{2F} \quad (4.10)$$

$$u_0 X_{02} = v_a x_{a2} + v_h x_{h2} \quad (4.11)$$

Combining Eqs. 4.3-11, the inlet/outlet flow rates and the average flow rate of auto purge are then obtained:

$$u_0 = \frac{x_{h2} \cdot mI}{(X_{01} - x_{h1}) \cdot 2F} \quad (4.12)$$

$$v_e = \frac{1 - X_{01}}{X_{01} - x_{h1}} \cdot \frac{mI}{2F} \quad (4.13)$$

$$v_a = \frac{1 - X_{01}}{X_{01} - x_{h1}} \cdot \frac{mI}{2F} - v_h \quad (4.14)$$

Flow rates shown in the above equations are in mol/sec. The rates are converted to ml/sec by using the ideal gas assumption at 1 atm and 20 °C for convenient description in the text and the table. The average flow rate of auto purge exhaust (Eq. 4.14) is a function of the inlet/outlet gas compositions, number of fuel cells, stack current, and the manual purge flow rate. The flow rate of fuel gas in the fuel cell system can also be determined by measuring the exhaust flow rate and the change in its composition.

#### *IV.3.2. Purge cell and MEA voltage in the stack*

A real fuel cell system is usually assembled in a stack format consisting of a group of fuel cells. In the cells near the fuel exhaust outlet, impurities gradually accumulate needing to be well managed in order to provide enough hydrogen fuel for these particular anodes to perform the electrochemical reaction. Periodical purge or continuous exhaust release is normally required for diluting or refreshing the exhaust build-up although a stack may be claimed as a dead-end structure. The exhaust purge is normally triggered by monitoring the voltage of the purge cell portion when reaching the threshold values [7]. In consideration of the system operation and safety reasons, the Nexa™ power system was chosen for the lab test.

The purge cell voltage was monitored as a function of operation time. Its data value (Fig. 4.3) was sensitively related to the nitrogen gas in the anode fuel line. There is no voltage drop with a pure hydrogen feed at a manual exhaust flow rate of 1.80 ml/sec. The system was then switched to a 7.3% nitrogen fuel feed. The fuel and exhaust gas management on the anode side was conducted by the system controls automatically

purging exhaust if the fuel cells were operated at an unacceptably low cell voltage. After the PEFC system was completely switched to the nitrogen feed, the flow rate of the manual exhaust decreased to 0.86 ml/sec. The auto purge frequency was 15.4 mHz. It was reduced to 12.5 mHz when the exhaust flow rate was increased to 1.90 ml/sec (The flow rate was measured as 3.63 ml/sec for a pure hydrogen feed). As shown in Fig. 4.4, data were also collected at different flow rates of the manual exhaust with a pure hydrogen fuel feed. During normal operation, the purge frequency ( $f_p$ ) was *ca.* 3.7 mHz at a stack power of 200 W. With a proper manual rate increase of 0.038 ml/sec, the minimum purge voltage (i.e. critical flow rate, discussed later in detail) no longer decreased and the auto purge stopped (Fig. 4.4). With the 2nd rate increase of the manual purge to 0.74 ml/sec, the maximum purge voltage was a steady 0.82 V. Even when the manual purge flow rate was later increased to 1.80 ml/sec, the purge voltage remained in the same range of values. Small differences in voltage were caused by a negligible change of temperature. The Nexa™ system, fed by pure hydrogen, was tested at a 200 W stack power level for membrane dry-out resulting in no voltage diminution during a testing period of 48 min at an exhaust flow rate of 5 ml/sec (Fig. 4.5). The measured purge frequency ( $f_p$ ) was *ca.* 16.3 mHz at a stack power of 1200 W.

The fuel cell system (Nexa™ #527) was tested at 7.5% nitrogen content, balanced with pure hydrogen. The stack and control system were successfully operated for start-up and the duration of inert gas intake. The single fuel cell, i.e., MEA voltage (No.13, 33 and 47 from the anode fuel inlet to the exhaust outlet) was measured at a level of 0.70 V at a stack power of 200 W, but the dynamic voltage signals were difficult to collect simultaneously for single fuel cells. A system from National Instruments™ was set up in

order to obtain voltage information for MEAs at different locations of the stack [10]. The voltage across each cell can then be monitored for further diagnosis purpose at different inert gas levels.

Carbon dioxide was more difficult than nitrogen to obtain a good gas mixture in the lab because carbon dioxide (1.964 mg/ml) is 22 times heavier than hydrogen (0.0893 mg/ml) at 1 atm and 0°C (STP). The fuel cell system with an exhaust flow rate of 1.70 ml/sec at 200 W stack power was successfully operated with a *ca.* 7% carbon dioxide feed for 50 min. Both PEFC stack tests with *ca.* 7% nitrogen or carbon dioxide demonstrated that the Nexa™ power module is capable of operation with higher levels of inert gases with an additional exhaust purge line.

#### *IV.3.3. Critical Flow Rate of the Anode Fuel Exhaust*

While the system was running, it was noticed that there exists a critical flow rate between the auto purge and manual purge line. If the manual exhaust flow rate is lower than the critical value, the system continually purges with automatic controls. If higher than the critical value, there is no need for the automated purge. This is potentially beneficial for fuel recycle mode design and for increasing the fuel efficiency. As shown in Fig. 4.6, the critical value can be approximately measured by manually adjusting the back pressure valve. The auto purge subsystem gradually stops when the manual purge flow rate is slowly increased to a certain limit, at which point, the purge cell voltage maintains a stable minimum value with no need for automatic purge.

After fuel cell system startup, the purge cell voltage reduced gradually and the anode fuel exhaust line purged for voltage restoration and performance recovery (Figs. 4.3 and 4.6). After an automatic purge occurred, the purge cell voltage increased a

maximum level. This is probably caused by a temporary inert gas release at catalytic active sites during the quick purge process. The voltage rapidly increased after the auto purge. The purge cell voltage then decreased quickly, followed by a peak of increase, and then moved to the next purge cycle. This may result from the fresh fuel gas which was purged into the anode in due form and replaced the impurities absorbed at the catalytic active sites. At this moment, the manual purge valve was slightly opened and the purge cell voltage gradually increased (Fig. 4.6). The flow rate was maintained at a minimum level and the purge cell voltage was also maintained as a constant. If a slight voltage change occurred, a small adjustment to the back pressure was necessary to keep this parameter constant. This minimum flow rate ( $v_e$ ), or critical flow rate of the anode fuel exhaust stream, was a useful parameter for calculating the auto purge frequency. As a whole, the critical flow rate is determined by measuring the manual purge flow rate ( $v_h$ ) at an auto purge flow rate ( $v_a$ ) close to 0. This minimum value can be written

$$v_{h,\min} = \lim_{v_a \rightarrow 0} = \frac{1 - X_{01}}{X_{01} - x_{h1}} \cdot \frac{mI}{2F} \quad (4.15)$$

Theoretically, the auto purge frequency can be approximately determined by using the above critical flow rate in conjunction with the released volume of gas in each auto purge. The fuel cell stack is safe for operation while its total purge flow rate is no less than this minimum flow rate. In the practical operation of the fuel cell system, the requirement for the overall auto purge flow rate is a little higher than the calculated value because the operational purge frequency ( $f_p$ ) cannot be set to a value of  $\infty$  (With the assumption of  $f_p \rightarrow 0$ , the critical minimum flow rate is obtained). There is also an

increase in the anode overpotential while the impurity builds up between the purge intervals. Once the manual purge reaches its critical value, the inert gas exhaust attains its maximum operational concentration of impurity

$$x_{h2,\max} = (1 - X_{01}) \left( 1 + \frac{mI}{2Fv_{h,\min}} \right) \quad (4.16)$$

at the minimum flow rate. Otherwise, the purge cell voltage, near the fuel exhaust side, decreases to an inoperable condition requiring further purge for MEA overpotential and PEFC lifetime protection.

As described earlier, the Nexa™ system and an additional exhaust line were connected to measure the critical flow rate. At the manual exhaust outlet, the GC gas sample for nitrogen composition was taken after recording data of the exhaust flow rate. The manual purge flow rate was measured during steady stack operation at a specified power level. The fuel consumption rate and total exhaust flow rate in all of the stack flow channels were calculated using Eqs. 4.10 and 4.13.

The auto purge flow rate is a dynamic value; thus, an average flow rate was approximated and substituted into the data. The concentration of inert gas in the exhaust decreased with increasing the manual exhaust flow rate. The manual flow rate was measured while the auto purge was stopped ( $f_p = 0$ ) and the voltage of the purge cell portion was constant. As shown in Table 4.1, the auto purge rates were close to zero, although no auto purge was actually observed during the test process. This type of operation provides a dual use of membranes in the MEAs as both gas purifiers and solid electrolytes. Optimization of the fuel and exhaust gas management potentially increases system energy efficiency. This operation reduces the system size and operational



complexity by eliminating the palladium purifying system between a fuel reformer and a PEFC stack, which normally requires ~250 psi and 300~400 °C to obtain a hydrogen fuel pure enough (>0.01%) for the PEFC system requirements under normal operating procedures.

In further lab tests, a hydrocarbon reformat containing high level of CO<sub>2</sub> and H<sub>2</sub>O was also used in the Nexa™ stack after troublesome CO and H<sub>2</sub>S poisons were removed. Because small amounts of poisonous carbon monoxide were introduced into the fuel cell system, the overall stack voltage dropped gradually (Fig. 4.7). The voltage of the purge cell at the end of the stack measured slightly higher than the average cell voltage in the PEFC stack. This means that a concentration gradient of carbon monoxide existed inside the fuel gas distribution channel. The front fuel cells in the stack were more likely to receive the poisons causing temporary catalyst deactivation. This phenomenon will be further examined in the diagnostic analysis of the fuel cell system with small amounts of poison in fuel gas feeds.

#### *IV.3.4. Fuel Cell Stack Efficiency and Overall System Efficiency*

The fuel cell efficiency is the genuine efficiency of the electrochemical reaction. Thermal (Energy) efficiency of the fuel cells is defined as the amount of useful energy produced relative to the change in stored chemical energy (commonly referred to as thermal energy, *i.e.*, enthalpy change) that is released when a fuel reacts with an oxidant [11]. The ideal energy efficiency of the H<sub>2</sub>/O<sub>2</sub> fuel cell ( $\eta_{fe}^{\circ} = \Delta G^{\circ} / \Delta H^{\circ}$ ) is 83% when the cell is reversibly operated to produce liquid water and heat is not considered. A more general expression for the energy efficiency of the fuel cells (or stack) is summarized

$$\eta_{fc} = \frac{-nF\bar{E}_{fc} + q_w/m}{\Delta H^\circ} = \frac{-nF\bar{E}_{fc} + q_w/m}{-nFE_{fc}^\circ / \eta_{fe}^\circ} \quad (4.17)$$

The fuel cell energy efficiency increases by the co-generation of heat and electricity if the formed heat ( $q_w$ ) from the cooling system is partially recycled for hot water etc. For a common PEM fuel cell where  $q_w$  is not employed for useful work ( $q_w = 0$ ), the single cell energy efficiency is simplified

$$\eta_{fe} = \frac{\eta_{fe}^\circ \cdot E_{fc}}{E_{fc}^\circ} \quad (4.18)$$

The fuel cell (stack) efficiency in actual operation is given

$$\eta_{fc} = \frac{\bar{E}_{fc}}{E_{fc}^\circ} = \frac{E_s}{mE_{fc}^\circ} \quad (4.19)$$

This expression is also called voltage efficiency.

Efficiencies of the PEFC stack and its system are the most significant concerns regarding the whole system performance. When the Nexa™ PEFC system was operated at *ca.* 200 W stack power with 7.5% nitrogen feed ( $v_h = 2.22$  ml/sec, Table 4.1), the fuel cell stack efficiency of 47 total cells was approximately 64% (stack voltage,  $E_s = 35.95$  V; theoretical cell voltage,  $E_{fc}^\circ \approx 1.2$  V). Due to the power consumed by the electronic controls and air compressor, the stack output efficiency for useful work was 75%. While nitrogen in the anode stream was concentrated from 7.5% to 91.6%, the fuel efficiency was still 99% with a manual exhaust flow rate of 2.22 ml/sec and without auto purge. The overall efficiency (the energy efficiency of the whole fuel cell system) is calculated

$$\eta_{oe} = \eta_{fu} \cdot \left( \frac{\eta_{fe}^{\circ} E_{fc}}{E_{fc}^{\circ}} \right) \cdot \eta_{so} \approx 0.394 \quad (4.20)$$

where the fuel gas contained 7.5% nitrogen and the PEFC was operated at its critical flow rate. The handbook [11] pointed out that the operation at higher fuel cell efficiency (> 50%) increases the capital cost but decreases the fuel cost. Further work is continued on the optimization of various efficiencies in order to rigorously understand the benefits of the operational method.

#### IV.4. Conclusions

The PEM stack in the Ballard Nexa™ system was fed with mixtures of hydrogen fuel and high levels of inert gases. After running the stack for a period of time, the purge cell voltage reduced gradually, requiring the anode fuel exhaust line to be purged for voltage restoration and performance recovery. The critical flow rate in the anode exhaust stream was obtained at a specified power level with a mass balance. Using this method of fuel gas and exhaust management, the flow rate of fuel gas in the fuel cell system was determined by measuring the exhaust flow rate and the change in its gas composition. This process provided a dual use of membranes in the MEAs as both gas purifiers and solid electrolytes. This operational method eliminated the need for a high temperature palladium separator and/or gas purifier. It also reduced the auto purge frequency required for stack performance recovery. The Nexa™ PEM fuel cell system successfully utilized hydrogen feeds with *ca.* 7% inert gases. The fuel cell stack was safely operated with its total purge flow rate at no less than this critical flow rate. Nitrogen in the anode stream was concentrated from 7.5% fuel feed up to 91.6% N<sub>2</sub> exhaust; thus, this operational

method still maintained a fuel efficiency of 99%. Further optimization of the fuel gas and exhaust gas management potentially increases the system energy efficiency.

#### **IV.5. Acknowledgements**

This work was performed under a U. S. Army contract at Auburn University (DASG 60-00-C-0070) administered through the U.S. Army Space & Missile Defense Command. I would like to recognize Wenhua H. Zhu who was the co-author for the original article. I'd like to thank Mr. Hongyun Yang for his valuable assistance and many discussions on the GC analysis. The authors also wish to acknowledge the contribution of Mr. Dwight Cahela and Ms. Georgian Allison for this work. This article may be found in full in the *Journal of Power Sources* [12].

#### **IV.6 Nomenclature**

$E$  voltage, V

$f$  frequency, Hz

$F$  Faraday's constant, 96487 A sec/mole

$\Delta G$  Gibbs free energy for electricity generation, kJ/mole

$\Delta H$  thermal energy (enthalpy change) available from the H<sub>2</sub>/O<sub>2</sub> reaction, kJ/mole

$I$  current through fuel cell stack, A

$m$  total number of the working fuel cells in the stack

$n$  number of electrons involved in one water molecule production

$q$  heat produced in the reaction which is contributed to useful work for energy saving, kJ/mole

- $u$  gas flow rate at inlet side, mol/sec in equations ( $*2.404 \times 10^4$  ml/sec at 20°C, 1 atm)
- $v$  gas flow rate at the outlet side, mol/sec in equations ( $*2.404 \times 10^4$  ml/sec at 20°C, 1 atm)
- $X$  fuel inlet volume fraction
- $x$  outlet exhaust volume fraction

***Greek***

- $\eta$  efficiency

***Subscripts***

- 0 fuel gas inlet
- 1 hydrogen fuel gas
- 2 inert gas
- $a$  auto purge outlet
- $e$  main channel exit of the fuel cell anode
- $fc$  fuel cell
- $fe$  fuel cell energy
- $fu$  fuel gas
- $h$  manual exhaust outlet(hand adjustment)
- $j$  number of the fuel cell started from the fuel inlet
- $oe$  overall efficiency of the fuel cell system
- $p$  auto purge
- $s$  fuel cell stack
- $so$  stack output
- $w$  useful work

#### IV.7 References

- [1] S. Gottesfeld and T. A. Zawodzinski, in: R. C. Alkire, H. Gerischer, D. M. Kolb, and C. W. Tobias (Eds.), *Advances in Electrochemical Science and Engineering*, 5, John Wiley & Sons, Inc., New York, NY, 1997, p.197.
- [2] F. C. Chen, R. J. Fiskum, in: International Joint Power Generation Conference, Atlanta, GA, 2003, pp.302-312.
- [3] J.V.C. Vargas, J.C. Ordonez, A. Bejan, *Int. J. Heat and Mass Transfer* 47 (2004) 4177–4193.
- [4] Boehm, G., Wilkinson, D. P., Knights, S., Schamm, R., and Fletcher, N. J., PCT Int. Appl., WO 2001043216 (2001).
- [5] Preidel, W., PCT Int. Appl., WO 2003052851 (2003).
- [6] B. Wells, T. D. Uong, C. J. Schembri, G. A. James, G. A. Skinner, and B. Giesecke, PCT Int. Appl., WO 2003010842 (2003).
- [7] R. H. Barton, T. D. Uong, C. J. Schembri, G. A. Skinner, PCT Int. Appl., WO 2003010845 (2003).
- [8] S. Ahmed, J. Kopasz, R. Kumar, and M. Krumpelt, *J. Power Sources* 112 (2002) 519–530.
- [9] V. Marshall, J. Kelland, P. Grosjean, and D. Bloomfield, in: *Proceedings of the 36<sup>th</sup> Power Sources Conference*, Cherry Hill, New Jersey, 1994, pp.83–86.
- [10] R.U. Payne, W.H. Zhu, and B. J. Tatarchuk, in: *Proceedings of the AIChE Annual Meeting: Fuel Cell Technology II*, Austin, Texas, 2004, 14h.
- [11] EG&G Technical Services, Inc. and Science Applications International Corp., *Fuel Cell Handbook*, 6th Edition, Chapter 2, U.S. Department of Energy, West Virginia, 2002, p.7 (Chapter 2).
- [12] W. H. Zhu, R. U. Payne, D. R. Cahela, and B. J. Tatarchuk, *J. Power Sources* 156 (2006) 512–519.

**Table 4.1.** Fuel gas and its exhaust gas compositions as well as different flow rates in the anode side of the system (Room temperature 20°C, fuel to system 20 psig).

| Stack power<br>$P_s$<br>(W) | Stack current<br>$I_s$<br>(A) | H <sub>2</sub> at inlet<br>$X_{01}$<br>(%) | N <sub>2</sub> at inlet<br>$X_{02}$<br>(%) | H <sub>2</sub> at outlet<br>$x_{h1}(x_{e1})$<br>(%) | N <sub>2</sub> at outlet<br>$x_{h2}(x_{e2})$<br>(%) | Bubble flow<br>$v_h^a$<br>(ml/sec) | H <sub>2</sub> used in the cells <sup>b</sup><br>$mI/(2F)$<br>(ml/sec) | Inlet flow<br>$u_0$<br>(ml/sec) | Outlet flow<br>$v_e$<br>(ml/sec) | Auto flow<br>$v_a$<br>(ml/sec) |
|-----------------------------|-------------------------------|--|--|---|---|------------------------------------|--|---------------------------------|----------------------------------|--------------------------------|
| 50                          | 1.22                          | 93.90                                      | 6.10                                       | 21.60   | 78.40   | 0.51                               | 7.143  | 7.75                            | 0.603                            | 0.090                          |
| 50                          | 1.34                          | 93.00                                      | 7.00                                       | 3.96  | 96.04   | 0.51                               | 7.85   | 8.47                            | 0.617                            | 0.109                          |
| 100                         | 2.58                          | 94.25                                      | 5.75                                       | 2.69  | 97.31   | 0.97                               | 15.11  | 16.06                           | 0.949                            | -0.02                          |
| 100                         | 2.58                          | 92.50                                      | 7.50                                       | 7.70  | 92.30   | 1.16                               | 15.11  | 16.45                           | 1.336                            | 0.176                          |
| 150                         | 4.40                          | 94.25                                      | 5.75                                       | 31.80   | 62.80   | 1.65                               | 23.65  | 25.83                           | 2.178                            | 0.53                           |
| 200                         | 5.64                          | 92.50                                      | 7.50                                       | 8.41  | 91.59   | 2.22                               | 33.02  | 35.96                           | 2.95                             | 0.725                          |
| 200                         | 5.47                          | 97.60                                      | 2.40                                       | 14.60   | 85.40   | 0.80                               | 32.03  | 32.96                           | 0.926                            | 0.126                          |
| 200                         | 5.47                          | 93.90                                      | 6.10                                       | 10.20   | 89.80   | 1.85                               | 32.03  | 34.36                           | 2.334                            | 0.484                          |

<sup>a</sup> The critical flow rate was approximately measured from the manual gas exhaust stream.

<sup>b</sup> The consumption flow rate of hydrogen fuel was converted to ml/sec as it was assumed the stream in the stack was at 20°C & 1 atm.

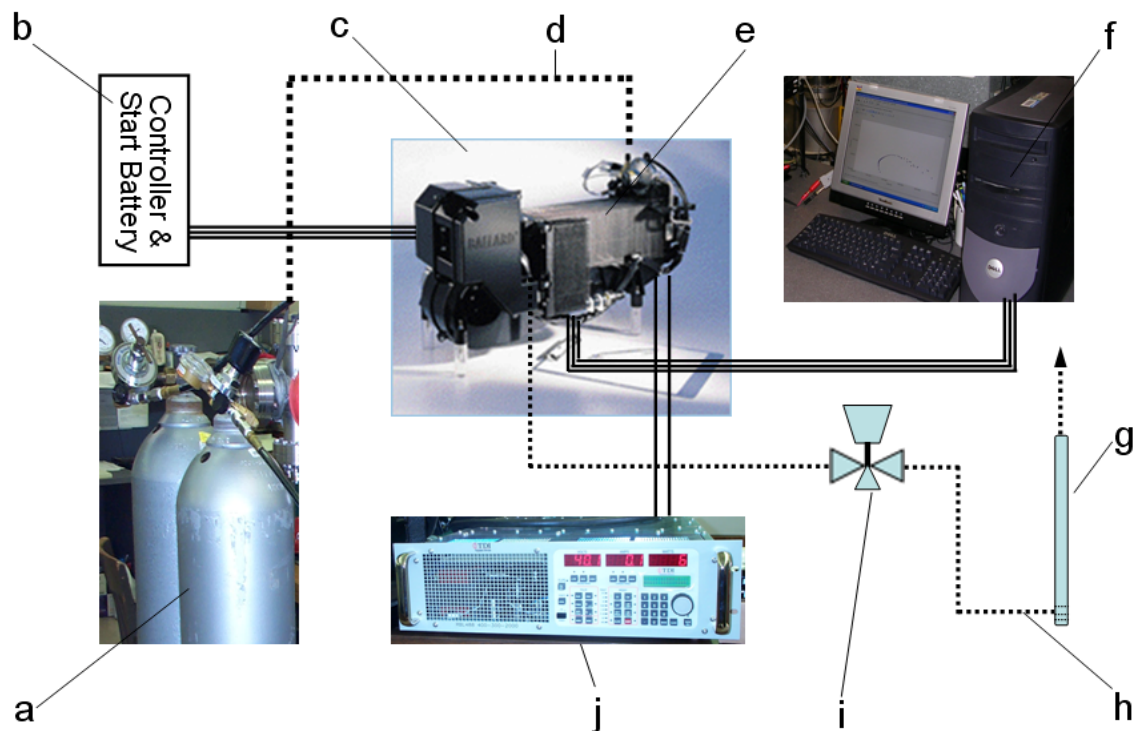


**Figure 4.1.** Schematic drawing of a Nexa™ PEFC stack added with a manual purge line. a) Fuel gas cylinders, b) Central controller unit and start battery, c) Nexa™ power system, d) Fuel gas line, e) Ballard® stack, f) Computer data collection, g) Bubble meter, h) Gas exhaust line, i) Back pressure valve, and j) Electronic load.



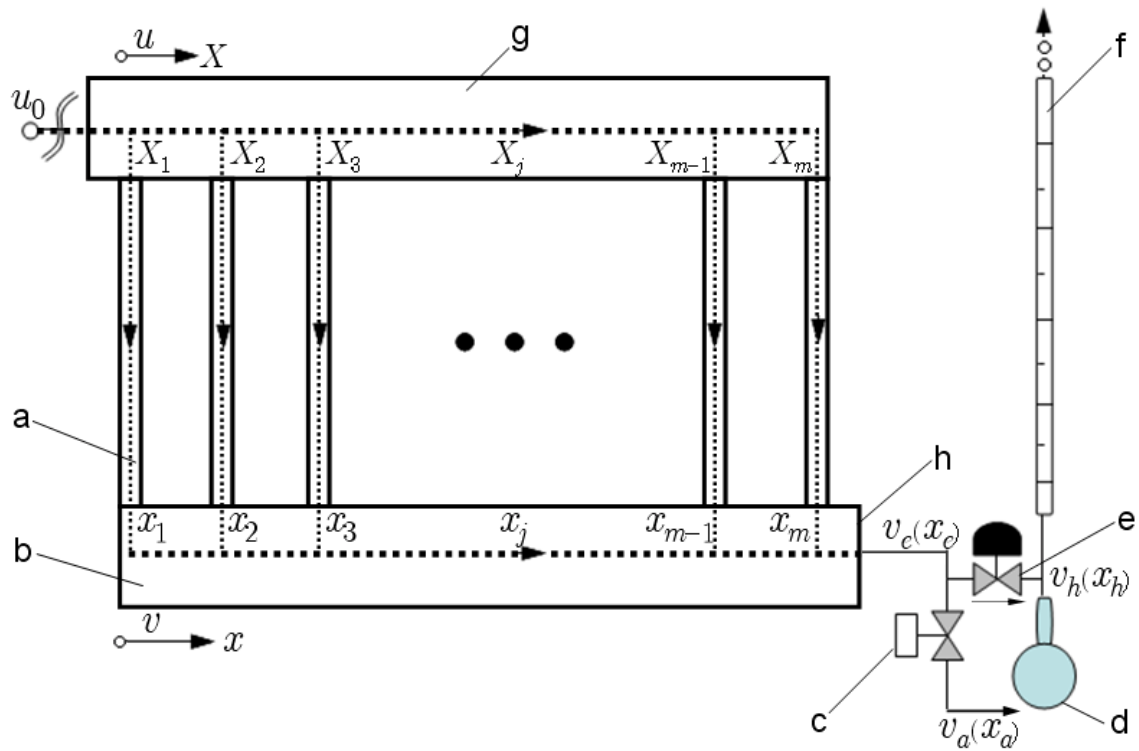


**Figure 4.2.** Simple flow diagram of anode fuel and exhaust stream in a PEFC stack. a) Fuel cell anode and fuel flow, b) Main exhaust flow channel, c) Auto purge valve (Average flow rate expressed as  $v_a$ ), d) Bubble generator, e) Back pressure valve, f) Bubble meter (Flow rate expressed as  $v_h$ ), g) Main fuel gas channel (feed for each cell assumed in parallel), h) Exhaust outlet (Flow rate expressed as  $v_e$ ).

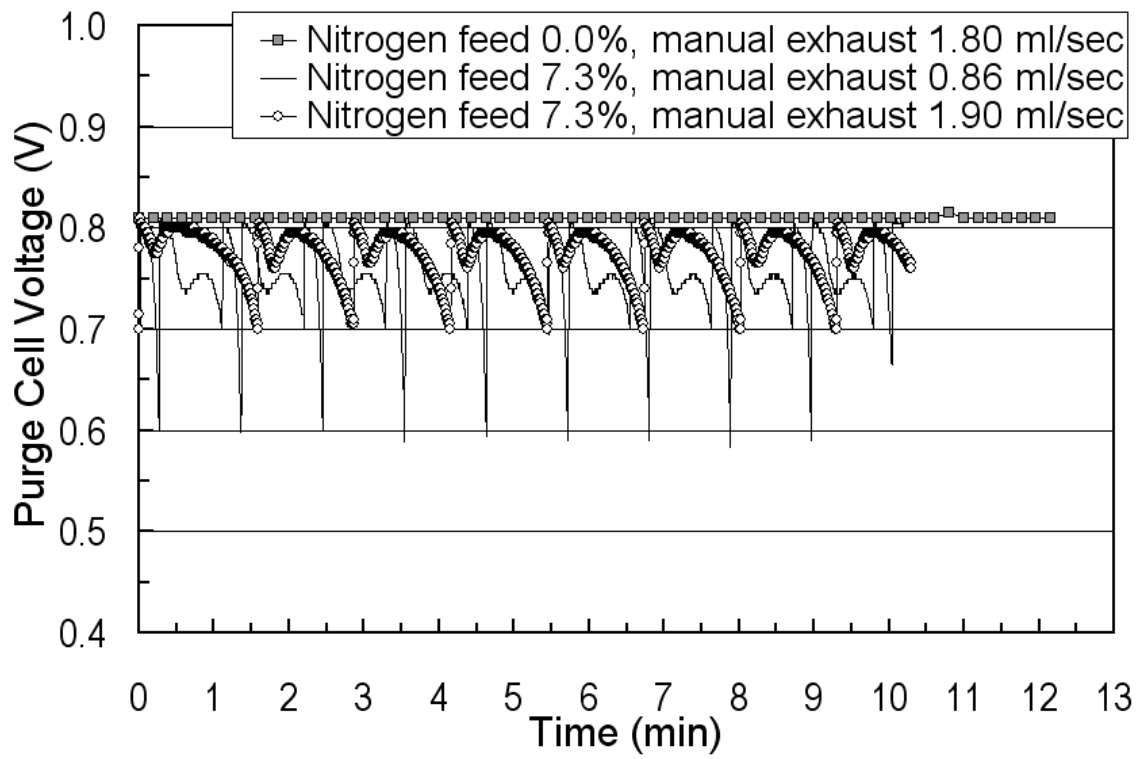


**Figure 4.3.** Purge cell voltage as a function of operation time with *ca.* 7.3% nitrogen fuel feed in comparison with pure hydrogen operation. Exhaust flow rate in-situ measured by the same fuel feed; Stack temperature, 31°C.

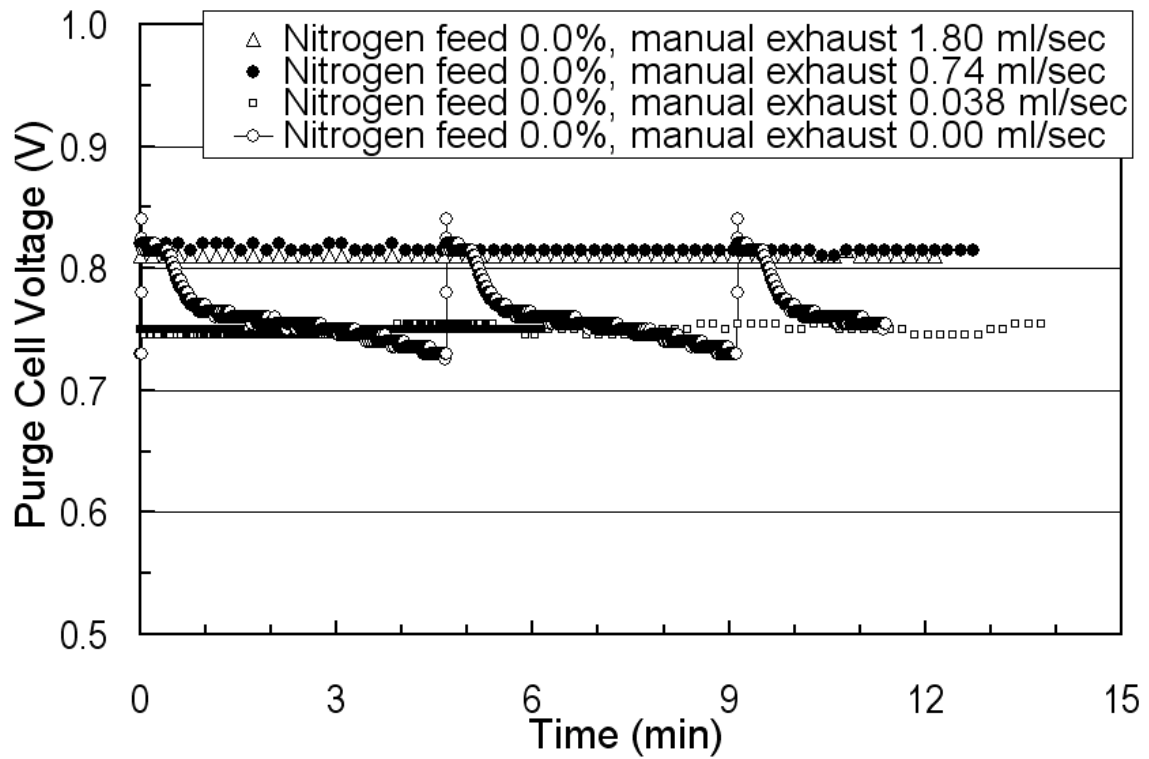


**Figure 4.4.** Purge cell voltage as a function of operation time without inert gas feed. Exhaust flow rate measured by pure hydrogen (>99.99%) feed; Stack temperature, 31°C.

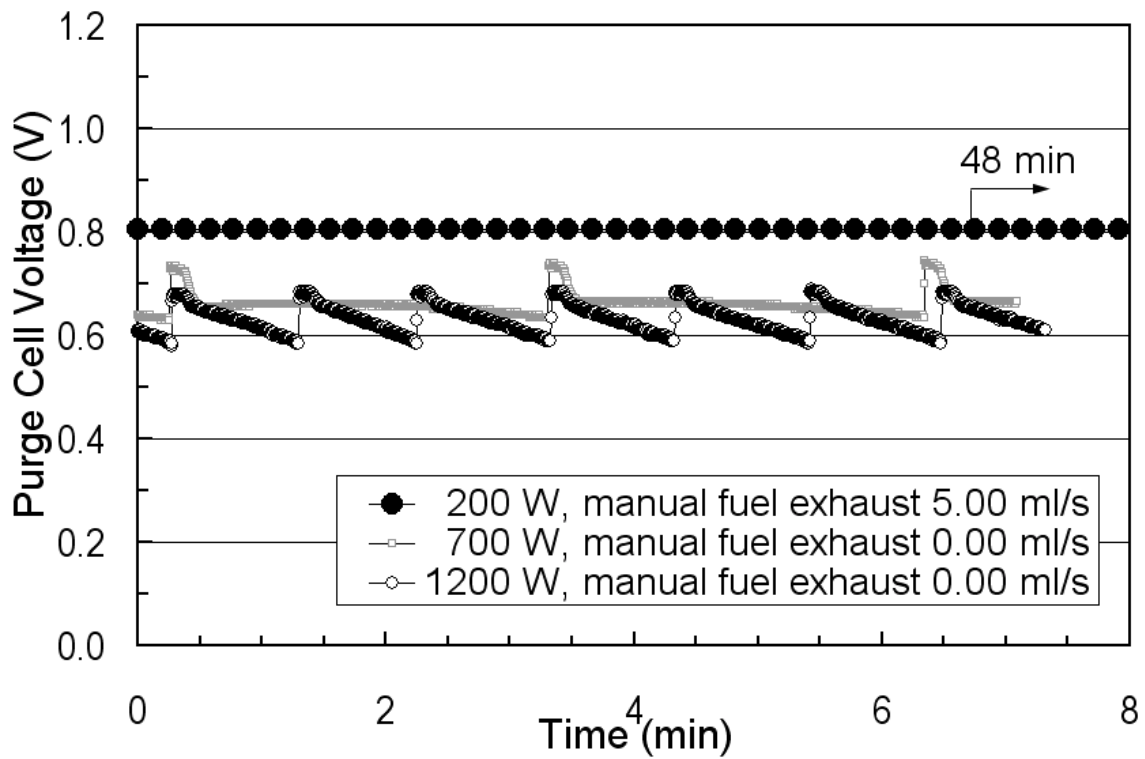


**Figure 4.5.** Membrane dry-out and purge frequency tests using pure hydrogen fuel at different stack power levels. Exhaust flow rate measured by pure hydrogen (>99.99%) fuel feed. Stack operated at 200 W (48 min tested), ~32°C; 700 W, ~50°C; 1200 W ~65°C.

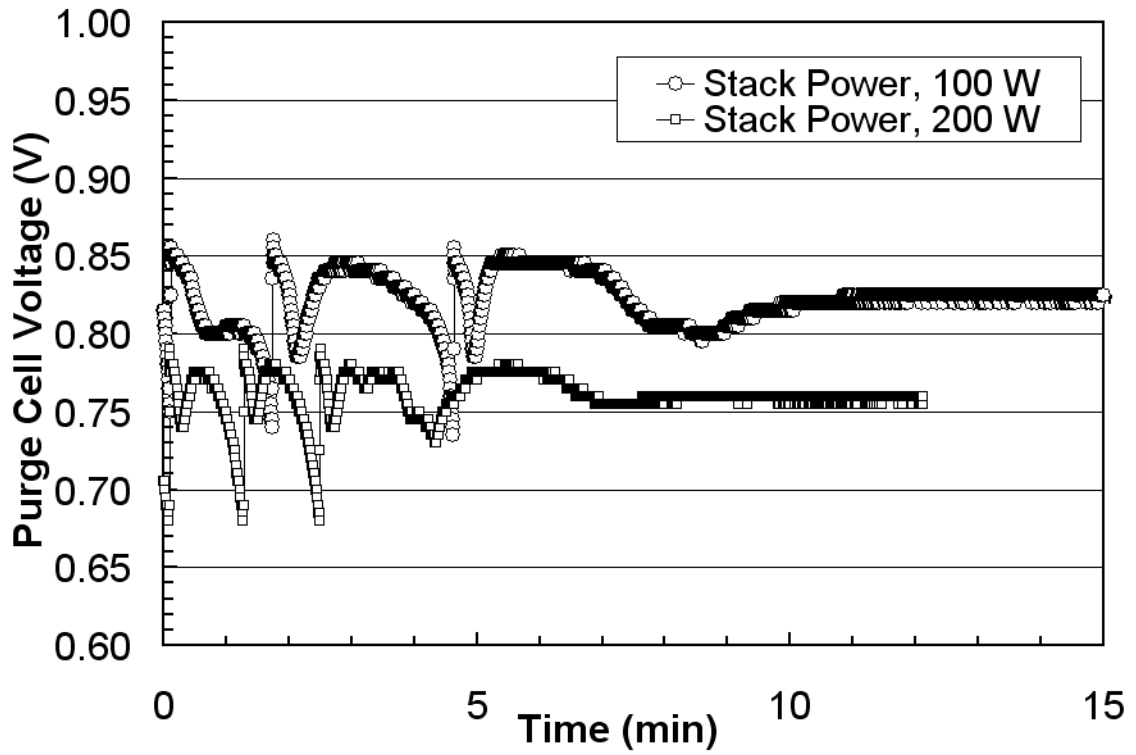


**Figure 4.6.** Purge cell voltage as a function of operation time at two different stack power levels. Manual exhaust purge started after two purge cycles; Stack temperature, 28~30°C.

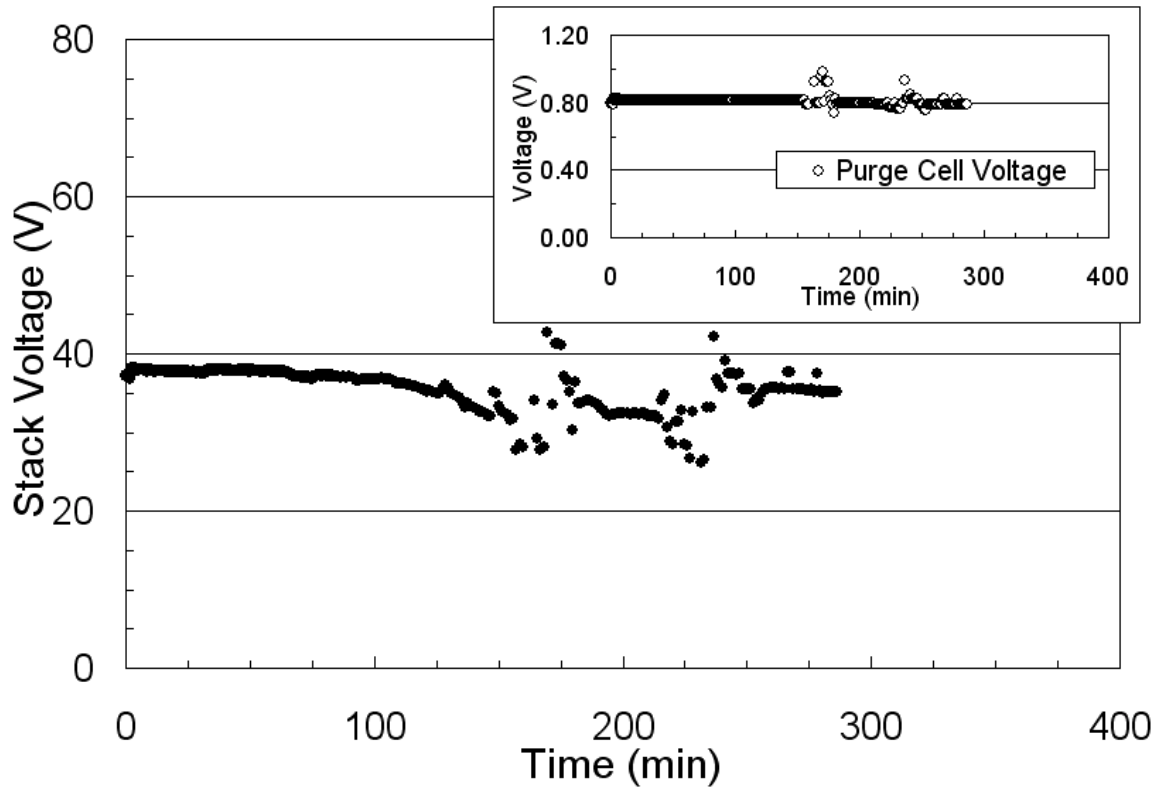


**Figure 4.7.** Stack and purge cell voltage as a function of operation time when using a hydrocarbon reformat containing high levels of CO<sub>2</sub> and H<sub>2</sub>O (hydrogen ~98%, CO < 100 ppm, CO<sub>2</sub> < 100 ppm, CH<sub>4</sub> ~2%, stack temperature 30°C).

## **Chapter V**

### **PEM Stack Test and Analysis in a Power System at Operational Load via AC**

#### **Impedance**

##### **V.1. Introduction**

During the past twenty years, fuel cell related engineering sciences and technologies have attracted more attention due to the need for an efficient, non-polluting power source for global transportation (cars, buses, ships, and submarines), for portable devices (mobile communication, lap-top, and vacuum tools), and for residential backup (combined power and heat generation with top-level energy efficiency) [1, 2]. Properly designed fuel cell systems can be a reliable and durable method to produce environmentally friendly energy for many applications. The polymer-electrolyte fuel cell (PEFC) is considered by many to be the most promising type of fuel cell for transportation and mobile power sources because of its low-temperature operation and ease of construction [3]. Significant progress is being made towards commercialization of producing PEFC power systems that attain the optimum balance of cost, efficiency, reliability, and durability. Characterization of a single fuel cell, a group of fuel cells, or fuel cell stacks in operation mainly refers to the electrochemical in-situ techniques [4]. Electrochemical impedance spectroscopy (EIS or AC impedance) is the most powerful tool for the determination of the Ohmic, activation, and concentration losses. Diard et

al. [5] conducted impedance measurement (load  $R = 1 \Omega$ ) of a four-cell HPower stack using pure  $H_2$  and  $O_2$  and estimated that the resistance of the polymer membrane was *ca.* 40% of the internal resistance. Hakenjos and his coworkers [6] tested their self-developed four-cell short stack using a multichannel frequency response analyzer allowing simultaneous impedance measurement of single cells (shunt resistor  $100 \text{ m}\Omega$ ). Yuan et al. [7] performed impedance measurement of a 500 W six-cell PEM stack using hydrogen and air. Excellent impedance arcs including air mass transport and anode activation loss demonstrated the effects of air shortage at  $30^\circ\text{C}$  and  $50^\circ\text{C}$ . Canut et al. [8] investigated Hydrogenics PEM stacks with 4–22 MEAs under membrane drying, fuel cell flooding, and anode catalyst poisoning conditions. For the above research and impedance work, the operating stoichiometry was maintained at 1.2–2.5, and relative humidity was controlled at 50–100%.

The drawbacks of the impedance technique are as follows: the process is complicated, the equipment is expensive, data interpretation is difficult, and high-power application is more sophisticated. The valuable information from impedance data can be simulated by non-linear least square fitting and interpreted using equivalent circuit elements, which is called equivalent circuit modeling. The present work mostly focuses on collecting AC impedance data from a fuel cell power system directly at operational loads. Impedance data samples and theoretical analysis are conducted in order to understand the phenomenon responsible for these test results. This paper makes use of the AC impedance technique to characterize a single fuel cell, a fuel cell group, or a whole stack in a fuel cell power system.



## V.2. Experimental Details

The PEM stack in the Ballard Nexa™ fuel cell system was employed in the lab test. The power module is a small, low maintenance, fully automated and highly integrated fuel cell system providing 1200 W of unregulated DC power. Its output current can reach 44 A, and stack voltage for 47 total fuel cells normally rises up to 41 V open-circuit. Due to the inexistence of manufacturing data, the fuel cell working area is estimated as *ca.* 122 cm<sup>2</sup>.

The automated operation is maintained by an embedded controller board. The controller uses the stack power to adjust the parameters for optimization of energy efficiency. For the stack test in the power system, the power source for the embedded controller board can be simultaneously switched from the fuel cell stack to a similar external power source after the system reached a steady temperature. The constant voltage level for the external power source is determined easily by measuring the stack voltage delivered to the controller after the stack reaches its steady state. The PEM stack, separated from the control subsystem, was tested for collecting the AC impedance data at different current levels. The supply pressures to the stack were 5.0 psig for the fuel and 2.2 psig for air oxidant. The stack was air cooled and had no outside fuel and oxidant humidification. The Gamry FC350™ fuel cell monitor [9] with a proper electronic load is available to work at a higher current range for measuring the ac impedance data. The Gamry AC impedance system can be normally operated up to 50 V and 300 A within a frequency range from 10 μHz to 20 kHz. The contact and wire resistance between the power output wires and the testing fuel cells was approximately measured as  $R_{wc} = 0.0218 \Omega$  using *i*-V techniques. The sinusoidal current signal from the FC350™, working in galvanostatic or

hybrid impedance mode, modulated the current from single or multiple fuel cell(s) or the PEFC stack. Simultaneously, the current information at the electric load was sent to the FC350™ monitor, and the fuel cell voltage was measured by the FC350™ directly. The FC350™ collected these data and generated the impedance data for further analysis.

The Gamry framework software allows measurements to be performed in a galvanostatic manner and a hybrid mode. Traditional measurements are performed using constant RMS amplitude for the AC signal. The problem with this technique is that the impedance of the cell varies significantly from high to low frequencies. For impedance to be accurate, the perturbation signal has to be sufficiently small to maintain a pseudo-linear  $i$ - $V$  operation. Hybrid measurements compensate for the change in cell impedance as frequency is varied by changing the AC current amplitude to keep measured AC voltage at a set of value. The previously measured impedance point is used in determining the new current amplitude, as the scan proceeds from 10 kHz to 10 mHz. In this work, the galvanostatic and hybrid EIS mode were applied for the experiments in order to observe the EIS behavior at various frequencies. For the entire stack in the system, it was tested with and without the embedded controller. For the impedance spectrum, the non-linear least squares fitting algorithm was applied to find the model parameters for best agreement between the model impedance spectra and the measured spectra. Future publications will present the equivalent circuit model and conduct simulation conducted in PSpice.

### V.3. Results and Discussion

Impedance denotes an opposition to the flow of electrons or current. It can be expressed as a complex number including the real component ( $Z_{re}$ , resistance) and the imaginary component ( $Z_{im}$ , capacitance and inductance). The measured impedance data ( $f$ -frequency,  $Z_{re}$ , and  $Z_{im}$ ) are then forwarded to data analysis, result simulation, and physical interpretation. Because the Nyquist plot is one of the popular formats for evaluating electrochemical impedance data, a schematic drawing of Nyquist plot is given as Fig. 5.1 according to both the published work [4, 10] and the experimental results. This schematic description allows better understanding of the in situ impedance data on the Nyquist plots.

#### V.3.1. Small Signal Applied to the EIS Test

Gamry indicates that a small AC signal (1–10 mV) is generally applied to a cell in a normal EIS test [11]. EIS techniques normally use very small excitation amplitudes, often in the ranges of 5–10 mV peak-to-peak [12]. The small excitation signal causes only minimal perturbation of the electrochemical test system, which ensures a pseudo-linear  $iR$  relationship. There is no large nonlinear response to the DC potential in the cell test, because the current is measured only at the excitation frequency. This small signal reduces errors caused by measuring over a nonlinear portion of the  $iR$  curve. For each test, the fuel cell system was started at a constant power or current level until it reached a steady temperature. Using the hybrid EIS mode, different small AC voltages from 5 mV to 300 mV were entered into the window interface as “AC Voltage”. Results reveal that the AC potential of 5 mV is so small that the points of the impedance data are scattered especially at the low frequency region. This means that 5 mV excitation signal is not

strong enough to cause the useful perturbation in the electrochemical system. The rest of the data points for the AC potential signals from 20 mV to 300 mV are approximately located on the same Nyquist curve. The impedance test was also conducted using AC current as the control variable from 20 mA to 500 mA. This is called Galvanostatic EIS mode, in which a constant AC current is applied and the resulting AC potential is measured. The Nyquist data from 20 mA AC excitation is random, while data from 60 mA to 500 mA AC signals are well matched.

The Galvanostatic EIS is the most common EIS technique for fuel cell studies, but it must be used carefully [9]. In consideration of single cell or cell groups at low temperature with higher impedance (activation losses), the hybrid EIS mode is applied to set an initial current, then the AC current is adjusted continually throughout the measurement to control the AC voltage. In this manner, the amplitude of the ac current is regulated so that the ac voltage does not extend beyond the linear range.

### *V.3.2. Ohmic Resistance in the Nyquist Plots*

The resistance  $R_{\Omega}$  (as shown in Fig. 5.1) represents the total Ohmic resistance of the fuel cell(s). It can be expressed as a sum of the contributions from the uncompensated wire/contact resistance  $R_{wc}$  and Ohmic resistances of each cell component,  $R_s$ . Resistance of a single cell component consists of the Ohmic resistance of the membrane  $R_m$ , anode  $R_a$ , cathode  $R_c$ , bipolar plates  $R_{bp}$ , and the contacts between the electrode/membrane and electrode/bipolar plate. The resistance for proton transport (ionic resistance) exists in the membrane electrolyte and also in the catalyst layer containing small amounts of Nafion additive. The resistance for electron conduction in solid materials is called electric resistance.

It is quite difficult to determine the exact contribution of the different components. For fuel cell stacks,  $R_m$  is the main contributor because the electric resistance of bipolar plates and contact layers/slots can be minimized through using highly conductive materials. The membrane resistance is inversely proportional to the surface area of the fuel cell working area. Many works focus on improving the proton conductivity of the membrane [1]; however, for impedance tests on a single cell or a three-cell group of the stack, the total Ohmic resistance is changed with the humidity condition of the membrane at room temperature (Fig. 5.2). Because the contact area is the same during tests, it is assumed that the contact resistance is the same for each test. The membrane resistance correlates to the condition of the humidity exchanger. For the whole stack, the total Ohmic resistance [10] is a function of the cell number ( $n$ )

$$R_{\Omega} = R_{wc} + nR_s \quad (5.1)$$

Using this equation, it is possible to approximately predict the Ohmic resistance of each cell component.

### *V.3.3. Single Cell Tests and Impedance Data Interpretation*

The fuel cells in the stack (#308) were tested separately at currents of 0.2, 0.5 and 1.0 A DC. After the stack was started, the embedded controller was separated from the system by applying a similar current using an external power supply. The Ohmic resistance is located on the  $Z_{re}$ -axis at the high frequency side of the impedance spectrum (Fig. 5.2). The fuel cells in the stack are fed counter-currently with oxygen and hydrogen. They are numbered from the hydrogen inlet side to the hydrogen exhaust side. Cells #10, #15, and #25 are located near the hydrogen inlet side, far away from the humidity exchanger at the cathode inlet. The main difference among five individual fuel

cells is the impedance behavior of the 47th cell in the stack. The 47th cell is located nearest to the humidified air inlet after the humidity exchanger and has the lowest Ohmic resistance ( $R_{\Omega} = 0.12 \Omega$ ). The mass transport losses are observed at the 47th cell due to impurity build-up. As shown in Fig. 5.2, there is no obvious difference in Ohmic (membrane) resistance if the test current changes for the same cell. Cells #10, #15, and #25 at the front side of the stack have a slightly higher resistance ( $R_{\Omega} = 0.32\text{--}0.48 \Omega$ ) at a current from 0.2 to 1.0 A because of the less humid environment. For the single-separated fuel cell test in a stack, a small humidity gradient accounts for the disparity in Ohmic resistance between cells nearby and far from the humidity exchanger.

#### *V.3.4. Group Cell Tests and Impedance Data Interpretation*

The results for the fuel cell groups of 12, 24, 36, and 47 cells are shown in Fig. 5.3. The activation loss (i.e. the polarization resistance) is exceedingly higher, because temperature of 26 °C is relatively low for the operation of PEM fuel cells. The polarization resistance ( $R_p$ ) is the sum of the anode activation losses ( $R_a$ ) and the cathode activation losses ( $R_c$ ). It increases with the number of fuel cells in the group, and approximately equals the sum of each cell's polarization resistance ( $R_{p,i}$ ).

$$R_p = \sum_{i=1}^n R_{p,i} \approx nR_{p,1} \quad (5.2)$$

Four different cell groups tested at 0.2 A load current and 26 °C. The cells were grouped in multiples of 12 up to the maximum number of cells (47). The effect of the cell numbers on the total Ohmic resistance can be neglected because most of impedances are contributed by the electrode polarization at a temperature of 26 °C. The polarization loop data can be extrapolated to the  $Z_{re}$ -axis in order to estimate the polarization resistance.

The 12-group cell resistance ( $R_p = 2.1 \Omega$ ) is almost doubled ( $R_p = 4.3 \Omega$ ) if it is extended to a 24-group cell, and tripled ( $R_p = 6.3 \Omega$ ) if it is extended to a 36-group cell. The resistance of the last 47-group cell (stack) is  $8.9 \Omega$ . From the Nyquist plot and data analysis, it is clear that the polarization resistance for the electrode activation losses is dominant in the fuel cell reactions for low-temperature PEFC operation.

The stack was then loaded with 5 A current maintaining a temperature of  $29^\circ\text{C}$  (Fig. 5.4). Because mass transport limitations occur at the low frequency side, impedance data are scattered on the Nyquist plot in said region. If the data points at the end loop of activation loss are extrapolated to the  $Z_{re}$ -axis, the polarization resistance approximately follows the relationship of Eq. 5.2. After the peaks of the imaginary impedance component, especially at the low frequency side, the loop data digress away from the normal loop curves. This is because mass transport limitations are occurring inside the fuel cells. At a 5 A load current, the mass transfer losses change the normal loop shape and size. The effects of mass transport become visible on the loop curves, especially the mass transport is observed for the total 47 fuel cells. This is identical with the anode purge cell pair located near to the 47th cell. In comparison to the AC current perturbation work [7], the Nyquist data points collected by the hybrid mode (AC voltage excitation) appear to be a hydrogen mass transport limitation occurring in the purge-cell pair.

### *V.3.5. Stack Test and Impedance Data Interpretation*

The stack #308 was tested with its embedded controller using 500 mA AC perturbation signal. This perturbation signal has a better Nyquist plot, as shown in Fig. 5.5. Because of the embedded control operation, the Nyquist plot has some

fluctuation or noise. The difference between this plot using 500 mA AC signal and the previous Nyquist plot appears at the low frequency end. The changes are mostly caused by mass transport loss at the air cathode side. The steady temperature for the stack is *ca.* 32 °C at an output current of 5 A. There are four types of losses on the single Nyquist curve as shown in Fig. 5.1. Ciureanu et al. [10] performed related work on the impedance spectrum and presented several interesting Nyquist plots about the air cathode. From the above mentioned tests and analysis for the frequency loop, it is concluded that the cathode activation losses and cathode mass transfer losses exist at the low frequency side of the Nyquist plot, and the loop size related to mass transport increases with the load current in the stack.

The bigger loop, at a current of 5.0 A, is the loss due to anode and cathode activation. At the same time for the fuel cell stack, the small loop at the low frequency side is mostly related to the mass transfer losses occurring at the cathode side. The loop shape is different from the hypothetical fuel cell in the literature [4], which uses an equivalent circuit model simulating mass transport loss through an infinite Warburg element at the cathode. The small loop on the low frequency side for the whole stack is similar to the Nyquist plot of the air cathode at a certain air flow rate. The difference in the loop portion associated with mass transport loss can be attributed to the different design of the fuel cell systems. Mass transport at the anodes or the cathodes may be alternatively dominant at different operating conditions due to the design of various controls or a change in operating parameters such as stoichiometry values and purge frequencies. By increasing the power output level, the activation loop is reduced and the mass transfer loss is increased. At a stack current of 46 A, the controller and mass



transport limitations scatter the Nyquist data points. The exhaust of the air cathode, including  $N_2$ , product of water, and other impurities, needs to be removed in order to allow the oxygen reactant to diffuse into the absorption/ reaction sites. At a 1339 W high-power level (stack current equals to 46 A), the mass transport losses increase for cathode processes at the low frequency (right) side of the loop, as shown in the Nyquist plot (Fig. 5.5). It is concluded that the controller adjustment causes the data point fluctuations in comparison with the Nyquist diagram without embedded controls (Fig. 5.6). On the other hand, as stack temperature increases, the activation loss is largely reduced.

A recent publication [13] shows us that the reason for the departure from an ideal impedance plot (Fig. 5.1) is not only due to the different operating conditions experienced by the cells but also because these conditions also vary along the cell length (inlet to outlet direction). However, it is well known that the double layer capacitance is correlated to the impedance arc and is proportional to the surface area of the electro-catalysts. If the anode is loaded enough electro-catalysts with high surface area, the impedance arc theoretically exists for anode activation loss. Since there is more limitation of the reaction at the air cathode, the catalyst/carbon loading at the cathode is doubled in order to reduce the limitation and match with the anode feature [14]. The reduced catalyst/carbon loading is reasonable to be one of the reasons for the impedance arc departure from an ideal impedance plot, because the reduced anode impedance arc is hidden in the larger cathode impedance loop.

The authors noticed that Yuan et al. [7] tested a 500 W six-cell PEM stack using hydrogen and air. The MEA in this stack consists of Nafion 115 membrane with a total

Pt catalyst loading of  $1.0 \text{ mg cm}^{-2}$ . This work with higher loading of electro-catalyst shows excellent impedance arcs including anode activation loss, cathode activation loss, and air mass transport loss during air shortage operation at  $30 \text{ }^\circ\text{C}$  and  $50 \text{ }^\circ\text{C}$ . The impedance arc departure from an ideal impedance plot usually occurs for a whole fuel cell or stack due to optimization of the electrode structure and performance.

After the embedded controller was disabled, its power was switched simultaneously to the external power supply, and then the AC impedance data were collected for the whole stack at different current levels. The Nyquist plots are shown in Fig. 5.6 (a and b). These Nyquist plots, after moving the noise of the embedded system controller away from the fuel cell system, describe the real reactions and processes happening in the fuel cell stack. Mass transport losses at the low frequency side are clearly shown on these six plots. The ohmic resistance from the Nyquist plot is  $R_\Omega = 0.067 \text{ } \Omega$ . The resistance for each cell component  $R_s$  is calculated as  $R_s = 117 \text{ m}\Omega \text{ cm}^2$  using Eq. 5.1. At a current of no more than  $350 \text{ mA cm}^{-2}$ , the saturated membrane resistances are simulated as  $40\text{--}125 \text{ m}\Omega \text{ cm}^2$  for  $50\text{--}175 \text{ }\mu\text{m}$  membrane [15]. The membrane thickness for the fuel cell stack is reasonably located in the range from  $50 \text{ }\mu\text{m}$  to  $164 \text{ }\mu\text{m}$  (Table 5.1). Based on the published  $i\text{--}V$  diagram [16], it is reasonable to assume that the membrane resistance equals to half of the resistance of each cell component, so the membrane resistance is obtained as  $59 \text{ m}\Omega \text{ cm}^2$ . Through linear interpolation as shown in Table 5.1, the membrane thickness is further estimated as *ca.*  $82 \text{ }\mu\text{m}$ , which is very close to the thickness of the Nafion<sup>®</sup> 1135 (3.5 mil,  $89 \text{ }\mu\text{m}$ ). However, the membrane thickness was measured as  $114 \text{ }\mu\text{m}$  (4.5 mil) on the small edges

around the stack. If the MEA in the stack uses 114  $\mu\text{m}$  thick membrane, it is not acceptable that the membrane resistance approximately equals to 70% resistance of a single cell component. The reason is that the membrane may be treated on the edges and become thicker for the edge sealing purpose. In considering that the minimum end-of-life (EOL) time is designed as 1500 h, the membrane thickness is estimated in the range between 51  $\mu\text{m}$  and 89  $\mu\text{m}$ . Diard et al. [5] utilized the constant membrane thickness (estimated as Nafion<sup>®</sup> 1135) and membrane conductivity ( $\sigma = 0.083 \text{ S cm}^{-1}$ ) to calculate the polymer membrane resistance as  $\sim 40\%$  of the internal resistance. This is a good theoretical value, but it neglects the thickness change during membrane compression and MEA formation. In consideration of membrane compression during hot press, the ratio of the membrane resistance to the total internal resistance is reasonably less than 40%, so the membrane resistance is close to Nafion<sup>®</sup> 112 (Table 5.1). Its theoretical membrane resistance is 61  $\text{m}\Omega \text{ cm}^2$  at a thickness of 51  $\mu\text{m}$ . The actual thickness in the MEA structure is estimated as *ca.* 34  $\mu\text{m}$  based on the 33% compression ratio (i.e. the ratio of simulated membrane resistance to its theoretical membrane resistance).

In comparison with the schematic drawing (Fig. 5.1), mass transport at the cathode affects the reactions at a current of 2.5 A and greater (Fig. 5.6b). The loop portion for mass transport limitation increases with the output current levels. At the 35 A output current, the loop portion of mass transport is almost equivalent to half of the whole Nyquist plot. It reveals that the cathode activation losses are quickly reduced as temperature increases, but limitations of mass transport inside the micropores and at the active sites increase with the power output level due to mass transfer requirement for further reactions. Removal of the gas-phase exhaust (mostly nitrogen diffusion) and

transport of water product (through heat transfer and pressure driving-force) are necessary for allowing fresh reactants to diffuse into the electrode reaction zone and continuously generate the electric power.

#### **V.4. Conclusion**

The EIS technique is an important tool to characterize a fuel cell stack or its system. For an individual fuel cell tested separately in a power system with a humidity exchanger, its Ohmic resistance ( $R_{\Omega}$ ) changes slightly with the cell location due to the humidity limitation. The Ohmic resistance for each cell component in the stack is approximately obtained as  $117 \text{ m}\Omega \text{ cm}^2$  at current from 2.5 A to 35 A. When the stack is electrically isolated from the embedded controller, the Nyquist plots are less noisy; hence, the reactions and processes are better described. The mass transport loss at the anode is observed from single cell and group cell tests and the loss is caused by the impurity build-up at the purge-cell pair. The pure stack Nyquist plot shows that mass transport losses at the cathode side approximately equal the activation losses at a 35 A stack output current (*ca.*  $287 \text{ mA cm}^{-2}$ ). The mass transport loss is observed from the stack impedance test and the loss is contributed by cathode air shortage. The mass transport losses are increased with increasing stack power output, while the activation losses are greatly reduced with increasing stack temperature. The membrane thickness is estimated in the range between  $51 \text{ }\mu\text{m}$  and  $89 \text{ }\mu\text{m}$ , its actual membrane resistance approximately equals to 35~54% of its total internal resistance. These AC impedance data can be further utilized to develop the equivalent circuit model for simulating the in situ stack behavior using the PSpice tool. The AC impedance method is simple and trouble-free for

implementing real time diagnostic capability suitable for evaluating the stack performance and the state-of-health of the fuel cells in the PEM stack.

## V.5. Acknowledgements

I would like to recognize Wenhua H. Zhu who was the co-author for the original article. This article may be found in full in the *Journal of Power Sources* [17].

## V.6. References

- [1] S. Gottesfeld, T. A. Zawodzinski, in: R. C. Alkire, H. Gerischer, D. M. Kolb, C. W. Tobias (Eds.), *Advances in Electrochemical Science and Engineering*, vol. 5, John Wiley & Sons, Inc., New York, 1997, p. 195.
- [2] N. Wagner, in: E. Barsoukov and J. R. Macdonald (Eds.), *Impedance Spectroscopy-Theory, Experiment, and Applications*, second ed., John Wiley & Sons, Inc., Hoboken, New Jersey, 2005, p. 496.
- [3] R. A. Lemons, *J. Power Sources*, 29 (1990) 251.
- [4] R. O'Hayre, S.-W. Cha, W. Colella, F. B. Prinz, *Fuel Cell Fundamentals*, John Wiley and Sons, Inc., New Jersey (2005) p. 212.
- [5] J. P. Diard, N. Glandut, B. L. Gorrec, C. Montella, *J. Electrochem. Soc.* 151 (2004) A2193–A2197.
- [6] A. Hakenjos, M. Zobel, J. Clausnitzer, C. Hebling, *J. Power Sources* 154 (2006) 360–363.
- [7] X. Yuan, J. C. Sun, M. Blanco, H. Wang, J. Zhang, D. P. Wilkinson, *J. Power Sources* 161 (2006) 920–928.
- [8] J. M. L. Canut, R. M. Abouatallah, D. A. Harrington, *J. Electrochem. Soc.* 153 (2006) A857–A864.
- [9] Gamry Instruments, *FC350<sup>TM</sup> Fuel Cell Monitor*, Warminster, PA, 2002, pp. 1–4.
- [10] M. Ciureanu, R. Roberge, *J. Phys. Chem. B.* 105 (2001) 3531–3539.

- [11] Gamry Instruments, *Electrochemical Impedance Spectroscopy Primer*, Warminster, PA, 2005, p. 6.
- [12] Princeton Applied Research, *Basics of Electrochemical Impedance Spectroscopy*, Application Note AC-1, 2005.
- [13] A. Schneider, S. A. Freunberger, D. Kramer, A. Wokaun, and G. G. Scherer, *J. Electrochem. Soc.* 154 (2007) B383–B388.
- [14] P. Costamagna, S. Srinivasan, *J. Power Sources* 102 (2001) 242–252.
- [15] T. E. Springer, T. A. Zawodzinski, S. Gottesfeld, *J. Electrochem. Soc.* 138 (1991) 2334.
- [16] D. M. Bernardi, M. W. Verbrugge, *J. Electrochem. Soc.* 139 (1992) 2477.
- [17] W. H. Zhu, R. U. Payne, D. R. Cahela, B. J. Tatarchuk, *J. Power Sources* 168 (2007) 211–217.

**Table 5.1.** Membrane thickness estimation using linear interpolation.

| Membrane resistance<br>( $\text{m}\Omega\cdot\text{cm}^2$ ) | Membrane thickness ( $\mu\text{m}$ )                       |   | Relationship between<br>membrane resistance ( $R_m$ )<br>and each cell component ( $R_s$ ) | Membrane data<br>reference<br>$R=L/\sigma$ ( $L$ – thickness,<br>$\mu\text{m}$ ; $\sigma^c$ – conductivity,<br>$0.083 \text{ S cm}^{-1}$ ) |
|---|--|---|--|--|
|   | Simulated<br>resistance vs.<br>thickness <sup>a</sup> [15] | Estimated<br>values by<br>interpolation |  |  |
| 40  | 50   |   | $R_m = 0.34R_s$  | Nafion <sup>®</sup> 112  |
| 41  |  | 51                                      | $R_m = 0.35R_s$  | (51 $\mu\text{m}$ , 61 $\text{m}\Omega\cdot\text{cm}^2$ )  |
| 59  |  | 82                                      | $R_m = 0.50R_s$  | Nafion <sup>®</sup> 1135   |
| 63  |  | 89                                      | $R_m = 0.54R_s$  | (89 $\mu\text{m}$ , 107 $\text{m}\Omega\cdot\text{cm}^2$ )   |
| 70  | 100  |   | $R_m = 0.60R_s$  | Nafion <sup>®</sup> 115  |
| 81  |  | (114) <sup>b</sup>                      | $R_m = 0.70R_s$  | (127 $\mu\text{m}$ , 153 $\text{m}\Omega\cdot\text{cm}^2$ )<br>Nafion <sup>®</sup> 117   |
| 90  |  | 127                                     | $R_m = 0.77R_s$  | (178 $\mu\text{m}$ , 214 $\text{m}\Omega\cdot\text{cm}^2$ )  |
| 100   | 140  |   | $R_m = 0.85R_s$  |  |
| 117   |  | <164                                    | $R_m < R_s$  |  |
| 125   | 175  |   | —  |  |

<sup>a</sup> The simulated membrane resistance and thickness can be viewed as constant at a current density of less than  $350 \text{ mA cm}^{-2}$ . The literature membrane was saturated before entering into the  $\text{H}_2/\text{Air}$  PEM fuel cell.

<sup>b</sup> The membrane thickness was measured at the small edges around the stack.

<sup>c</sup> DuPont product information, Nafion<sup>®</sup> PFSA Membranes, NAE101, November 2002.

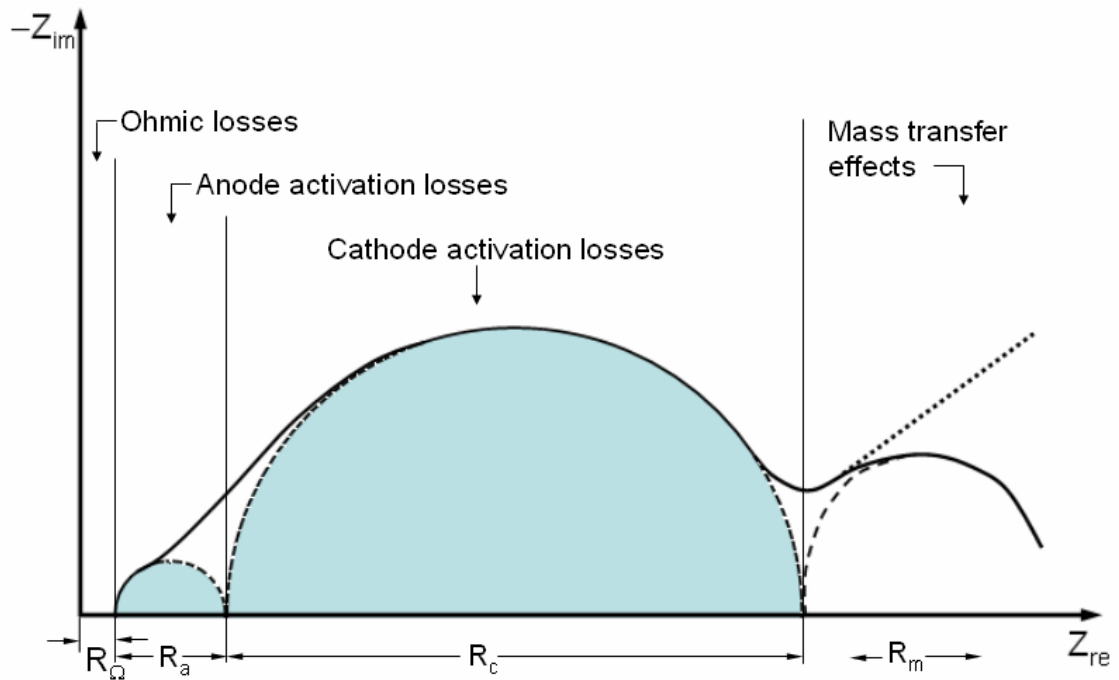


**Figure 5.1.** Nyquist plot from a hypothetical PEM fuel cell stack (or fuel cells in the stack). The four regions represent four losses in the fuel cells, and the size of each loop is correlated to the relative magnitude of each losses.



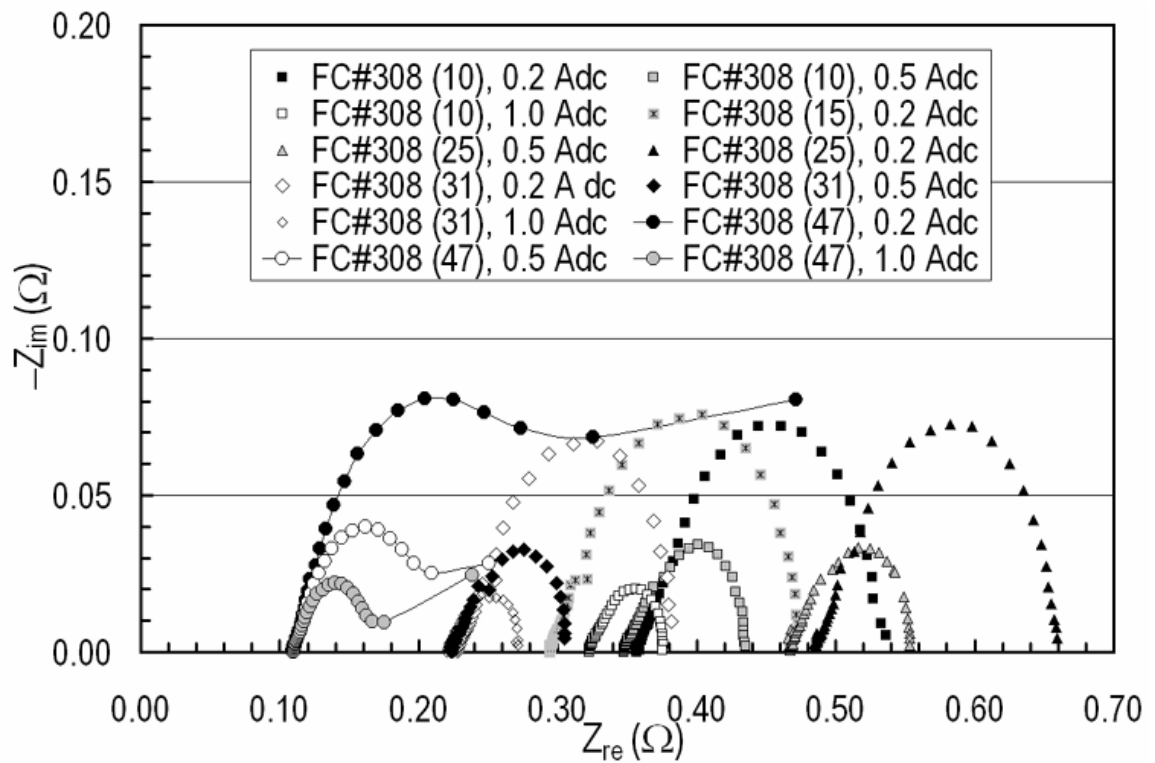


**Figure 5.2.** Nyquist plot of stack #308 using 10-20 mV AC voltage signals applied to the PEFC stack without an embedded system controller at a test-starting current from 0.2 A to 1.0 A and a temperature of *ca.* 26°C.

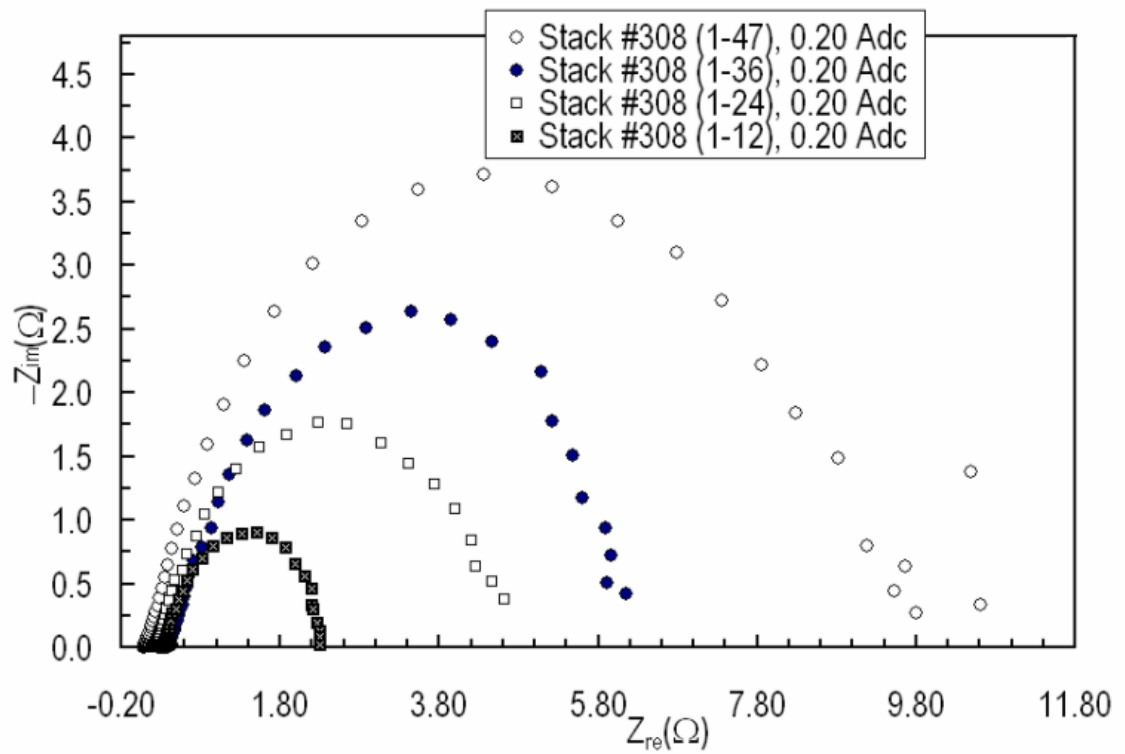


**Figure 5.3.** Nyquist plot of stack #308 using 10 mV AC voltage signals applied to the PEFC stack without an embedded system controller at a test-starting current of 0.20 A DC current and a temperature of 26°C.

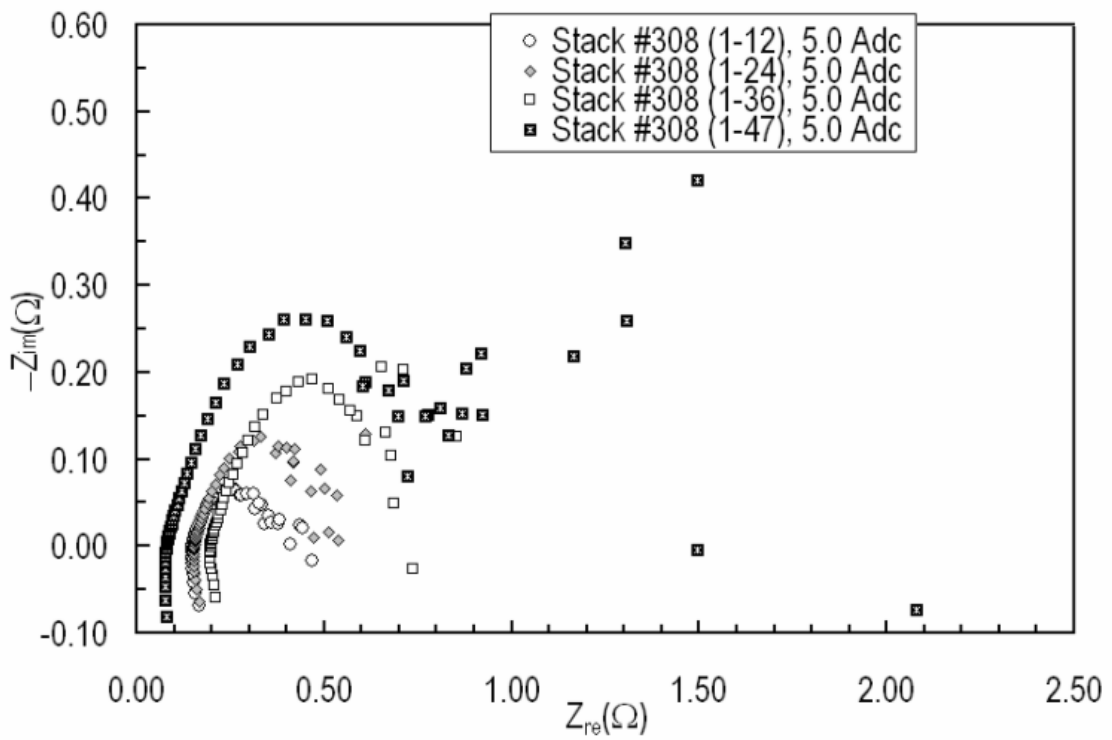


**Figure 5.4.** Nyquist plot of stack #308 using 10-20 mV AC voltage signals applied to the PEFC stack without an embedded system controller at a test-starting current of 5.0 A DC current and a temperature of 29°C.

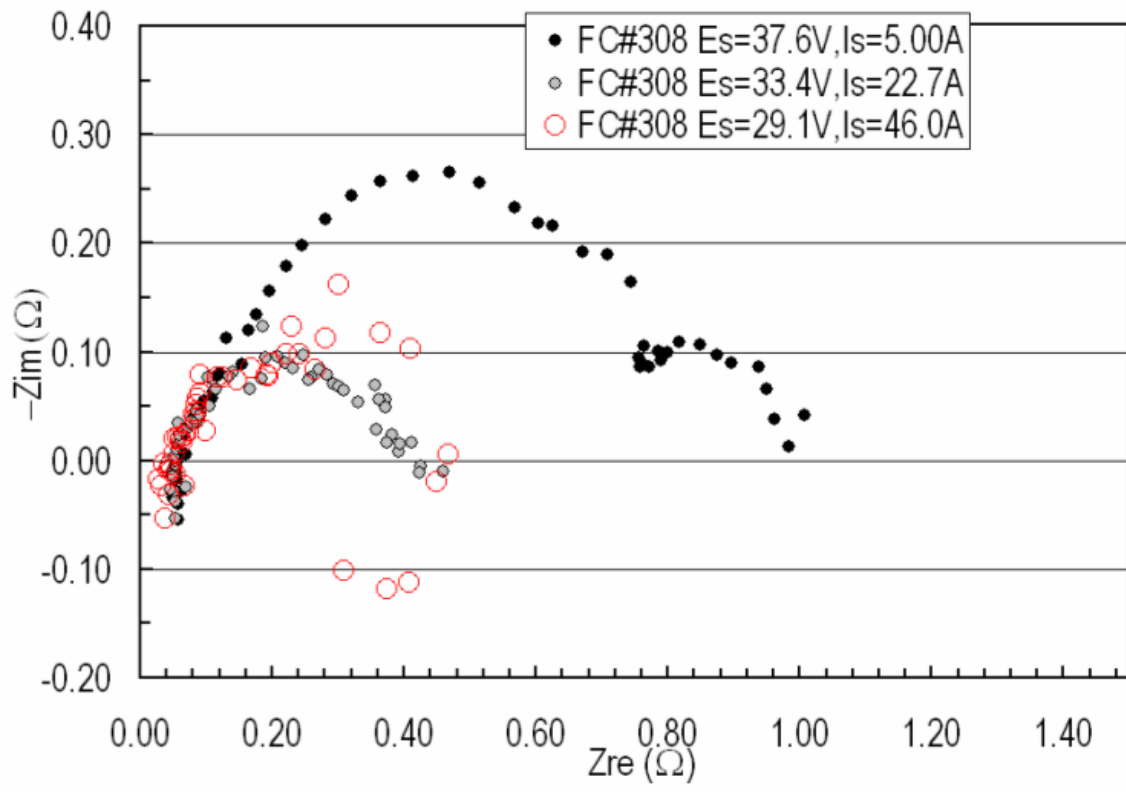


**Figure 5.5.** Nyquist plot of stack #308 using 500 mA AC current signals applied to the PEFC stack with an embedded system controller at a test-starting current from 5.0, 22.7 to 46 A and a temperature of 33, 54, and 65°C.

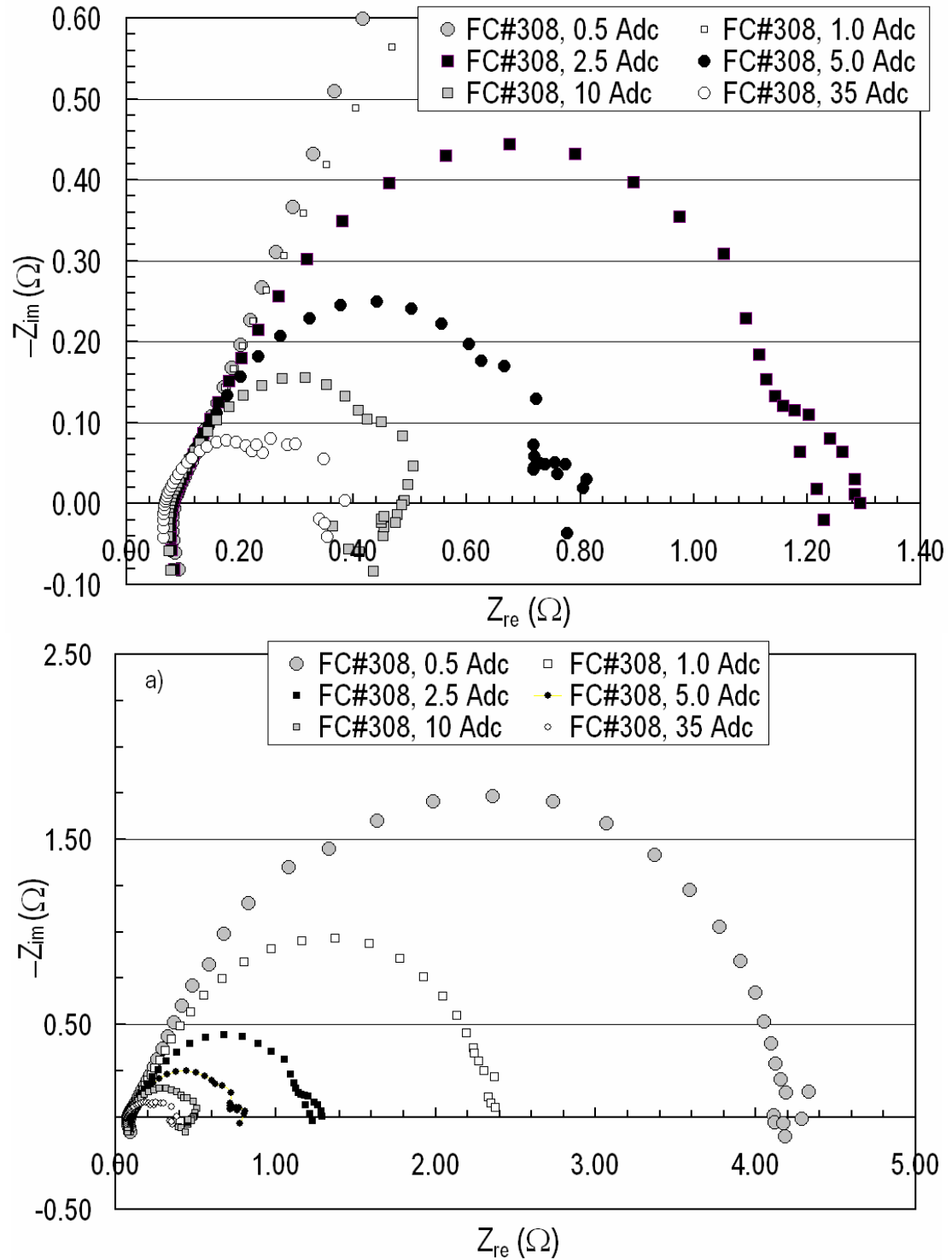


**Figure 5.6.** Nyquist plot of stack #308 using 250-500 mA AC current signals applied to the PEFC stack without an embedded system controller at a test-starting current from 2.5 A (250 mA AC, the rest are applied with 500 mA AC current) to 35 A and a temperature from 29°C to 65°C. a) Complete Nyquist diagram, b) Enlarged part of the Nyquist diagram.

## Chapter VI

### Equivalent Circuit Elements for PSpice Simulation of PEM Stacks at Pulse Load

#### VI.1. Introduction

Proton exchange membrane (PEM) fuel cells directly and continuously convert the chemical energy of a reaction between gaseous fuel and gaseous oxidant into electrical energy. Determination of the fuel cell degradation, recoverable poisoning, state of single MEA health, and stability of long-term stack operation are challenges for current fuel cell investigation [1]. Most AC impedance work was conducted on the air electrode and cathode catalyst layer [2-4]. Dynamic AC impedance measurements are attractive as an in-situ technique for fuel cell diagnostics and simulation [5]. Holz and Vielstich measured AC impedance data for Teflon-bonded oxygen porous electrodes of an alkali fuel cell [6]. This work developed an equivalent circuit containing resistors (solution resistance, charge transfer, and O<sub>2</sub> adsorption), capacitors (double-layer capacitance and O<sub>2</sub> adsorption capacitance on catalyst), and Warburg impedances (O<sub>2</sub> and ion diffusion to catalyst). Springer applied AC impedance to the polymer electrolyte fuel cell (PEFC or PEMFC) including equation implementation, model simplification and verification, least squares fitting, and interpretation of impedance features [7]. Diard et al. conducted impedance measurement (load  $R = 1 \Omega$ ) of a 10 W four-cell HPower stack using pure H<sub>2</sub> and O<sub>2</sub> and estimated that the resistance of the polymer membrane was *ca.*

40% of the internal resistance [8]. Wagner examined the impedance spectra of a PEM fuel cell and simulated the measured EIS with an equivalent circuit in order to split the cell impedance into electrode impedances and electrolyte resistance by varying the operating current through load changes [9]. However, the physical elements were not analyzed and no proper values were given for these elements. Instead, it emphasized the correlation between impedance of the fuel cell and  $i$ - $V$  curve. Wilkinson and St-Pierre [10] obtained some useful parameters with AC impedance separating kinetic, Ohmic and mass transport effects for PEM fuel cells using different gas compositions such as O<sub>2</sub>, air, and 79% He/21% O<sub>2</sub>. Yuan et al. performed impedance measurement of a 500 W six-cell PEM stack using hydrogen and air [11]. Impedance arcs including air mass transport and anode activation loss demonstrated the effects of air shortage at 30°C and 50°C. There is no doubt that the study of the whole PEM stack system with solid electrolyte membranes is extremely difficult if using a traditional reference electrode. Kuhn et al. [12] first introduced a pseudo reference electrode into the fuel cell for separation of the anode and cathode to study the anodic kinetic parameters.

Electrochemical impedance spectroscopy (EIS) is a powerful tool used to formulate a hypothesis when EIS data is fit to an equivalent circuit model. The number of circuit elements and types of circuit models are determined by a perfect fit using the curve-fitting software and suitable interpretation of the circuit models and physical elements. The “Goodness of fit” is a chi-squared parameter ( $\chi^2$ ), normally included in the curve-fitting software [13]. Boukamp recommended that after a new circuit element is introduced into the circuit model, the value of  $\chi^2$  should decrease by tenfold [14]. If the result of an additional circuit element does not improve the goodness of fit, one

should keep the simpler model, search for an improved circuit model, or use another circuit element.

Several circuit elements are usually used in the fuel cell circuit modeling. The Gerischer element describes a preceding chemical reaction in the bulk reaction and also can be applied to model the porous electrode process [15]. The most common and simplest diffusion circuit element to use is called the Warburg diffusion element [16]. It can be used to model semi-infinite linear diffusion, i.e., unrestricted diffusion to a large planar electrode. When a thin film process (finite diffusion) is involved in the reaction process, the O and T elements are useful for real diffusion simulation [13]. The constrained diffusion circuit element (O) is present in situations such as the rotating disk electrode when the electroactive species must diffuse to the electrode surface through a thin diffusion layer, outside of which the solution is well mixed. The constrained diffusion circuit element (T) is characteristic of a type of film which contains a fixed amount of electroactive substance, such as in batteries, supercapacitors, or conducting polymer membrane. For PEM fuel cells, mass transport happens only by diffusion in a region near to the electrodes, the “Nernst diffusion layer”. The concentration of species outside of this layer is homogenous for a period of time. The fuel gas or oxygen has to diffuse through the Nernst diffusion layer to reach the active reaction sites on the electrode. The O circuit element is applied to describe this Nernst diffusion impedance. Gamry named this diffusion impedance as the “Porous Bounded Warburg” circuit element [17, 18]. The  $C_{pe}$  (constant phase element) is a non-intuitive element which reflects the response of a real-world system when the center of the impedance arc is located below the  $Z_{re}$ -axis. Smooth mercury electrodes do not have depressed semi-



circles. In EIS experiments, replacing the capacitor with  $C_{pe}$  can yield better fitting results in comparison with the fitted results obtained by using a pure capacitor, represented by a parallel plate condenser [19]. One physical explanation for the  $C_{pe}$  element is that it is caused by electrode roughness. This can be seen at carbon electrodes with a distribution of active sites (with varying activation energies) on the surface [13]. Electrochemical impedance spectroscopy is a powerful diagnostic tool and plays an important role in basic understanding of dynamic electrochemical processes. This paper uses AC impedance as an in-situ diagnostic tool to perform non-destructive tests and analysis for a single PEM stack and for PEM stack pairs operated in parallel or series. Through applying reasonably simulated curve fits to obtain the equivalent circuit elements, these physical elements are then put into the PSpice circuit in order to compare the tested pulse data with PSpice simulation results.

## **VI.2. Experimental**

The purpose of this work originally started as a way to use various electrochemical methods to evaluate a real-world fuel cell system. Except for the current-voltage ( $i$ - $V$ ) curve, the diagnostics using the EIS impedance technique can obtain more useful parameters about the PEM fuel cell system at load. Impedance data need fit to an equivalent circuit diagram containing different physical elements such as charge transfer resistances ( $R_f$ ), Ohmic series resistances ( $R_s$ ), double-layer capacitances ( $C_{dl}$ ), and Nernst impedance ( $R_N$ - $C_N$ ), where  $R_f$  is related to the anode and cathode activation kinetics,  $R_s$  is related to the electrolytes,  $C_{dl}$  is related to the surface area of the electrocatalysts on the anodes and cathodes, and  $R_N$ - $C_N$  are related to the additional

diffusion step or contributed by production of liquid water or reactive intermediates. In this preliminary PEM stack work, the above physical elements are included for simplification purpose. More elements related to mass transport, reaction mechanism, or pseudo capacitance may be added into the equivalent circuit model in the near future in order to have a better description of the stack operating behavior. The Nexa™ fuel cell modules including the PEM stacks (Ballard Power Systems, Inc., British Columbia, Canada) were bought for the experimental tests. The fuel cell system is a small, low maintenance, fully automated, and highly integrated system. It provides 1200 W of unregulated DC power. Its output current can reach up to 44 A and stack voltage for 47 total fuel cells normally rises up to 41 V open-circuit. The fuel cell geometric working area is estimated as *ca.* 122 cm<sup>2</sup> due to the inexistence of manufacturing data. The automated operation is maintained by an embedded controller board. Some tests were performed by electrically isolating the PEM stack from the controller board to obtain pure stack impedance data. After starting the fuel cell system according to the manufacture's procedure, isolation was accomplished by connecting the board to an external power supply and the fuel cell stack was then ready for testing. At this point, an AC impedance experiment only probes the whole fuel cell stack except for the voltage tabs. For the preliminary test and impedance data measurement, this is a good approximation. Since voltage tabs are normally designed to have minimal electrical impact (high impedance) on the system under investigation, their effects are negligible to the impedance measurements. The PEM stack was then operated for collecting the AC impedance data at different current levels after being separated from the control subsystem. The supply pressures to the stack were 5.0 psig for hydrogen fuel and

2.2 psig for air oxidant. The fuel cell system was air cooled and had an attached humidity exchanger using exhaust water as a humidity resource [20].

The Gamry FC350<sup>TM</sup> fuel cell monitor (Gamry Instruments, Inc., Warminster, PA) with a proper electronic load (Fig. 6.1) is available to work at a higher current range for measuring AC impedance data [21]. The contact and wire resistance between the power output wires and the testing fuel cell power source was approximately measured using  $i$ - $V$  technique at different current levels. The true sine wave signal from the FC350<sup>TM</sup> system, working in galvanostatic or hybrid impedance mode, modulated the current from a single cell, multiple fuel cells, or the PEM stack(s). Simultaneously, the current information at the electronic load was sent to the computer, and the fuel cell voltage was also measured by the FC350<sup>TM</sup> monitor directly. The Gamry system collected these values and generated the impedance data for further analysis. In addition, a calibration process was applied to the Gamry FC350<sup>TM</sup> impedance system after it was set up. The system was connected with an external resistive dummy cell. The universal dummy cell is a 2 k $\Omega$  0.05% accurate resistor in the position marked “calibration”. The Gamry framework provides a calibration script and the calibration process followed by the manual instructions after the system installation was finished. The framework software allows measurements to be performed in a galvanostatic manner and a hybrid mode. Traditional measurements are performed using constant RMS amplitude for the AC signal. The problem with this technique is that the impedance of the cell varies significantly from high to low frequencies. For impedance to be accurate, the perturbation signal has to be sufficiently small to maintain a pseudo-linear  $i$ - $V$  operation. Hybrid measurements compensate for the change in cell impedance as frequency is

varied by changing the AC current amplitude to keep measured AC voltage at a set value. The previously measured impedance point is used in determining the new current amplitude as the scan proceeds from 10 kHz to 10 mHz. In this work, the hybrid EIS mode was applied for the experiments in order to observe the EIS behavior at various frequencies. For the entire stack in the system, it was tested with and without the embedded controller. For the measured impedance spectrum, the Echem Analyst software [17] including a complete equivalent circuit modeling package was applied to find the model parameters for best agreement between the model impedance spectra and the measured data. The Levenberg-Marquardt algorithm was utilized in the NLLS fitting process.

The general circuit elements ( $L$ ,  $R$ , and  $C$ ) are applied to the equivalent circuit models for nonlinear simulation. Because the PEM stack is much more complicated than the situation of a single cell, the circuit is kept as simple as possible. This simplification enables us to have better initial understanding of the stack behavior under operating conditions, because various impedance parameters and losses including anode, cathode, and membrane electrolyte change with different operating conditions and power output levels. After the equivalent circuit elements were obtained, these data can be further put into the PSpice circuit for pulse simulation. For the preliminary tests on stack evaluation and diagnostics, the circuit elements in the PSpice simulation are fitted to data obtained with the controller board and electronic devices in order to keep the simulation process simplified. A software package including MicroSim Schematics and Waveform Analyzer (MicroSim Corporation, Version 8.0) was utilized as the PSpice simulation tool. The stack was loaded with different current amplitudes at a 20% duty cycle and

200 Hz frequency. Pulse test data for the stack(s) were collected using the PLZ electronic load and an AWG710 Tektronix digital oscilloscope.

### **VI.3. Results and Discussion**

#### *VI.3.1. Stack current-voltage curves through periodic current interruption*

For a PEM stack in a fully automated and highly integrated system, it is extremely difficult to maintain an isothermal stack temperature in order to obtain the current-voltage curves for stack characterization. The periodic current interruption method was applied to the lab test for approximately evaluating the current-voltage curves [22]. The stack output voltage is a function of the operating current (Fig. 6.2). The stack output voltage is higher with increasing stack temperature. For a more accurate evaluation, an external power source may be used to provide the power for the stack's system controller board, compressor, and other electronic devices. The standard  $i$ - $V$  curves can be obtained based on the fuel cell working area, which was estimated as *ca.* 122 cm<sup>2</sup> due to the inexistence of manufacturing data.

#### *VI.3.2. Stack impedance data and simulation*

The stack #515 was operated until it reached its steady state at a certain current level. Then, impedance data were collected by the Gamry system at various frequencies from 10 kHz to 10 mHz. The impedance test is normally stopped once data is out of the normal test range and not acceptable. The Bode plots are shown in Fig. 6.3, i.e. real part of impedance and phase angle shift are plotted as functions of frequency. The measured Ohmic series resistance ( $R_S = 55 \text{ m}\Omega$ ) related to the membrane electrolyte is clearly indicated in Fig. 6.3. The simulated average value for the Ohmic series resistance,  $\overline{R_S} =$

52 mΩ ( $\overline{R_S} = \sum_{i=1}^n R_{S,i}$ , Table 6.1), is well matched with the measured data. As shown in

Table 6.1, the measured Ohmic series resistance ( $\overline{R_S} = 70$  mΩ) is increased due to changing the power source for the embedded electronic devices from the fuel cell stack to the external power source. The wire and contact resistance ( $R_W$ ) was determined by measuring the voltage drop at a specified current. The stack Ohmic resistance including membrane electrolyte resistance is  $R_{El} = R_S - R_W$ . In connection with the Ohmic series resistance value with embedded control devices, the total resistance for the controller board, compressor and other electronic devices can be estimated by Ohm's law. The Ohmic resistance of the control circuit in parallel with the PEM stack can be determined in the high frequency region where the capacitance is viewed as a wire and the circuit is simplified. This resistance is a useful parameter for the PEM system evaluation.

The Nyquist plots are shown in Fig. 6.4a and 6.4b including both measured data and simulated curves. The circuit model of  $LR(RC)(RC)(RC)$  is applied to all impedance data simulation for the stack #515 and the stack #881. At the high frequency side of the half semicircle as shown in Fig. 6.4a, the simulated curves are matched well with the measured data. But at low frequency side near the  $Z_{re}$ -axis, the simulated Nyquist curves are not identical with the measured data, especially at smaller currents of 5 A or 8 A when the PEM stack is connected to the control devices. This noise is caused by the control devices as evidence by comparing Fig. 6.4a with the result after the control devices disconnected from the PEM stack and powered by an external power source (Fig. 6.4b). After the control devices are isolated from the stack power, the measured data are slightly depressed below the simulated curve at a load current of 5 A. Another

stack #881 exhibits the similar behavior as shown in Fig. 6.5. Although measured data are basically matched with the simulated curves, the equivalent circuit model still needs improvement to sensitively describe the phenomena of air diffusion limitation on the cathode side. The values of simulated physical elements are shown in Table 6.1 according to the measured impedance data. The physical interpretation for the simulated elements is also listed for two stacks in this table. The stack Ohmic resistance (bipolar plate contact and membrane electrolyte resistance) can be determined by the measured Ohmic series resistance excluding the wiring and contacting resistance after the control devices were switched to an external power source. After the stack's Ohmic, wire and contact resistances were determined, the control device's resistance could be calculated if necessary. The anode resistance relating to the activation kinetic loss was easily distinguished by considering a much lower anode resistance, identified as  $R_{f,A}$  in Table 6.1. Because the catalyst loading level at the cathode side is reasonably 2–3 times higher than that at the anode side [23], it is not difficult to determine the cathode resistance related to its activation kinetic loss when the cathode side resistance is still assumed as 2–3 times higher than the anode side resistance, identified as  $R_{f,C}$  in Table 6.1. The other  $RC$  in the circuit corresponds to a finite diffusion step which is called a 'Nernst impedance' [9, 24]. This is considered to be a frequency behavior related to a higher load of the fuel cell where there is a finite diffusion overvoltage. Wagner and his co-authors use the 3rd  $RC$  circuit near to the low frequency side to describe the high current density behavior. From this work as shown in Fig. 6.4b, it reveals that it is not well matched between the measured data and the simulated curves. The experimental data show that air cathode diffusion losses gradually increase with operating current from 5 A to 13 A

(*ca.* 41–107 mA cm<sup>-2</sup>, Fig. 6.4). This may be generally considered as Wagner’s finite diffusion over-voltage. However, the simulated Nyquist plots especially at the third *RC* circuit are well matched with the measured impedance data from 21–35 A (*ca.* 172–287 mA cm<sup>-2</sup>). The air-cathode diffusion loss in the testing PEM stack is considered to be almost half of the total losses when the stack is running within the above current densities. As a whole, the 3*RC* circuit related simulation curves approximately describe the behavior of different series Ohmic resistance, activation and diffusion losses. But from 5–13 A (30°C to 39°C), it is not clear why the diffusion losses at the air cathode are not fitting well with the simulated curves, which is called a “knot” feature. The rest of the third *RC* circuit curve near to the lower frequency side is considered as the finite diffusion loss (overvoltage). The model needs further consideration on describing that the air cathode diffusion loss increases with operating current densities, because more air is necessary to diffuse into the cathode reactions while more nitrogen and water needs to be transferred to the exhaust channels.

At a current of 35 A (*ca.* 287 mA cm<sup>-2</sup>), the measured impedance data are scattered and not well matched with simulated curves, mainly at the low frequency side. This is considered to be caused by liquid water production and removal from the cathode reaction zone. Water in liquid phase may plug the pores or diffusion channels and may also flood the active reaction sites at a high load current, because at a low load current the PEM stack uses much less hydrogen fuel and air oxidant producing less water and yielding a smooth-loop Nyquist plot. At the reaction zone, protons are recombining with adsorbed oxygen, and then water and heat are produced. Generated water removal further promotes mass transport at the reaction site. Water transport including phase



change caused by heat transfer greatly promotes water and nitrogen transfer from the reaction zone to the exhaust channel. The adjustment of the active reaction sites (flooded or non-flooded, active or non-active) possibly changes the Nernst impedance which is mostly related to cathode side mass transport losses. As a whole, the knot features are observed in these Nyquist plots, especially for the last third of the loop at the low frequency side when operating at a lower current level (5–6 A individual stack, 10 A for stacks in parallel and 5 A for stacks in series). The preliminary explanation is that this feature is potentially caused by the air cathodes, possibly by the production of liquid water or the reactive intermediates. At low current levels, this phenomenon is obvious, and the simulation results deviate more at the low frequency side. At higher current level operation, the knot feature is not obvious, because of the increasing driving force for mass transfer and the balance between reactant diffusion and product removal. Although there are some unstable impedance data points, the simulation curves are well matched with the experimental data. The general equivalent circuit model is the main purpose for this work. Better understanding of these knot features may be obtained through the use of better instrument techniques and experimental improvements.

### *VI.3.3. Stack operation in parallel*

When two Nexa™ PEM stacks were operated in parallel, two power systems were assumed as one power source. The AC impedance measurement was conducted for the whole parallel stacks. The 3RC circuit model is still applied for simulation of two parallel stacks. The values of the simulated physical elements are shown in Table 6.2. The Nernst impedance is much higher than the cathode and anode impedance according to the analysis for the single PEM stack. Starting from a 30 A load, the cathode

activation kinetic loss slightly decreases and the Nernst impedance loss gradually increases, which is identical behavior to the single stack's Nernst impedance at higher current operation. The Nyquist plots of the PEM stacks in parallel operation are shown in Fig. 6.6. The simulated Nyquist curves have similar results to the single tested PEM stack. The air cathode mass transport loss starts to increase from 10–21 A current at operational load. The impedance data describing cathode mass transport (The second part of the impedance loop) gradually matches with the Nyquist plots using the  $LR(RC)(RC)(RC)$  circuit model after it is loaded with 21 A current or higher. After a load of total 30 A (*ca.* 15 A for each stack, current each stack is different due to different stack impedances), the simulated Nyquist curves are identical with the measured impedance data (Fig. 6.6b). The 3RC circuit model still needs further improvement at low current levels, especially for the process simulation when the cathode Nernst impedance starts to increase in the parallel circuit.

#### *VI.3.4. Stack operation in series*

Two Nexa<sup>TM</sup> power systems were operated in series. Two PEM stacks embedded with control board and electronic devices were assumed as one power source and AC impedance measurement was conducted for two series stacks. A voltage divider was applied for AC measurement due to the 50 V limitation of the Gamry system. The 3RC circuit model is applied for simulation of two series stacks, similar to the parallel operation. The values of the simulated physical elements are shown in Table 6.2. The Nernst impedance is much higher than the cathode and anode impedance. Starting from a 15 A load for each stack, the cathode activation kinetic loss slightly decreases and the Nernst impedance loss gradually increases, which is identical behavior to the single

stack's Nernst impedance at higher current operation. The Nyquist plots of the PEM stacks in series operation are shown in Fig. 6.7b. The simulated Nyquist curves have the similar results as the single tested PEM stack. The increased cathode mass transport loss gradually matches with the  $LR(RC)(RC)(RC)$  circuit model curves since it starts a load of 15 A current. At a load of 30 A for stack pairs in series, the simulated Nyquist curves mainly reflect the effect of the cathode Nernst impedance (Fig. 6.7). The anode exhaust build-up and associated periodic purge may also cause the data points' fluctuations around the simulated curves. This anode mass transport limitation has been demonstrated when AC impedance tests included the purge cells where the anode exhaust builds up and less hydrogen fuel exists [25]. The cathode mass transport loss (or called Nernst impedance) is not visible when operating at low current levels in the series circuit..

#### *VI.3.5 PSpice simulation versus experimental data*

SPICE is a powerful general purpose analog circuit simulator that is used to verify circuit designs and to predict the circuit behavior. This is of particular importance for integrated circuits as its name implies: Simulation Program for Integrated Circuits Emphasis [26]. PSpice is a SPICE analog circuit simulation software that runs on personal computers. It was developed by MicroSim and used in electronic design automation or simulation, providing industry-standard solutions for accurate analog and mixed-signal simulations such as non-linear transient analysis which calculates the voltage and current as a function of time when a large signal is applied. PSpice is a full-featured, mixed-signal simulator [27]. It is a useful tool to improve design performance, yield, and reliability. All analyses can be done at different temperatures.

A TDI electronic load was applied for the initial pulse test. Pulse ringing was observed at higher current pulse load. Three lead acid batteries (Total voltage, 37.2 V) and a resistive electronic load (PLZ-1003W, 1 kW, Kikusui Electric Corporation) were chosen for further pulse test in order to determine from where the pulse noise came. Test results show that the TDI electronic load is an inductive load and is not proper for the pulse tests. The pulse tests for the stack(s) were conducted through the constant current mode and data were collected using a digital oscilloscope. The tested pulse voltage and current for the single stack #515 are compared with the PSpice simulation results, as shown in Fig. 6.8. The simulated curves are well matched with the pulse test data. The stacks #515 and #881 were then operated in parallel and series, separately. The measured pulse data and PSpice simulation results are independently shown in Figs. 6.9 and 6.10. For the impedance measurement and equivalent circuit model development, two stacks (#515 and #881) are assumed to be one bigger stack with featured stack parameters. For the parallel operation, the total impedance was smaller than either of two stacks. The simulated pulse curve has less voltage drop in comparison with the experimental pulse results. This error is possibly caused by measurement of the wire and contact resistance due to the smaller total parallel impedance. The location of the voltage probe is also important to the value of the pulse voltage. The series operation results are shown in Fig. 6.10. Due to higher voltage of two stacks, the peaks of the current pulse tend to be slightly slanted during measurement. In general, the PSpice simulated pulse curves are well matched with the test pulse data.

The simulated electrochemical cell or stack behaviors through suitable physical elements in the equivalent circuit are potentially matched with the real world reactions.

No matter what type of reasonable circuit model in use, the PSpice simulation theoretically generates the same or similar results in the circuit diagram if essential physical circuit elements are properly included and arranged in the circuit model. For better understanding of the individual stack model and the *3RC* multi-stack circuit model, the relationship between single and multi-stacks is necessary for validation of the measurement method. In comparison with one simple *3RC* circuit model for two stack pairs, the individual stack circuit model was also tested for the validation purpose. As listed in Table 6.3, both simulated results and measured data are generally well matched and the errors are between 0.65% and 4.5%. The relative errors for the parallel stack pairs are higher than that of stack pairs in series, because the power system in parallel has much lower impedance. The individual stack model deviates slightly more from experimental data in comparison to one *3RC* circuit model. This is mainly caused by a lower error in the stack pairs, and the two-individual stack circuit is necessary to pay more attention on wire and contact resistances. The simulation deviation may be reduced further by better circuit model development and more accurate experimental measurements.

#### **VI.4. Conclusions**

The PEFC stack in a commercial power system was successfully characterized by impedance measurements. Impedance data for single stack, parallel, and series stacks were obtained in the Nexa<sup>TM</sup> system with or without embedded system controller and other electronic devices. The equivalent circuit model with three-time constants was developed using these real-time response data generated by AC sinusoidal excitation.

Physical elements, electrochemical processes, and phenomenon inside the fuel cells or stacks were identified by further data interpretation. Losses from Ohmic conduction, anode activation, cathode activation, and mass transfer were approximately separated and determined. Simulated pulse results from equivalent circuit elements and a PSpice tool demonstrate good agreement with the pulse data measured from the PEFC stack(s). Electrochemical impedance spectroscopy can serve as a diagnostic tool and perform non-destructive tests and analysis of the PEFC stacks and cells, especially for PSpice pulse simulation.

#### **VI.5. Acknowledgements**

I would like to recognize Wenhua H. Zhu who was the co-author for the original article. I also wish to acknowledge the contribution from Dr. Donald R. Cahela. Mr. Amar Tiwari is also appreciated for reading this manuscript. This article may be found in the *Journal of Power Sources* [28].

#### **VI.6. References**

- [1] N. Wagner, in: E. Barsoukov, J. R. Macdonald (Eds.), *Impedance Spectroscopy-Theory, Experiment, and Applications*, John Wiley & Sons, 2005, p.498.
- [2] S. Ahn, B. J. Tatarchuk, *J. Electrochem. Soc.* 142 (1995) 4169.
- [3] M. Eikerling, A. A. Kornyshev, *J. Electroanal. Chem.* 107 (1999) 475.
- [4] R. Makharia, M. F. Mathias, D. R. Baker, *J. Electrochem. Soc.* 152 (2005) A970.
- [5] J. R. Selman, Y. P. Lin, *Electrochimica Acta* 38 (1993) 2063.
- [6] R. Holz, W. Vielstich, *J. Electrochem. Soc.* 131 (1984) 2298.

- [7] T. E. Springer, *Electrochemical Society proceedings*, vol.99-14, 1999, p. 208.
- [8] J. P. Diard, N. Glandut, B. L. Gorrec, C. Montella, *J. Electrochem. Soc.* 151 (2004) A2193.
- [9] N. Wagner, *J. App. Electrochem.* 32 (2002) 859.
- [10] D. P. Wilkinson, J. St-Pierre, 'Durability', in: W. Vielstich, H. Gasteiger, A. Lamm (Eds.), *Handbook of Fuel Cells—Fundamentals, Technology, and Applications*, John Wiley and Sons, 2003, pp. 611-626.
- [11] X. Yuan, J. C. Sun, M. Blanco, H. Wang, J. Zhang, D. P. Wilkinson, *J. Power Sources* 161 (2006) 920.
- [12] H. Kuhn, B. Andreaus, A. Wokaun, G. G. Scherer, *Electrochimica Acta* 51 (2006) 1622.
- [13] R. S. Rodgers, Research Solutions & Resources, 2005, <http://www.consultrsr.com/resources/eis/index.htm>.
- [14] B. A. Boukamp, *Solid State Ionics* 18-19 (1986) 136.
- [15] M. González-Cuenca, W. Zipprich, B. A. Boukamp, G. Pudmich, F. Tietz, *Fuel Cells* 1 (2001) 256.
- [16] A. J. Bard, L. R. Faulkner, *Electrochemical Methods—Fundamentals and Applications*, John Wiley & Sons Ltd., Singapore, 1998, p. 376.
- [17] Gamry Instruments, Gamry Echem Analyst Software—"Porous Bounded Warburg", 2007.
- [18] Gamry Instruments, *Electrochemical Impedance Spectroscopy Primer*, Warminster, PA, 2007, p. 6.
- [19] V. D. Jovic, Determination of the correct value of  $C_{dl}$  from the impedance results fitted by the commercially available software, <http://www.gamry.com>, Warminster, PA, 2003.
- [20] Ballard Power Systems, *Nexa Power Module Installation Manual*, British Columbia, Canada, 2002, pp.1-49.
- [21] Gamry Instruments, *FC350™ Fuel Cell Monitor*, Warminster, PA, 2002, pp.1-4.
- [22] W. H. Zhu, R.U. Payne, D.R. Cahela, B. J. Tatarchuk, *J. Power Sources* 128 (2004) 231.

- [23] P. Costamagna, S. Srinivasan, *J. Power Sources* 102 (2001) 242.
- [24] N. Wagner, E. Gulzow, B. Muller, M. Lang, *Electrochim. Acta* 43 (1998) 3785.
- [25] W. H. Zhu, R. U. Payne, B. J. Tatarchuk, *J. Power Sources* 168 (2007) 211.
- [26] Wikipedia Encyclopedia, Wikimedia Foundation, Inc., 2007, <http://en.wikipedia.org/wiki/PSPICE>, <http://en.wikipedia.org/wiki/SPICE>.
- [27] PSpice Simulation, Cadence Design Systems, San Jose, CA, 2007, [http://www.cadence.com/products/orcad/pspice\\_a\\_d/index.aspx](http://www.cadence.com/products/orcad/pspice_a_d/index.aspx).
- [28] W. H. Zhu, R. U. Payne, R. M. Nelms B. J. Tatarchuk, *J. Power Sources* 178 (2008) 197.



**Table 6.1.** Simulated physical elements and values of the PEM stacks #515 and #881 using the  $LR(RC)$  ( $RC(RC)$ ) equivalent circuit. (<sup>a</sup> 26A equivalent circuit fits were estimated by linear interpolation.)

| Circuit Simulation Elements                                | $L_0$             | $R_s$                   |                  | $R_1$   | $C_1$       | $R_2$            | $C_2$       | $R_3$                     | $C_3$       | Levenberg-Marquardt Method |
|--|-------------------|-------------------------|------------------|---|-------------|------------------|-------------|---------------------------|-------------|----------------------------|
| Physical Interpretation                                    | Wiring inductance | Ohmic series resistance |                  | Cathode activation kinetics and Nernst impedance related to the additional step |             |                  |             | Anode activation kinetics |             | Goodness of fit            |
| Load Current   | $L_0$             | $R_s$                   | $R_{EI}$         | $R_{f,C}$   | $C_{f,C}$   | $R_N$            | $C_N$       | $R_{f,A}$                 | $C_{dl,A}$  |                            |
| A  | $\mu\text{H}$     | $\text{m}\Omega$        | $\text{m}\Omega$ | $\text{m}\Omega$  | $\text{mF}$ | $\text{m}\Omega$ | $\text{mF}$ | $\text{m}\Omega$          | $\text{mF}$ |                            |
| <i>FC #515 with control board &amp; electronic devices</i> |                   |                         |                  |   |             |                  |             |                           |             |                            |
| 5  | 1.158             | 58.00                   | 66.23            | 133.2   | 73.04       | 438.3            | 145.8       | 44.78                     | 21.94       | 2.973e-03                  |
| 8  | 1.155             | 54.45                   | –                | 133.8   | 66.58       | 283.5            | 186.8       | 43.84                     | 20.45       | 1.671e-03                  |
| 13   | 1.198             | 53.11                   | 60.28            | 119.5   | 551.7       | 152.6            | 70.40       | 48.23                     | 21.04       | 1.024e-03                  |
| 21   | 1.144             | 49.80                   | 57.37            | 107.3   | 1023        | 144.2            | 75.25       | 48.06                     | 21.04       | 1.432e-03                  |
| 26 <sup>a</sup>  | 1.150             | 48.11                   | –                | 109.5   | 806.6       | 130.3            | 70.37       | 43.23                     | 20.76       | –                          |
| 28   | 1.152             | 47.44                   | 54.78            | 110.4   | 720.0       | 124.8            | 68.43       | 41.30                     | 20.65       | 2.449e-03                  |
| 35   | 0.6956            | 50.35                   | 53.16            | 127.9   | 389.8       | 105.1            | 63.69       | 29.86                     | 29.53       | 4.966e-03                  |
| <i>FC #515 w/o control board &amp; electronic devices</i>  |                   |                         |                  |   |             |                  |             |                           |             |                            |
| 5  | 0.9166            | 77.91                   | 66.23            | 141.5   | 67.91       | 538.4            | 126.2       | 33.87                     | 19.25       | 1.526e-03                  |
| 13   | 0.8550            | 71.96                   | 60.28            | 174.2   | 58.31       | 152.9            | 367.3       | 33.06                     | 21.02       | 1.151e-03                  |
| 21   | 0.8186            | 69.05                   | 57.37            | 159.1   | 61.90       | 31.87            | 908.0       | 31.60                     | 24.58       | 1.650e-03                  |
| 28   | 0.8381            | 66.46                   | 54.78            | 136.6   | 63.65       | 109.3            | 889.6       | 29.06                     | 25.16       | 1.981e-03                  |
| 35   | 0.8455            | 64.84                   | 53.16            | 103.1   | 61.65       | 103.4            | 407.9       | 22.94                     | 24.95       | 4.23e-03                   |
| <i>FC #881 with control board &amp; electronic devices</i> |                   |                         |                  |   |             |                  |             |                           |             |                            |
| 5  | 0.7433            | 61.85                   | –                | 135.3   | 81.21       | 523.6            | 151.7       | 47.69                     | 23.69       | 3.70E-03                   |
| 6  | 0.7246            | 61.99                   | 68.30            | 135.7   | 82.68       | 432.2            | 165.9       | 47.59                     | 23.64       | 2.560e-3                   |
| 8  | 0.7315            | 59.83                   | 66.14            | 123.0   | 77.16       | 371.7            | 173.4       | 43.54                     | 23.73       | 1.576e-3                   |
| 13   | 0.7330            | 58.05                   | 63.87            | 138.6   | 77.82       | 236.1            | 256.4       | 42.79                     | 24.95       | 1.426e-3                   |
| 21   | 0.7395            | 55.41                   | 60.05            | 178.3   | 91.02       | 135.2            | 1234        | 52.56                     | 26.42       | 1.901e-3                   |
| 26 <sup>a</sup>  | 0.7340            | 54.20                   | 58.60            | 141.5   | 90.11       | 160.6            | 757.4       | 46.65                     | 27.63       | –                          |
| 28   | 0.7318            | 53.71                   | 58.03            | 126.8   | 89.74       | 170.8            | 566.8       | 44.29                     | 28.12       | 2.196e-3                   |
| 35   | 0.7392            | 51.54                   | 55.95            | 96.81   | 59.73       | 233.7            | 288.7       | 25.66                     | 27.19       | 8.468e-3                   |
| <i>FC #881 w/o control board &amp; electronic devices</i>  |                   |                         |                  |   |             |                  |             |                           |             |                            |
| 6  | 0.8805            | 79.98                   | 68.30            | 113.5   | 66.51       | 487.8            | 140.6       | 30.89                     | 17.68       | 1.956e-3                   |
| 8  | 0.8900            | 77.82                   | 66.14            | 111.8   | 68.07       | 392.3            | 153.1       | 30.04                     | 18.73       | 1.799e-3                   |
| 13   | 0.9007            | 75.55                   | 63.87            | 117.7   | 68.61       | 257.0            | 204.8       | 29.41                     | 21.15       | 1.230e-3                   |
| 21   | 0.8724            | 71.73                   | 60.05            | 162.9   | 82.43       | 157.1            | 847.9       | 37.25                     | 26.48       | 1.380e-3                   |
| 28   | 0.8735            | 69.71                   | 58.03            | 169.2   | 99.90       | 211.3            | 1216        | 44.09                     | 27.06       | 3.865e-3                   |
| 35   | 0.8987            | 67.63                   | 55.95            | 103.6   | 78.72       | 214.6            | 336.0       | 26.87                     | 25.20       | 5.314e-3                   |

**Table 6.2.** Simulated physical elements and values of the PEM stack #515 co-operated with the PEM stack #881 using the LR (RC)(RC)(RC) equivalent circuit.

| Circuit Simulation Elements  | $L_0$             | $R_s$                   | $R_1$            | $C_1$   | $R_2$       | $C_2$            | $R_3$                     | $C_3$            | Levenberg-Marquardt Method |
|--|-------------------|-------------------------|------------------|---|-------------|------------------|---------------------------|------------------|----------------------------|
| Physical Interpretation  | Wiring inductance | Ohmic series resistance |                  | Cathode activation kinetics and Nernst impedance related to the additional step |             |                  | Anode activation kinetics |                  | Goodness of fit            |
| Load Current   | $L_0$             | $R_s$                   | $R_{EI}$         | $R_{f,C}$   | $C_{f,C}$   | $R_N$            | $C_N$                     | $R_{f,A}$        |                            |
| A  | $\mu\text{H}$     | $\text{m}\Omega$        | $\text{m}\Omega$ | $\text{m}\Omega$  | $\text{mF}$ | $\text{m}\Omega$ | $\text{mF}$               | $\text{m}\Omega$ | $\text{mF}$                |
| <b>#515   #881</b> <i>Two stacks in parallel with control board &amp; electronic devices</i> |                   |                         |                  |   |             |                  |                           |                  |                            |
| 10   | 1.157             | 38.82                   | 63.83            | 156.1   | 229.8       | 287.5            | 26.28                     | 34.63            | 1.942e-03                  |
| 21   | 1.139             | 33.75                   | 69.17            | 129.2   | 127.8       | 430.5            | 22.70                     | 36.17            | 1.224e-3                   |
| 26 <sup>a</sup>  | 1.141             | 32.78                   | 70.27            | 133.3   | 100.5       | 806.3            | 24.04                     | 36.63            | –                          |
| 30   | 1.142             | 32.00                   | 87.36            | 136.5   | 78.74       | 1107             | 25.12                     | 36.99            | 1.130e-3                   |
| 40   | 1.138             | 31.44                   | 79.24            | 156.2   | 72.06       | 1492             | 25.62                     | 39.94            | 1.686e-3                   |
| 50   | 1.158             | 31.56                   | 71.73            | 153.0   | 84.33       | 1411             | 22.48                     | 43.91            | 2.754e-3                   |
| 60   | 1.182             | 30.79                   | 61.20            | 148.4   | 89.87       | 1019             | 19.99                     | 45.75            | 3.877e-3                   |
| <b>#515 – #881</b> <i>Two stacks in series with control board &amp; electronic devices</i>   |                   |                         |                  |   |             |                  |                           |                  |                            |
| 5  | 4.120             | 155.5                   | 264.3            | 41.63   | 834.1       | 78.62            | 107.4                     | 9.314            | 3.690e-03                  |
| 10   | 4.168             | 136.3                   | 360.2            | 40.47   | 437.0       | 185.7            | 118.5                     | 9.009            | 4.050e-03                  |
| 13 <sup>a</sup>  | 4.217             | 132.0                   | 362.2            | 40.41   | 360.3       | 284.5            | 116.1                     | 9.354            | –                          |
| 15   | 4.250             | 129.1                   | 363.6            | 40.37   | 309.1       | 350.3            | 114.5                     | 9.584            | 4.840e-03                  |
| 21   | 4.210             | 125.1                   | 308.7            | 42.03   | 309.8       | 350.3            | 103.5                     | 10.16            | 5.781e-3                   |
| 25   | 4.222             | 121.7                   | 231.2            | 37.47   | 338.3       | 214.4            | 89.24                     | 9.843            | 5.689e-3                   |
| 30   | 4.248             | 122.3                   | 247.4            | 40.12   | 378.9       | 286.2            | 86.64                     | 10.55            | 7.719e-3                   |

<sup>a</sup> The values of the equivalent circuit elements at a specified load current were estimated based on the linear interpolation.

**Table 6.3.** Simulated pulse voltage at its peak current versus the measured data value

| Two stacks #515 and #881 operating in parallel and series | Pulse voltage in parallel (V) |  |           | Pulse voltage in series (V) |  |       |
|---|-------------------------------|--|-----------|-----------------------------|--|-------|
|   | Start voltage at 0.01 A       | Pulse voltage at a load of 26 A current <sup>a</sup> | Error (%) | Start voltage at 0.01 A     | Pulse voltage at a load of 13 A current <sup>a</sup> | Error |
| Simulated results of a two-individual stack circuit model | 39.00                         | 37.83  | 4.50      | 77.00                       | 74.60  | 1.17% |
| Simulated results of two stacks as one 3RC circuit model  | 39.00                         | 37.56  | 3.75      | 77.00                       | 74.22  | 0.65% |
| Measured data values through digital oscilloscope         | 39.08                         | 36.20  | —         | 77.06                       | 73.74  | —     |

<sup>a</sup> All simulated values and measured data were recorded at the second pulse voltage location. The average pulse voltage was calculated using the beginning, middle, and end values of the pulse voltage.

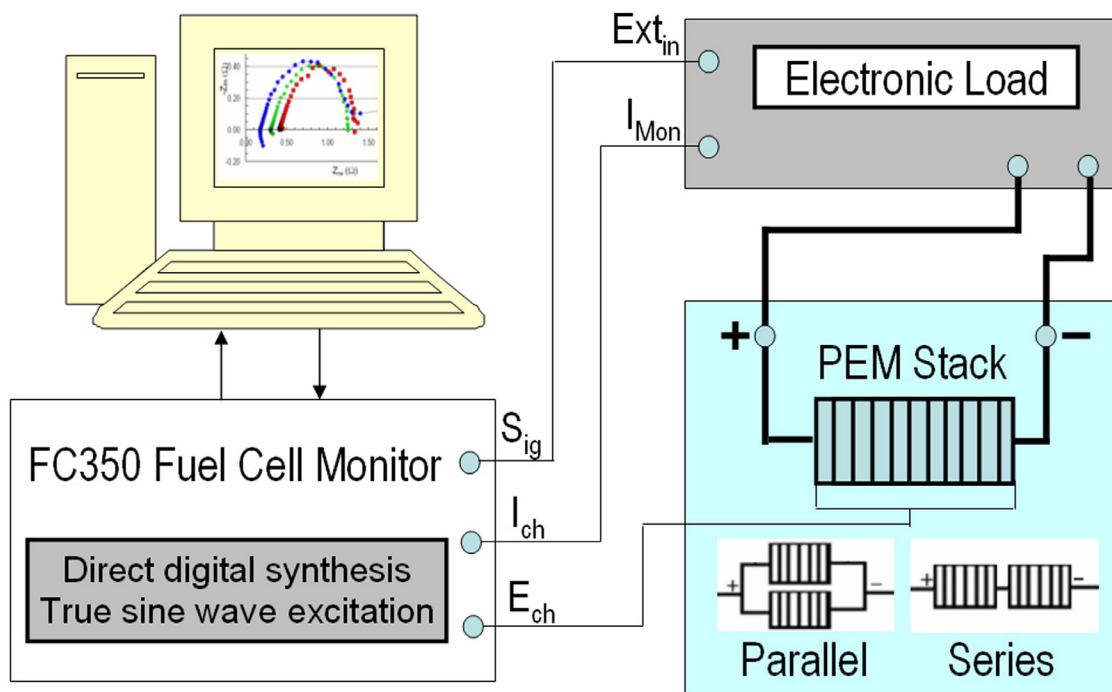


**Figure 6.1.** Diagram of AC impedance data measurement from a Gamry FC350™ fuel cell monitor and an electronic load. Single fuel cell stack or PEM stacks in parallel/series arrangement.

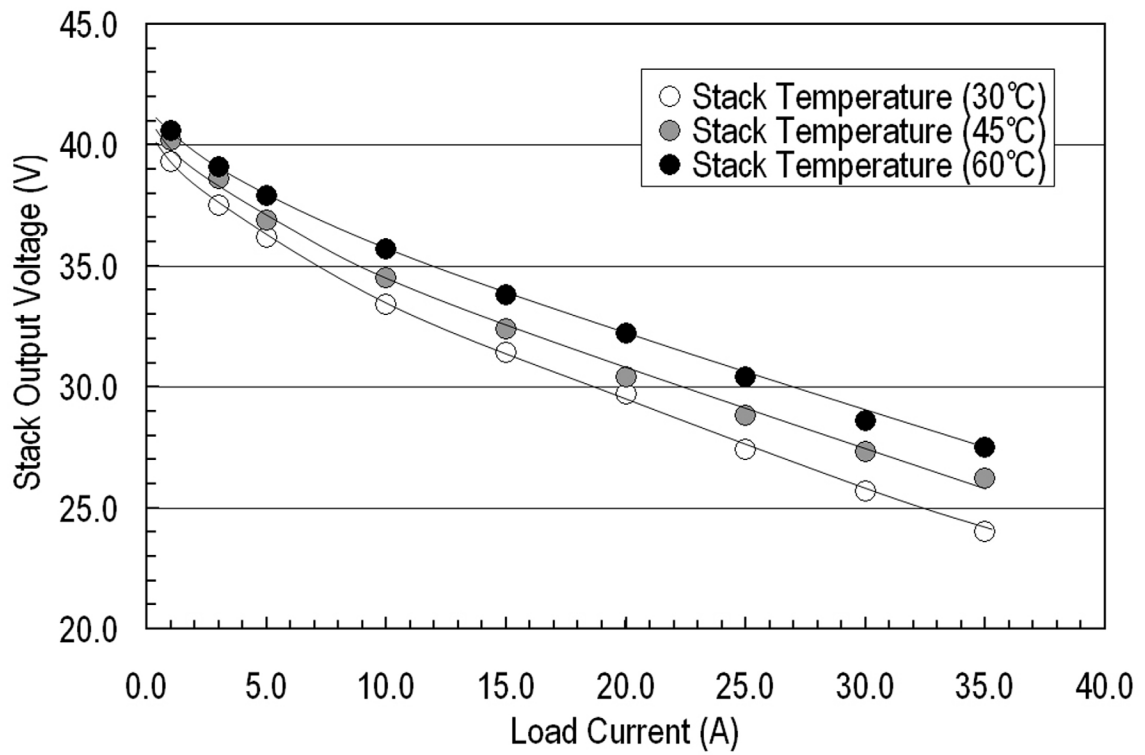


**Figure 6.2.** Polarization curves measured from the BPS Nexa™ stack with periodic current interruption to maintain isothermal stack temperature.

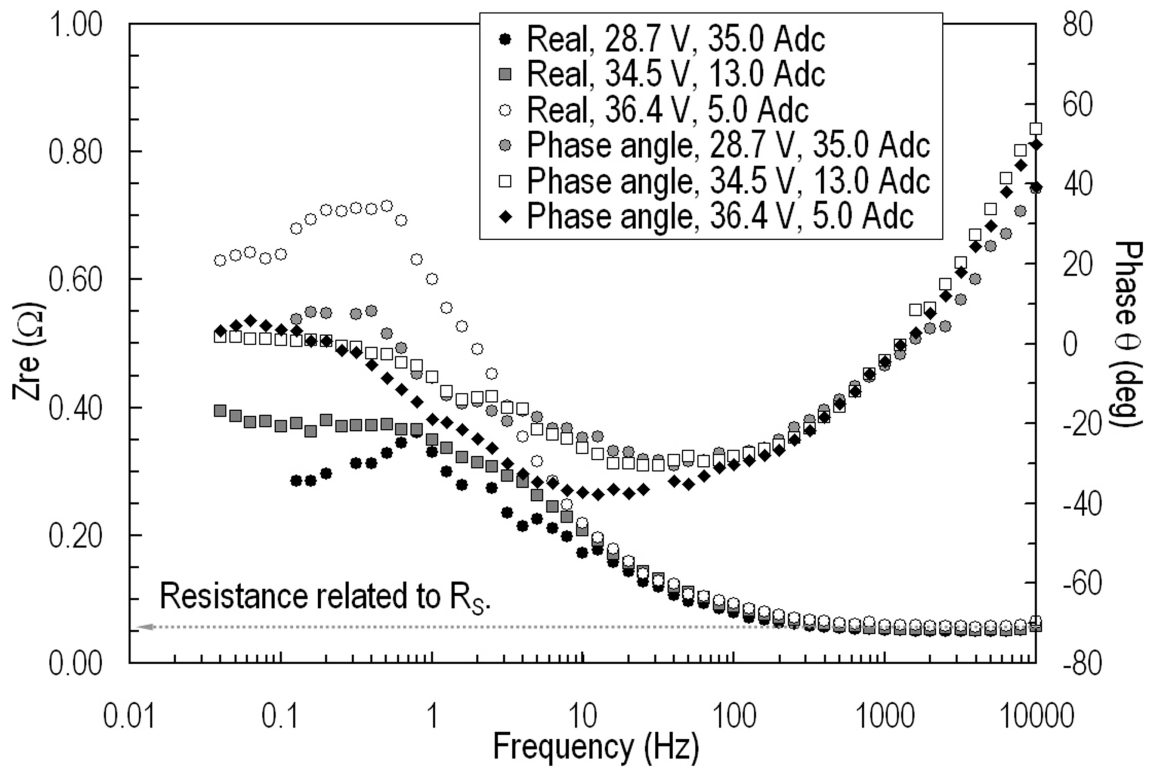


**Figure 6.3.** Bode plots of the PEM stack #515 embedded with system controller, compressor, and other electronic devices in the Nexa™ power module. The voltage and current in the graph is the value just beginning of the impedance test startup, and the hybrid mode uses 150 mV AC.

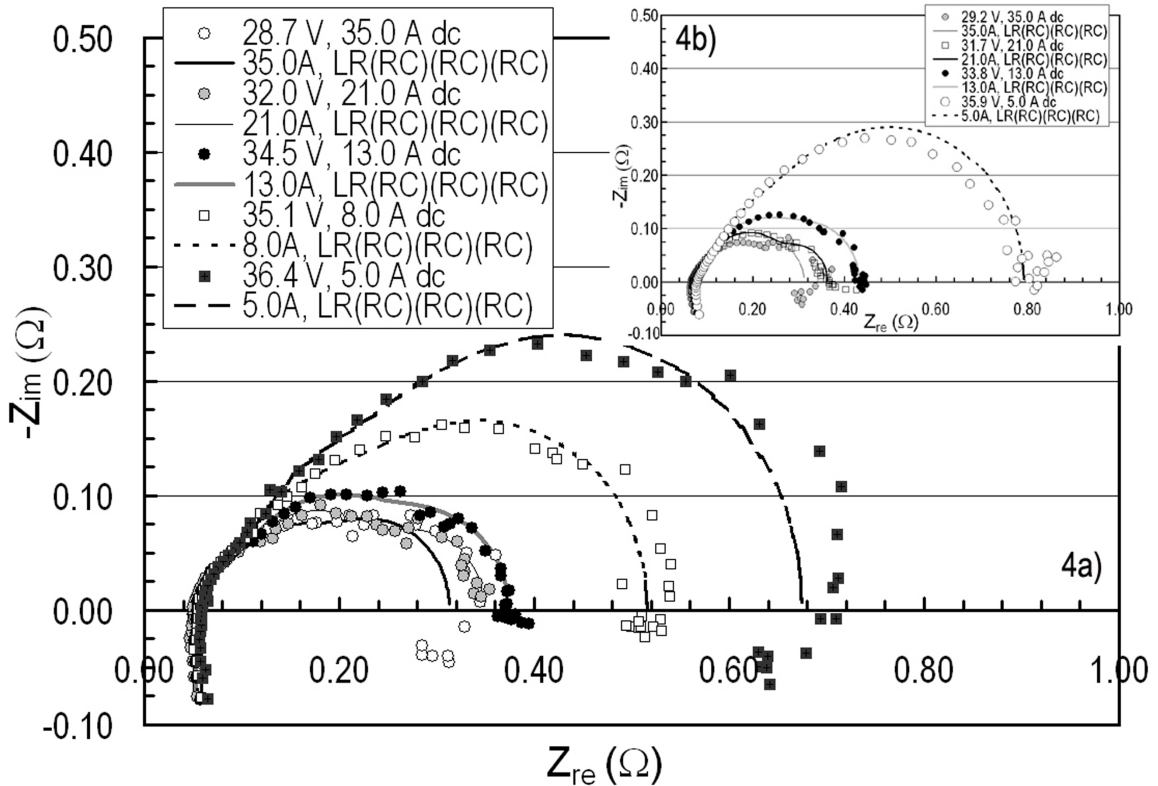


**Figure 6.4.** Nyquist plots of the PEM stack #515 in the Nexa™ PEM system. The voltage and current in the graph is the value just beginning of the impedance test startup, and the hybrid mode uses 150 mV AC. a) The PEM stack is equipped with embedded system controller, compressor, and other electronic devices; b) The PEM stack is running while its controller board and other electronic devices uses an external power source. The simulated curves in all figures using  $LR(RC)(RC)(RC)$  circuit model.

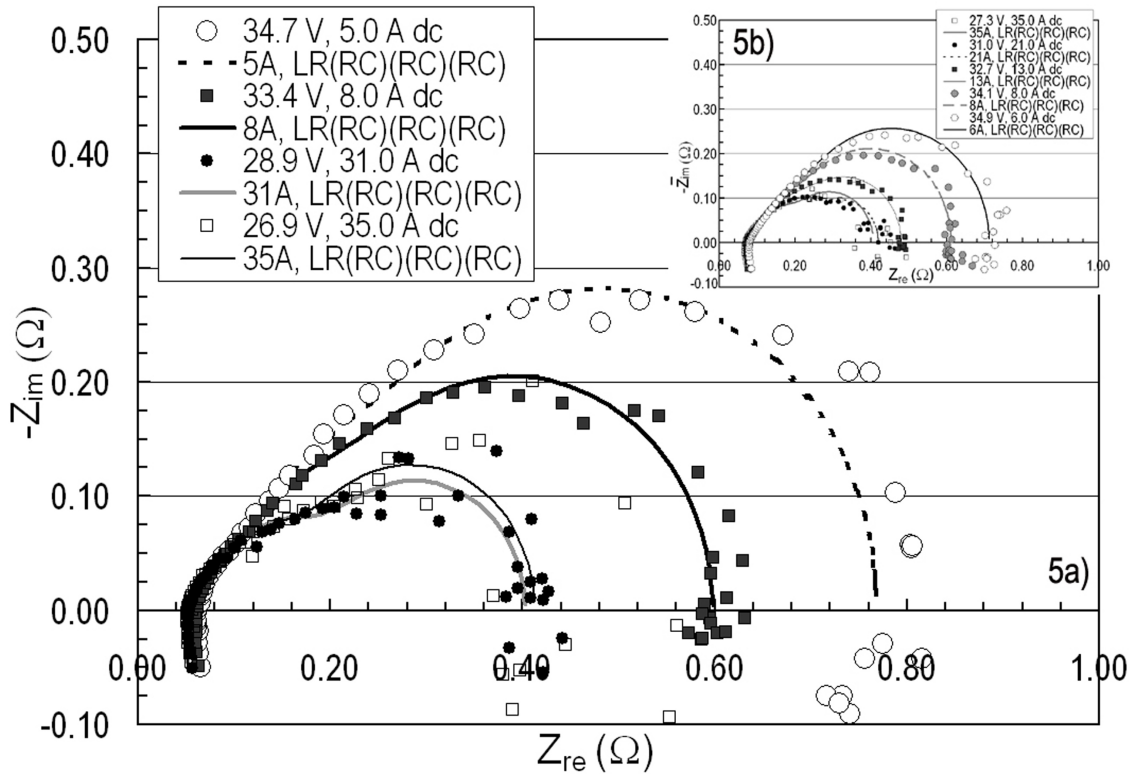


**Figure 6.5.** Nyquist plots of the PEM stack #881 in the Nexa™ PEM system. The voltage and current in the graph is the value just beginning of the impedance test startup, and the hybrid mode uses 150 mV AC. a) The PEM stack is equipped with embedded system controller, compressor, and other electronic devices; b) The PEM stack is running while its controller board and other electronic devices uses an external power source. The simulated curves in all figures using  $LR(RC)(RC)(RC)$  circuit model.



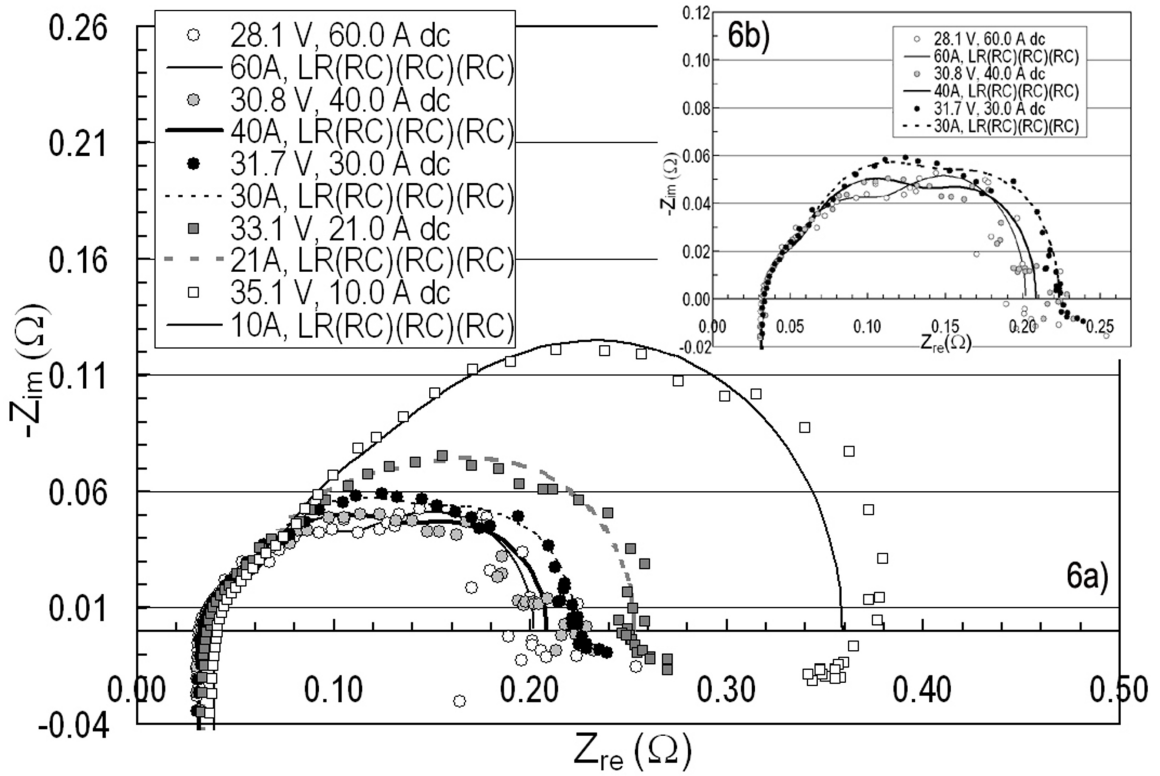


**Figure 6.6.** Nyquist plots of the PEM stacks #515 and #881 in parallel operation embedded with system controller, compressor, and other electronic devices. The voltage and current in the graph is the value just beginning of the impedance test startup, and the hybrid mode uses 150 mV AC. a) Operating current ranging from 10 A to 60 A. b) Enlarged Nyquist plots at higher current from 30 A to 60 A.

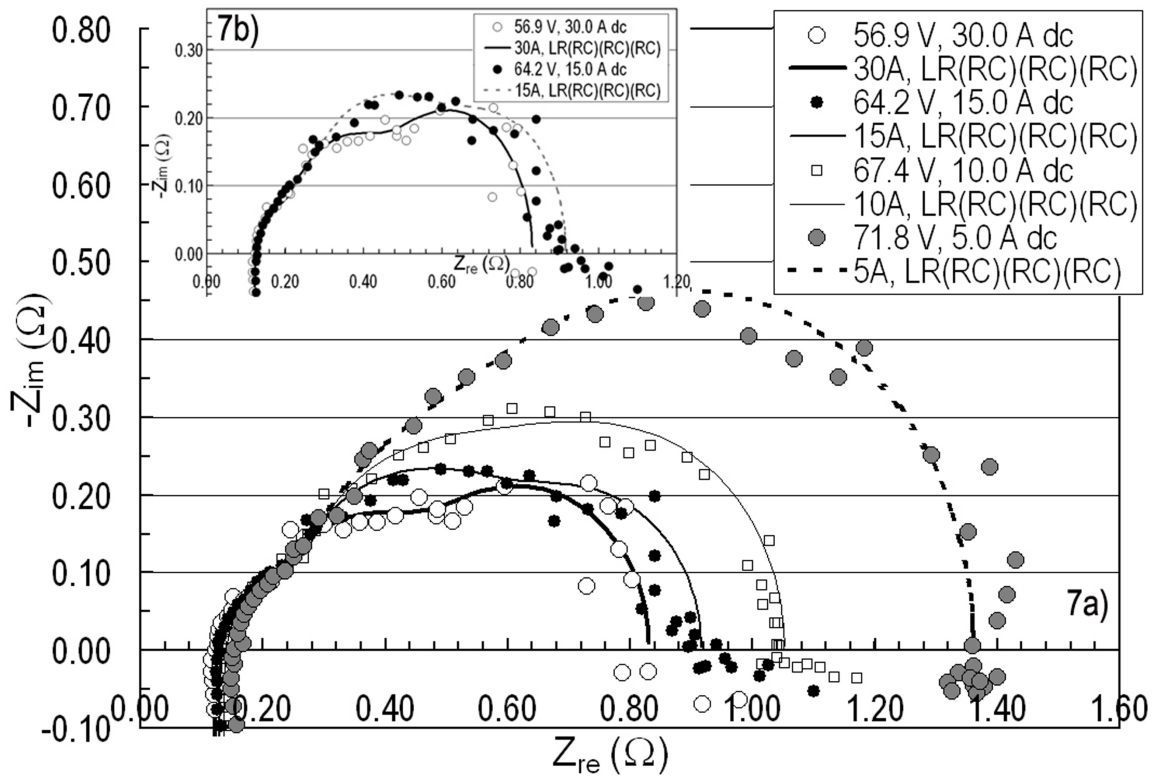


**Figure 6.7.** Nyquist plots of the PEM stacks #515 and #881 in series operation embedded with system controller, compressor, and other electronic devices. The voltage and current in the graph is the value just beginning of the impedance test startup, and the hybrid mode uses 150 mV AC. a) Operating current ranging from 5 A to 30 A. b) Enlarged Nyquist plots at higher current from 15 A to 30 A.

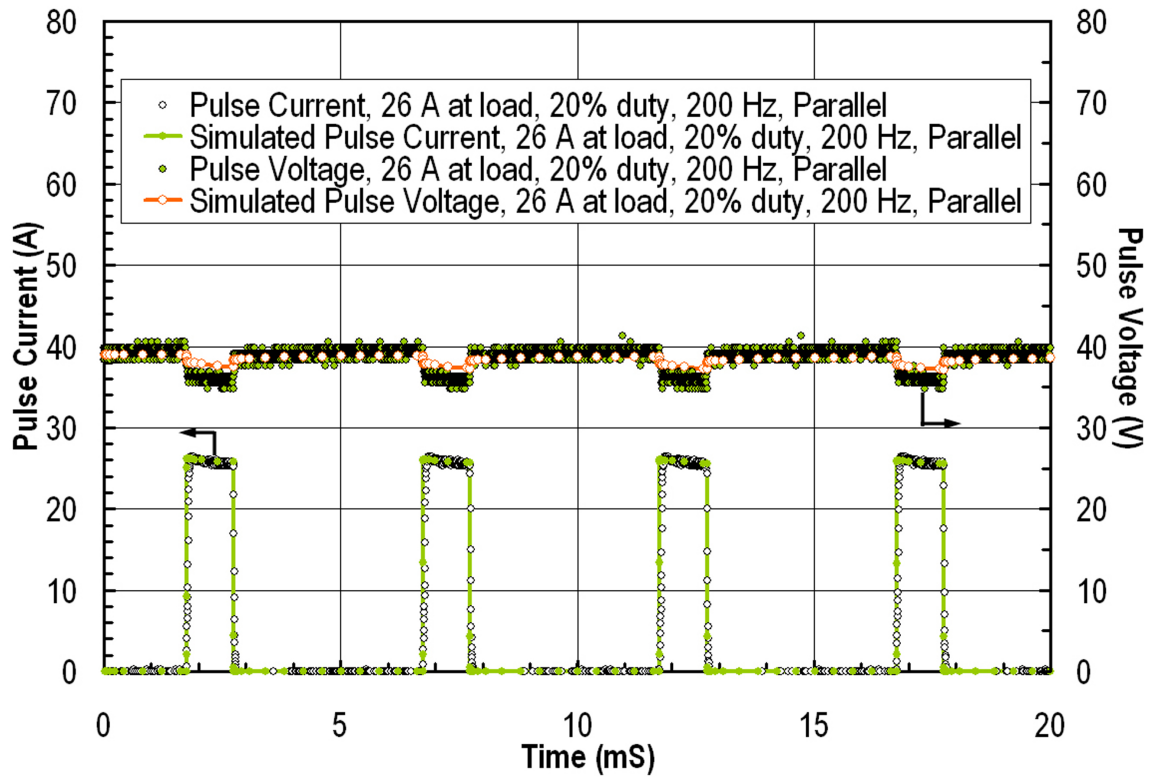


**Figure 6.8.** Pulse current and voltage in comparison of PSpice simulation results for the stack #515 at load. Current 35 A, duty 20%, and test frequency 200 Hz.

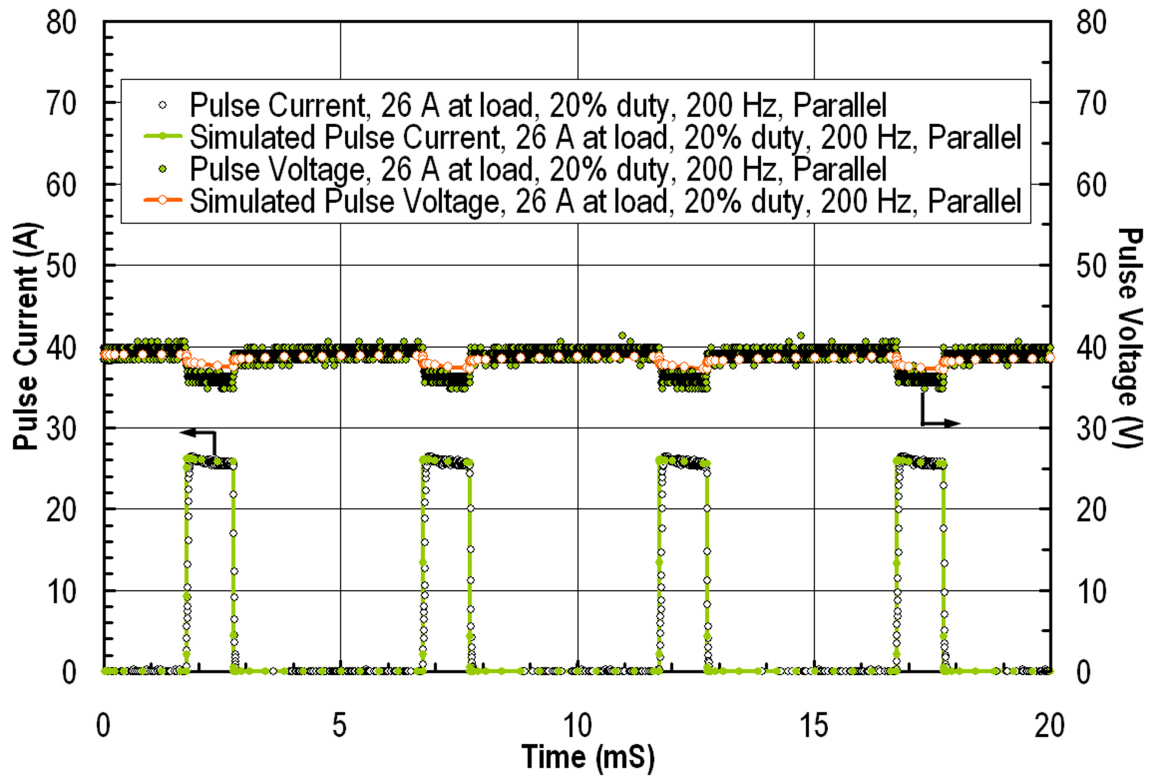


**Figure 6.9.** Pulse current and voltage in comparison of PSpice simulation results for the stacks #515 and #881 in parallel operation at load. Current 26 A, duty 20%, and test frequency 200 Hz.

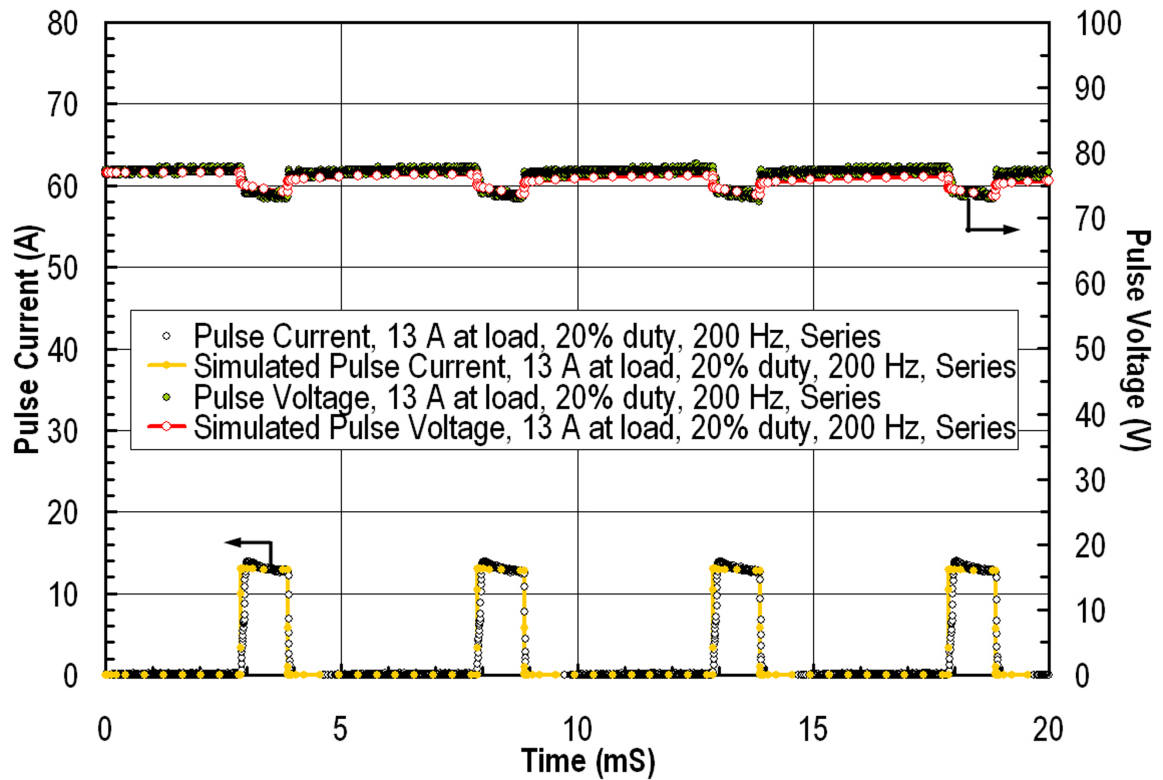


**Figure 6.10.** Pulse current and voltage in comparison of PSpice simulation results for the stack #515 and #881 in series test at load. Current 13 A, duty 20%, and test frequency 200 Hz.

## **Chapter VII**

### **Equivalent Circuit Modeling of SOFC Cells and Stacks at Load**

#### **VII.1. Introduction**

The need for alternate forms of energy has become a popular and well funded area of research as gas prices, tensions in the Middle East, global energy consumption, and people's fear of their impact on the environment have all increased. Fuel cells could become a major supply of energy over the next few decades, especially in applications such as mobile power and uninterrupted power supplies. In order to implement fuel cells into a power system, the dynamic load response of the device must be well understood. Impedance spectroscopy is an effective tool for obtaining such knowledge.

Impedance spectroscopy is a measurement technique capable of assessing the dynamic response characteristics of an electrochemical system and is performed by superimposing an AC signal on the DC output of an electrochemical cell and measuring the impedance over a spectrum of frequencies. The data are often fitted with an equivalent circuit model, which is a circuit of electrical elements producing a similar load response to the device under investigation. These models are useful for designing the power conditioning system, through which the electrochemical device supplies power to a load. Equivalent circuits are also beneficial for stack diagnostics, because the different circuit elements theoretically represent different relaxation processes occurring in the

electrochemical cell(s); hence, fit data can be used to distinguish which processes are limiting cell behavior and to what extent. AC impedance is further useful for assessing system design and component fabrication, monitoring system aging and state of health, designing process controls, and performing quality control.

Many researchers have employed impedance spectroscopy to test solid oxide fuel cells [1-13]. Because of equipment limitations, most AC impedance has been performed near open circuit voltage (OCV). The few studies that have tested a cell under load have overcome the power limitations by testing electrodes much smaller than average [2, 7, 10]. In the following work, impedance spectroscopy has been used to test solid oxide fuel cells and stacks at load yielding data that have been fitted to equivalent circuits.

## **VII.2. Experimental**

AC impedance was applied to solid oxide fuel cells (Ceramatec, Inc.) of two different sizes: button cells and larger, planar cells. Both consisted of a zirconia based electrolyte (~170  $\mu\text{m}$  thick), a nickel based anode, and a manganite based cathode. The cells were fed at ~15 psig with air on the cathode side and mixtures of hydrogen and nitrogen bubbled through water on the anode side. Cell temperature was maintained with furnaces controlled by a LabVIEW™ (National Instruments) program. Furnaces were cooled down to 500°C during long intervals between tests (i.e. overnight) to minimize cell aging.

The button cells consisted of an 8  $\text{cm}^2$  disc of electrolyte onto either side of which 2  $\text{cm}^2$  electrodes had been brushed. A small reference electrode of the same material as the corresponding electrode was brushed on both sides of the electrolyte near the

electrode, as depicted in Fig. 7.1. Button cell anodes were infiltrated with one of two catalysts, which will be referred to as 'A' and 'B'. Cells were tested using a Solartron Analytical 1255A frequency response analyzer in conjunction with a Schlumberger SI-1286 potentiostat/galvanostat. The test was controlled and data were recorded through a LabVIEW™ program. Separate spectra were acquired galvanostatically for the anode, cathode, and total-cell at a given current. In each case, the system was perturbed with a sinusoidal wave with amplitude of 5 mV over a spectrum of 1.0 Mhz to 10 mHz. The independent variables studied were cell current, cell temperature, and anode feed composition. Gas mixtures were altered using rotameters upstream from the water bubbler maintaining a total flow of 29 SCCM. The total flow was chosen to be three times the stoichiometric quantity required for the maximum current tested to limit gaseous mass transport effects. Outlet gas compositions were measured with a molecular sieve column in an Agilent 3000A gas chromatograph and analyzed with Agilent's Cerity Network Data System software. Inlet compositions were assumed to be equal to those of the outlet at open circuit.

The planar stack consisted of five cells, each with an electrode area of 61 cm<sup>2</sup> (Fig. 7.2). The stack was fed with 1.5 SLPM air and 2.2 SLPM differing anode mixtures of hydrogen and nitrogen bubbled through water. Anode inlet compositions were measured using the same Agilent system as before. Stack temperature was regulated to be 800°C using a similar furnace and LabVIEW™ program as in the button cell tests. Impedance spectra were measured with an FC350™ potentiostat (by Gamry Instruments) in conjunction with a TDI-Dynaload® RBL488 programmable load. Data were acquired at different stack currents for the cells on both ends of the stack (cell #s 1 and 5) and the



middle cell (cell #3), as well as for the entire stack. The sinusoidal waves were generated galvanostatically with currents producing a maximum potential amplitude of 5 mV (35 - 140 mA RMS depending on the operating DC current). All spectra collected from either cell size were fitted to equivalent circuits with Gamry's Echem Analyst software using the Levenberg-Marquardt algorithm.

### **VII.3. Results and Discussion**

Impedance data were analyzed in terms of equivalent circuits based on assumed reaction mechanisms. Anode and cathode data were fitted to their respective circuits to determine how each was affected by the experimental variables. Total-cell equivalent circuits were then based on a combination of the anode and cathode models. The button cell analyses were then applied to the fuel cell stack and cells therein.

#### *VII.3.1. Button Cells*

The button cell measurements were essential to perform before testing the full-sized cells, because conditions are stable and the electrodes can be measured separately. The picayune nature of the button cell minimized temperature and current distribution over the active surface. Of even greater significance was the ability to use a reference electrode on the button cells in order to separately test anode from cathode. Installing reference electrodes in a stack proves difficult, except for the cells at either end of the stack. Cathode and anode data were analyzed separately, before the measured total-cell impedance was tested against the total anode and cathode circuits connected in series.

### VII.3.1.1. Anode

The overall anode reaction in an SOFC fed with hydrogen is the hydrogen oxidation reaction (HOR):



Many researches [3, 5, 14, 15] have proposed different reaction mechanisms by which this reaction proceeds; however, no general consensus has been achieved. Normally, it is preferable to derive the frequency response of the impedance of an electrochemical reaction from species mass balances [16, 17] and then to choose an equivalent circuit model, the impedance of which has the same time dependence. Because several mechanisms are possible for the HOR (each with a different frequency dependent impedance), the equivalent circuit is chosen based on the experimental data.

Impedance spectroscopy was applied to button cell anodes with varying DC current, cell temperature, hydrogen concentration, and catalyst composition. Each is expected to vary the cell kinetics, which in turn increases or decreases the impedance depending on the experimental variable. Diluting the hydrogen feed increases cell impedance, because the potential energy available for the reaction has diminished from that of a pure feed at a similar current. The complex plane plots in Fig. 7.3 depict the expected trend. The shape of the curves is consistent with the rest of the data obtained for other experimental variables consisting of three “loops”. If the large, high frequency semicircle is ascribed to charge-transfer, then the low frequency arcs are likely related to adsorbed intermediates or mass transfer. Assuming the former, the frequency response of impedance can be assumed to be similar to that of the equivalent circuit model [18] in Fig. 7.4. Because of inductance in the test leads, an inductor is also added in series to the

circuit to obtain the fits. The reasoning behind the assumptions of the anode model will be elucidated throughout the discussion of the data and fits.

Anodes were tested, on which two different catalysts ('A' and 'B') with similar compositions were infiltrated, except that one of the components of 'B' bonds strongly with oxygen. The most obvious difference in the fits of the two is that of the charge double layer (Table 7.1). A constant phase element (CPE) with impedance

$$Z_{CPE} = 1/Q_0(j\omega)^\alpha \quad (7.2)$$

commonly replaces  $C_d$  for solid electrodes [20], which is necessary for adequate fits of the data obtained from 'A'. The frequency response of the HOR on 'B', however, exhibits no depression angle ( $\alpha = 1$ ) behaving as a pure capacitor. The general cause for CPE behavior is thought to be either surface inhomogeneity or surface roughness [21]. Because there is unlikely to be much difference in surface roughness between the anodes infiltrated with 'A' than those with 'B', the cause for the CPE behavior is likely the distribution of reaction rates (or lack thereof) due to the degree of homogeneity of the surface on which the charge-transfer reaction occurs. The purely capacitive behavior of 'B' indicates that charge-transfer occurs on a homogenous surface. Coupled with the decrease in  $R_{ct}$  of 'B' with respect to 'A' at the same conditions, the behavior suggests that the charge-transfer step(s) proceeds on the surface of 'B'. Since a component of 'B' bonds strongly with oxygen, oxygen spillover [3] is the probable charge-transfer step



The reaction mechanism on 'A' is not clear from the present analysis; however, the similar shape of the Nyquist plots (Fig. 7.4) of the two suggests that they follow the same

process, but on different surfaces. It should be further noted that the values for  $C_d$  and  $C_{d,ave}$  are higher than those typically reported ( $30 \mu\text{F cm}^{-2}$ ) for smooth electrodes [22] because of the increased real surface area from the geometric area. Increased electrode area on the order of 1000 is common for porous electrodes [23] and is consistent with the values reported herein.

Equivalent circuit model fits are listed for different temperatures in Table 7.2, which demonstrates that  $R_{\Omega}$  and  $R_{ct}$  decrease with increasing temperature. Heating a cell typically decreases impedance by increasing the kinetic thermal driving force of the reaction exponentially according to an Arrhenius relationship ( $\sim \exp(-K/T)$ ), which is particularly evident in the high temperatures required for operating SOFCs. Temperature also increases the diffusivity of reactants in both gas and solid phases, but by different mechanisms. In the gas phase, an increase in temperature increases the average molecular kinetic energy of the gas improving diffusivity (see also Eq. 7.4). Mass transfer effects in the electrolyte are evident in its conductivity, because the increase in thermal energy increases the ion mobility by narrowing the energy barrier that must be overcome to “jump” between lattice sites. Since reactant diffusivity is improved in all phases at higher temperatures, reactant concentrations should be higher reducing impedance. Both the kinetic and ion conduction trends are apparent in the data fits, specifically in the variation of  $R_{\Omega}$  and  $R_{ct}$  with temperature.

Another aspect of the model that can be tested by temperature variation is the positive low frequency loop, fitted by  $R_{\theta}$  and  $C_{\theta}$ . Many researchers attribute this behavior to gaseous mass transfer [4-6, 9, 10, 24], which is primarily Knudsen

$$D_{KH} = 97.0\bar{F}\sqrt{T/m_H} \quad (7.4)$$

in the studied electrodes, indicating that the mass transfer resistance should be less at higher temperature. While the value of  $R_\theta$  follows the expected trend at open circuit potential in Table 7.2, the value at a current density of  $175 \text{ mA cm}^{-2}$  exhibits the opposite; thus, the expected variation of  $R_\theta$  with polarization needs to be investigated to determine the cause of the low frequency loop. Increasing polarization increases current (reactant flux) thereby depleting reactant concentrations near the electrode surface and increasing mass transfer resistance. Furthermore, if the low frequency “shoulder” of the Nyquist plot was due to mass transfer, its impedance would dominate the inductive adsorption effects at the lowest frequencies. Since mass transfer is not the cause of the positive low frequency loop, then it must be related to a sorption step [6, 11, 12].

The behavior of the anode  $R_{ct}$  at various polarization levels is inconsistent in following the expected trend. Typically, cell impedance is decreased with increasing polarization (current), because the energy required to surmount the activation barrier is most at low overpotentials. Table 7.2 shows that  $R_{ct}$  increases when the DC current is raised from  $175$  to  $300 \text{ mA cm}^{-2}$ , although the other listed values behave as anticipated. A possible explanation is that reactant partial pressure at the interface is decreased as products are formed at a faster rate by the increased cell current. This would explain why  $R_{ct}$  does not deviate from the expected trend with increasing current, until the current is sufficiently high. Unfortunately, not enough current levels were tested to verify to establish a more defined relationship with respect to  $R_{ct}$ .

### VII.3.1.2.Cathode

In a solid oxide fuel cell, the half reaction occurring at the cathode is the oxygen reduction reaction (ORR):



The literature contains several different proposed mechanisms by which the ORR may proceed [13, 25-27]. Assuming a simple reaction mechanism [21, 26] of



and negligible mass transfer, a common equivalent circuit for reactions consisting of one adsorbed intermediate [21] may be derived (Fig. 7.5). Similar to the anode fits for catalyst 'A', a CPE replaces  $C_d$  for all of the cathode fits. CPE behavior is expected, because of the variety of surfaces on which oxygen can react. Some researchers [28, 29] have proposed reaction mechanisms in which oxygen competitively adsorbs on the electrode or electrolyte, before diffusing along the respective surface to the triple phase boundary. A distribution of adsorption rates results from the inhomogeneous reaction surface, which is one of the scenarios under which CPE frequency dependence exists [19]. After replacing the  $C_d$  with a CPE, the single intermediate equivalent circuit model was fitted to the cathode data to determine values for the electrical components.

Data were obtained for the cathode at different temperatures and load currents to which the cathode equivalent circuit elements were fitted. The model is well fitted to the data (Fig. 7.6), which appear on a Cole-Cole plot as a depressed semicircle with a significantly smaller low frequency arc than that of the anode. The temperature

dependence of the cathode impedance appears similar to that of the anode, decreasing as the thermal energy in the system is increased. The cathode impedance also exhibits a similar dependence to the cell current (Table 7.3) as the anode. Both of these effects have been discussed in detail in the previous section; hence, no further explanation is necessary.

As with the anode, low frequency arcs are typically attributed to mass transport or adsorption. Deseure et al. [24] show in their impedance simulations that spectra with small low frequency arcs are possible depending on the diffusion coefficient, electrode porosity, and grain size. Other researchers have measured cathode impedance spectra with the same shape as those presented here with Huang [30] attributing his low frequency arcs to pore diffusion and Oishi et al. [31] relating their high frequency loop to the grain boundary and their low frequency loop to the interface. If mass transfer is the cause of the low frequency behavior, then  $R_\theta$  should be related to the mass transfer resistance. In such a case,  $R_\theta$  would increase with increasing current, which is the opposite of the trend of the fits at 800°C (see Table 7.3). Oishi et al.'s explanation of the high frequency loop being due to the grain boundary cannot be applicable to the present case, because of the large deviation in its impedance with respect to varying load currents. The low frequency arc is likely related to adsorption; however, its contribution to the impedance of the system is small enough to be neglected without compromising the accuracy of the other fitted variables. Its inclusion is simply to aid in determining the ORR mechanism and to ensure that each loop in the data is fitted.

### VII.3.1.3.Total-Cell

The frequency dependent impedance was measured between the anode and cathode under each of the same conditions listed for the prior tests. The full cell equivalent circuit is typically that of the anode added in series with the cathode, wherein the Ohmic contributions are combined into a single resistor with some deviance from the actual sum due to the electrolytic contribution occurring through-plane. Such an arrangement would theoretically be well fitted to total-cell data assuming its spectrum is comparable to the sum of the individual electrode spectra at the same conditions; however, Fig. 7.7 depicts a large arc dominating the low frequency data from the full cell. The extraneous arc is not unique to the button cells and exists in the larger cell spectra (Fig. 7.8) as well, albeit with an abscissa shifted to a higher frequency.

To aid the identification of the process responsible for the low frequency impedance arc, the data have been fitted to two different equivalent circuits. Both models consist of the cathode and anode equivalent circuits used for the single electrode fits in series and fixed to the previously obtained values. A single  $R_{\Omega}$  is in series with both circuits along with an  $L$  for lead inductance (as in the previous models). To fit the low frequency loop, a parallel resistor and capacitor were added in series to one of the circuits, while a finite diffusion element (FDE) was added to the other. The impedance of the FDE is approximated as [32]

$$Z_{FDE} = \left(1/Y_0\sqrt{j\omega}\right) \tanh\left(B\sqrt{j\omega}\right) \quad (7.8)$$

where



$$Y_0 = \frac{(nF)^2 A}{R_{ig} T} \left( \sum \frac{1}{c_i \sqrt{D_i}} \right)^{-1} \quad (7.9)$$

and

$$B = \delta / \sqrt{D_i} \quad (7.10)$$

Table 7.4 lists fitted values of the low frequency elements which may help illuminate the cause of the extra loop. The additional set of  $Y_0$  and  $B$  in Table 7.4a proves that their values are only slightly altered when the elements are instead arranged in series with the Faradaic impedance of the anode or cathode. The same relationship can be inferred for  $R_{lf}$  and  $C_{lf}$  because of the similar shape of their impedance on a Nyquist plot to that of an FDE. The consistent fits for the additional parallel  $RC$  or FDE is significant, because information can be inferred from their values without knowing the location of the limiting process *a priori*.

Recalling the earlier discussions related to low frequency loops, their possible causes are adsorption, mass transfer, or the grain boundary. Because the loop does not exist in either anode or cathode spectra, it must be due to an electrolytic process or one that occurs to an equal extent at the respective reference electrode as at the working. Only reactant concentration and grain boundary effects may occur to similar extents at both the working and reference electrode in the studied arrangement; hence, sorption is not the source of the low frequency arc. The grain boundary is also not likely to be the cause of the low frequency loop, because its effects are typically observed at a higher frequency than that of charge-transfer [33]. Furthermore, fitted values of  $C_{lf}$  are far too large to be associated with the grain boundary or charge-transfer (if the grain boundary was assumed to be related to the high frequency loop). The high frequency arc has

already been shown to be theoretically well explained with charge-transfer (see section VII.3.1.1); hence, grain boundary effects are absent from the measured data, and mass transport is the probable cause of the extraneous impedance loop.

The impedance of mass transfer by diffusion is quantified by the fitted values of the FDE, which respond as expected to variations in temperature and reactant concentration. Heating the cell imparts more thermal energy to the system facilitating mass transport and decreasing impedance (or increasing diffusivity). Recalling the dependence of Eq. 7.8 and Eq. 7.9 on diffusivity verifies the change in  $Y_0$  and  $B$  in the fits with respect to temperature at the same cell current and reactant concentration (Table 7.4a). The relationship between  $Y_0$  and reactant concentration is more straightforward, increasing impedance as the feed is diluted with inert gas as explicitly shown in Eq. 7.8 and verified in Table 7.4b. The approximately constant value of  $B$  with respect to changing hydrogen concentration and cell current is also as expected, as they are variables not expected to appreciably alter  $D_i$  or  $\delta$ .

Justifying the assignment of the low frequency arc to diffusion is more difficult when considering its behavior with respect to load current and the paucity of a corresponding curve in the anode or cathode data. The former is simpler to explain, when the current dependence of the potential difference between the anode and cathode reference electrodes (Fig. 7.9) is considered. If the concentrations of all of the reactants at the references are constant, then the potential difference between the two should be independent of the current through the cell. The curves plotted in Fig. 7.9 indicate that concentration in fact varies at the reference surface. The absence of the mass transfer arc from anode or cathode impedance spectra is then justified as existing at working and

reference electrode to the same extent, thus cancelling each other out in the single electrode measurements. The behavior of  $Y_0$  with varying load current is more difficult to explain, because its expected behavior is the opposite of what is observed. As the reactant mass flux to the interface (or load current) is increased, the hydrogen concentration is decreased corresponding to an increase in the total impedance of the cell (including that of mass transfer). The data clearly demonstrate that the low frequency impedance instead decreases as more load current is passed through the cell. Such behavior is predicted by Eq. 7.9 if water concentration is considered, because its value is increased from its low initial value. High mass transfer impedance at low current is also observed in lanthanum strontium manganese oxide (LSM) electrodes, which are known to be poor ion conductors at low overpotentials [25]. Impedance spectra obtained for thin, dense LSM films on yttria stabilized zirconia [34] have abscissa in a similar frequency regime as depicted in the present study for the total-cell. These arcs have been attributed to oxide (or vacancy) diffusion through the film, as confirmed by the shift of the abscissa frequency at differing film thicknesses. Even though the cathode of the Ceramtec cells is not composed of LSM, the properties of other manganite based materials could well be similar.

Since mass transfer is the best explanation for the low frequency loop in the total-cell impedance spectra, the FDE is a better choice to add to the circuit than the parallel combination of  $R_f$  and  $C_f$ . As expressed in Eq. 7.9,  $Y_0$  is composed of contributions from each reactant. An exact representation of the total-cell equivalent circuit would include a cathode FDE in series with the Faradaic cathode impedance, as well as a similar arrangement for the anode. Such a configuration is cumbersome and would complicate

the fitting, because the contributions of anode and cathode mass transfer are superimposed in the data. Recalling that the fitted values for  $Y_0$  and  $B$  are approximately independent of location in the circuit, a single FDE in the circuit is best for data fitting. Further experiments need to be performed with varying oxygen concentration to determine the contribution of each reactant to the values of  $Y_0$  and  $B$ .

It should be noted that factors relating to the test setup may also give rise to unexpected behavior, such as the extra low frequency loop. Studies [35-37] have suggested that bonding a reference electrode to the same face of a solid electrolyte as the working electrode may produce erroneous data under certain circumstances; however, such effects are not likely responsible for the extra arc in the total-cell fits, because none of the referenced studies showed similar low frequency effects. Primdahl et al. observed a low frequency impedance arc related to gas conversion, when the reference electrode was located in a different atmosphere from the working electrode [38]. They proposed that the passage of AC current changes gas concentration at the active surface, most noticeably at low frequencies, resulting in a Nernstian potential loss. Such is not observed when the working and reference electrodes are at the same concentration, which could be the cause of the previously discussed reference  $i-V$  behavior in Fig. 7.9. The possibility of the gas conversion impedance being related to the measured total-cell spectrum is investigated in the next section, because the entire low frequency loop is better resolved in the full sized cell measurements (Fig. 7.8).

Cathode behavior would be expected to be independent of anode feed composition; however, the fits predict that the cathode impedance varies slightly with decreased hydrogen concentration. Unfortunately, cathode data were not individually

measured for the diluted anode feeds, because the anode impedance and its effect on that of the total-cell were the primary foci of the tests. Fig. 7.10 shows plots of the cathode fits with varying anode reactant. The fits are only slightly altered, but the variation is consistent. Cathode impedance could change due to the decrease in the electric field between the electrodes, which may change a number of variables enough to affect the cathode kinetics. Equally plausible is that it is an artifact of the inaccuracies inherent in the model, unstable cell conditions, or equipment precision. Only by measuring the cathode impedance spectrum with varying anode reactant concentration may the cause of the behavior be determined. Although the reason for the cathode impedance's dependence on hydrogen concentration is unknown, it is also observed in the fits of the larger fuel cell stacks.

### *VII.3.2. Fuel Cell Stack*

The circuit models and the variation of their fitted values with respect to hydrogen concentration, load current, and cell temperature of the button cell tests were applied to the analyses of the larger fuel cell stacks. Ideally, the frequency dependent impedance of the cells in the stack would be the same as that of the button cells at similar test conditions, only scaled to a different size; however, larger electrochemical cells are inherently non-ideal. Due to the sheer size of the cells, the current, temperature, and reactant concentration are distributed along the active surface. Additionally, the arrangement of the cells in the stack can result in further disparities in temperature and concentration between different cells. The aforementioned problems are compounded by the consistency in manufacturing the constituents of the stack and their inevitable

degradation over time. AC impedance performed at load is a significant technique for evaluating the nonidealities inherent in fuel cell systems.

In order to fit the data obtained from the planar cells, a simpler equivalent circuit than that of the button cells is necessary. While the model given in section VI.3.1.4 is nearly exact, applying the same model to the cell without any foreknowledge of the values of any of the elements is rife with uncertainty. Rather, the simplest model from which accurate fits may be obtained is preferred. From the previous circuit, it would seem the minimum number of elements producing a time constant required to fit the data would be three: a FDE (or parallel low frequency  $RC$ ) and a parallel  $RC$  for both the anode and cathode. Fig. 7.8 shows that the three time constant model is too simple, needing a fourth time constant to fit the data more exactly. The added elements are ascribed to anode adsorption, because its affect on cell impedance is the next most significant in the button cell tests behind the three already included; hence, it is in series with the Faradaic impedance branch of the anode in the large cell equivalent circuit model depicted in Fig. 7.11. It should be noted that  $C_d^c$  is not replaced with a CPE in the large cell model, because the relatively small size of the superimposed activation loops is such that the fitting algorithm would fit another part of the curve with the anode  $RC$ . Additionally, distributed elements are not preferred in a model to be used for designing process controls and power conditioning systems. The FDE has already been shown (section VII.3.1.4) to be easily replaced with a parallel  $RC$  without sacrificing much accuracy to accommodate the aforementioned purpose, so it is retained for the time being.

Generally, the large cell equivalent circuit fitted values exhibited trends consistent with previously discussed theory. Table 7.5 demonstrates the same effects of hydrogen dilution as observed in the button cells: as hydrogen concentration is decreased,  $R_{ct}^a$  is increased, while  $R_{ct}^c$  and  $Y_0$  (congruent with  $C_d$ ) are decreased. The approximately constant  $B$  is also significant, because it is confirmed by the notion that  $\delta$  and  $D_i$  are unchanged in these tests. The negative values of  $R_\theta$  and  $C_\theta$  indicate that the inductive behavior of anode adsorbed intermediates is more significant than the capacitive portion. The same fits could be obtained without negative values, if the parallel  $RC$  was replaced with a series  $RL$  moved to be in parallel with the anode  $R_{ct}$  [39]. Table 7.6 shows  $R_{ct}^a$  decreasing with current of each examined cell, which is more theoretically accurate than the behavior of the button cells.  $R_{ct}^c$ , on the other hand, has a maximum at  $52 \text{ mA cm}^{-2}$ . The variation of the FDE is slightly different than with the button cells, although the two were not tested over similar current ranges.  $Y_0$  proceeds as expected between the low and medium currents, but decreases from medium to high current indicating increased mass transfer resistance. The size of the cell likely contributes the difference between the button and larger cells, because reactant depletion at the cell outlet is more prevalent at higher currents and expected to have a more deleterious effect on larger cells. Variation in  $B$  at low current is consistent with button cell measurements and will be discussed in greater detail later.

Ideally, area specific impedances should be approximately equal between button cells and large cells; yet, nonuniformity of different processes in larger cells prevents this theory from being well observed. The ratio between the fitted values (Table 7.7) quantifies the difference comparing the two sizes of fuel cells fitted to the same

equivalent circuit. One of the most significant factors limiting ideal scalability is reactant distribution. The larger an electrode, the more locally variant is the reactant concentration. Since kinetics is driven by concentrations of reactants and products, the reaction rate (electric current) is more unevenly distributed in a larger cell. Compounding the issue is pressure drop, which affects gas concentrations and exists to a greater degree in larger cells. While impedances do not scale perfectly from the button cells to the full sized cells, they are close enough to provide a reasonable starting point for fitting the data and for analyzing which process governs each circuit element.

For the specific cells in this study, the thicknesses of the mixed conducting layer of the electrodes were significantly different from the button cells in the previous section. The total thickness (including mixed conducting components) for the large cell anode and cathode is approximately 52-55  $\mu\text{m}$  and 77-80  $\mu\text{m}$ , respectively, compared to 307-358  $\mu\text{m}$  and 347-398  $\mu\text{m}$  for the button cell. This difference corresponds to a large difference in the ratio of real surface area to geometric area of the electrodes, which is another factor that makes scaling resistances and capacitances between the two sizes difficult. More significant is the effect on mass transfer that thinner electrodes impose, which is visually evident in the low frequency semicircle being fully resolved for the large cell impedance compared to that of the button cells over the same frequency spectrum. The shift of the abscissa frequency is quantified by the  $B$  parameter of the FDE, which changes due to the diffusion layer thickness. Since diffusivity is far less in solids than gases, oxygen ion (or vacancy) diffusion in the cathode is assumed to be predominant. The ratio of  $B$  of the button cells (from the more accurate model fits) to that of the large cell is approximately four, which is quite close to the ratio of the cathode thicknesses (4.33-5.16). The reason



the ratio is not exactly within the expected range is due to the approximation of combining all of the reactants into the form of Eqs. 7.8-10 (see [21] for an exact expression).

Another issue that obscures the true nature of scaling electrodes is the temperature distribution within the stack. Fuel cell reactions are highly exothermic, such that the reactions heat the stack above the surrounding temperature. Depending on how well the outer cells of a planar stack are thermally insulated, one would expect them to be at a lower temperature than those with less surface area in contact with the environment. In the stack under investigation, cell #3 is in the middle of the stack flanked by cell #s 1 and 5 on the outsides. The two outside cells are not identical, with cell #5 having a thermally insulating layer adjacent to the outer wall that is unique to it. Because the temperature of cell #1 is lower than the other cells in the stack, it lacks the thermal energy necessary to drive the reaction as fast, thus limiting performance in a stack of cells connected in series. One need not know the geometry of the system to deduce that cell #1 is at a lower temperature than the others; such can be deduced from the model fits. While increased  $R_{ct}$ s may indicate a decreased temperature, the trend may also be induced by inconsistent electrode microstructure, catalyst loading, and/or reactant concentration. Coupling the  $R_{ct}$  behavior with the increase in  $R_{\Omega}$  and  $B$  for cell #1 relative to the other cells proves the root of the problem, because decreased electrolyte conduction and diffusivity are indicative of lower temperatures. The analyses of the fitted large cell data show how impedance spectroscopy can be used to mechanistically discriminate the factors that limit stack performance.

In section VII.3.1.4, the low frequency impedance loop of the total-cell was discussed without considering the possibility of gas conversion being the cause. Primdahl et al. modeled similar low frequency arcs with a parallel  $R_{lf}$  and  $C_{lf}$  in series with the electrode equivalent circuit (similar to the fits described in the previous section) and approximately replicated the fitted values with a constantly stirred tank reactor (CSTR) model yielding the following relationships: [38]

$$R_{lf} = \frac{R_{ig} T}{(2F)^2 J} \left( \frac{1}{x_w} + \frac{1}{x_H} \right) \quad (7.11)$$

$$C_{lf} = \frac{4F^2 P_V}{(R_{ig} T)^2 A} \left( \frac{1}{x_w} + \frac{1}{x_H} \right)^{-1} \quad (7.12)$$

where the resistance and capacitance are area specific. Applying the proposed model to the cells in question shows that gas conversion may be partially responsible for the extra arc. While a 61 cm<sup>2</sup> planar cell is expected to deviate from a single tank CSTR model due to the previously discussed distributed conditions, the general variation of impedance with each of the independent variables should be unchanged. Increases in cell current, temperature, or hydrogen concentration predict that  $R_{lf}$  should decrease and  $C_{lf}$  should increase, a tendency observed in the button cell fits in Tables 7.4a and 7.4b. The fits to the larger cells listed in Tables 7.8a and 7.8b, on the other hand, show only  $C_{lf}$  obeying the same trend as the button cells, when concentration and temperature are the experimental variables. The difference in the variation of the fits with respect to changes in current is likely caused by the difference between inlet and outlet gas concentrations being greater than in the linearization criterion of the derivation of Eq. 7.11 and 7.12 [38]; however, the same reason does not apply to the fits at differing gas concentrations

and temperatures, because they were fitted to data obtained at a low enough current for the linearization criterion to be valid. Furthermore, increasing current tends to raise the stack temperature, the effects of which are opposite regarding mass transfer and gas conversion impedance. Fluctuations in  $R_{lf}$  with respect to temperature could also be different than expected due to nonuniform flow distribution, which induces an increase in  $R_{lf}$  and a decrease in  $C_{lf}$  as demonstrated in Table 7.8c. The relationship between gas conversion impedance and  $J$  has been demonstrated experimentally by Momma et al., who applied it to determine the flow distribution through a 46-cell stack [40]. Whether the low frequency arc is due entirely to gas conversion is not conclusive enough to apply the same method to test the flow distribution in the Ceramatec stack.

Neither gas conversion nor mass transfer is likely to exclusive cause the low frequency impedance loop. The two can scarcely be distinguished from the appearance of the arc, because a parallel  $RC$  and FDE are similarly shaped on a Nyquist plot as evident in the  $\chi^2$  values of the fits. The functionality of Eqs. 7.9 and 7.11 indicates that  $R_{lf}$  and  $Y_0$  will often vary inversely; however, such a relationship is not always observed in the values listed in Table 7.8. The correlation between fitted values and changes in hydrogen concentration or temperature are more congruent with mass transfer, while gas conversion better explains that of gas flow rate. The effects of gas conversion and mass transfer are most likely present concurrently being superimposed as an arc in the low frequency region of a Nyquist plot.

Data for the entire fuel cell stack were also obtained under the same test conditions as the single cell tests previously described. Fig. 7.12 depicts some of the obtained curves, each of which is similar in shape to the individual cells; hence, the same

equivalent circuit that was fitted to the cell data may be similarly applied to the full cell data. While the individual cell tests were designed to determine which processes limit cell output and to what degree, the full cell test is intended to obtain a simple, purely electronic model to replicate the dynamic response of the stack. To make the model purely electronic, the FDE of the equivalent circuit has been replaced with a parallel  $RC$ . Obtaining fits for the circuit elements over the expected range of operation allows for the stack to be dynamically modeled over said range. The utility in eliminating all distributed elements from the model is to facilitate circuit simulation, which can be used to design process controls and to assess the optimum setup of operating conditions, power conditioning systems, and combination of multiple stacks.

#### **VII.4. Conclusions**

In the work presented, impedance spectroscopy was successfully applied to solid oxide fuel cells and stacks at different operating conditions. Equivalent circuit models were proposed for the cell based on data obtained for each electrode. The models were fitted to the data to determine which physical processes limit cell performance and to what degree. The equivalent circuit models for each electrode consisted of a charge-transfer time constant and two or one adsorptive time constants for the anode and cathode, respectively. An additional time constant exists at low frequency in the total-cell data, which is related to mass transfer and gas conversion. A simplified version of the total-cell model was applied to the cells in a five cell stack. The cause for an underperforming cell in the stack was attributed to temperature, based on a comparison with the data from other cells. The entire fuel cell stack was fitted to a model similar to

that of the single cells, only with distributed elements replaced with physical electrical elements. The stack circuits may be used to model its dynamic behavior to facilitate system design. The work contained herein is useful for assessing in-situ stack dynamics, stack aging, state of health, system controls, component fabrication, and quality control.

### VII.5. Acknowledgements

I would like to thank Dr. S. Elangovan, Mark Timper, Dennis Larsen, Lyman Frost, Anthony Nickens and everyone else at Ceramatec Inc. who helped make this project possible. I would also like to thank Dr. Jeffrey W. Fergus for his help with understanding solid state electrolytes. Additionally, I would like to recognize Ronald Putt for his knowledge of electrochemistry and for proofreading this manuscript.

### VII.6. Nomenclature

| <b>Roman Letters</b>  | <b>Definition</b>  |
|-----------------------|--|
| <i>A</i>              | Area   |
| <i>C</i>              | Capacitance  |
| <i>c</i>              | Concentration  |
| <i>D</i>              | Diffusivity  |
| <i>e'</i>             | Electron   |
| <i>F</i>              | Faraday's constant   |
| <i>J</i>              | Flow rate per area of electrode                                    |
| <i>j</i>              | Imaginary constant (-1) <sup>-5</sup>                              |
| <i>i</i>              | Current density  |
| <i>L</i>              | Inductance   |
| <i>M</i>              | Free metal site  |
| <i>m</i>              | Molar mass   |
| <i>n</i>              | Stoichiometric number of electrons involved in a chemical reaction |
| <i>P</i>              | Pressure   |
| <i>Q<sub>0</sub></i>  | CPE constant   |
| <i>R</i>              | Resistance   |
| <i>R<sub>ig</sub></i> | Ideal gas constant   |
| $\bar{r}$             | Average pore radius (in m)   |

|     |   |
|-----|---|
| $V$ | Vacancy                                   |
| $v$ | Volume of CSTR                            |
| $T$ | Temperature (in K unless otherwise noted) |
| $x$ | Mole fraction at inlet                    |
| $Z$ | Impedance                                 |

### Greek Letters

|          |  |
|----------|--|
| $\alpha$ | Constant ( $0 \leq \alpha \leq 1$ ) related to departure from pure capacitor |
| $\delta$ | Diffusion layer thickness  |
| $\omega$ | Angular frequency  |

### Subscripts

|          |  |
|----------|--|
| $ad$     | Adsorbed species                               |
| $ct$     | Charge-transfer                                |
| $d$      | Double-layer                                   |
| $H$      | Hydrogen                                       |
| $i$      | Species  |
| $K$      | Knudsen (in $\text{m}^2 \cdot \text{s}^{-1}$ ) |
| $L$      | Related to Adsorption                          |
| $lf$     | Low frequency                                  |
| $M$      | Metal surface                                  |
| $w$      | Water  |
| $\theta$ | Related to Adsorption                          |
| $\Omega$ | Ohmic  |

### Superscripts

|           |                 |
|-----------|-----------------|
| $a$       | Anode           |
| $c$       | Cathode         |
| $\times$  | Neutral charge  |
| $\bullet$ | Positive charge |

## VII.7. References

- [1] Rasmus Barford, Mogens Mogensen, Trine Klemensø, Anke Hagen, Yi-Lin Liu, Peter Vang Hendriksen, *J. Electrochem. Soc.*, 154 (2007) B371–B378.
- [2] A. Bieberle, L. P. Meier, and L. J. Gauckler, *J. Electrochem. Soc.*, 148 (2001) A646–A656.
- [3] A. Bieberle, L. J. Gauckler, *Solid State Ionics*, 146 (2002) 23–41.
- [4] Darja Kek, Mogens Mogensen, Stane Pejovnik, *J. Electrochem. Soc.*, 148 (2001) A878–A886.

- [5] Wolfgang G. Bessler, *J. Electrochem. Soc.*, 153 (2006) A1492–A1504.
- [6] Haruo Kishimoto, Katsuhiko Yamaji, Teruhisa Horita, Yue-Ping Xiong, Natsuko Sakai, Manuel E. Brito, Harumi Yokokawa, *J. Electrochem. Soc.*, 153 (2006) A982–A988.
- [7] A. Mary Sukeshini, Bahman Habibzadeh, Benjamin P. Becker, Chad A. Stoltz, Bryan W. Eichhorn, Gregory S. Jackson, *J. Electrochem. Soc.*, 153 (2006) A705–A715.
- [8] Yixiang Shi, Ningsheng Cai, Chen Li, Cheng Bao, Eric Croiset, Jiqin Qian, Qiang Hu, Shaorong Wang, *J. Power Sources*, 172 (2007) 235–245.
- [9] Yixiang Shi, Ningsheng Cai, Chen Li, Cheng Bao, Eric Croiset, Jiqin Qian, Qiang Hu, Shaorong Wang, *J. Electrochem. Soc.*, 155 (2008) B270–B280.
- [10] M. J. L. Østergård, M. Mogensen, *Electrochimica Acta.*, 18 (1993) 2015–2020.
- [11] F. Mauvy, C. Lalanne, S. Fourcade, J. M. Bassat, J. C. Grenier, *J. Euro. Ceram. Soc.*, 27 (2007) 3731–3734.
- [12] S. P. Jiang, S. P. S. Badwal, *J. Electrochem. Soc.*, 144 (1997) 3777–3784.
- [13] P. Holtappels, I. C. Vinke, L. G. J. de Haart, U. Stimming, *J. Electrochem. Soc.*, 146 (1999) 2976–2982.
- [14] Huayang Zhu, Robert J. Kee, Vinod M. Janardhanan, Olaf Deutschmann, and David G. Goodwin, *J. Electrochem. Soc.*, 152 (2005) A2427–A2440.
- [15] V. N. Chebotin, M. V. Glumov, A. D. Neuimin, S. F. Palguyev, *Sov. Electrochem. Soc.*, 7 (1971) 55–61.
- [16] David A. Harrington, *J. Electroanal. Chem.*, 449 (1998) 9–28.
- [17] H. Kuhn, B. Andreaus, A. Wokaun, G. G. Scherer, *Electrochimica Acta.*, 51 (2006) 1622–1628.
- [18] D. B. Zhou, H. Vander Poorten, *J. Electrochem. Soc.*, 145 (1998) 936–945.
- [19] G. J. Brug, A. L. G. Van Den Eeden, M. Sluyters-Rehbach, J. H. Sluyters, *J. Electroanal. Chem.*, 176 (1984) 275–295.
- [20] J. Ross Macdonald, Donald R. Franceschetti, in: J. Ross Macdonald (Ed.), *Impedance Spectroscopy*, John Wiley and Sons, Inc., New York, pp. 90–95.

- [21] A. Lasia, in: B. E. Conway, J. O'M. Bockris, R. E. White (Eds.), *Mod. Asp. Electrochem.*, 32, Kluwer Academic / Plenum Publishers, New York, 1999, pp. 143–242.
- [22] Ryan P. O'Hayre, Suk-Won Cha, Whitney Colella, Fritz B. Prinz, *Fuel Cell Fundamentals*, John Wiley and Sons Inc., New York, p.214.
- [23] James Larminie, Andrew Dicks, *Fuel Cell Systems Explained*, John Wiley & Sons Inc., New York, 1998, p. 44.
- [24] J. Deseure, Y. Bultel, L. Dessemond, E. Siebert, P. Ozil, *J Applied Electrochem.*, 37 (2007) 129–136.
- [25] Stuart B. Adler, *Chem. Rev.*, 104 (2004) 4791–4843.
- [26] Y. M. Choi, H. Abernathy, R. Williams, M. Liu in: S. C. Singhal, J. Mizusaki (Eds.) *Proceedings of the Ninth International Symposium on Solid Oxide Fuel Cells*, The Electrochemical Society Proceedings Series, PV 2005-07 Pennington, NJ (2005) pp. 790–795.
- [27] B. Yildiz, G. Jose la O', Y. Shao-Horn in: S. C. Singhal, J. Mizusaki (Eds.) *Proceedings of the Ninth International Symposium on Solid Oxide Fuel Cells*, The Electrochemical Society Proceedings Series, PV 2005-07 Pennington, NJ (2005) pp. 1509–1520.
- [28] M. Prestat, J. F. Koenig, L. J. Gaukler, *J. Electroceram.*, 18 (2007) 87–101.
- [29] Ann Mari Svensson, Svein Sunde, Kemal Nişancıoğlu, *J. Electrochem. Soc.*, 145 (1998) 1390–1400.
- [30] K. Huang in: S. C. Singhal, J. Mizusaki (Eds.) *Proceedings of the Ninth International Symposium on Solid Oxide Fuel Cells*, The Electrochemical Society Proceedings Series, PV 2005-07 Pennington, NJ (2005) pp. 1561–1570.
- [31] N. Oishi, Y. Yoo, I. Davidson in: S. C. Singhal, J. Mizusaki (Eds.) *Proceedings of the Ninth International Symposium on Solid Oxide Fuel Cells*, The Electrochemical Society Proceedings Series, PV 2005-07 Pennington, NJ (2005) pp. 1645–1651.
- [32] Bob Rogers, Research Solutions and References, 2008, <http://www.consultrsr.com/resources/eis/diff-o.htm>.



- [33] N. Bonanos, B. C. H. Steele, E. P. Butler in: J. Ross Macdonald (Ed.), *Impedance Spectroscopy*, John Wiley and Sons Inc., New York, pp. 191–237.
- [34] Tsutomu Iori, Tatsunori Hara, Yoshiharu Uchimoto, Zempachi Ogumi, Zen-ichiro Takehara, *J. Electrochem. Soc.*, 145 (1998) 1999–2004.
- [35] S. B. Adler, *J. Electrochem. Soc.*, 149 (2002) E166–E172.
- [36] Bernard A. Boukamp, *Solid State Ionics*, 143 (2001) 47–55.
- [37] J. Winkler, P. V. Hendriksen, N. Bonanos, M. Mogensen, *J. Electrochem. Soc.*, 145 (1998) 1184–1192.
- [38] S. Primdahl, M. Mogensen, *J. Electrochem Soc.*, 145 (1998) 2431–2438.
- [39] Chu-Nan Cao, *Electrochimica. Acta.*, 35 (1990) 837–844.
- [40] A. Momma, Y. Kaga, K. Takano, K. Nozaki, A. Negishi, K. Kato, T. Kato, T. Inagaki, H. Yoshida, K. Hosoi, K. Hoshino, T. Akbay, J. Akikusa, M. Yamada, N. Chitose, *Solid State Ionics*, 174 (2004) 87–95.

**Table 7.1.** Fitted equivalent circuit elements for button cell anodes infiltrated with different catalysts. The cells were operating on 97% H<sub>2</sub> and balanced H<sub>2</sub>O at 800°C.

| Catalyst  | 'A'          |              |              |              | 'B'          |              |              |
|---|--------------|--------------|--------------|--------------|--------------|--------------|--------------|
|   | <u>0.000</u> | <u>50.00</u> | <u>175.0</u> | <u>300.0</u> | <u>0.000</u> | <u>175.0</u> | <u>300.0</u> |
| $i$ (mA*cm <sup>-2</sup> )                      | 160.4        | 164.8        | 161.5        | 160.9        | 300.6        | 219.2        | 211.0        |
| $R_{\Omega}$ (mΩ*cm <sup>2</sup> )              | 22.40        | 52.88        | 47.28        | 62.88        | 95.58        | 45.66        | 47.40        |
| $R_{ct}$ (mΩ*cm <sup>2</sup> )                  | 300.6        | 105.1        | 78.05        | 38.86        | 26.97        | 40.93        | 35.88        |
| $Q_0$ (mS*cm <sup>-2</sup> *s <sup>1-α</sup> )  | .5919        | .7992        | .8443        | .8879        | 1.000        | 1.000        | 1.000        |
| $\alpha$  | 25.42        | 8.808        | 9.070        | 21.58        | 45.88        | 5.362        | 4.904        |
| $R_{\theta}$ (mΩ*cm <sup>2</sup> )              | .02854       | .09180       | .1820        | .09290       | 3.423        | 7.295        | 2.606        |
| $C_{\theta}$ (F*cm <sup>-2</sup> )              | 213.6        | 13.74        | 1.359        | 7.248        | -128.2       | -3.146       | -3.234       |
| $R_L$ (mΩ*cm <sup>2</sup> )                     | 706.0        | 61.96        | 30.36        | 75.12        | -264.4       | 13.41        | 6.346        |
| $L$ (mH*cm <sup>2</sup> )                       | 1.272        | 1.966        | 4.186        | 31.00        | 45.84        | 13.21        | 18.91        |
| $\chi^2$ (*10 <sup>-6</sup> ) <sup>a</sup>      | 8.739        | 26.58        | 26.49        | 17.44        | 26.97        | 40.93        | 35.88        |
| $C_{d,ave}$ (mF*cm <sup>-2</sup> ) <sup>b</sup> |              |              |              |              |              |              |              |

<sup>a</sup> $\chi^2$  is the nonlinear least squares residual.

<sup>b</sup> $C_{d,ave}$  is the average capacitance of a CPE computed from the relationship derived by Brug et al. [19].

**Table 7.2.** Fitted equivalent circuit elements for button cell anodes operating on 97% H<sub>2</sub> and balance H<sub>2</sub>O at varying temperature and load current density.

| $T$ (°C)                                   | 750    |        | 800    |        |        |
|--|--------|--------|--------|--------|--------|
|  | 0.000  | 175    | 0.000  | 175    | 300    |
| $i$ (mA*cm <sup>-2</sup> )                 | 394.8  | 347.2  | 300.6  | 219.2  | 211.0  |
| $R_{\Omega}$ (mΩ*cm <sup>2</sup> )         | 97.32  | 72.98  | 95.58  | 45.66  | 47.40  |
| $R_{ct}$ (mΩ*cm <sup>2</sup> )             | 34.97  | 36.56  | 26.97  | 40.93  | 35.88  |
| $C_d$ (mF*cm <sup>-2</sup> )               | 29.78  | 5.940  | 45.88  | 5.362  | 4.904  |
| $R_{\theta}$ (mΩ*cm <sup>2</sup> )         | 8.910  | 2.198  | 3.423  | 7.295  | 2.606  |
| $C_{\theta}$ (F*cm <sup>-2</sup> )         | -75.86 | -3.928 | -128.2 | -3.146 | -3.234 |
| $R_L$ (mΩ*cm <sup>2</sup> )                | -307.0 | 7.526  | -264.4 | 13.41  | 6.346  |
| $L$ (mH*cm <sup>2</sup> )                  | 10.00  | 10.14  | 45.84  | 13.21  | 18.91  |
| $\chi^2$ (*10 <sup>-6</sup> ) <sup>a</sup> |        |        |        |        |        |

<sup>a</sup> $\chi^2$  is the nonlinear least squares residual.

**Table 7.3.** Fitted equivalent circuit elements for button cell cathodes operating on 97% H<sub>2</sub> and balanced H<sub>2</sub>O at varying temperature and load current density.

| <i>T</i> (°C)  | 750   |         | 800   |       |       |
|--|-------|---------|-------|-------|-------|
| <i>i</i> (mA*cm <sup>-2</sup> )                                      | 0.000 | 175     | 0.000 | 175   | 300   |
| <i>R</i> <sub>Ω</sub> (mΩ*cm <sup>2</sup> )                          | 203.2 | 212.2   | 152.7 | 141.9 | 146.5 |
| <i>R</i> <sub>ct</sub> (mΩ*cm <sup>2</sup> )                         | 348.4 | 306.0   | 164.9 | 164.5 | 172.4 |
| <i>Q</i> <sub>θ</sub> (mS*cm <sup>-2</sup> *s <sup>1-α</sup> )       | 29.78 | 23.01   | 21.85 | 23.83 | 27.48 |
| <i>α</i>   | .6523 | .6352   | .7101 | .6979 | .6682 |
| <i>R</i> <sub>θ</sub> (mΩ*cm <sup>2</sup> )                          | 9.340 | 71.68   | 12.67 | 6.310 | 4.240 |
| <i>C</i> <sub>θ</sub> (F*cm <sup>-2</sup> )                          | 67.75 | 0.01056 | 7.50  | 10.12 | 12.47 |
| <i>χ</i> <sup>2</sup> (*10 <sup>-6</sup> ) <sup>a</sup>              | 63.47 | 21.48   | 912.1 | 12.21 | 23.24 |
| <i>C</i> <sub><i>d,ave</i></sub> (mF*cm <sup>-2</sup> ) <sup>b</sup> | 1.531 | .8000   | 1.629 | 1.551 | 1.309 |

<sup>a</sup>*χ*<sup>2</sup> is the nonlinear least squares residual.

<sup>b</sup>*C*<sub>*d,ave*</sub> is the average capacitance of a CPE computed from the relationship derived by Brug et al. [19].

**Table 7.4.** Values for a parallel  $RC$  or a finite diffusion element fitted to the low frequency impedance loops of button cells operating at (a)  $175 \text{ mA}\cdot\text{cm}^{-2}$  with varying temperature and hydrogen feed concentration and (b)  $800^\circ\text{C}$  and varying load current density, fed with  $x_w = .03$ ,  $x_H$  as indicated, and balance  $\text{N}_2$ . Another finite diffusion element fitted in series with the Faradaic impedance is also listed in 4a showing little difference from the series fits.

| a)  |             |             |             |             |             |             |
|---|-------------|-------------|-------------|-------------|-------------|-------------|
| $T$ ( $^\circ\text{C}$ )  | 750         |             |             | 800         |             |             |
| $x_H$   | <u>.970</u> | <u>.637</u> | <u>.473</u> | <u>.970</u> | <u>.455</u> | <u>.331</u> |
| $R_{lf}$ ( $\text{m}\Omega\cdot\text{cm}^2$ )                           | 120.1       | 137.4       | 138.5       | 123.6       | 146.9       | 172.3       |
| $C_{lf}$ ( $\text{F}\cdot\text{cm}^{-2}$ )                              | 51.85       | 41.40       | 40.60       | 88.35       | 78.55       | 58.45       |
| $Y_0$ ( $\text{S}\cdot\text{cm}^{-2}\cdot\text{s}^{1/2}$ )              | 31.25       | 26.13       | 25.66       | 37.98       | 35.56       | 26.76       |
| $B$   | 4.700       | 4.412       | 4.493       | 5.643       | 6.090       | 5.441       |
| $Y_0$ ( $\text{S}\cdot\text{cm}^{-2}\cdot\text{s}^{1/2}$ ) <sup>a</sup> | 31.43       | 26.42       | 25.71       | 40.64       | 33.32       | 27.53       |
| $B^a$   | 4.713       | 4.435       | 4.493       | 5.079       | 5.831       | 5.532       |

<sup>a</sup> Values where the diffusion element is in series with the Faradaic impedance of the cathode and anode for  $750^\circ\text{C}$  and  $800^\circ\text{C}$ , respectively.

| b)   |              |              |              |              |              |              |
|--|--------------|--------------|--------------|--------------|--------------|--------------|
| $x_H$  | .455         |              |              | .331         |              |              |
| $i$ ( $\text{mA}\cdot\text{cm}^{-2}$ )                     | <u>0.000</u> | <u>175.0</u> | <u>300.0</u> | <u>0.000</u> | <u>175.0</u> | <u>300.0</u> |
| $R_{lf}$ ( $\text{m}\Omega\cdot\text{cm}^2$ )              | 620.4        | 146.9        | 100.0        | 638.8        | 172.3        | 126.4        |
| $C_{lf}$ ( $\text{F}\cdot\text{cm}^{-2}$ )                 | 16.42        | 78.55        | 103.4        | 16.99        | 58.45        | 75.65        |
| $Y_0$ ( $\text{S}\cdot\text{cm}^{-2}\cdot\text{s}^{1/2}$ ) | 7.310        | 35.56        | 45.15        | 7.215        | 26.76        | 35.28        |
| $B$  | 5.849        | 6.090        | 5.595        | 6.078        | 5.441        | 5.313        |

**Table 7.5.** Fitted equivalent circuit elements for three individual cells in a five cell stack operating at 800°C and 52.46 mA\*cm<sup>-2</sup> and on varying anode feeds. Feeds were 3% H<sub>2</sub>O, 97-38.5% H<sub>2</sub>, and balance N<sub>2</sub>.

|   | Cell #1 |        | Cell #3 |        | Cell #5 |        |
|---|---------|--------|---------|--------|---------|--------|
|   | .970    | .646   | .970    | .646   | .970    | .646   |
| $x_H$   |         | .385   |         | .385   |         | .385   |
| $R_Q$ (mΩ*cm <sup>2</sup> )                   | 1261    | 1287   | 657.6   | 661.9  | 792.4   | 792.4  |
| $R_{ct}^c$ (mΩ*cm <sup>2</sup> )              | 181.7   | 175.3  | 142.5   | 117.3  | 97.72   | 88.45  |
| $C_d^c$ (mF*cm <sup>-2</sup> )                | 4.669   | 5.082  | 5.775   | 6.430  | 5.800   | 5.707  |
| $R_{ct}^a$ (mΩ*cm <sup>2</sup> )              | 243.7   | 254.2  | 218.1   | 232.6  | 176.5   | 186.7  |
| $C_d^a$ (mF*cm <sup>-2</sup> )                | 13.60   | 15.19  | 14.15   | 12.22  | 11.47   | 10.89  |
| $R_{\theta}^a$ (mΩ*cm <sup>2</sup> )          | -38.25  | -67.59 | -58.78  | -72.65 | -60.45  | -72.47 |
| $C_{\theta}^a$ (F*cm <sup>-2</sup> )          | -5.843  | -3.838 | -2.813  | -2.418 | -2.503  | -1.502 |
| $Y_0$ (S*cm <sup>-2</sup> *s <sup>1/2</sup> ) | 2.051   | 1.599  | 1.857   | 1.554  | 1.907   | 1.595  |
| $B$   | 1.668   | 1.543  | 1.467   | 1.394  | 1.457   | 1.383  |
| $\chi^2$ (*10 <sup>-6</sup> ) <sup>a</sup>    | 26.9    | 44.3   | 90.4    | 97.8   | 76.4    | 126    |
|   |         | 63.7   |         | 171    |         | 182    |

<sup>a</sup> $\chi^2$  is the nonlinear least squares residual.

**Table 7.6.** Fitted equivalent circuit elements for three individual cells in a five cell stack fed with 97% H<sub>2</sub> and balanced H<sub>2</sub>O and operating at 800°C and varying load currents.

|  | Cell #1 |        |        | Cell #3 |        |        | Cell #5 |        |        |
|--|---------|--------|--------|---------|--------|--------|---------|--------|--------|
|  | 1.639   | 52.46  | 147.5  | 1.639   | 52.46  | 147.5  | 1.639   | 52.46  | 147.5  |
| $i$ (mA * cm <sup>2</sup> )                      | 1296    | 1261   | 1124   | 655.1   | 657.6  | 611.2  | 794.8   | 792.4  | 774.7  |
| $R_{\Omega}$ (mΩ * cm <sup>2</sup> )             | 122.5   | 181.7  | 147.1  | 96.38   | 142.5  | 95.65  | 62.83   | 97.72  | 85.83  |
| $R_{ct}^c$ (mΩ * cm <sup>2</sup> )               | 5.467   | 4.669  | 5.034  | 6.511   | 5.775  | 5.328  | 7.970   | 5.800  | 5.962  |
| $R_{ct}^a$ (mΩ * cm <sup>2</sup> )               | 341.7   | 243.7  | 199.9  | 296.2   | 218.1  | 214.2  | 228.9   | 176.5  | 156.4  |
| $C_d^a$ (mF * cm <sup>-2</sup> )                 | 8.179   | 13.60  | 13.91  | 9.175   | 14.15  | 10.54  | 8.323   | 11.47  | 11.49  |
| $R_d^a$ (mΩ * cm <sup>2</sup> )                  | -150.6  | -38.25 | -90.34 | -137.8  | -58.78 | -139.3 | -189.8  | -60.45 | -155.1 |
| $C_d^a$ (F * cm <sup>-2</sup> )                  | -1.060  | -5.842 | -11.08 | -1.148  | -2.813 | -8.566 | -0.9115 | -2.503 | -2.221 |
| $Y_0$ (S * cm <sup>-2</sup> * s <sup>1/2</sup> ) | 1.442   | 2.051  | 1.931  | 1.397   | 1.857  | 1.821  | 1.337   | 1.907  | 1.731  |
| $B$  | 2.402   | 1.668  | 1.565  | 2.156   | 1.467  | 1.376  | 2.148   | 1.457  | 1.259  |
| $\chi^2$ (*10 <sup>-6</sup> ) <sup>a</sup>       | 239     | 26.9   | 303    | 563     | 90.4   | 411    | 505     | 76.4   | 450    |

<sup>a</sup>  $\chi^2$  is the nonlinear least squares residual.

**Table 7.7.** Fitted equivalent circuit elements of button cells and prismatic cells operating at 800°C and varying load currents and on varying hydrogen inlet concentration. Fit values for the two sizes at similar conditions are compared in the scaling ratio,  $S$ .

| Size                              | $x_H$              |                    |                   |                |
|-----------------------------------|--------------------|--------------------|-------------------|----------------|
|                                   | 0.970              | .327               | .385              | .434           |
| $i$ (mA*cm <sup>-2</sup> )        | button #3<br>0.000 | button #5<br>175.0 | large #3<br>1.639 | large<br>147.5 |
| $R_{ct}^c$ (mΩ*cm <sup>-2</sup> ) | 91.46              | 72.28              | 99.61             | 83.22          |
| $S$                               | 1.053              | 1.187              | 1.173             | .5743          |
| $C_d^c$ (mF*cm <sup>-2</sup> )    | 1.577              | 1.905              | 7.238             | 2.076          |
| $S$                               | 4.129              | 3.130              | 3.478             | 4.514          |
| $R_{ct}^a$ (mΩ*cm <sup>-2</sup> ) | 186.0              | 138.2              | 300.9             | 145.6          |
| $S$                               | 1.593              | 1.132              | 1.604             | 1.023          |
| $C_d^a$ (mF*cm <sup>-2</sup> )    | 9.095              | 9.420              | 10.17             | 11.31          |
| $S$                               | 1.009              | 1.219              | .8901             | 1.383          |

<sup>a</sup> Data from the button cell with anode catalyst ‘A.’ The rest of the data is with anodes catalyst ‘B.’



**Table 7.8.** Values for a parallel RC or a finite diffusion element fitted to the low frequency impedance loops of three cells in a five cell planar stack operating at 800°C and a) 1.69 mA\*cm<sup>-2</sup> and fed with 3% H<sub>2</sub>O, 97-38.5% H<sub>2</sub>, and balance N<sub>2</sub>, b) varying load currents and fed with 3% H<sub>2</sub>O, 64.6% H<sub>2</sub>, and balance N<sub>2</sub>, and c) at 52.46 mA\*cm<sup>-2</sup> and varying the anode feed rate composed of 97% H<sub>2</sub> and balance H<sub>2</sub>O, where the total *J* is assumed to be evenly distributed between the five cells in the stack.

|   | Cell #1      |              | Cell #3      |              | Cell #5      |              |
|---|--------------|--------------|--------------|--------------|--------------|--------------|
| a)  |              |              |              |              |              |              |
| $x_H$   | .970         | .646         | .970         | .646         | .970         | .646         |
|   | <u>.385</u>  | <u>.385</u>  | <u>.385</u>  | <u>.385</u>  | <u>.385</u>  | <u>.385</u>  |
| $R_{if}^a$ ( $\Omega$ *cm <sup>2</sup> )            | 1.373        | 1.538        | 1.263        | 1.479        | 1.301        | 1.427        |
|   | <u>1.430</u> | <u>1.430</u> | <u>1.340</u> | <u>1.340</u> | <u>1.447</u> | <u>1.238</u> |
| $C_{if}^a$ (F*cm <sup>2</sup> )                     | 1.658        | 1.586        | 1.465        | 1.342        | 1.447        | 1.238        |
|   | <u>1.185</u> | <u>1.185</u> | <u>1.018</u> | <u>1.018</u> | <u>1.338</u> | <u>1.202</u> |
| $Y_0$ (S*cm <sup>-2</sup> *s <sup>1/2</sup> )       | 1.441        | 1.332        | 1.397        | 1.211        | 1.338        | 1.202        |
|   | <u>2.025</u> | <u>2.025</u> | <u>1.727</u> | <u>1.727</u> | <u>2.149</u> | <u>2.098</u> |
| $B$   | 2.402        | 2.487        | 2.155        | 2.21         | 2.149        | 2.098        |
|   | <u>1.743</u> | <u>1.743</u> | <u>1.727</u> | <u>1.727</u> | <u>2.098</u> | <u>1.743</u> |
| b)  |              |              |              |              |              |              |
|   |              |              |              |              |              |              |
| $I$ (mA*cm <sup>-2</sup> )                          | 1.639        | 52.46        | 1.639        | 52.46        | 1.639        | 52.46        |
|   | <u>147.5</u> | <u>147.5</u> | <u>147.5</u> | <u>147.5</u> | <u>147.5</u> | <u>147.5</u> |
| $R_{if}^a$ ( $\Omega$ *cm <sup>2</sup> )            | 1.538        | .7570        | 1.479        | .7039        | 1.427        | .6960        |
|   | <u>3.805</u> | <u>3.805</u> | <u>1.146</u> | <u>1.146</u> | <u>1.238</u> | <u>1.127</u> |
| $C_{if}^a$ (F*cm <sup>2</sup> )                     | 1.586        | 1.310        | 1.342        | 1.156        | 1.238        | 1.127        |
|   | <u>.6934</u> | <u>.6934</u> | <u>.8605</u> | <u>.8605</u> | <u>1.202</u> | <u>1.594</u> |
| $Y_0$ (S*cm <sup>-2</sup> *s <sup>1/2</sup> )       | 1.332        | 1.600        | 1.211        | 1.552        | 1.202        | 1.594        |
|   | <u>.5659</u> | <u>.5659</u> | <u>1.056</u> | <u>1.056</u> | <u>2.098</u> | <u>1.520</u> |
| $B$   | 2.487        | 1.543        | 2.210        | 1.393        | 2.098        | 1.383        |
|   | <u>2.615</u> | <u>2.615</u> | <u>1.530</u> | <u>1.530</u> | <u>1.383</u> | <u>1.520</u> |
| c)  |              |              |              |              |              |              |
|   |              |              |              |              |              |              |
| $J$ ( $\mu$ mol*s <sup>-1</sup> *cm <sup>-2</sup> ) | 3.168        | 4.979        | 3.168        | 4.979        | 3.168        | 4.979        |
|   | <u>.6570</u> | <u>.6570</u> | <u>.6283</u> | <u>.6283</u> | <u>.7759</u> | <u>.6082</u> |
| $R_{if}^a$ ( $\Omega$ *cm <sup>2</sup> )            | .8632        | .6570        | .8131        | .6283        | .7759        | .6082        |
|   | <u>1.716</u> | <u>1.716</u> | <u>1.417</u> | <u>1.417</u> | <u>1.734</u> | <u>1.446</u> |
| $C_{if}^a$ (F*cm <sup>2</sup> )                     | 1.910        | 1.716        | 1.648        | 1.417        | 1.734        | 1.446        |
|   | <u>2.051</u> | <u>2.051</u> | <u>1.857</u> | <u>1.857</u> | <u>1.952</u> | <u>1.907</u> |
| $Y_0$ (S*cm <sup>-2</sup> *s <sup>1/2</sup> )       | 1.956        | 2.051        | 1.900        | 1.857        | 1.952        | 1.907        |
|   | <u>1.668</u> | <u>1.668</u> | <u>1.467</u> | <u>1.467</u> | <u>1.843</u> | <u>1.457</u> |
| $B$   | 2.049        | 1.668        | 1.863        | 1.467        | 1.843        | 1.457        |
|   | <u>1.457</u> | <u>1.457</u> | <u>1.467</u> | <u>1.467</u> | <u>1.457</u> | <u>1.457</u> |

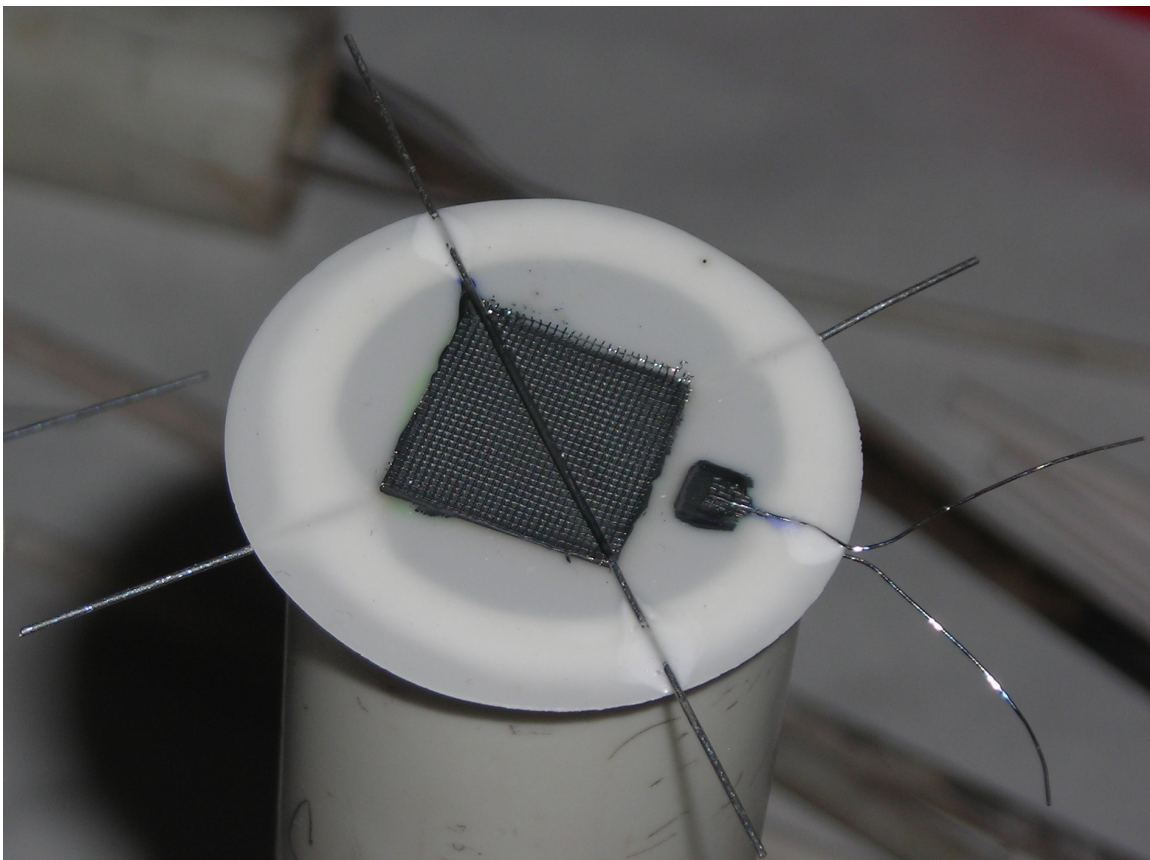


**Figure 7.1.** Picture of a button cell, where the cathode is the large electrode and the reference, the smaller. The opposite face of the electrolyte appears the same, with an anode and anode reference electrode.

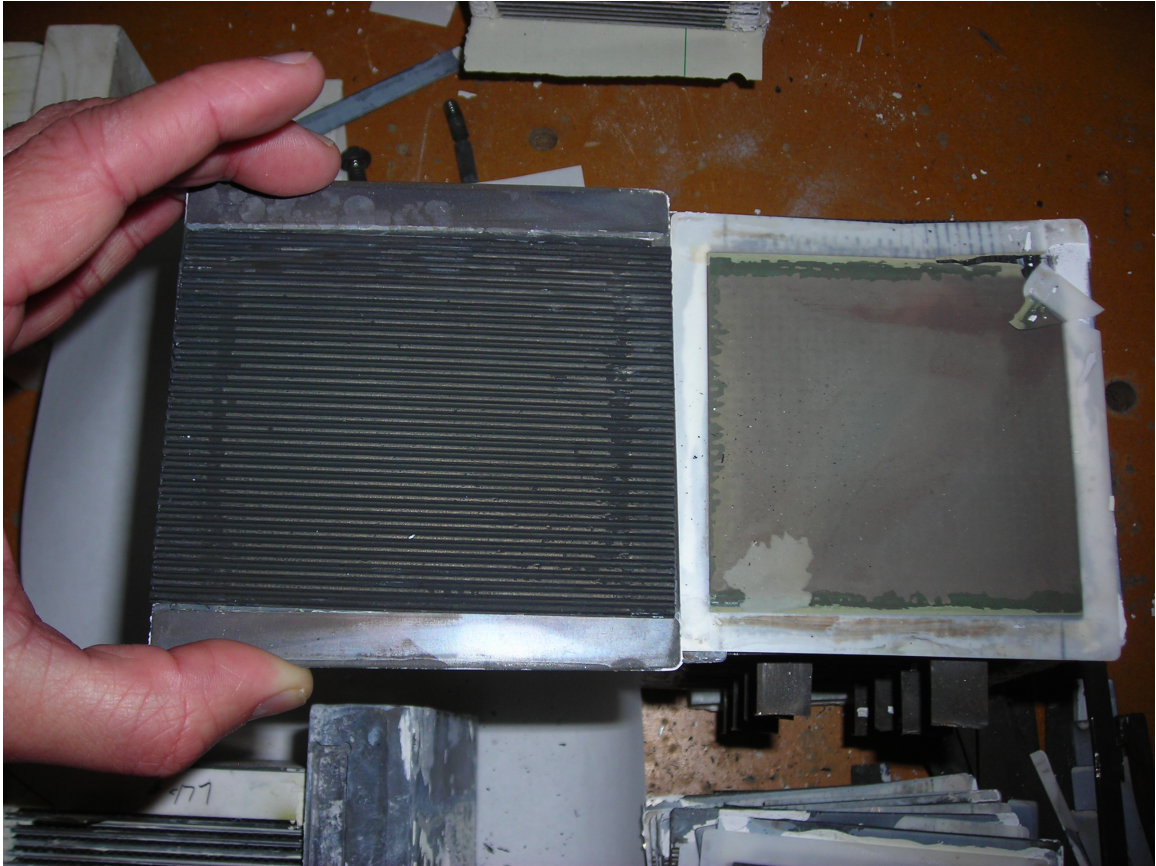


**Figure 7.2.** Picture of a planar fuel cell with a bipolar flow field plate on the left and an electrode on the right.

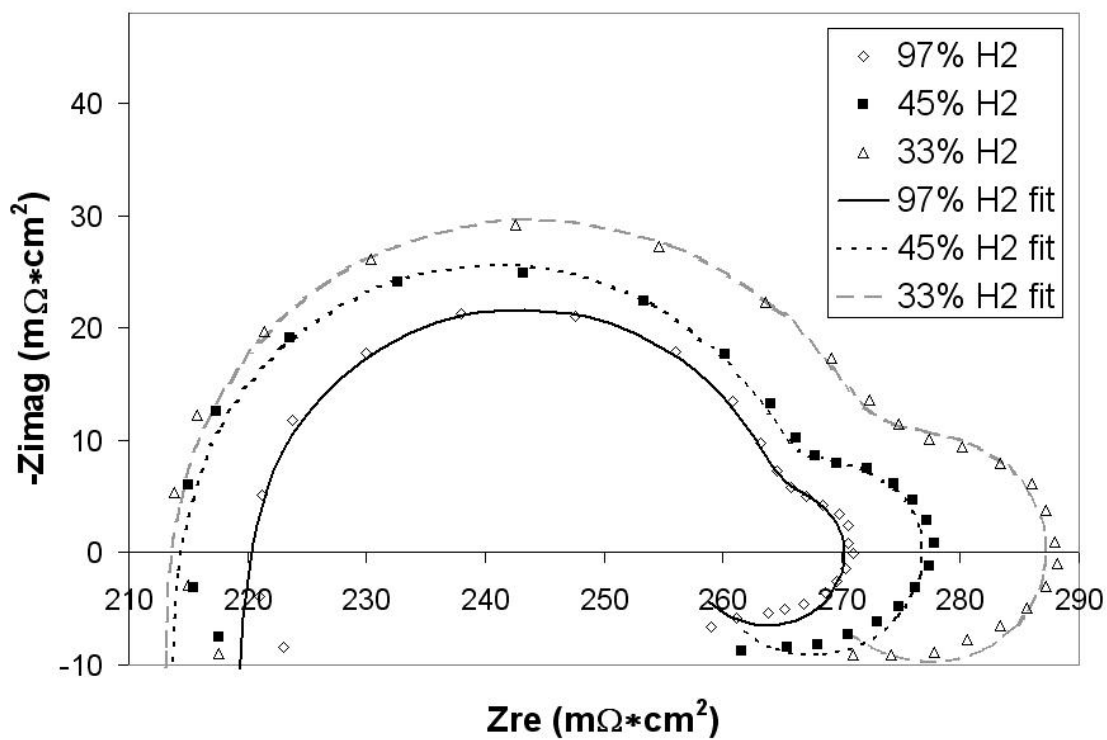


**Figure 7.3.** Nyquist plot for a button cell anode operating at 800°C and 175 mA\*cm<sup>-2</sup> and fed with 3% H<sub>2</sub>O and H<sub>2</sub> diluted with varying amounts of N<sub>2</sub>.

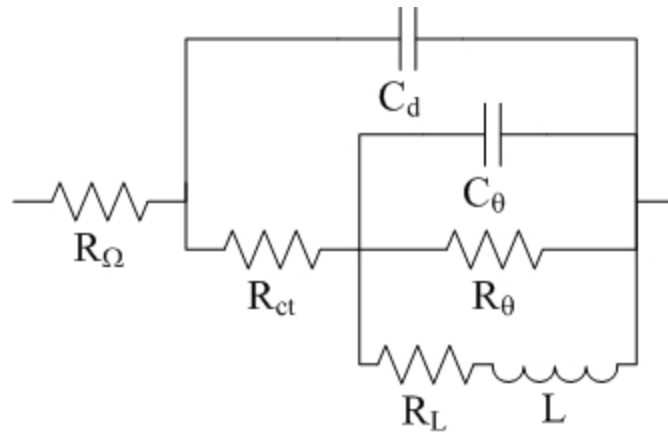


**Figure 7.4.** Equivalent circuit model for a button cell anode. The circuit has three time constants associated with the parallel  $RC$ s ( $R_{ct} C_d$  and  $R_\theta C_\theta$ ) and the series  $RL$  ( $R_L L$ ).

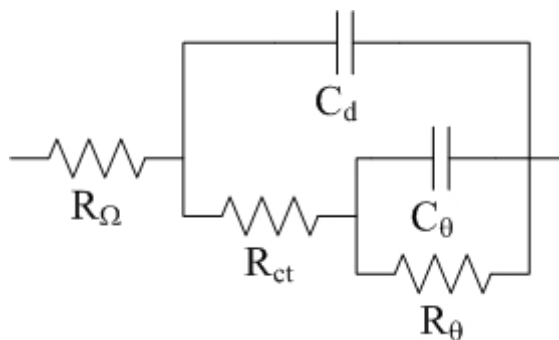


**Figure 7.5.** Equivalent circuit model for a button cell cathode. The circuit has three time constants associated with the parallel RCs ( $R_{ct} C_d$  and  $R_{\theta} C_{\theta}$ ).

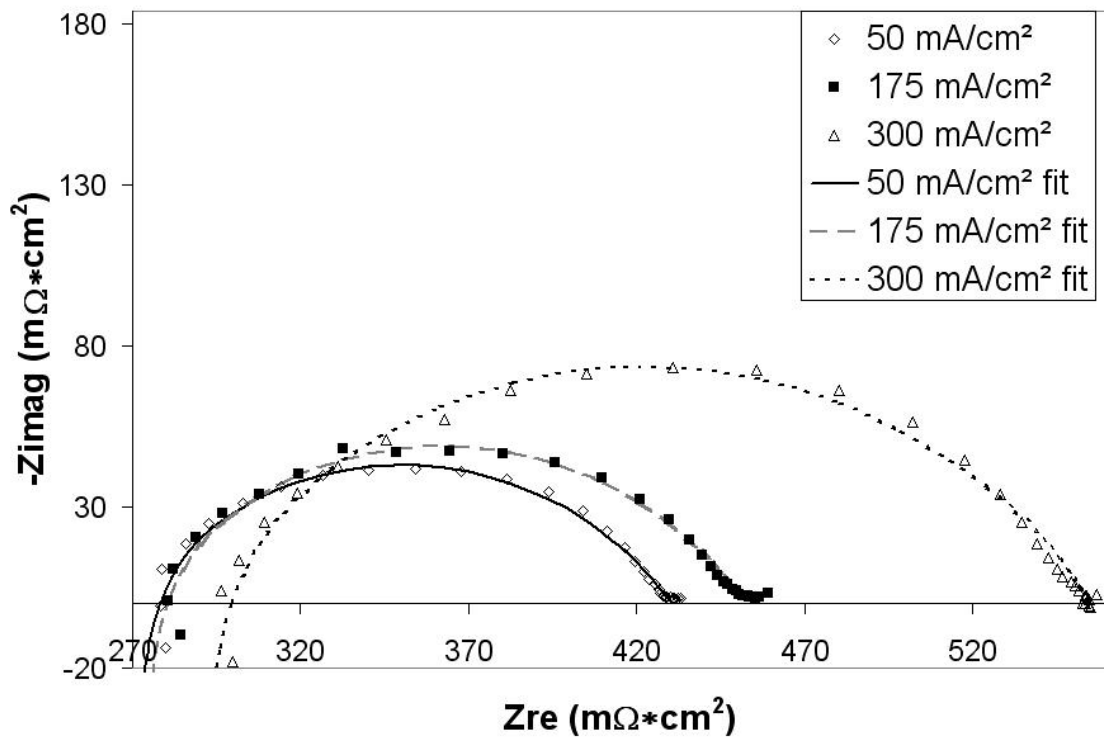
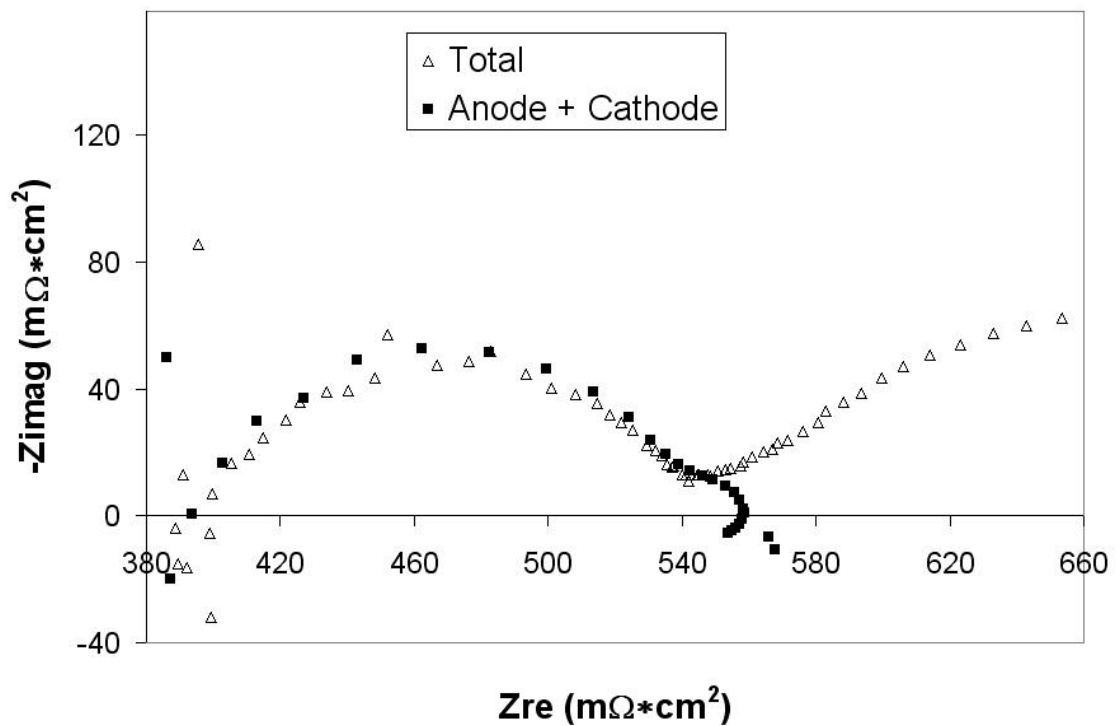
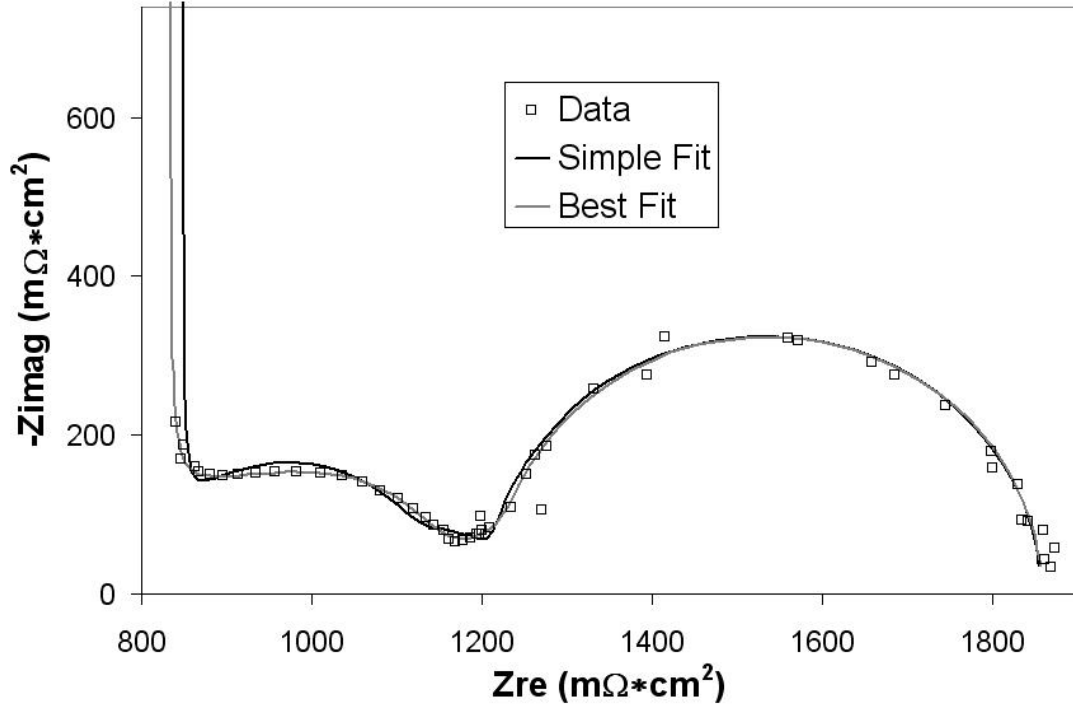


Figure 7.6. Nyquist plot for a button cell cathode at 800°C with varying load current.



**Figure 7.7.** Nyquist plot of the total cell compared with the sum of the individual anode and cathode spectra for a button cell operating at  $800^\circ\text{C}$  and  $175 \text{ mA} \cdot \text{cm}^{-2}$  and fed with 3%  $\text{H}_2\text{O}$  and balance  $\text{H}_2$ . The anode and cathode sum has been offset such that the high frequency intercept of the two would be the same. A large low frequency arc is unique to the measured total cell impedance.





**Figure 7.8.** Nyquist plot of a planar fuel cell operating at 800°C and 52 mA\*cm<sup>-2</sup> and fed with 3% H<sub>2</sub>O, 45% H<sub>2</sub>, and balance N<sub>2</sub>. The cell has been fitted to two different equivalent circuits: one with three time constants, the other with four.

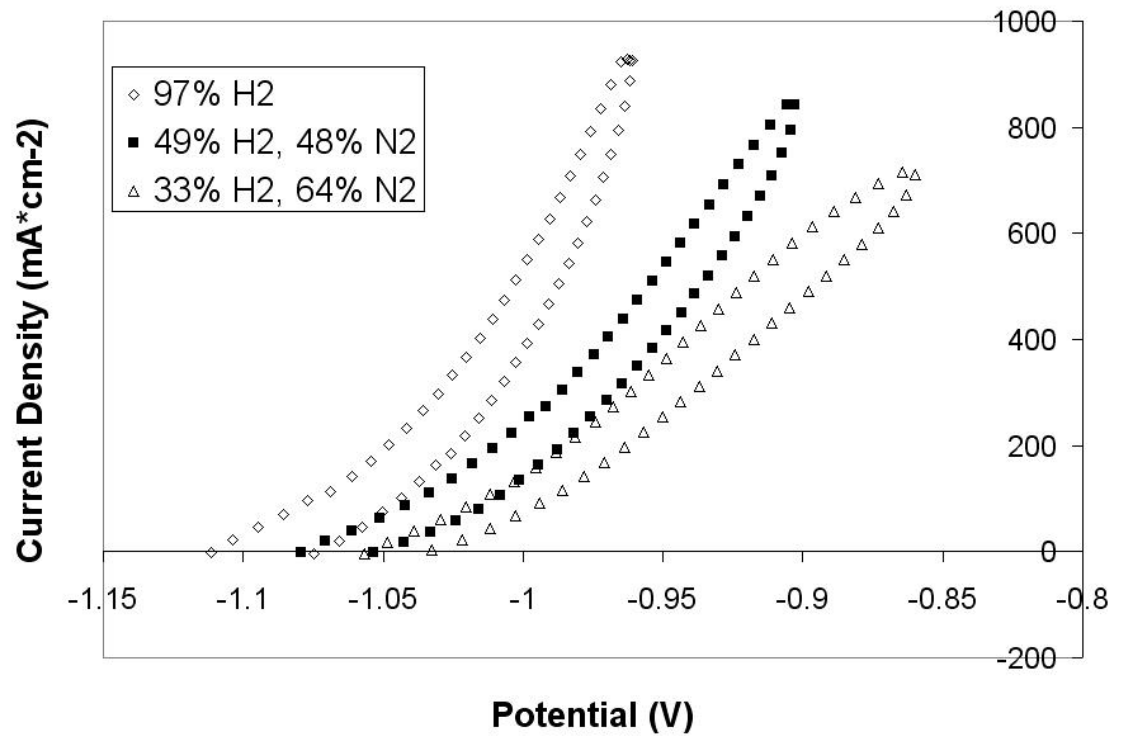


**Figure 7.9.** Potential difference between anode and cathode reference electrodes plotted as a function of load current.

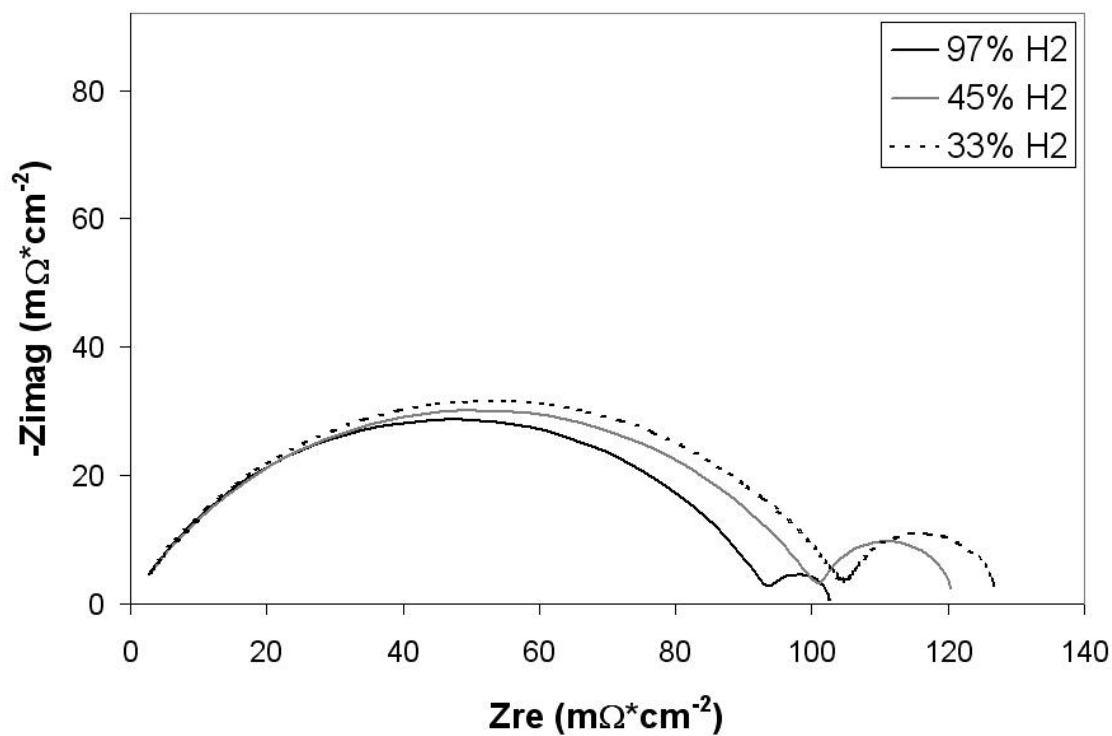


**Figure 7.10.** Nyquist plots of the cathode equivalent circuit from total button cell data fits of a cell operating at 800°C and 175 mA\*cm<sup>-2</sup> and fed with 3% H<sub>2</sub>O and H<sub>2</sub> diluted with varying amounts of N<sub>2</sub>.

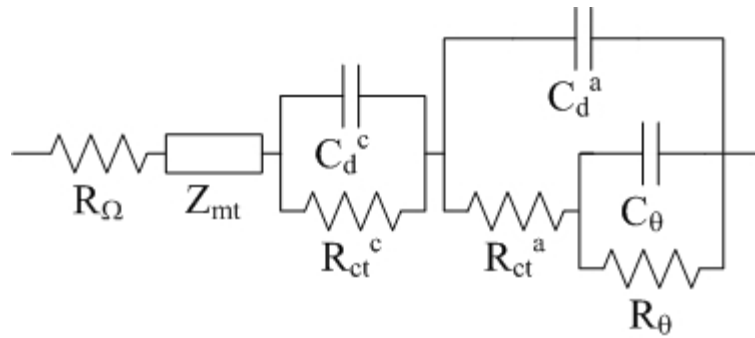


**Figure 7.11.** Large cell equivalent circuit model. The circuit has four time constants associated with the parallel RCs ( $R_{ct}^a C_d^a$ ,  $R_{ct}^c C_d^c$  and  $R_\theta C_\theta$ ) and the finite diffusion element ( $Z_{dif}$ ).

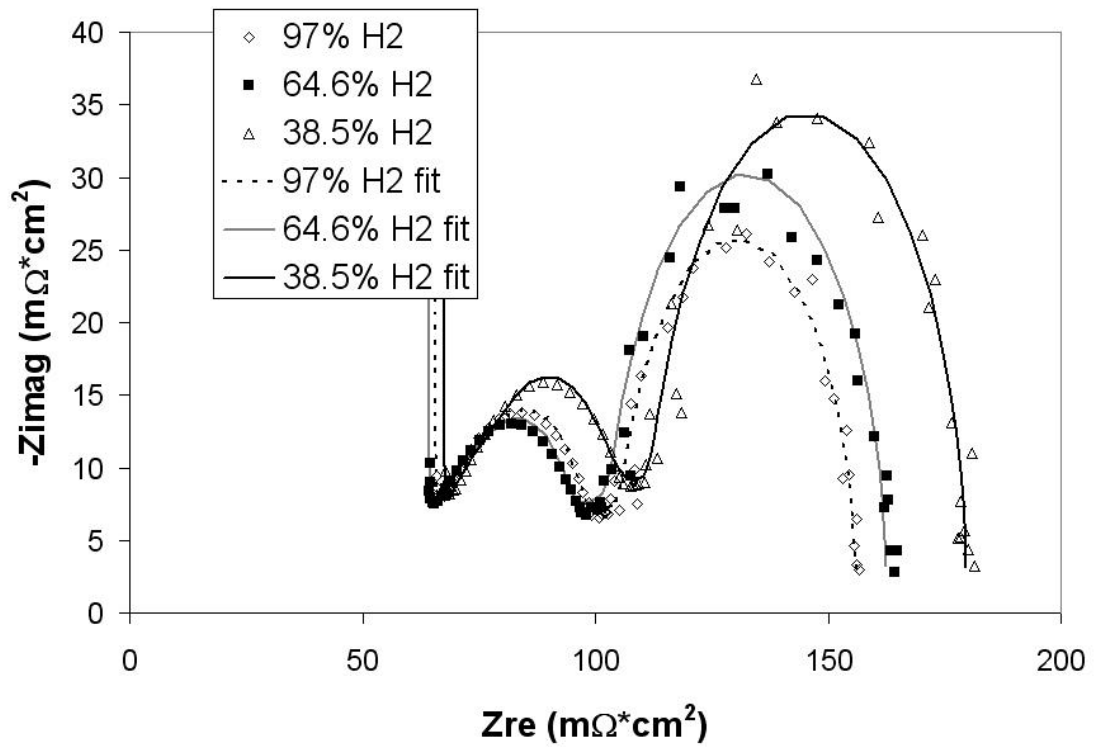


**Figure 7.12.** Nyquist plot of a planar fuel cell stack operating at 800°C and 52 mA\*cm<sup>-2</sup> and fed with 3% H<sub>2</sub>O, varying H<sub>2</sub>, and balance N<sub>2</sub>. The data have been fitted to a four time constant equivalent circuit.

## **Section C**

### **Unpublished Work**

The following section describes work that has been performed, but does not warrant publishing. The experiments and analysis contained in Section C center around two techniques: Electrochemical Impedance Spectroscopy (EIS) and Residence Time Distribution (RTD) modeling. Both techniques have been developed to an extent and have proven useful for investigating PEM fuel cell stacks; however, failures in test setup or model computation prevented the research goals from being fully realized.

## **Chapter VIII**

### **Equivalent Circuit Models and Kinetic Parameters for Commercial PEM Fuel Cells**

#### **Obtained from Impedance Spectroscopy**

#### **VIII.1 Introduction**

Modeling fuel cell systems is essential to understanding how said systems respond to nonideal operating conditions. In order to properly model the electric output of the system, the evaluation of the reaction parameters that govern the electrochemical reactions occurring at the electrode surfaces is critical. AC impedance is an experimental technique capable of probing the relaxation times of the processes occurring at the

electrode. When fit to an appropriate equivalent circuit model, electrochemical impedance spectroscopy (EIS) data may be used to quantitatively describe the interfacial processes. These fits are of even greater value, when the equivalent circuit topology has been derived from kinetic equations and reaction mechanisms, such that the rate constants governing the reactions may be calculated from the fits. The following work will present EIS experiments performed on individual PEM fuel cells in a larger stack and the kinetic constants obtained from the fitted data.

## **VIII.2 Experimental**

EIS was performed on a Nexa™ stack using an FC350™ potentiostat (made by Gamry Instruments) in conjunction with a TDI-Dynaload® electronic load as in Chapters V.2 and VI.2; however, the purpose of these experiments was to obtain pure impedance data for individual fuel cells. The current is controlled for the whole stack with the load as in the previous measurements, and the resulting potential difference was measured between opposite edges of the anode and cathode of a cell in the stack. The current configuration is unchanged for single cell experiments from that of the full stack, because the cells are connected in series with an equivalent current passing through each. The stack was electrically isolated from the parasitic control board by powering it with a separate stack or another suitable external power supply. In order to maintain constant conditions in the cells, the purge valve at the anode outlet was left slightly open. Not only does a constant exhaust flow maintain steady impurity concentrations within the cell, but it also avoids any electrical disturbances from the automated purge process. Steady-state conditions are imperative for accurate impedance spectroscopy [1], because

electrode kinetics is sensitive to reactant concentrations [2]. Data were successfully obtained at different load conditions and for various cells in the stack.

### VIII.3 Equivalent Circuit Models

Several equivalent circuit models were applied to the data in an attempt to acquire kinetic parameters and determine the causes of diverse behavior amongst fuel cells. The literature contains a multitude of theories for deriving equivalent circuit models [3–6], which complicates the choice of which approach to use. Another difficulty in developing an accurate model from which to obtain kinetic data is that several different circuit topologies may yield the exact same fit to the data. For example, if one of the three parallel  $RC$ s in the model presented in Chapter VI is instead connected in series with one of the other parallel resistors (Fig. 8.1), the fit to the impedance data is unchanged. The only way for the fit of the data to be the same between the two models is for the values of the resistances and capacitances to change, which begs the question of which circuit topology is appropriate for obtaining kinetic information? The answer lies in what process each circuit element is meant to represent. Two of the parallel  $RC$ s in the models must represent the two electrodes and the lone resistor, the membrane [3–6]. If the third  $RC$  is in series with the electrode processes as in the Chapter VI model, then it must be attributed to an electrolytic process. Ion conductivity is already accounted in the Ohmic resistance, leaving mass transport of protons in the membrane as the only remaining process to which the third  $RC$  may be attributed. The nesting of a parallel  $RC$  inside of another  $RC$  (as in Fig. 8.1) is often used to represent the relaxation of an adsorbed reaction intermediate, which is present in either electrode reaction [5–7]. In this case, the



capacitance is not related to the charge double layer, but is instead referred to as pseudocapacitance. By comparing the fitted parameters of the two models, the more accurate of the two should be clear.

Table 8.1 gives fit parameters for the two configurations of the three-*RC* model at different DC currents. The hydrogen oxidation reaction (HOR) on platinum is a much faster reaction than the oxygen reduction reaction (ORR) on platinum [8,9]; hence, the *RC* with the smallest impedance in either model is attributed to the anode. Double-layer capacitance is believed to be primarily dependent on active electrode area and only slightly on temperature and reaction rate [6]. The fits of the experimental data show that the capacitance attributed to the anode double-layer increases with reaction rate (or temperature), but only by about 30%. The cathode is assumed to be composed of the same material as the anode; thus, the double-layer capacitance of the cathode should exhibit similar behavior to that of the anode. The nested *RC* is the only model between the two with capacitor fits that remotely resemble the anode behavior, being roughly constant ( $\approx 2.6$  F). The double-layer capacitance of the cathode is between two and three times larger than that of the anode, because cathode sluggishness is often combated with higher catalyst loading (higher active surface area) than the anode.

The other test to determine which circuit topology is more accurate is the behavior of the *RC* that is either associated with pseudocapacitance or ionic mass transfer depending on the model. The impedance of the ionic mass transfer *RC* should theoretically increase with current, because supplying ions to the electrode surface is more difficult as the demand (current) increases. Data fits for the three-*RCs* in series model instead exhibit decreasing impedance with increasing current for the electrolytic

mass transfer  $RC$ . The nested  $RC$  model further proves to be more theoretically sound, because the ORR on platinum is believed to have a strongly adsorbed reaction intermediate [10] (a requirement for pseudocapacitance) [11]. Pseudocapacitance should exhibit a parabolic shape with respect to current [5], which is approximately the trend observed over the limited range of currents. The model presented in Fig. 8.1 is more accurate than the three- $RC$ s in series model because of the behavior of the double-layer, the cathode reaction mechanism, and the poor diffusion predictions of the series model.

### *VIII.3.1 Cathode Equivalent Circuit*

A model with the same circuit topology as the cathode in the nested  $RC$  model was derived mathematically by Zhou et al. [12] for the case of the ORR on platinum in 6 M KOH at low current densities. At higher current densities, their derivation added another relaxation time in the form of a series resistor and inductor ( $RL$ ) in parallel with the nested  $RC$  (Fig. 8.2) representing a change in the reaction mechanism. The addition of an inductor to the equivalent circuit causes the fit on a Nyquist plot to predict points below the  $Z_{re}$  axis (Fig. 8.3). Table 8.2 lists the fitted parameters of the  $RL$  model and of the nested  $RC$  model in addition to a least-squares regression error ( $\chi^2$ ). The error quantifies what is visually evident in Fig. 8.3, that the  $RL$  model more closely fits the experimental data at higher currents than does the nested  $RC$  model. Boukamp has proposed that the addition of a new circuit element should be rejected, if it does not improve  $\chi^2$  by an order of magnitude [13]. While the addition of the  $RL$  to the model improves  $\chi^2$  at each of the tested currents, Boukamp's criterion is not satisfied. Despite this drawback, the  $RL$  model more accurately describes the processes governing the ORR

and matches the experimental data at higher current densities better than does the nested  $RC$  model.

### *VIII.3.2 Anode Equivalent Circuit Model and Kinetic Parameters*

#### *VIII.3.2.1 Charge Transfer Approach*

In order to determine the anode kinetic parameters, a derived anode equivalent circuit is connected in series to the appropriate cathode model and the Ohmic resistance and lead inductance. If Butler-Volmer kinetics is assumed to govern the anode, then the total cell may be represented at low currents with the model in Fig. 8.1. The HOR readily occurs on platinum, meaning the potential will be small, especially at low currents. Making use of the approximation  $e^x \approx 1 - x$  at small exponentials, the Butler-Volmer equation is expressed as

$$I = -I_0 \alpha z f \eta \quad (8.1)$$

where the reactant concentrations are near their equilibrium values due to the small current. The charge-transfer resistance is the negative ratio of potential to current (Ohm's law), so the exchange current is solved as

$$I_0 = \frac{RT}{\alpha z F R_{ct}} \quad (8.2)$$

where  $R_{ct}$  corresponds with the anode resistance in the model fit. Because the electrode is solid, the data were also fitted to a circuit wherein the anode capacitor was replaced with a constant phase element. Figs. 8.4–8.5 show exchange currents plotted as a function of cell current for anodes with double-layers modeled with capacitors and phase elements, respectively. At currents greater than 7.00 A, the high current cathode model was employed in the total cell equivalent circuit. Herein lies another reason that the  $RL$  model

was retained despite the Boukamp criterion, because the fit data show the anode resistor fits for the  $RL$  model are more than 20% higher than those of the nested model (Table 8.2). The exchange current should be approximately equal at low current according to Eq. 8.2; yet, neither a model with a phase element nor capacitor yield fits with the expected trend. Temperature could have some effect on the value of the exchange current, because the equilibrium concentrations to which the exchange current is relative are affected by temperature in terms of the equation of state and the saturation conditions of water. The temperature variation accounts for differences as current increases, but the temperature fluctuations between points at smaller currents are minimal. Another reason that the charge-transfer resistances are not constant is that the rate determining step in the HOR is the adsorption of hydrogen [14]; thus, the Butler-Volmer model should not apply even at low currents. In order to properly obtain kinetic parameters from EIS data, a more complicated mathematical derivation is necessary, especially at higher currents where temperature and reaction mechanism change.

#### *VIII.3.2.2 Transfer Function Approach*

A method for computing anode kinetic parameter from impedance data applicable at all currents is to derive impedance equations from the expected reaction mechanism. Gabrielli and Tribollet [15] introduced an approach based on transfer functions to obtain interfacial information without the need for equivalent circuits. Kuhn et al. [16] derived an impedance equation for the HOR by applying the transfer function approach to the Tafel-Volmer mechanism. The HOR mechanism is well known to have parallel charge-transfer pathways, the Volmer and Heyrovsky [14]. At overpotentials of 50 mV and less, the Volmer reaction dominates the Heyrovsky assuming that mass transfer to the

electrode is fast [14,17]. The cathode contributes almost all of the activation overpotential to the total cell; hence, the anode overpotential should be within the Tafel-Volmer dominated region throughout the operational range of the stack. Kuhn et al. [16] derive the total impedance of the Faradaic branch as

$$1/Z_F = C(j\omega - A)^{-1} B + D \quad (8.3)$$

where

$$A = \left[ -2k_{ad}P_H(1-\theta) - 2k_{des}\theta - 2k_{ec} \sinh(f\eta) \right] / \rho \quad (8.4)$$

$$B = \frac{-2f\theta k_{ec}}{\rho} \cosh(f\eta) \quad (8.5)$$

$$C = 2k_{ec} \sinh(f\eta) \quad (8.6)$$

$$D = 2f\theta k_{ec} \cosh(f\eta) = 1/R_{ct} \quad (8.7)$$

For the equivalent circuit model given in Fig. 8.6, the Faradaic impedance (that in parallel with the double-layer capacitance) is written as

$$1/Z_F = (j\omega L + R_L)^{-1} + 1/R_{ct} \quad (8.8)$$

which is equivalent to Eq. 8.3 when

$$L = 1/BC \quad (8.9)$$

and

$$R_L = -A/BC \quad (8.10)$$

In order to solve for the unknown parameters, Eqs. 8.4–8.10 may be used along with model fits in conjunction with the steady-state mass balance on the catalyst, also called the state equation (not to be confused with a thermodynamic equation of state):

$$\rho\dot{\theta} = k_{ad}P_H(1-\theta)^2 - k_{des}\theta^2 - 2\theta k_{ec}\sinh(f\eta) = 0 \quad (8.11)$$

and the observation equation:

$$I = 2\theta k_{ec}\sinh(f\eta) \quad (8.12)$$

The parameters were solved from impedance data which were fitted using the total-cell model at high current, which consists of the anode and cathode circuits (Figs. 8.6 and 8.2, respectively) connected in series with an  $R_\Omega$  and  $L_{lead}$ . Because the value of  $\rho$  is unknown, the system of equations is underspecified. The constants are calculated in Table 8.3 assuming that  $k_{ad}$  is twice  $k_{des}$ , which is a relationship approximated from the fits of Kuhn et al. [16]. The rate constant fits are not constant as their names would imply, but vary over the current range. The non-constant rate laws also exist in the parameters fitted by Kuhn et al. [16], but no explanation is given in their text. One parameter that should be approximately constant over the range of experimental conditions is  $\rho$ , which is the moles of platinum reaction sites on the electrode in terms of charge; however, such is the case only at 11.98 and 14.03 A. If rate constants are instead calculated based on an assumed  $\rho$ , the ratio of the rate constant of adsorption to that of desorption differs considerably from two. When the  $\rho$  is less than the values given in Table 8.3, negative  $k_{des}$  are calculated. If higher  $\rho$  values than those in Table 8.3 are used instead, then the desorption rate constant becomes far larger than that of adsorption. The larger  $\rho$  is consistent with values calculated from different manufacturer's specifications [18], and the larger  $k_{des}$  is consistent with values calculated by Wang et al. [17]. The kinetic parameters obtained from the transfer function approach may be used to model anode kinetics in other tests, such as the RTD tests presented in Section IX.

#### VIII.4 Summary

EIS has been applied to individual PEM cells at varying currents, and the resulting data have been successfully fitted to a number of equivalent circuit models. By comparing the fitted values at different conditions, the best anode circuit is determined to be that of a single adsorbed intermediate. Applying the transfer function approach proves to be the best method for obtaining rate constants specific to the cell. For more accurate results to be obtained, a reference electrode seems necessary to separate anode and cathode effects. Furthermore, a  $\rho$  value is unknown for the MEAs and must be assumed to prevent the system of equations from being underspecified. The method of using equivalent circuit elements to compute kinetic constants is beneficial to understanding what physical processes limit cell output and to what extent.

#### VIII.5 Nomenclature

|           |  |
|-----------|--|
| $C_d$     | double-layer capacitance                                       |
| $F$       | Faraday's constant   |
| $f$       | F/RT   |
| $I$       | current  |
| $I_0$     | exchange current   |
| $k_{ad}$  | rate constant of adsorption                                    |
| $k_{des}$ | rate constant of desorption                                    |
| $k_{ec}$  | exchange rate constant between adsorbed hydrogen and electrode |
| $L$       | inductance due to adsorbed intermediates                       |

|              |  |
|--------------|--|
| $L_{lead}$   | wire inductance of test leads  |
| $P_H$        | partial pressure of hydrogen   |
| $R$          | ideal gas constant   |
| $R_{ct}$     | charge-transfer resistance   |
| $R_L$        | resistance in series with an inductor due to reaction intermediates  |
| $R_{\Omega}$ | Ohmic resistance   |
| $T$          | stack temperature  |
| $Z$          | impedance  |
| $Z_F$        | impedance of Faradaic processes                                      |
| $Z_{im}$     | imaginary component of impedance (reactance)                         |
| $Z_{re}$     | real component of impedance (resistance)                             |
| $z$          | stoichiometric number of electrons involved in an electrode reaction |

### **Greek Letters**

|                  |  |
|------------------|--|
| $\alpha$         | transfer coefficient                                 |
| $\eta$           | overpotential  |
| $\theta$         | catalyst surface coverage of hydrogen                |
| $\dot{\theta}$   | time derivative of $\theta$                          |
| $\theta^{\circ}$ | catalyst surface coverage of hydrogen at equilibrium |
| $v_0$            | exchange rate constant of Volmer reaction            |
| $\rho$           | charge capacity of electrode surface                 |
| $\chi^2$         | nonlinear least squares fit error                    |



## Superscripts

- a* process occurring at the anode
- c* process occurring at the cathode

## VIII.6 References

- [1] Gamry Instruments, *Basics of Electrochemical Impedance Spectroscopy*, Application Note, Warminster, PA, 2007, p. 6.
- [2] J. S. Newman, *Electrochemical Systems*, second ed., Prentice-Hall, Inc., Englewood Cliffs, NJ, 1991, p. 12.
- [3] A. J. Bard, L. R. Faulker, *Electrochemical Methods: Fundamentals and Applications*, second ed., John Wiley & Sons Inc., New York, 1998, p. 376.
- [4] W. Choi, P. N. Enjeti, J. W. Howze, in *Applied Power Electronics Conference and Exhibition*, The Institute of Electrical and Electronics Engineers Proceedings Series, Piscataway, NJ, 2004, p. 355.
- [5] A. Lasia, in: B. E. Conway, J. O'M. Bockris, R. E. White (Eds.), *Mod. Asp. Electrochem.*, 32, Kluwer Academic / Plenum Publishers, New York, 1999, p. 143–248 (chapter 2).
- [6] M. Sluyters-Rehbach, J. H. Sluyters, in: A. J. Bard, (Ed.), *Electroanal. Chem.*, 4, Marcel Dekker, Inc., New York, 1970, p. 3–42 (chapter 1).
- [7] J. O'M. Bockris, S. Srinivasan, *Fuel Cells: Their Electrochemistry*, McGraw-Hill Book Company, New York, 1969, p. 103.
- [8] J. Larminie, A. Dicks, *Fuel Cell Systems Explained*, John Wiley & Sons Inc., New York, 1998, p. 44.
- [9] R. P. O'Hayre, S. W. Cha, W. Colella, F. B. Prinz, *Fuel Cell Fundamentals*, John Wiley and Sons Inc., New York, 2006, p. 82.
- [10] J. Roques, A. B. Anderson, *Surface Science*, 581 (2005) 105.
- [11] I. D. Raistrick, in: J. R. Macdonald, (Ed.), *Impedance Spectroscopy: Emphasizing Solid Materials and Systems*, John Wiley & Sons, New York, 1987, p. 27.

- [12] D. B. Zhou, H. Vander Poorten, *J. Electrochem. Soc.*, 145 (1998) 936–945.
- [13] B. A. Boukamp, *Solid State Ionics*, 18–19 (1986) 136.
- [14] S. Chen, A. Kucernak, *J. Phys. Chem. B*, 108 (2004) 13984–13994.
- [15] C. Gabrielli, B. Tribollet, *J. Electrochem. Soc.*, 141 (1994) 1147–1157.
- [16] H. Kuhn, B. Andreaus, A. Wokaun, and G. G. Scherer, *Electrochimica. Acta.*, 51 (2006) 1622–1627.
- [17] J. X. Wang, T. E. Springer, R. R. Adzic, *J. Electrochem. Soc.*, 153 (2006) A1732–A1740.
- [18] C. Marr, X. Li, *J. Power Sources*, 77 (1999) 17–27.

**Table 8.1.** Equivalent circuit model fits for cell #22 at 1.00–14.08 A using two different circuit topologies with 3 parallel RCs.

| 3 Series RC Model |                 |                            |                          |             |                          |             |                     |           |                               |  |
|-------------------|-----------------|----------------------------|--------------------------|-------------|--------------------------|-------------|---------------------|-----------|-------------------------------|--|
| $I$ (A)           | $L_{lead}$ (nH) | $R_{\Omega}$ (m $\Omega$ ) | $R_{ct}^a$ (m $\Omega$ ) | $C_d^a$ (F) | $R_{ct}^c$ (m $\Omega$ ) | $C_d^c$ (F) | $R_N$ (m $\Omega$ ) | $C_N$ (F) | $\chi^2$ (*10 <sup>-3</sup> ) |  |
| 1.00              | -15.34          | 1.810                      | 1.148                    | .8908       | 3.385                    | 4.725       | 41.94               | 5.814     | 1.209                         |  |
| 3.60              | -14.65          | 1.724                      | 1.017                    | .9666       | 3.490                    | 4.093       | 12.31               | 8.077     | 2.151                         |  |
| 7.20              | -14.63          | 1.653                      | .6420                    | .9629       | 2.001                    | 3.103       | 6.876               | 6.474     | 5.847                         |  |
| 10.78             | -14.71          | 1.618                      | .7119                    | 1.065       | 2.508                    | 3.288       | 4.197               | 11.14     | 1.410                         |  |
| 14.08             | -13.94          | 1.581                      | .6915                    | 1.144       | 2.478                    | 3.337       | 3.110               | 15.06     | 2.554                         |  |
| Nested RC Model   |                 |                            |                          |             |                          |             |                     |           |                               |  |
| 1.00              | -15.34          | 1.810                      | 1.149                    | .8909       | 10.56                    | 2.607       | 34.76               | 4.076     | 1.209                         |  |
| 3.60              | -14.64          | 1.723                      | 1.011                    | .9645       | 7.339                    | 2.702       | 8.460               | 8.319     | 2.151                         |  |
| 7.20              | -14.63          | 1.653                      | .6416                    | .9627       | 4.103                    | 2.097       | 4.774               | 6.723     | 5.847                         |  |
| 10.78             | -14.71          | 1.618                      | .7119                    | 1.065       | 3.999                    | 2.539       | 2.706               | 14.03     | 1.410                         |  |
| 14.08             | -13.94          | 1.581                      | .6914                    | 1.144       | 3.559                    | 2.732       | 2.029               | 19.63     | 2.554                         |  |

**Table 8.2.** Equivalent circuit model fits for cell #22 at 7.13–14.08 A showing the difference in fit when a series  $RL$  is added in parallel to the nested  $RC$ .

| $I$ (A) | Nested RC Model |                     |                            |             |                          |             |                            |                  |                     |            |  | $\chi^2$ (* $10^{-3}$ ) |
|---------|-----------------|---------------------|----------------------------|-------------|--------------------------|-------------|----------------------------|------------------|---------------------|------------|--|-------------------------|
|         | $L_{lead}$ (nH) | $R_G$ (m $\Omega$ ) | $R_{ct}^a$ ( $\mu\Omega$ ) | $C_d^a$ (F) | $R_{ct}^c$ (m $\Omega$ ) | $C_d^c$ (F) | $R_{\theta}$ (m $\Omega$ ) | $C_{\theta}$ (F) | $R_L$ (m $\Omega$ ) | $L_c$ (mH) |  |                         |
| 7.13    | -14.63          | 1.653               | 642.0                      | 0.9629      | 4.104                    | 2.098       | 4.772                      | 6.727            |                     |            |  | 5.847                   |
| 10.78   | -14.71          | 1.618               | 711.9                      | 1.065       | 3.999                    | 2.539       | 2.706                      | 14.03            |                     |            |  | 1.410                   |
| 14.08   | -13.94          | 1.581               | 691.0                      | 1.144       | 3.559                    | 2.731       | 2.030                      | 19.61            |                     |            |  | 2.554                   |
|         |                 |                     |                            |             |                          |             |                            |                  | RL Model            |            |  |                         |
| 7.13    | -14.86          | 1.668               | 940.2                      | 1.026       | 5.682                    | 2.854       | 3.834                      | 17.15            | 0.5654              | 7.239      |  | 1.082                   |
| 10.78   | -14.80          | 1.625               | 840.9                      | 1.089       | 4.475                    | 2.921       | 2.425                      | 24.97            | 4.208               | 7.687      |  | .8812                   |
| 14.08   | -14.05          | 1.588               | 857.6                      | 1.174       | 4.005                    | 3.287       | 1.974                      | 45.55            | 1.117               | 2.717      |  | .9683                   |

**Table 8.3.** Rate constants and other parameters calculated from *RL* equivalent circuit model fits for cell #22 at 3.6–14.08 A.

| $I$ (A) | $R_{ct}$ ( $\mu\Omega$ ) | $R_L$ ( $\mu\Omega$ ) | $L$ ( $\mu\text{H}$ ) | $\rho$ (C) | $\theta$ | $k_{ec}$ (A) | $k_{ad}$ (A/atm) | $k_{des}$ (A) |
|---------|--------------------------|-----------------------|-----------------------|------------|----------|--------------|------------------|---------------|
| 3.60    | 868.4                    | -1663                 | -2.122                | .0324      | .272     | 55.3         | 5.97             | 2.98          |
| 7.13    | 810.0                    | -1519                 | -1.809                | .0602      | .264     | 60.6         | 11.7             | 5.85          |
| 11.88   | 803.5                    | -1576                 | -1.994                | .1058      | .2788    | 56.20        | 20.77            | 10.38         |
| 14.08   | 724.6                    | -1461                 | -1.598                | .1082      | .2870    | 60.75        | 25.77            | 12.89         |

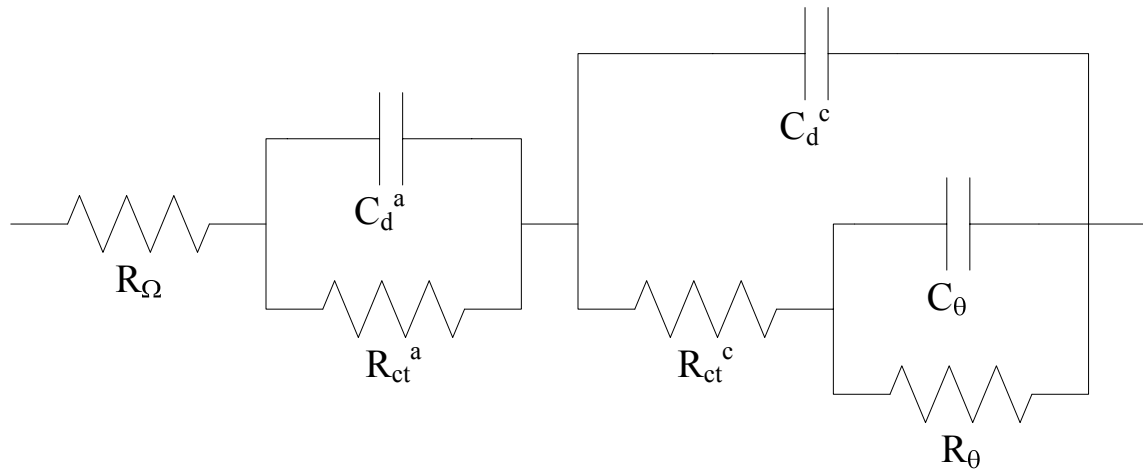


**Figure 8.1.** 3 RC equivalent circuit model for a fuel cell, wherein a parallel RC has been nested into the cathode RC to represent adsorptive behavior.

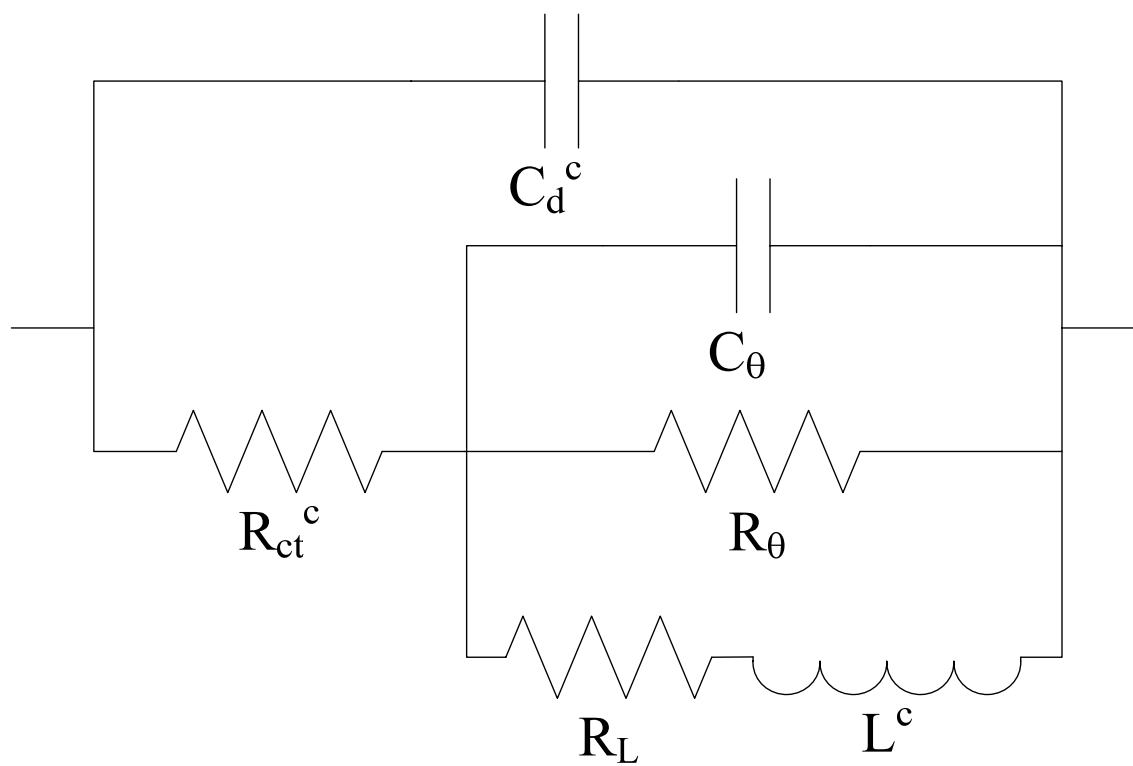


**Figure 8.2.** Equivalent circuit model for the ORR occurring at high currents [12].

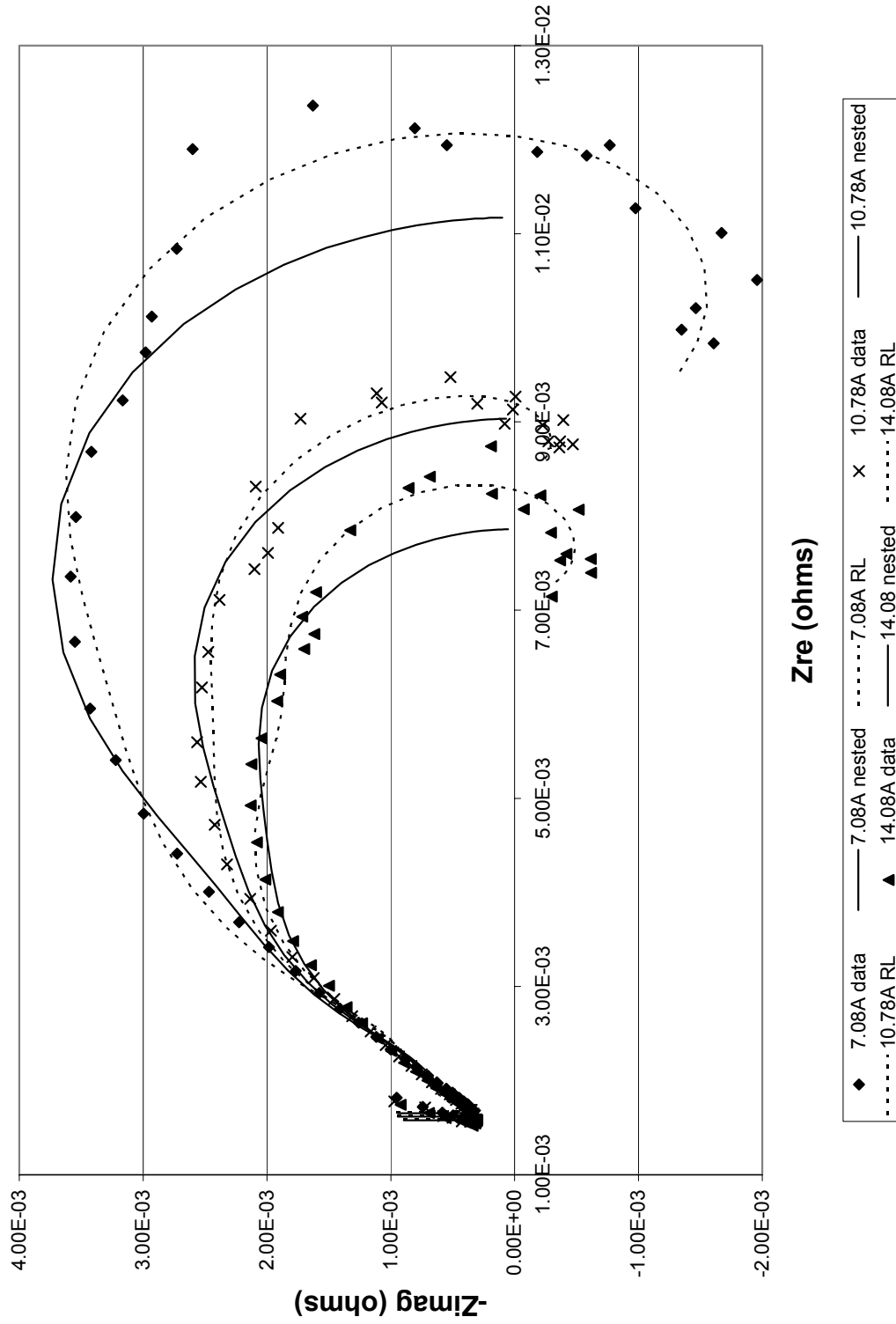


**Figure 8.3.** Nyquist plots for cell #22 from 7.08 A – 14.08 A current fitted to the nested RC (solid line) and the RL (dashed line) equivalent circuit



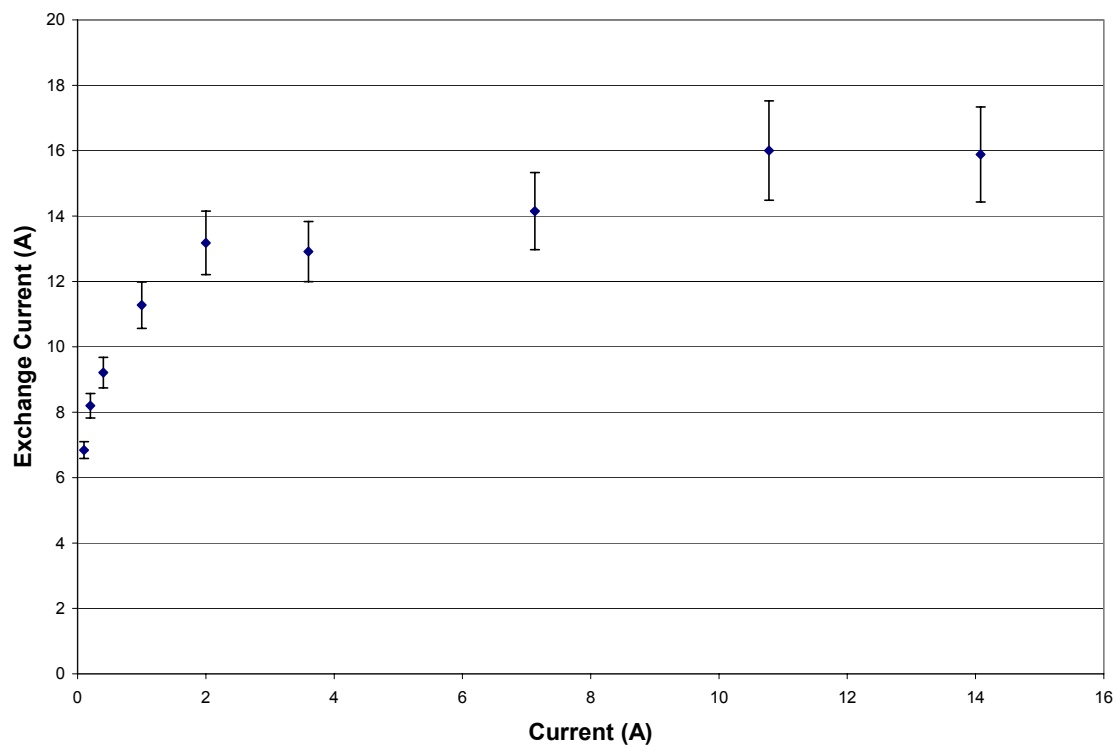


**Figure 8.4.** Anode exchange current calculated from charge-transfer resistances obtained from fits to EIS data at each current level using an equivalent circuit model, wherein a capacitor was employed to model the anode charge double-layer. Error bars indicate the percent error from that of the fitted resistance.

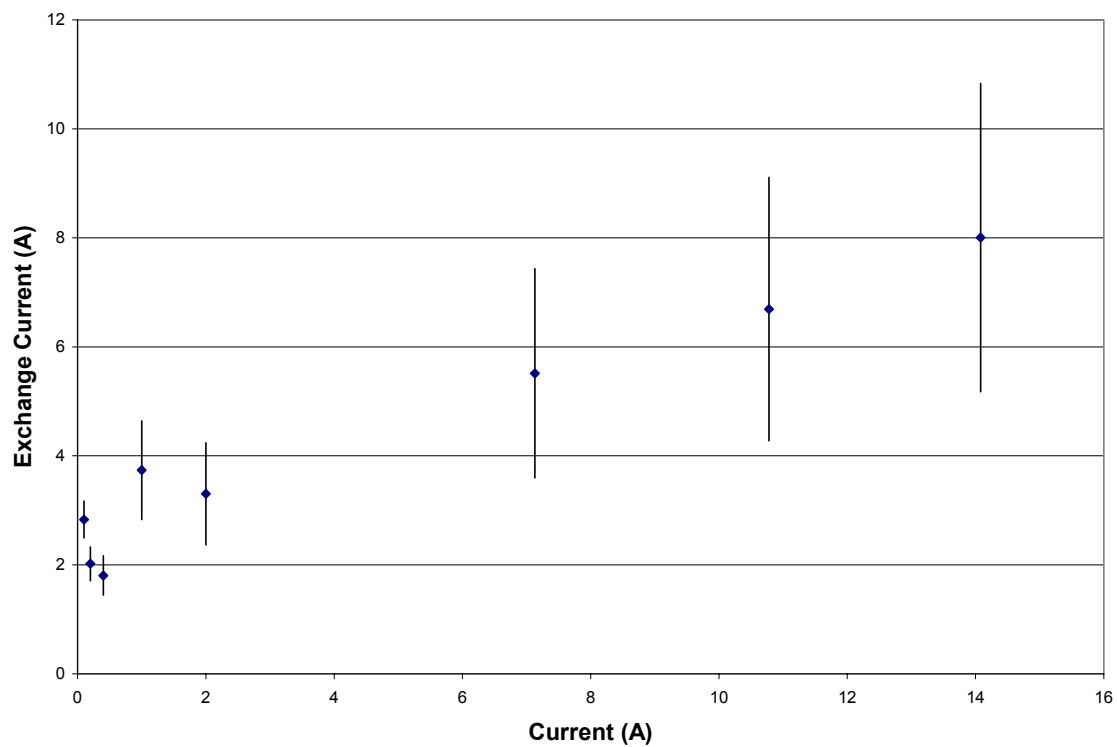


**Figure 8.5.** Anode exchange current calculated from charge-transfer resistances obtained from fits to EIS data at each current level using an equivalent circuit model, wherein a phase element was employed to model the anode charge double-layer. Error bars indicate the percent error from that of the fitted resistance.

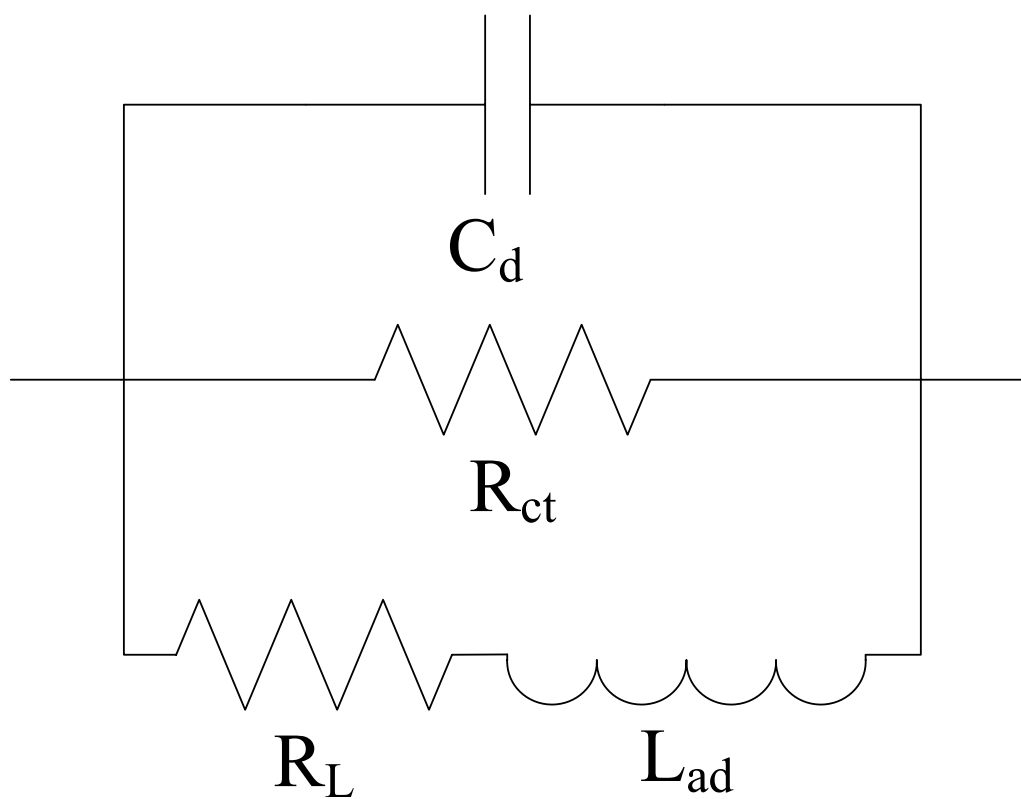


**Figure 8.6.** Equivalent circuit model for the HOR considering the Tafel-Volmer reaction mechanism.

## **Chapter IX**

### **Residence Time Distribution of Anode Impurity Pulses in a PEM Stack**

#### **IX.1. Introduction**

Fuel purity is a significant limitation that inhibits the widespread use of PEM fuel cells by increasing cost, the need for pre-processing, and complexity in control circuitry [1,2]. Most PEM stacks require greater than 99.99% pure hydrogen, which is not practical for several reasons [2,3]. The only place on Earth where hydrogen gas is abundant is in the upper-most part of the atmosphere, because it is much less dense than other gasses. Harvesting gas in the exosphere would be an expensive method to obtain hydrogen; hence, it must be produced from a hydrogen rich source such as fossil-fuels or ammonia. Most production methods will lead to a mixture of hydrogen and other impurities; therefore, the fuel production method requiring the least amount of post-process conditioning (impurity removal) is preferable from an efficiency perspective. The desire to operate fuel cells with higher levels of impurity justifies the need to understand how different impurities flow in a fuel cell (FC) stack, which is useful for optimization of stack designs as well as stack diagnostics.

## IX.2. Experimental

A 47-cell Ballard<sup>®</sup> Nexa<sup>™</sup> Stack was used to investigate the residence time distribution (RTD) of inert gases (Ar and He) and reversible poisons (CO). The Nexa<sup>™</sup> stack used in this work has similar specifications to those used in each of the prior chapters (except Chapter VII), including the exhaust valve modification detailed in Section IV.2. A TDI-Dynaload<sup>®</sup> RBL488 electronic load was employed to draw a constant current from the stack. A backpressure valve was used in conjunction with a needle valve to regulate the anode exhaust flow rate, which was measured using a bubble flow meter. A septum was installed just upstream from the anode stack entrance to be used as the injection portal for pulse RTD experiments. Separate voltage taps were applied to each bipolar plate to measure the potential difference across each cell in the stack. The time dependent cell potentials were collected at two SCXI-1300 terminal blocks, multiplexed through SCXI-1104C modules in an SCXI-1000 chassis, and interpreted by a PCI-6280 DAQ card (all made by National Instruments<sup>™</sup>). A LabVIEW<sup>™</sup> program written by the author controlled the data acquisition process, which began after the stack reached a steady-state.

The fuel cell stack was powered with ultrahigh purity grade hydrogen gas (Airgas, Inc.) and ambient air according to the startup procedure detailed in the product manual [3]. The load was programmed to draw a constant current from the stack, and the anode exhaust valve was opened to the desired outlet flow. Once the stack temperature, potential, and anode exhaust rate were each stable, the system was ready for the injection. Data were collected for approximately one or two minutes prior to the injection time in order to obtain a baseline for initial cell potential and to ensure that steady conditions had

indeed been attained. A tracer pulse of 5, 10, or 15 cm<sup>3</sup> was then injected through the septum into the anode feed stream. The time dependent potential of each cell in the stack was recorded until the stack conditions had returned to steady-state. Using these potential data, it is possible to evaluate the amount of time required for the tracer gas to exit the system and model gas flow through the stack.

### **IX.3. Experimental Results**

Experimental data for pulse tests performed on a Nexa™ fuel cell stack show a complex flow scheme and strong mixing behavior. The layout of the inlet and outlet flows in the manifold are determined by the time and potential associated with each cell's minimum voltage drop relative to those of the other cells. The degree of mixing in the stack is observed in the amount of time required for the cells in the stack to return to their initial potential with more time indicating more mixing.

The data for the pulse tests are represented somewhat unconventionally for the sake of clarity. Initial cell potentials are intentionally offset so that each is separated by 10 mV in order to prevent cell potentials from being superimposed on one another. The offset also allows for the vertical axis gridlines to act as visual references for initial cell potentials and for the potential scale. Only select cells are plotted on Figs. 9.1 and 9.2, because the offset would require far too large of a scale to represent data for 47 cells wherein the nuances would be difficult to resolve. Cell numbers, indicated on the right side of the figures, are numbered from the cell closest to the hydrogen inlet (#1) to the one closest to the anode exhaust outlet (#47). The potential axis being indicative of a potential scale instead of exact potentials may be confusing, but certainly less perplexing

than trying to analyze a jumbled mess of data. Contrasting Fig. 9.1 and 9.2 to Fig. 9.3 illustrates how the clarity of the data has been improved with the offset potentials.

Data shown in Figs. 9.1–9.3 depict experimental data from which information about the stack flow pattern may be deduced. The manifold feed scheme described in a Ballard<sup>®</sup> patent [4] explains that the first 43 cells fed in parallel are fed in series to the next parallel pair, which is fed in series with the final parallel pair (Fig. 9.4). The purpose of feeding the cells in such a manner is to intentionally concentrate impurities in the last two cells (nearest the anode outlet) so that impurities may be effectively removed by periodically opening the purge valve at the anode outlet. Experimental data suggest that this flow scheme is not exactly the one employed in the Nexa<sup>™</sup> stack. Fig. 9.1 shows pulse data for cells evenly spaced over the first group of parallel cells. (Note that the cells not shown in Fig. 9.1 that are in the parallel group appear approximately similar.) The first 43 appear to be fed in parallel as the patent suggests, as implied by the similar time required to reach the minimum potential between the cells. The cells do not, however, conform to a uniform curve shape or minimum potential, which is likely a result of manufacturing inconsistencies. In order to investigate the flow scheme of the cells nearer to the purge valve, Fig. 9.2 depicts the data for the cell #s 41-47. Again using the time at which potential is minimum, it is clear that cell #s 46 and 47 are fed in parallel after all of the preceding cells (as in the patent). Cell #s 44 and 45 are the two that seem to behave differently than the source has suggested. Not only do the two reach a minimum potential at different times, but the shapes of the two curves are different; thus, cell #s 44 and 45 appear to be fed in series rather than parallel. The same behavior is exhibited in Fig. 9.5, which shows the same cells with a similar impurity pulse at a higher

flow rate. The reason that the minimum potential of Cell #44 is not as small as and more dispersed than #s 1-43, is that the anode flow rate is much greater in the inlet manifold to the first 43 cells than their outlet manifold flow rates; consequentially, the impurity gas exiting cell #1 would arrive at the inlet to cell #44 long after the impurity exiting cell #43. The theory explaining the behavior of cell # 44 is based on the assumption that the cross-sectional area of the inlet and outlet manifolds of the first 43 cells are the same, which would be simpler to manufacture and assemble than plates with different manifold sizes. In order to better justify the theory explaining the flow arrangement of the fuel cells in the Nexa™ stack, a mathematical model has been constructed to compare with experimental observations.

### *IX.3.1. Determining Anode Volume*

In order to model the stack flow, the internal volume of the anode side of the stack has been determined by experimental means. A monometer was connected to the anode exhaust outlet of the PEM stack, while the stack was not running. A 20 cm<sup>3</sup> injection of hydrogen was shot into the septum and the resulting pressure increase in the monometer was noted. The total anode volume is then determined using the ideal gas law. Initial conditions of the stack can be written as

$$n_0 = \frac{P_0 V_{an}}{RT_0} \quad (9.1)$$

Similarly for the injection

$$n_{inj} = \frac{P_{amb} V_{inj}}{RT_{amb}} \quad (9.2)$$

Combining the two yields



$$n_0 + n_{inj} = \frac{P_0 V_{an}}{RT_0} + \frac{P_{amb} V_{inj}}{RT_{amb}} = \frac{P_f V_{an}}{RT_0} \quad (9.3)$$

Rearranging the terms to express the anode volume as

$$V_{an} = \frac{T_0 P_{amb}}{T_{amb} \Delta P} V_{inj} \quad (9.4)$$

where  $\Delta P = P_f - P_0$ . After subtracting out the volume outside of the manifold, end plates, and cells; the total anode volume is determined to be 425 cm<sup>3</sup>. Subtracting out the manifold and endplate volumes gives the total cell volume, which is divided by the number of cells yielding an average cell volume of 7.95 cm<sup>3</sup>.

### *IX.3.2. Determining Crossover*

The existence of crossover gas was discovered by performing gas chromatography (GC) analysis of the anode exhaust. An Agilent 6890 GC was used with a Molesieve 13X molecular sieve packed column from Restek Corporation. The data were analyzed with the GC Chemstation software, also made by Agilent Technologies, Inc. A gas sampling tube was inserted into the anode exhaust line down stream of the needle valve and upstream from the bubble flow meter. The fuel cell stack was loaded from 50 to 500 W with varying outlet flow rates in order to test the crossover. The stack was allowed to reach a steady state before the gas was sampled and injected into the GC column. Different anode exhaust flow rates were used to change the concentration of the impurities in the sample improving the accuracy of the measurements.

Gas crossover is termed as such, because it is believed to be cathode gas that “crosses over” into the anode side. Leaks are only partially responsible for crossover, because there is evidence that membranes are slightly permeable to cathode gases [5,6,7].

The gases present on the cathode side are water and air; hence, they are expected to be the gases found in the GC samples. Water is absorbed by molecular sieves and not detectable by the GC. The measured exhaust flow rates have been modified to account for water by assuming saturation conditions in the bubble flow meter and ambient temperature. The amount of nitrogen crossover has been calculated to be approximately 4 std. cm<sup>3</sup>/min. Because oxygen readily reacts at the catalyst layer in a fuel cell, its crossover is only 3% of the total nitrogen crossover and is virtually negligible. Knowing the amount of crossover gas is crucial to being able to accurately model the flow of impurities in a fuel cell stack.

### *IX.3.3. Model Description*

The following model is derived on the premise of being the least complex model that accurately predicts experimental behavior. The complexity of the model is imperative to take into account due to the increase in computation time required to solve the model, which is exacerbated by the total number of cells in a modeled stack. Before a model can be applied to all of the cells in the stack, it must first accurately predict the behavior of a single cell. The model derived below will attempt to describe cell #22, because it is believed to be in the middle of the first group of cells fed in parallel [4]. The tanks-in-series model [8,9] for nonideal reactors is used to determine gas distribution within the flow field plates and the anode feed manifold. In the reaction zone, kinetics and solubility relationships are applied to predict changes in potential due to changes in reactant concentration. Three different forms of these models have been attempted for the cells thus far with only minimal success. The number of tanks used to represent the FCs and the arrangement of the tanks are the primary difference between the three. In

keeping with the philosophy of minimized complication, the proposed models began at the simplest level becoming more complex with the next generation.

#### *IX.3.4. Manifold Model*

The anode manifold is the structure through which fuel is delivered to and exhaust is removed from each FC. In the model, each FC has an associated inlet manifold and an outlet manifold consisting of a number of tanks-in-series that varies depending on the operating conditions and cell location. The section between the septum and anode manifold (the pre-manifold) consists of the septum, pipe into the stack, and end plate anode inlet (Fig. 9.6). An accurate model must account for the pre-manifold in order to replicate the dispersion occurring in the impurity pulse between the injection port and the first cell.

The pre-manifold is the simplest section of the system to model, because the total flow is constant throughout:

$$\dot{V}_{in} = 47 \frac{IRT}{2FP} + \dot{V}_{out} - \dot{V}_{cross} \quad (9.5)$$

where the volumetric flow rates are understood to be set to an equivalent condition by the ideal gas law. Dividing Eq. 9.5 by the cross-sectional area will give the linear velocity, which may be used to find the variance of the flow, which is equivalent to the number of equally sized CSTRs in series [10]:

$$N = \sigma^2 = \frac{uL}{2D} + 1 \quad (9.6)$$

In order to model the flow through the tanks, the CSTR design equation is employed as

$$\frac{dC_H}{dt} = \frac{N}{V} (\dot{n}_{H0} - \dot{n}_H) \quad (9.7)$$

where the  $1/V$  term is multiplied by  $N$  to account for the equal division amongst the tanks of the total pre-manifold volume. Eq. 9.7 is solved by Verner's method of integration [11].

The same basic concept is used for the manifold, only the flow rate changes depending on the location relative to a given cell. As mentioned in the experimental results, the first 43 cells are fed in series. Assuming the flow rate into each of the FCs in parallel is

$$\dot{n}_{cell} = \frac{\dot{V}_{in} P_0}{43RT_0} \quad (9.8)$$

then the flow into the manifold tank that feeds cell number  $\nu$  is

$$\dot{n}_{\nu 0} = \frac{\dot{V}_{in} (44 - \nu) P_0}{43RT_0} \quad (9.9)$$

and the flow into the outlet manifold from cell number  $\nu$  is

$$\dot{n}_{\nu 0} = \nu \left( \dot{n}_{cell} - \frac{I}{2F} \right) \quad (9.10)$$

In order to determine how many tanks are required to model the dispersion in the manifold, the same method used for the pre-manifold is applied. An average velocity is used in Eq. 8.6, which is expressed for cell #22 as

$$\bar{u}_{1-22} = \frac{\dot{V}_{in}}{A} \left( 1 - \frac{11}{43} \right) \quad (9.11)$$

Applying Eq. 9.11 to Eq. 9.6 will approximate the number of tanks needed to model the dispersion in the inlet manifold. Table 9.1 shows results for the number of tanks required to model the manifold between cell #s 1–22 according to Eq. 9.6. Unless the number of manifold tanks is solved to be one or more per cell (22 or more in this case), then some of

the tanks must feed more than one cell. These tanks are assumed to feed two cells and should be located in the region where flow is most turbulent and the most mixing occurs, which would be nearest the manifold inlet. The flow balance for the tanks feeding cell number  $\nu$  and  $\nu + 1$  is

$$\dot{n}_{0\nu} = 2\dot{n}_{cell} + \dot{n}_{0\nu+2} \quad (9.12)$$

and for the tanks further downstream that only feed cell number  $\nu$  Eq. 9.12 is written as

$$\dot{n}_{0\nu} = \dot{n}_{cell} + \dot{n}_{0\nu+1} \quad (9.13)$$

The concentration of hydrogen in each tank is determined according to Eq. 9.7 with a slight volume modification depending on whether the tank feeds two cells:

$$\frac{dC_H}{dt} = \frac{43}{2V_{man}}(\dot{n}_{H0} - \dot{n}_H) \quad (9.14a)$$

or one cell:

$$\frac{dC_H}{dt} = \frac{43}{V_{man}}(\dot{n}_{H0} - \dot{n}_H) \quad (9.14b)$$

Eqs. 9.11–9.14b are meant to describe the part of the inlet manifold that feeds the first 22 cells; however, the same logic may be applied to model an inlet manifold feeding a different number of cells.

### *IX.3.5. Fuel Cell Models*

#### *IX.3.5.1. Stirred Model*

Three different models have been derived for the FCs based on variations of the tanks-in-series method, but none has fit the experimental data well. The first model attempted was a typical tanks-in-series model, where the number of tanks was obtained by matching the variance of the experimental data to the model [8]. The widely dispersed

data is indicative of strong deviation from plug flow and of two equally sized tanks-in-series. The model assumes isothermal and isobaric conditions exist in the cell and that each FC in the stack contributes equally to the nitrogen crossover. Because the anode feed is dry and the cathode feed is humidified and fed at a high stoichiometric ratio ( $> 5$ ), water is expected to diffuse to the anode side [12]. The cell outlet flow is assumed saturated, since the outlet flow is much less than that of the inlet. The saturation assumption implies that the second tank is concentrated to the saturation limit. The tank nearest the cell inlet (tank 1) is assumed to have the same exiting water flow rate as the outlet (tank 2), which is expressed as

$$\dot{n}_w = \frac{x^*}{1-x^*} \left( \dot{n}_{cell} - \frac{I}{2F} + \frac{\dot{n}_{cross}}{47} \right) \quad (9.15)$$

The electrode is assumed to be an equipotential surface implying that the current is distributed to render the total potential equivalent between the cell tanks. Assuming that the cathode conditions are constant, the equilibrium potential (Nernstian) loss from an electrode in contact with pure hydrogen is written for tank  $\tau$  as

$$\Delta E_{eq,\tau} = \frac{RT}{2F} \ln x_{H,\tau} \quad (9.16)$$

Activation losses are assumed to obey the Butler-Volmer relationship in the form of

$$I_\tau = i_0 \frac{A_s}{2} \sqrt{\frac{C_{H,\tau}}{C_{H,ref}}} \left[ e^{\alpha z f \eta} - e^{-\alpha z f \eta} \right] \quad (9.17)$$

where  $\alpha = .5$  and  $z = 2$  [13]. Since the fuel cells in the stack are electrically connected in series, the total current is equivalent through each of the cells implying:

$$I = I_1 + I_2 \quad (9.18)$$

where 1 and 2 are indices relating to the two tanks representing the cell.

The outlet flows are expressed for the cell inlet tank (1) as

$$\dot{n}_1 = \dot{n}_{cell} - \frac{I_1}{2F} + \frac{\dot{n}_{cross}}{2(47)} + \dot{n}_w \quad (9.19)$$

and for the cell outlet tank (2) as

$$\dot{n}_2 = \dot{n}_1 - \frac{I_2}{2F} + \frac{\dot{n}_{cross}}{2(47)} + \dot{n}_w \quad (9.20)$$

Hydrogen concentration is determined for each tank according to Eq. 9.7 with  $N = 2$ .

From thenceforth, the first model will be referred to as the stirred model, because of the strong mixing that it predicts.

Fig. 9.7 shows the predictions for the stirred model against experimental data at 500 W. The dispersion of the experimental data is well replicated in the model, which is to be expected being the basis for choosing two tanks. The stirred model vastly under predicts the minimum voltage, because too much mixing is present in the model. The figure also shows that the minimum occurs too early in time, which is further indicative of the model deviating too much from plug flow. The poor fit of the stirred model is a clear indication that a more plug-like model should be used.

#### *IX.3.5.2.Plug Model*

As a basis of comparison, the next model that is presented is one with little deviation from plug flow, which will be referred to as the plug model. This model is again tank-in-series; however, many more tanks are used in the plug model. The assumptions used in the plug model are the same as in the stirred with the exception of the equipotential electrode, because solving for current distribution in hundreds or

thousands of tanks would be difficult and time consuming. Assuming a distributed potential may also be a good assumption, because the bipolar plates are thin (1.2 mm thick at the cooling channels). The active electrode area is assumed for the model to be 10 cm x 10 cm. The gas diffusion layer (GDL) is assumed to be 80% porous and 400  $\mu\text{m}$  thick, which is at the high end of the GDL thickness range [14, 15, 16]. Channel depth is assumed to be .65 mm, slightly more than half of the total bipolar plate thickness. Channel and rib widths are assumed to be 2.16 mm and .89 mm, respectively [17], and to be arranged in a serpentine pattern. In order to solve for the number of tanks-in-series required in the plug model, Eq. 9.6 is applied to the geometry listed above. Flow in the GDL is considered to occur solely in the same direction as the flow channels compressed into said section. The area of the GDL above the ribs is taken to be split lengthwise, such that flow on either side occurs in the same direction of that in the nearest channel. The total cross-sectional area to be used in determining the fluid velocity is

$$A = w_{chan} (d_{chan} + \phi d_{gdl}) + \phi w_{rib} d_{gdl} \quad (9.21)$$

The velocity is then used in conjunction with Eq. 9.6 to determine the number of tanks-in-series to be utilized in the plug model. Note that the number of tanks for each serpentine channel decreases further from the cell inlet as the fluid velocity decreases due to reactant consumption. The flow out of tank number  $\tau$  in the plug model is expressed

$$\dot{n}_{\tau} = \dot{n}_{\tau-1} + \frac{V_{\tau}}{V_{cell}} \left( \dot{n}_{cross} - \frac{I}{2F} \right) + \dot{n}_w \quad (9.22)$$

where the current and crossover nitrogen are evenly distributed amongst the total volume of the cell. The hydrogen concentration for each tank is similarly constructed as Eq. 9.7:



$$\frac{dC_H}{dt} = \frac{(\dot{n}_{H,\tau-1} - \dot{n}_{H,\tau})}{V_\tau} \quad (9.23)$$

Eqs. 9.22 and 9.23 are true for each of the cell tanks except for the tank fed by the manifold, where the  $\tau - 1$  term is replaced the cell inlet flow (Eq. 9.8).

The change in electrode potential in the plug model is determined entirely by applying the Nernst equation:

$$\Delta E = \frac{RT}{2F} \ln \frac{x_H}{x_{H0}} \quad (9.24)$$

The cell potential is assumed to be dominated by the tank where Eq. 9.24 is the most negative. Activation losses are neglected in the plug model, because the points on the electrode with less Nernstian losses (greater hydrogen concentration) will increase their local reaction rate in an attempt to balance the electrode potential. Hydrogen oxidation on platinum is too facile for the electrode to be able to increase the local polarization in the high concentration regions enough to become an equipotential surface while maintaining the same total electrode current. This means that there is no local activation in the low concentration region of the electrode, where the Nernstian potential dominates. The flows in the model do not reflect this distribution of the electrode current (as explained earlier), which should not substantially effect the accuracy due to the small dispersion of the tracer gas coupled with the many tanks used to describe a single cell.

Fig. 9.8 depicts the plug model output and the experimental data for the voltage response of cell #22 to a  $10 \text{ cm}^3$  pulse of argon injected into a stack at 500 W. The plug model does not accurately predict the experimental behavior of the cell in any regard. The dispersion of the tracer is completely incongruent between the two with the predicted

voltage curve exhibiting far less dispersion than the experimental data. The plug model vastly over predicts the minimum cell potential, because the tracer is too concentrated locally in the model. The minimum potential also occurs much later in time in the model than in the experimental data indicating that some of the cell volume is being bypassed. Each of the aforementioned defections in the model occurs, because gas flows differently through the flow field channels than through the porous GDL; hence, the two should be modeled separately.

#### *IX.3.5.3.Mixed Model*

The third model (the mixed model) that has been attempted is a combination of the two other models, wherein the flow field behaves more like the plug model and the GDL behaves more like the stirred model. The reason the GDL behaves differently than the channels is due to its porous nature. Gas flow in the channels is possible due to the pressure drop from the inlet of the cell to the outlet. Additionally, there is a pressure gradient that drives gas from the flow field channel, through the GDL, and to the catalyst layer. Because these pressure drops exist in two dimensions, some gas will flow between adjacent channels by moving through the porous GDL over the rib, thus bypassing a portion of the channel volume [2]. This phenomenon is also responsible for convective mixing occurring within the GDL; hence, the GDL should perform more like the stirred model.

The mixed model makes use of the basic assumptions of the plug model. The difference with the mixed model is that channel tanks also feed into GDL tanks (Fig. 9.9), so assumptions unique to the mixed model must be proposed to govern the flow between the separate tanks. Each GDL tank is assumed to be fed by the tanks representing three

adjacent channels running the length of the active area. All of the flow between the channel tanks and the GDL tanks is assumed to occur from channel to GDL and never from GDL to channel (i.e. back diffusion against the pressure gradient is neglected). The outlet flow for channel tank  $c$  feeding GDL tank  $g$  is written as

$$\dot{n}_c = \dot{n}_{c-1} - \frac{V_c}{V} \left( \frac{I}{2F} + \dot{n}_{g0} \right) \quad (9.25)$$

For the cell tank nearest to the cell inlet, the  $c - 1$  term is replaced with the cell inlet flow rate (Eq. 9.8). If the ratio of GDL feed flow to reactant consumption flow is assumed constant, the following constant may be introduced:

$$\xi = 1 + \frac{2F\dot{n}_{g0}}{I} \quad (9.26)$$

The GDL tank outlet flow may be expressed for tank  $g$  being fed by channel tank  $c$  as

$$\dot{n}_g = \frac{V_g}{V} \left[ (\xi - 1) \frac{I}{2F} + \dot{n}_{cross} \right] + \dot{n}_{g-1} \quad (9.27)$$

For the GDL tank nearest to the cell inlet, the  $g - 1$  term is replaced the total cell water flow rate (Eq. 9.15). The channel tank nearest to the cell outlet is unique to the rest, because the excess gas from the GDL tanks flows into this channel tank combining to form the total cell outlet flow. The outlet flow for the final channel tank  $c$  that exchanges gas with GDL tank  $g$  can be written as

$$\dot{n}_c = \dot{n}_{c-1} - \frac{I\xi V_c}{2VF} + \dot{n}_g \quad (9.28)$$

Hydrogen concentrations are solved similarly to those of the other two models:

$$\frac{dC_{H,c}}{dt} = \frac{\left[ \dot{n}_{H,c-1} - C_{H,c} \left( \dot{n}_c + \frac{I\xi V_c}{2VF} \right) \right]}{V_c} \quad (9.29a)$$

and for the GDL tanks:

$$\frac{dC_{H,g}}{dt} = \frac{\dot{n}_{H,g-1} - \dot{n}_{H,g} + \sum \dot{n}_{H,g0}}{V_g} - \frac{I}{2VF} \quad (9.29b)$$

where the summation is indicative of the hydrogen flow rate from the channel tanks into the GDL. Eqs. 9.29a and 9.29b are solved for each tank in the model using the same algorithm as the plug and stirred models. Potentials are assumed to behave as in the plug model, where Nernstian losses dominate according to Eq. 9.24.

Fig. 9.9 shows the same 500 W data set that has been used as the basis of comparison, but with the mixed model predictions superimposed onto the data. The mixed model improves certain aspects of the fit; however, it does not predict the experimental results within a reasonable degree of accuracy. As expected, the mixed model predictions show some characteristics of each the mixed and stirred model predictions. The minimum potential drop predicted in the mixed model is more negative than that of the stirred model, but less negative than that of the plug model. The time required for the cell to obtain a minimum potential is also in between the two, being longer than that of the stirred model and shorter than that of the plug model. The shape of the voltage curve predicted in the mixed model is quite different. The predicted tail appears to match the dispersion of the experimental data; however, the wave-like shape before the minimum voltage is a deviation from the experiment unique to the mixed model. Each wave of potential drop is likely due to impurity build up in each GDL tank (i.e. one wave per GDL tank). Clearly the mixed model needs to be modified in order to accurately predict experimental data.

#### IX.4. Summary

Gas flow models have been formulated to predict the residence time distribution of inert gases in a single fuel cell in a Nexa™ stack at load. The stirred and plug models were derived to test the degree of mixing in the cell, which showed that the real behavior of the cell is between the two extremes. The mixed model was derived to account for the differences between the two flow structures (the flow channels and the GDL) through which gas propagates in the system. While the mixed model was not successful at correctly predicting the experimental data, it may prove to be successful with proper modification. Once a working model has been obtained that accurately predicts the behavior of a single fuel cell, it may then be applied to the entire stack and tested against various impurities.

#### IX.5. Nomenclature

|                 |  |
|-----------------|--|
| $A$             | cross-sectional area                                       |
| $A_s$           | area of electrode surface                                  |
| $C_H$           | hydrogen concentration                                     |
| $C_{H,ref}$     | hydrogen concentration at reference conditions             |
| $D$             | dispersion coefficient [10]                                |
| $d_{chan}$      | channel depth  |
| $d_{gdl}$       | GDL thickness  |
| $\Delta E$      | potential difference from initial conditions               |
| $\Delta E_{eq}$ | equilibrium potential difference from reference conditions |

|                    |   |
|--------------------|---|
| $F$                | Faraday's constant  |
| $f$                | F/RT  |
| $I$                | current   |
| $I_\tau$           | current in tank $\tau$  |
| $i_0$              | exchange current density  |
| $L$                | length  |
| $N$                | number of tanks-in-series                                       |
| $n_0$              | initial moles of gas in the anode                               |
| $n_{inj}$          | moles in pulse injection  |
| $\dot{n}_{cell}$   | molar flow rate into each FC in the first group fed in parallel |
| $\dot{n}_{cross}$  | molar flow rate of crossover gas                                |
| $\dot{n}_H$        | molar flow rate of hydrogen out of the compartment              |
| $\dot{n}_{H0}$     | molar flow rate of hydrogen into the compartment                |
| $\dot{n}_w$        | molar flow rate of water out of the FCs                         |
| $\dot{n}_{\nu 0}$  | molar flow rate into the manifold tank that feeds $\nu$         |
| $\dot{n}_\tau$     | molar flow rate out of tank $\tau$                              |
| $\dot{n}_{\tau 0}$ | molar flow rate into tank $\tau$                                |
| $P$                | stack pressure  |
| $P_0$              | initial pressure  |
| $P_{amb}$          | ambient pressure  |
| $P_f$              | final pressure  |

|                   |   |
|-------------------|---|
| $\Delta P$        | $P_f - P_0$   |
| $R$               | ideal gas constant  |
| $T$               | stack temperature   |
| $T_0$             | initial temperature   |
| $T_{amb}$         | ambient temperature   |
| $t$               | time  |
| $u$               | linear velocity   |
| $\bar{u}_{1-22}$  | mean linear velocity between cell #1 and #22                |
| $V$               | total volume of modeled part                                |
| $V_{an}$          | anode dead volume   |
| $V_{cell}$        | volume of a single fuel cell                                |
| $V_{inj}$         | volume of pulse injection                                   |
| $V_{man}$         | volume of inlet manifold                                    |
| $V_{\tau}$        | volume of tank $\tau$                                       |
| $\dot{V}_{cross}$ | total volumetric flow rate of crossover gas                 |
| $\dot{V}_{in}$    | total volumetric flow rate into the anode side of the stack |
| $\dot{V}_{out}$   | total volumetric flow rate of anode exhaust                 |
| $w_{chan}$        | channel width   |
| $w_{rib}$         | rib width   |
| $x_{H0}$          | initial mole fraction of hydrogen                           |
| $x_H$             | mole fraction of hydrogen                                   |
| $x^*$             | mole fraction of saturated water vapor                      |

$z$  stoichiometric number of electrons involved in an electrode reaction

### Greek Letters

$\alpha$  transfer coefficient

$\eta$  overpotential ( $E - \Delta E_{eq}$ )

$\nu$  cell index number

$\xi$  ratio of GDL feed flow to reactant consumption flow

$\sigma^2$  variance

$\tau$  tank index number

$\phi$  porosity

## IX.6 References

- [1] J. Larminie, A. Dicks, *Fuel Cell Systems Explained*, John Wiley & Sons Inc., New York (1998).
- [2] R. P. O'Hayre, S. W. Cha, W. Colella, F. B. Prinz, *Fuel Cell Fundamentals*, John Wiley and Sons Inc., New York (2006).
- [3] Ballard Power Systems, Inc., *Nexa™ Power Module Installation Manual*, Burnaby, BC (2002).
- [4] R. H. Barton, T. D. Uong, C. J. Schembri, G. A. Skinner, PCT Int. Appl., WO 003010845 (2003).
- [5] J. Shim, H. Y. Ha, S. A. Hong, I. H. Oh, *J. Power Sources*, 109 (2002) 412.
- [6] S. Ma, M. Odgaard, E. Skou, *Solid State Ionics*, 176 (2005) 2923.
- [7] K. M. Nouel, P. S. Fedkiw, *Electrochimica. Acta.*, 16–17 (1998) 2381.
- [8] O. Levenspiel, *The Chemical Reactor Omnibook*, OSU Bookstores Inc., Corvallis, OR (2002).
- [9] H. S. Fogler, *Elements of Chemical Reaction Engineering*, third ed., Prentice-Hall, Inc., Upper Saddle River, NJ (1999).



- [10] O. Levenspiel, *Chem. Eng. Sci.*, 17 (1962) 576.
- [11] E. Hairer, S. P. Norsett, G. Wanner, *Solving Ordinary Differential Equations*, second ed., Springer-Verlag, Berlin, NY, 1993, p. 181.
- [12] M. M. Mench, Q. L. Dong, C. Y. Wang, *J. Power Sources* 124 (2003) 90.
- [13] Q. Liu, Q. Yan, J. Wu, in: R. K. Shah, E. U. Ubong, S. Samuelson (Eds.), *3<sup>rd</sup> International Conference on Fuel Cell Science, Engineering, and Technology*, The American Society of Mechanical Engineers Proceedings Series, New York, 2005, p. 111.
- [14] R. O'Hayre, T. Fabian, S. Litster, F. B. Prinz, J. G. Santiago, *J. Power Sources* 167 (2007) 118.
- [15] Ballard<sup>®</sup> Material Products, Inc., *AvCarb<sup>™</sup> Technical Specifications*, Lowell, MA (2004).
- [16] Toray Industries, Inc., *Toray Carbon Fiber Paper Basic Data*, Decatur, AL.
- [17] H. Ju, C. Y. Wang, S. Cleghorn, U. Beuscher, *J. Electrochem. Soc.* 152 (2005) A1645.
- [18] W. L. McCabe, J. C. Smith, P. Harriott, *Unit Operations of Chemical Engineering*, sixth ed., McGraw-Hill, New York, 2001, p. 550.

**Table 9.1.** Number of tanks-in-series required to simulate flow through the anode feed manifold between cell #s 1–22 of a stack from 500–900 W. Velocities are given for the manifold inlet and the plenum for cell #22, as well as the mean between the two. The number of tanks must be an integer, so the rounded  $N$  is listed in addition to the exact value of  $N$  calculated from Eq. 9.6.

|                          | Stack Power |       |       |
|--------------------------|-------------|-------|-------|
|                          | 500 W       | 700 W | 900 W |
| $u_{\text{in}}$ (cm/s)   | 111         | 170   | 233   |
| $u_{22}$ (cm/s)          | 56.6        | 86.9  | 119   |
| $\bar{u}_{1-22}$ (cm/s)  | 83.6        | 128   | 176   |
| $D$ (cm <sup>2</sup> /s) | 34.8        | 77.1  | 139   |
| $N$ calculated           | 18.6        | 13.2  | 10.3  |
| $N$ rounded              | 19          | 13    | 10    |

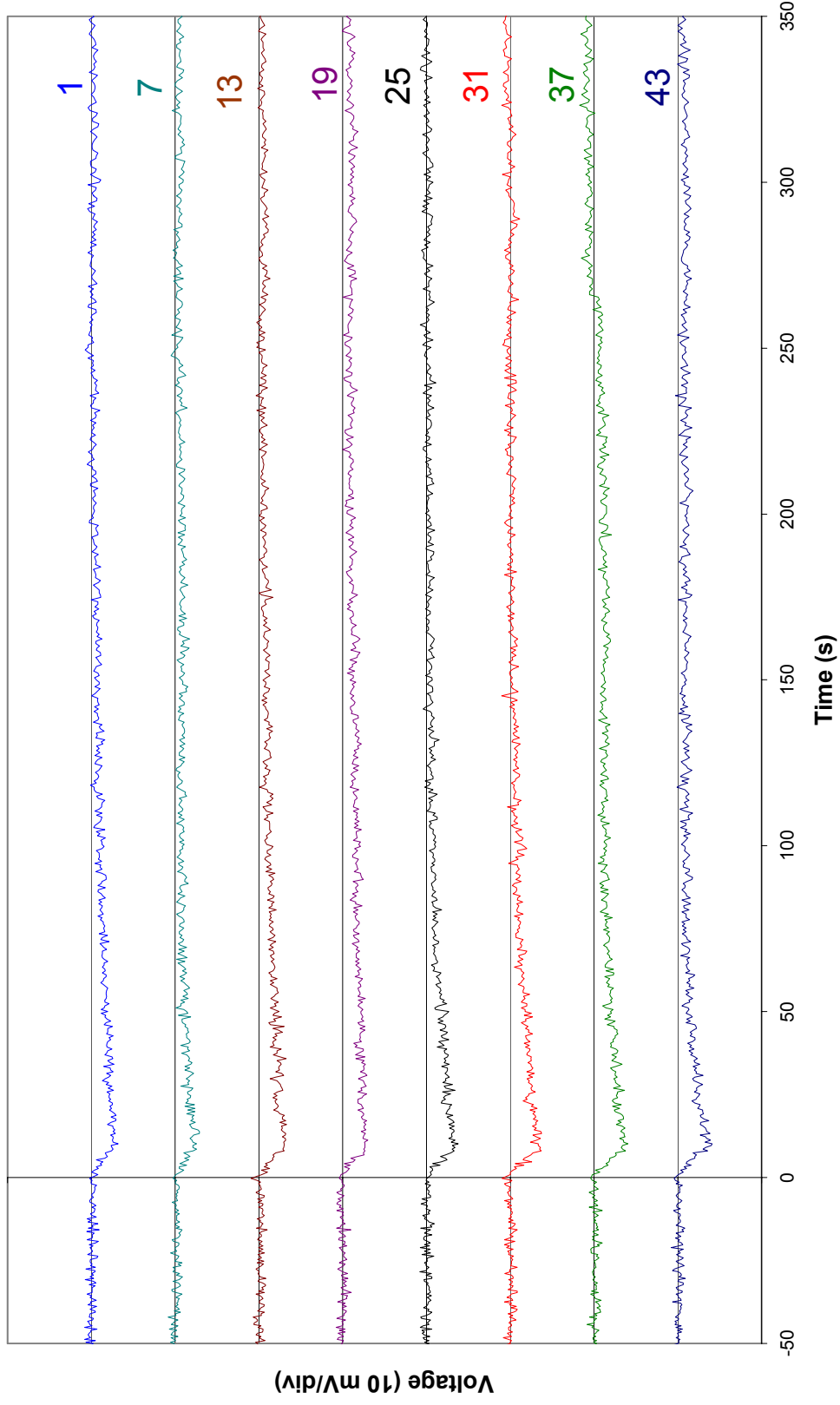


**Figure 9.1.** Cell potentials of every sixth cell in a stack at 500 W plotted as a function of time relative to a  $10 \text{ cm}^3$  pulse injection of Ar. Potentials are offset such that the distance between each horizontal gridline is 10 mV.

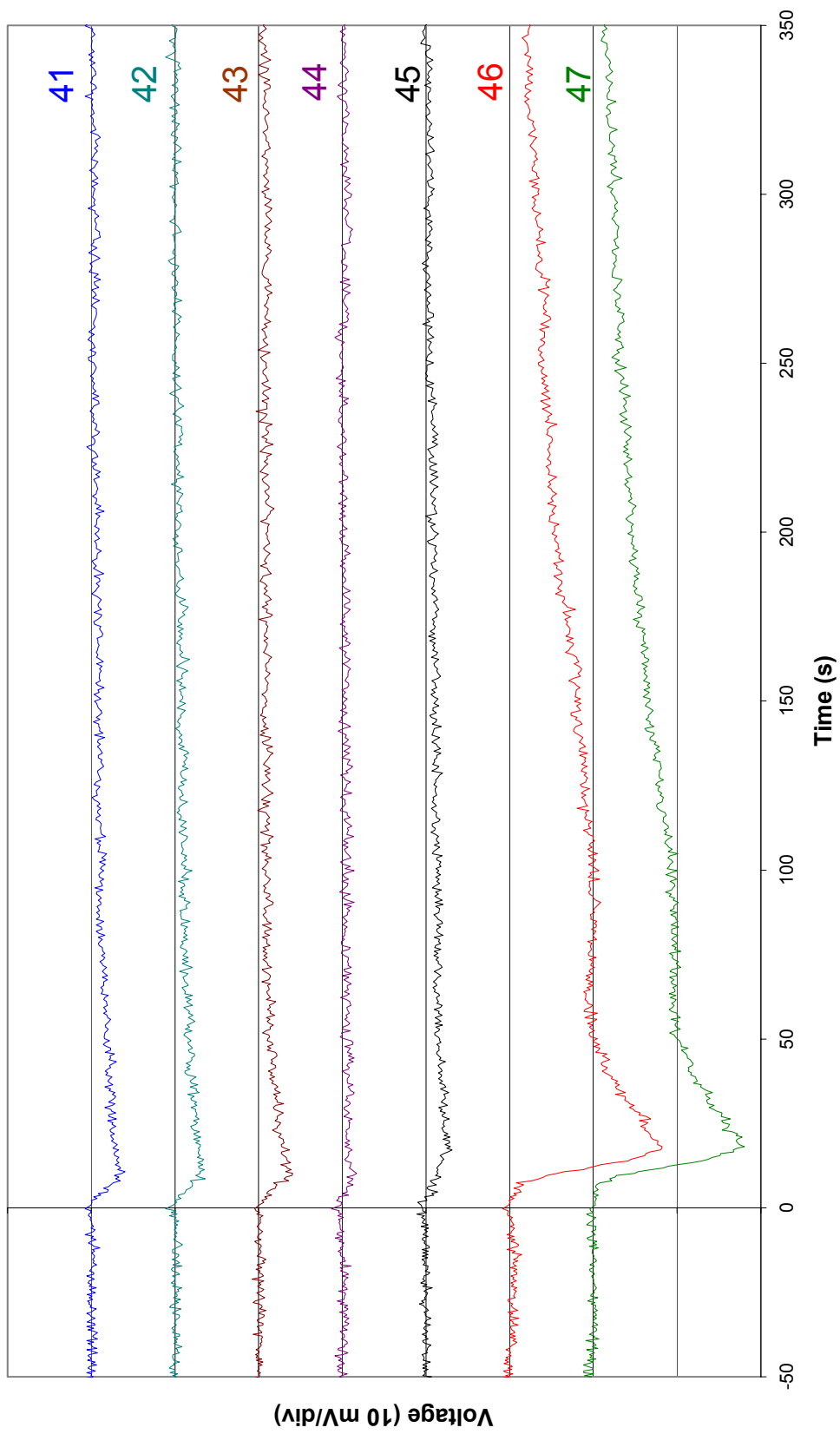


**Figure 9.2.** Cell potentials of the seven cells closest to the anode outlet in a stack at 500 W plotted as a function of time relative to a 10 cm<sup>3</sup> pulse injection of Ar. Potentials are offset such that the distance between each horizontal gridline is 10 mV.

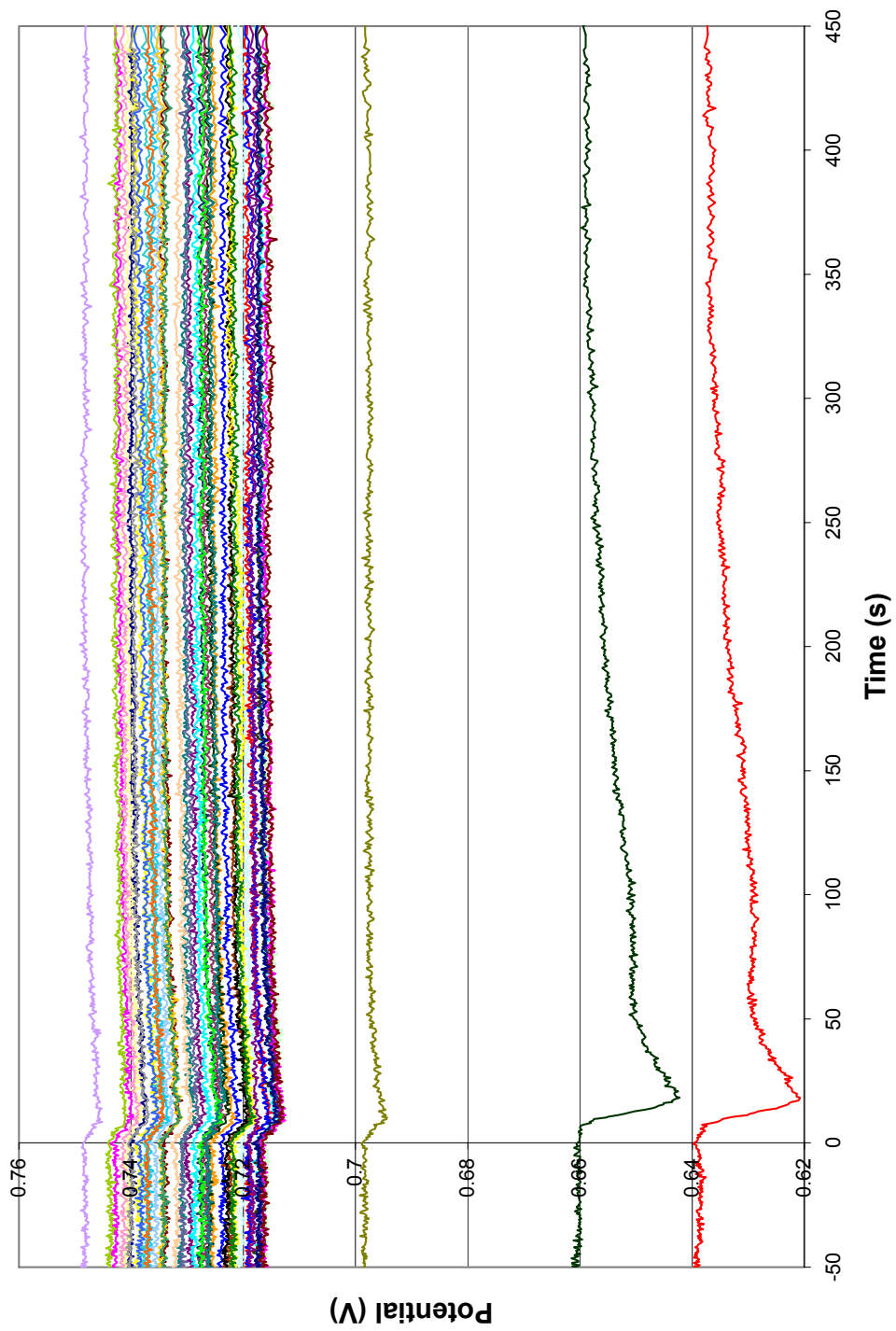


**Figure 9.3.** Cell potentials of each cell in a stack at 500 W plotted as a function of time relative to a 10 cm<sup>3</sup> pulse injection of Ar.

Cell #'s 1, 2, 3, ..., 42, 43, 44, 45, 46, 47

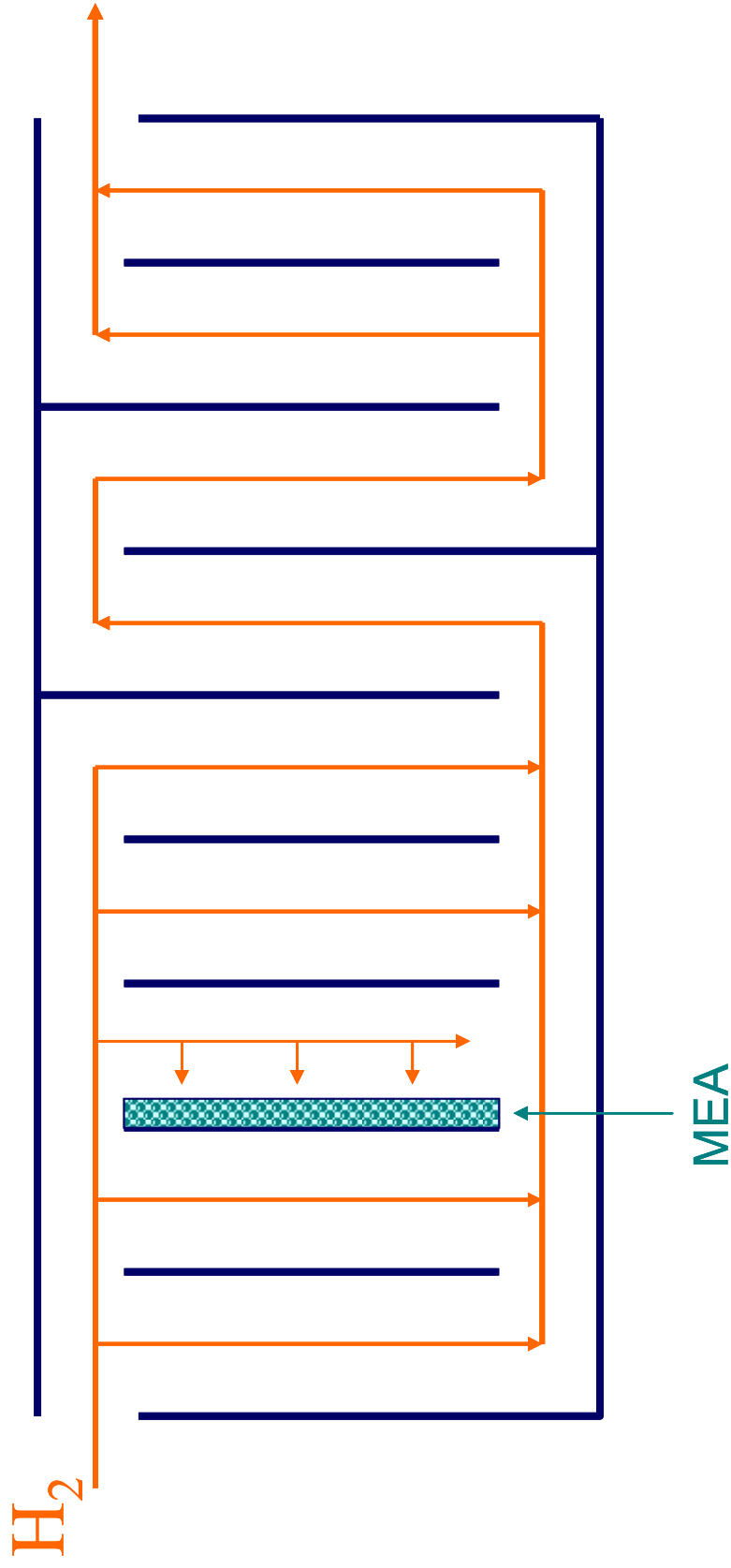


**Figure 9.4.** Flow diagram for the Nexa™ stack[4] wherein the manifold feeds three groups of fuel cells in parallel, #s 1–43, #s 44–45, and #s 46–47. Each of these three groups is fed in series to the next.

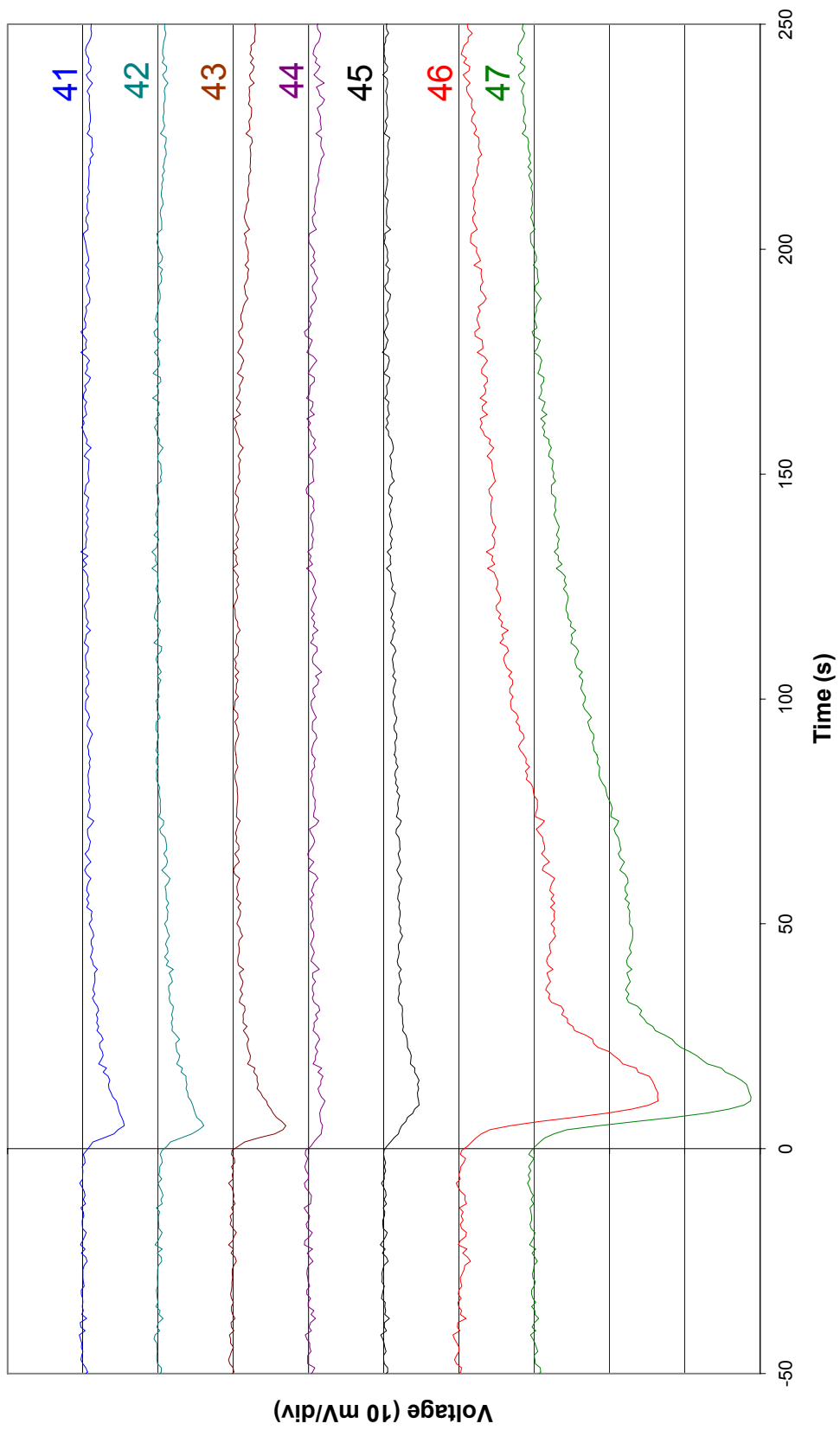


**Figure 9.5.** Cell potentials of the seven cells closest to the anode outlet in a stack at 700 W plotted as a function of time relative to a 10 cm<sup>3</sup> pulse injection of Ar. Potentials are offset such that the distance between each horizontal gridline is 10 mV.

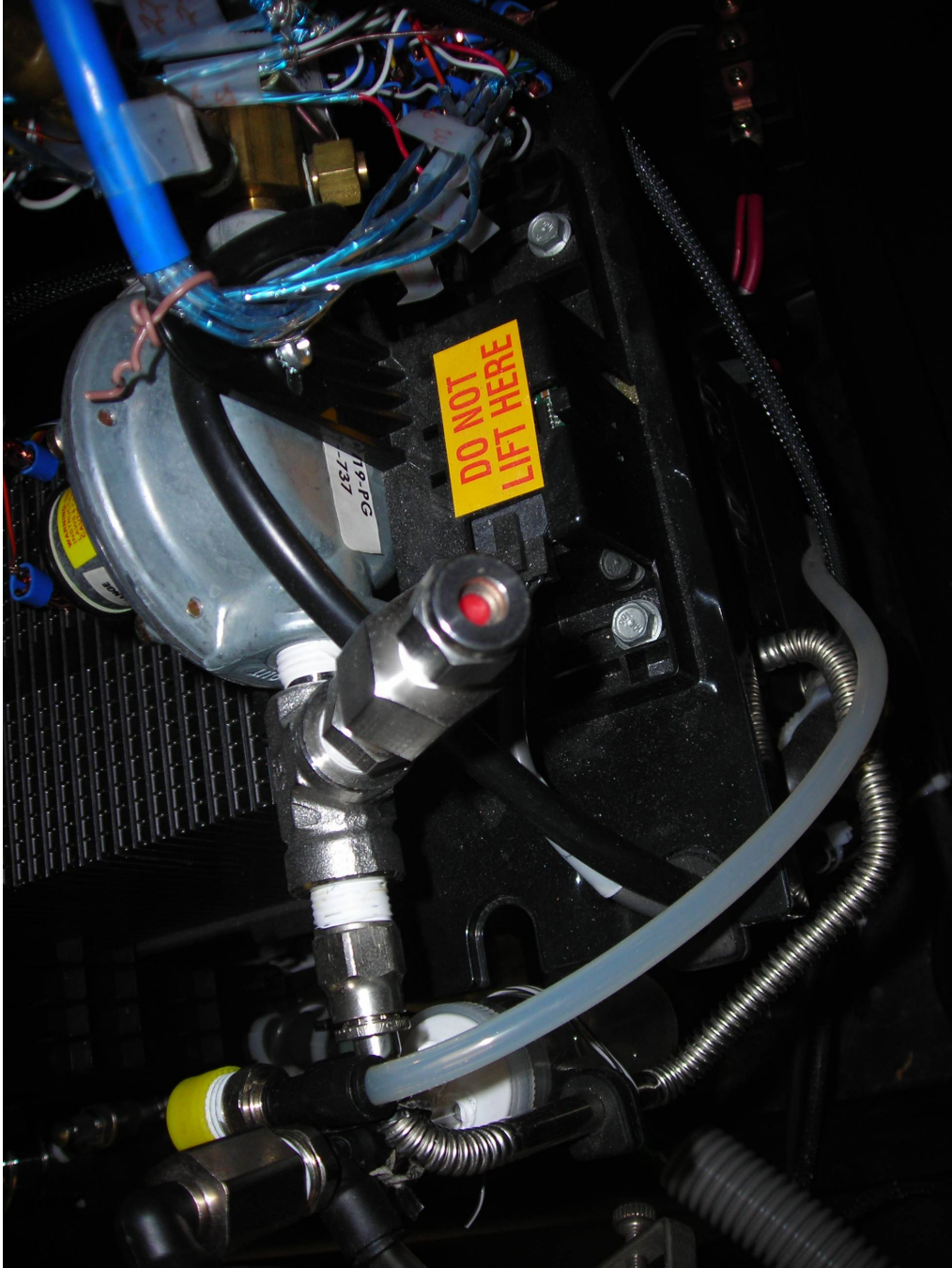


**Figure 9.6.** Diagram showing the septum (center of the picture) in line with the metal pipe that wraps around to feed the anode side of the fuel cell stack.



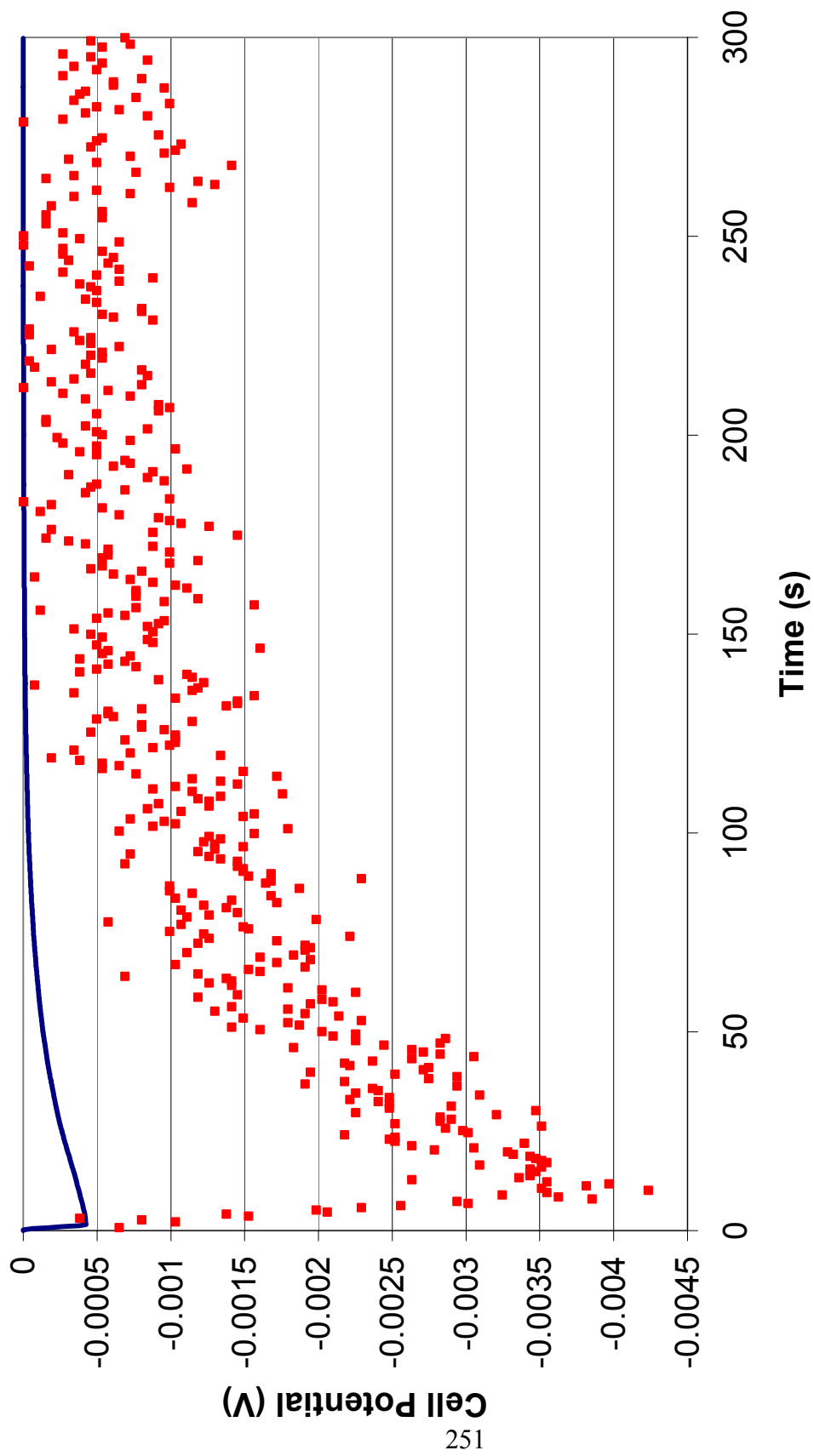


Figure 9.7. Stirred model potential predictions for cell #22 in a stack at 500 W plotted as a function of time relative to a 10 cm<sup>3</sup> pulse injection of Ar.

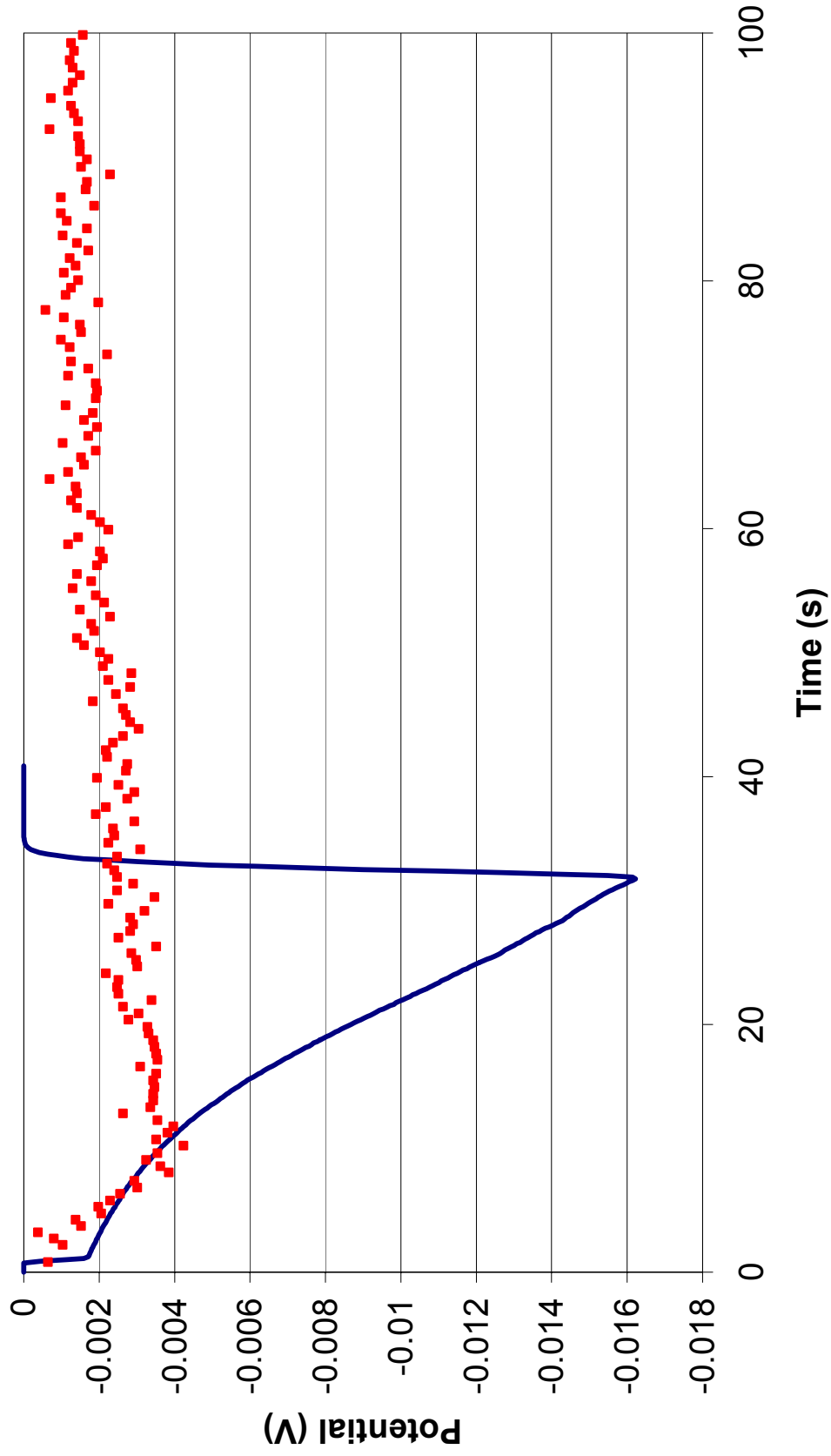
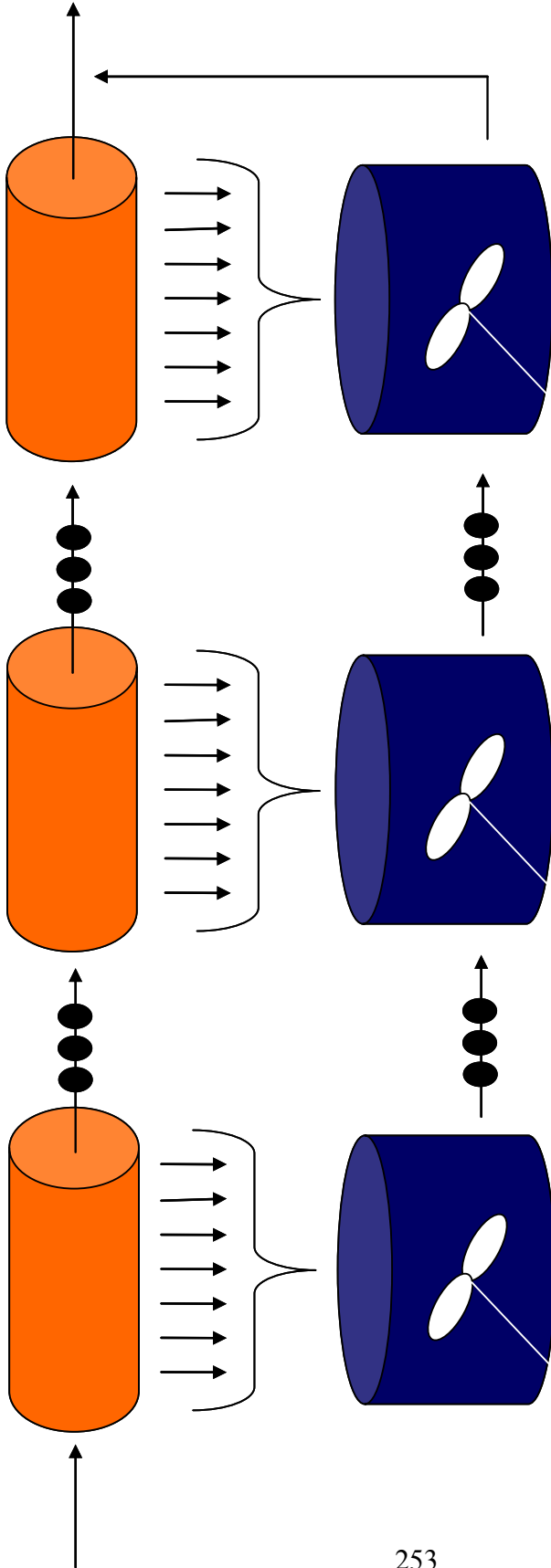


Figure 9.8. Plug model potential predictions for cell #22 in a stack at 500 W plotted as a function of time relative to a 10 cm<sup>3</sup> pulse injection of Ar.

## Flow Channels



## GDL

**Figure 9.9.** Diagram of the mixed model, wherein the flow channels are modeled with many tanks-in-series behaving plug-like, and the GDL is modeled with few tanks-in-series behaving stirred-like. The ellipses denote that more tanks exist in the model than the few shown in the diagram.

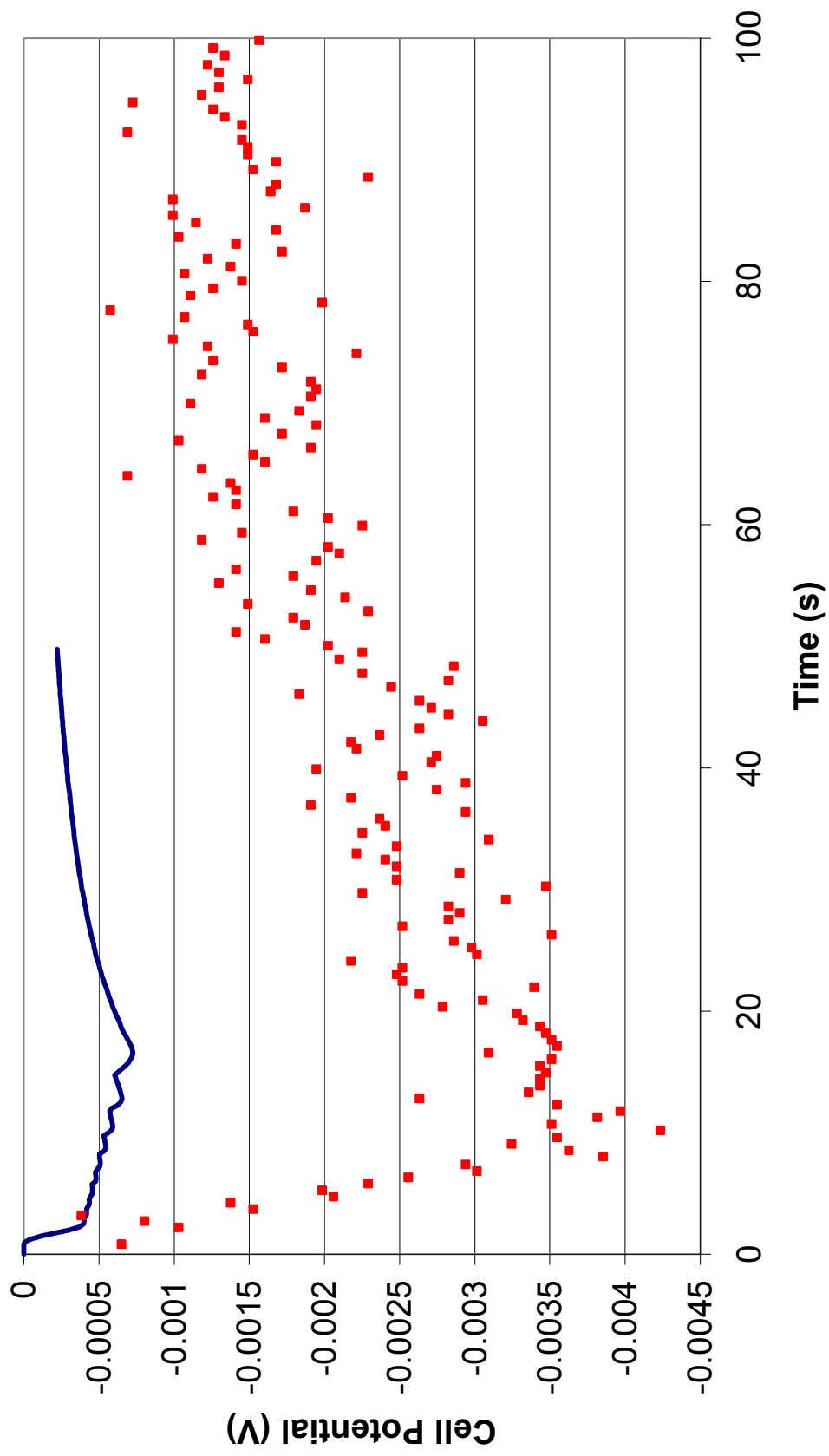


Figure 9.10. Mixed model potential predictions for cell #22 in a stack at 500 W plotted as a function of time relative to a 10 cm<sup>3</sup> pulse injection of Ar.

## Chapter X

### Conclusions and Recommendations for Future Work

#### X.1. Conclusions

The research presented in this dissertation demonstrates how commercial fuel cell stacks and their cells may be tested and analyzed to obtain meaningful results. Because fuel cells are electrochemical systems, their performance is assessed by multidisciplinary means. The duality of electrochemistry is evident in the procedures previously described in the text: stack uniformity, mass and energy balances, and residence time distribution are classical chemical engineering techniques, while impedance spectroscopy, equivalent circuit models, and circuit simulation are of a more electrical nature.

##### *X.1.1. Chemical Techniques*

Reactor uniformity, mass balances, and residence time distribution theory are chemical engineering techniques that were applied to fuel cells in the work presented in this dissertation. Reactor (cell/stack) uniformity was discussed in chapter III, which revealed the variation between different stacks and cells within each stack. The knowledge of which cells in a stack are limiting its performance is crucial to improving stack layout and assessing the manufacturing consistency of cells and stacks. Chapter IV outlined the use of a modified stack with a continuously open anode outlet, the critical flow of which was calculated from species mass balances. The steady exhaust stream

improved stack impurity tolerance, which is significantly low under the default operating scheme. The residence time distribution of gases flowing through a stack was measured and presented in chapter IX, which showed in which cells feed impurities accumulate and to what extent. The ability to spatially evaluate gas distribution is useful for improving stack layout and impurity tolerance.

### *X.1.2. Electric Techniques*

Despite the fact that this work is a chemical engineering dissertation, techniques that are more electrically based were necessary to employ, because fuel cells are ultimately sources of electrical power. Impedance spectroscopy was utilized extensively throughout chapters V–VIII to assess the dynamic behavior of fuel cell stacks and the cells therein at load. The ability to collect impedance data for an entire polymer electrolyte membrane (PEM) fuel cell stack and smaller groups of cells within the stack was discussed in chapter V, which laid the foundation for the subsequent chapters. The next chapter (VI) demonstrated how impedance data was fitted to equivalent circuit models, which were applied to circuit simulations of PEM stack pairs in series and parallel. The simulations agreed closely with physical tests performed at the simulated load conditions confirming the beneficial use of impedance spectroscopy to assess stack output at varying loads. AC impedance was also implemented in chapter VII to formulate equivalent circuit models for solid oxide fuel cell (SOFC) anodes, cathodes, cells, and stacks at load. The electrical techniques described above were related to chemical principles in chapter VIII, wherein the computation of reaction rate constants from equivalent circuit model fits was detailed. Testing the dynamic behavior of fuel

cells under significant load (as in Chapters V–VIII) is unique to the work presented in this dissertation.

## **X.2. Recommendations for Future Work**

The following section briefly outlines the suggested future direction of this project including more SOFC work, stack modifications for the determination of kinetic constants, and improvements in residence time distribution (RTD) studies.

### *X.2.1. Further SOFC Applications*

Further opportunities exist for studying SOFCs based on the success of the work presented in chapter VII. To improve the results already presented, the exact cause of the low frequency loop needs to be resolved, which may be achieved by increasing the number of anode feed compositions tested and changing electrode and/or electrolyte (i.e. diffusion layer) thickness. Other alterations may be made to feed compositions, such as cathode oxygen concentration and adding CO to the anode mix. Air was the only oxidant fed to the cathode, so increasing oxygen concentration may help in deducing the oxygen reaction mechanism and the cause of the low frequency impedance loop. Because CO is oxidized on SOFC anodes, button cell anodes fed with mixtures of CO should exhibit different impedance spectra than those in chapter VII. Likely a parallel charge-transfer path would need to be added to the anode equivalent circuit model to account for CO oxidation. A less theoretical experiment is to apply the circuit simulation technique described in chapter VI to SOFC stacks and to test the results against measured data, in much the same manner as already performed on PEM stacks. In addition to the planar cells that have been examined, tubular SOFCs may also be tested and analyzed under the same conditions to contrast the differences between the two geometries. Changing feed

compositions and component thicknesses, performing dynamic circuit simulations, and probing tubular stacks are a few of the many possible future directions, in which the SOFC testing project may proceed.

### *X.2.2. Improving Evaluation of Kinetic Constants*

A couple of modifications must be made to ensure favorable results in determining the kinetic rate constants of a PEM cell, which was discussed in chapter VIII. Installing a reference electrode into the Nexa™ stack would improve the accuracy of the data fits, because the anode and cathode could be probed separately. The reference would have to be inserted into one of the cells on either end of the stack due to the bipolar nature of the interior plates. Additionally, the accuracy of the correlations between rate constants and circuit elements could be improved, because in the referenced work, the expressions were derived based on an oversimplified Butler-Volmer expression. Rederiving the equations for the equivalent circuit elements and installing a reference electrode in the stack would greatly improve the ability to accurately compute the rate constants for a PEM cell from impedance spectra.

### *X.2.3. Improving RTD Measurements*

The purpose for the RTD work presented in chapter IX is to obtain a working mathematical model to predict the RTD curves associated with impure gas flow in a PEM fuel cell stack. Before a stack model can be proposed, a single cell model must accurately predict cell voltage. The three models that have been attempted have failed; thus, the primary future objective is to derive an accurate model. There are an infinite number of modifications that can be made to the existing models, such as accounting for mixed convection and diffusion. Using a step change in impurity concentration instead



of a pulse experiment should be simpler scenario to model and could form the basis of a model for the pulse tests. Once a model has been obtained that accurately predicts the behavior of a single cell, said model may be applied to all of the cells in the stack according to the stack layout. Afterward, impurities with different properties may be input to the stack to further test the model. In summary, the most effective way to improve the RTD work is by obtaining a model that accurately predicts the steady-state behavior of a cell in the stack. While presenting useful information on its own, the work contained in this dissertation may also be expanded upon for further insight into fuel cell power production.